Phase Inversion in dispersed liquid-liquid pipe flow

Kwun Ho Ngan

A thesis submitted to University College London in fulfillment of the requirements

for the degree of Doctor of Philosophy

Department of Chemical Engineering

University College London

London WC1E 7JE

October 2010

*To my family
and Ting Ting*

Abstract

This thesis presents the experimental and theoretical investigations on the development of phase inversion in horizontal pipeline flow of two immiscible liquids. It aims to provide an understanding on the flow development across the phase inversion transition as well as the effect on pressure drop.

Experimental investigation on phase inversion and associated phenomena were conducted in a 38mm I.D. liquid pipeline flow facility available in the Department of Chemical Engineering at University College London (UCL). Two sets of test pipelines are constructed using stainless steel and acrylic. The inlet section of the pipeline has also been designed in two different configurations – (1) Y-junction inlet to allow dispersed flow to be developed along the pipeline (2) Dispersed inlet to allow formation of dispersion immediately after the two phases are joined. Pressure drop along the pipeline is measured using a differential pressure transducer and is studied for changes due to redistribution of the phases during inversion. Various conductivity probes (ring probes, wire probes, electrical resistance tomography and dual impedance probe) are installed along the pipeline to detect the change in phase continuity and distribution as well as drop size distribution based on the difference in conductivity of the oil and water phases.

During the investigation, the occurrence of phase inversion is firstly investigated and the gradual transition during the process is identified. The range of phase fraction at which the transition occurs is determined. The range of phase fraction becomes significantly narrower when the dispersed inlet is used. The outcome of the investigation also becomes the basis for subsequent investigation with the addition of glycerol to the water phase to reduce the interfacial tension. Based on the experimental outcome, the addition of glycerol does not affect the inversion of the oil phase while enhancing the continuity of the water phase.

As observed experimentally, significant changes in pressure gradient can be observed particularly during phase inversion. Previous literatures have also reviewed that phase inversion occurs at the maximum pressure gradient. In a horizontal pipeline, pressure gradient is primarily caused by the frictional shear on the fluid flow in the pipe and, in turn, is significantly affected by the fluid viscosities. A study is conducted to investigate on the phase inversion point by identifying the maximum mixture viscosity (i.e. maximum pressure gradient) that an oil-in-water (O/W) and water-in-oil (W/O) dispersion can sustain. It is proposed that the mixture viscosity will not increase further with an increase in the initial dispersed phase if the inverted dispersion has a lower mixture viscosity. This hypothesis has been applied across a wide range of liquid-liquid dispersion with good results. This study however cannot determine the hysteresis effect which is possibly caused by inhomogeneous inversion in the fluid system.

A mechanistic model is developed to predict the flow characteristics as well as the pressure gradient during a phase inversion transition. It aims to predict the observed change in flow pattern from a fully dispersed flow to a dual continuous flow during phase inversion transition. The existence of the interfacial height provides a selection criterion to determine whether a momentum balance model for homogeneous flow or a two-fluid layered flow should be applied to calculate the pressure gradient. A friction factor is also applied to account for the drag reduction in a dispersed flow. This developed model shows reasonable results in predicting the switch between flow patterns (i.e. the boundaries for the phase inversion transition) and the corresponding pressure gradient.

Lastly, computational fluid dynamic (CFD) simulation is applied to identify the key interphase forces in a dispersed flow. The study has also attempted to test the limitation of existing interphase force models to densely dispersed flow. From the study, it is found that the lift force and the turbulent dispersion forces are significant to the phase distribution in a dispersed flow. It also provides a possible explanation to the observed flow distribution in the experiments conducted. However, the models available in CFX are still unable to predict well in a dense dispersion (60% dispersed). This study is also

suggested to form the basis for more detailed work in future to optimize the simulation models to improve the prediction of phase inversion in a CFD simulation.

Acknowledgement

Table of Contents

List of Figures

9

Chapter 3

Chapter 4

13

Chapter 5

16

Chapter 6

Appendix A

Appendix C

List of Tables

Nomenclature

Roman symbols

A	cross sectional area
C	coefficient in Equation 2.11
C_D	drag force coefficient
C_L	lift force coefficient
CLD	chord length distribution
C_{TD}	turbulent dispersion force coefficient
(dP/dx)	pressure drop
D	pipe diameter
d	drop diameter
d_{max}	maximum drop diameter
d_{10}	linear mean diameter
d_{32} (D_{32})	Sauter mean diameter
d_{95}	drop diameter of 95% percentile
DSD	drop size distribution
E	steady state entrainment fraction
Entl	entrainment fraction at lower layer
Entu	entrainment fraction at upper layer
Eo	Eötvös number
ERT	electrical resistance tomography
F	force
F_D	drag force term
F_{lift}	lift force term

F_M	interphase force term
F_{TD}	turbulent dispersion force term
f	friction factor
f_{DR}	friction factor with drag reduction used in Equation 7.8
Fr	Froude number
g	gravity
I	turbulence intensity
K	constant used in Equation 2.5.
k	turbulent kinetic energy
k	crowding factor in Equation 6.10
k_1	coefficient used in Equation 2.11
k_1	coefficient used in Table 2.5
k_2	coefficient used in Equation 2.11
k_2	coefficient used in Table 2.5
k_D	empirical deposition rate constant used in Equation 7.2
L	turbulent length scale
N	agitation speed
n	number density
n	coefficient used in Equation 2.11
n	coefficient used in Equation 2.12
n	coefficient used in Equation 7.8
O	oil
OC	oil continuous
O/W	oil-in-water
ΔP	pressure gradient

P_k	shear production of turbulence
Q	volumetric flowrate
QCV	quick closing valve
r	drop radius
R_b	rate of drop break-up
R_c	rate of drop coalescence
R_{dep}	rate of deposition
R_{ent}	entrainment rate
Re	Reynolds number
S	perimeter
S	source term
S	slip ratio
S_i	length of interface
S_v	slip ratio
T	Reynolds stress tensor
T_{cd}	Turbulence modulation terms used in Equation 2.30 and 2.31
t	time
U	velocity
U^*	frictional velocity used in Equation 7.3 and 7.4
V_{cum}	cumulative volume fraction of drops
V_{ent}	volume of entrainment fraction
W	water
WC	water continuous
W_d	mass flow rate of the dispersed phase used in Equation 7.2
We	Weber number

WF$_{critical}$	critical water fraction
W/O	water-in-oil

Greek symbols

α	volume fraction
Δ	change
ε	energy dissipation rate
μ	viscosity
μ$_\varphi$	effective viscosity used in Chapter 6
μ$_r$	relative viscosity used in Table 6.1
π	pi
ρ	density
τ	shear stress
σ	interfacial tension
λ	wavelength
Φ	phase fraction
Φ	dispersed phase fraction in Equation 6.1
Φ$_{max}$	maximum packing factor
φ	phase fraction
δ$_{xy}$	Kronecker delta
θ	contact angle
υ	viscosity

Subscripts

c	continuous phase
d	dipsersed phase
I	interfacial
i	interfacial
l	lower
m	mixture
o	oil
s	superficial
t	turbulent
u	upper
w	water

Superscripts

I	inversion

Chapter 1: Introduction

1.1 MULTIPHASE FLOW IN PETROLEUM INDUSTRY

In an offshore oil production operation, crude oil is pumped from the reservoirs through the wellhead and pipelines to the processing platform or FPSO (floating platform, storage and offloading) unit where phase separation will take place. Along the transportation pipeline, the crude oil stream will tend to contain a percentage of water due to natural inclusion of groundwater, leakage along the long pipeline, or deliberate injection of water into the reservoir to enhance oil recovery. Water content tends to increase as the well ages and, at some extreme situation, wells are still in operation with a production stream of 98% of water or more. Gas may also be present especially at the riser when the production stream undergoes a pressure reduction from the reservoir. As such, a mixture of fluids is generally flowing simultaneously in the pipeline. This type of flow stream is commonly known as multiphase flow.
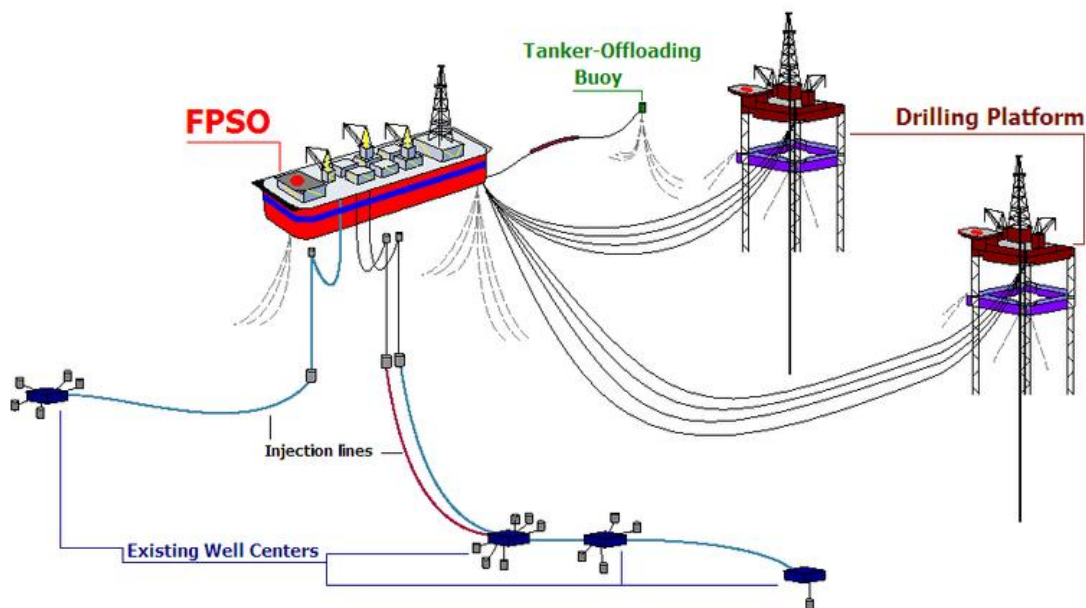
Figure 1.1 Offshore production pipeline schematic from well centres to production platforms and FPSO.

As oil exploitation has moved further from shore, hostile climate and greater water depth threaten the construction of oil production platforms. Many satellite wells have to be connected and relayed to existing platforms through long transportation pipelines. A complex network of pipeline is thus developed. Maintaining the consistency of the fluid flow becomes a technical challenge. The situation is worsened with depleting well where the reservoir pressure is no longer sufficient to drive the flow.

In order to combat the increasing operating costs for offshore production while maintaining high efficiency and consistency for oil recovery, technological advances have been ongoing which have led to various technology commercialisation. For example, multiphase boosting technology was introduced offshore to ensure that oil recovery will not be disrupted by insufficient reservoir pressure and, preferably, can also be enhanced by artificial boosting. The first commercial subsea multiphase boosting system is the Shell multiphase underwater booster system (Smubs). A review on the deployment of multiphase technology in the North Sea is presented in Leporcher et. al (2001) with a focused case study on the DUNBAR project.

Currently, R&D in multiphase technology is still on high demand to tackle the continual challenge on the demand for crude oil. Understanding the nature of these multiphase flows has been complex and this is especially the case with oil/water mixture flow. Literatures on the simultaneous flow of oil/water mixture has become more transparent over the recent years. These literatures have primarily presented the different flow regimes that can be observed across a wide range of operating conditions. Some authors have extended the scope to review the effect of flow regime changes on pressure gradient across pipeline (e.g. Angeli & Hewitt, 1998; Ioannou, 2006; Trallero, 1995; Pal 1993).

1.2 FUNDAMENTALS OF MULTIPHASE FLOW

In this thesis, multiphase flow refers to fluid flow with two immiscible phases. In particular, oil/water flow will be focused to extend the investigation on this system. One of the most significant differences between two-phase flow and single phase flow is the presence of flow regimes (i.e. how the two phases are distributed). The development of

these flow regimes are determined by the change of operational condition (e.g. the input flow velocities of the phases and the way they are introduced). Other influencing factors, e.g. fluid rheological properties and pipe material, can also significantly affect the spatial distribution of the phases. The effect of some of these influencing factors will be investigated and presented in subsequent chapters.

1.2.1 THE OCCURRENCE OF PHASE INVERSION

As the flow rate increases or the Reynolds number is sufficiently high, one of the phases may be broken up into dispersed drops in the continuum of the other phase. If the concentration of the dispersed phase is gradually increased, this phase will become closely packed and, at some point, the drops coalesce and the phase continuity will switch. The initial continuous phase will on the other hand become dispersed as a result. The change of phase continuity is generally referred to as phase inversion. The corresponding phase fraction at which this change occurs is called the phase inversion point. The occurrence of a catastrophic inversion process is however arguable.

Phase inversion investigation begins from work in agitated vessels where two immiscible liquids are mixed. Experimental results showed that a hysteresis effect occurs between the inversions from either phase as the continuous phase (i.e. the dispersed phase tends to remain dispersed). This results in the formation of an ambivalent region (i.e. a range of phase fractions) over which either phase can be continuous (Selker and Sleicher, 1965; Luhning and Sawistowski, 1971; Arashmid and Jefferys, 1980). Literature reviews that the width of the ambivalent region is dependent on the initial setup condition, viscosity ratio of the two phases as well as the vessel wall material.

The occurrence of phase inversion will lead to changes in the system with different rheology. Understanding the phase inversion process is thus important as its occurrence can be beneficial (e.g. polymerisation) or catastrophic (e.g. significant changes in pressure gradient in pipeline). Failure to account for the occurrence of phase inversion can lead to reduced pipeline capacity and lower oil productivity.

In addition to the experimental investigation on the behaviour of the mixture flow during phase inversion, research has also been conducted to predict the critical phase fraction at which phase inversion occurs (e.g. Yeh et al., 1964; Luhning & Sawistowski, 1971; Arashmid & Jefferys, 1980; Brauner & Ullman, 2002). However without a well developed understanding on the actual mechanism for phase inversion, the suggested models still have a wide discrepancy between the prediction and the actual experimental results.

1.3 OBJECTIVES OF STUDY

The work presented in this thesis summarizes the work conducted at the University College London (UCL). The main aim of the work is to gain further understanding on the phase inversion process and subsequently evaluate the effects of various influencing conditions on the change in phase inversion occurrence as well as the corresponding impact on the flow. Prediction models for phase inversion and simulation of highly concentrated dispersion will aim to identify improvement to better account for the phase distribution and inversion especially for scenarios where experimental investigation is not permitted.

The objectives for the experimental and theoretical investigations can be summarized as follows:

Objectives for experimental investigation:

(1) To understand the flow development and the formation of flow regimes which will eventually lead to the onset of phase inversion as the operating conditions are changed.

(2) To investigate the occurrence of phase inversion using various measurement techniques and account for the spatial distribution during the phase inversion process. In addition, measurement of pressure gradient will be made as the indication on the energy requirement for the fluid flow during phase inversion.

(3) To investigate the effect of various influencing factors (e.g. fluid rheology, pipe materials, etc) on phase inversion occurrence. It will also be made available the corresponding effect on pressure gradient due to the changes.

(4) To apply the developed technology of dual impedance probe for the investigation on the changes in drop size distribution during phase inversion. This will aid in the learning on the mechanism of phase inversion based on the drop coalescence and break-up.

(5) To obtain the necessary data in the development of prediction models as well as input conditions necessary for computational simulation of dense dispersed flow.

Objectives for numerical modelling:

(1) To apply the mechanism of momentum balance of the fluids and predict the critical phase fraction for phase inversion to occur.

(2) To predict the flow conditions during phase inversion based on the momentum balance of the fluid flow.

(3) To establish an understanding on the fluid motion of densely dispersed two-phase flow through computational simulations.

1.4 STRUCTURE OF THE THESIS

In order to achieve the thesis objectives, the investigations described in this thesis is organised as follows. A literature review is conducted in Chapter 2 to cover past studies on the experimental conditions at which phase inversion occurs and the associated phenomena. It also covers the theoretical studies on the mechanism causing the occurrence of inversion. Lastly, literatures covering the application of computational fluid dynamics are also reviewed to apply the necessary techniques for simulation studies.

Chapter 3 presents the experimental facilities at which the occurrence of phase inversion will be investigated. The instrumentations used in the experimental investigations will be described in detail. The use of these instrumentation and the presentation of how phase inversion is developed in an oil/water system is presented in Chapter 4. The associated

change in the drop size distribution of the dispersed phase and pressure gradient will also be discussed. In Chapter 5, the effect of changing the interfacial tension of the oil/water system is tested by the addition of glycerol. The investigation will provide an understanding on the corresponding changes to the phase distribution, drop size and associated pressure gradient.

In Chapter 6, a prediction model is developed to estimate the critical phase fraction at which phase inversion will occur based on the criteria of momentum balance. This model development was initiated due to the observation of a peak in pressure gradient at near to the phase inversion point. Chapter 7 extends on the development in Chapter 6 and other models developed in UCL (e.g. the entrainment model by Al-wahaibi and Angeli (2009)) to predict the phase distribution and corresponding pressure gradient based on the momentum balance. A selection criterion is thus developed to select either the homogenous mixture model or the two-fluid model for the determination of the pressure gradient.

In Chapter 8, an attempt is made to establish an understanding on the fluid motion of a densely dispersed two-phase system through computational fluid dynamics. Various interphase forces are studied to identify their significance in distributing the two phases. Current limitations of CFD for dense dispersion will also be discussed.

Lastly, an overview on the investigation outcome will be presented in Chapter 9 and future works are recommended for review.

Chapter 2: Literature Review

2.1 OVERVIEW

This chapter presents a review of both experimental and theoretical studies on phase inversion during oil-water flows. In Section 2.2, the liquid-liquid flow regimes in pipelines and the relevant flow pattern maps will be reviewed. Section 2.3 discusses the occurrence of phase inversion together with the effect of various parameters both in stirred vessels and pipelines. Prediction models for phase inversion are then presented in Section 2.4 based on several proposed inversion mechanisms. Among the model parameters, drop size of the dispersed phase and its distribution is regarded to be important. Observation of various types of drop size distributions in experiments are presented in Section 2.5 and commonly used characteristic diameters for drop size will also be introduced. In addition, understanding of the interaction between the fluid phases in a dispersed flow is important but complex. In Section 2.6, the use of computational fluid dynamics (CFD) simulations to predict the interactions of the fluid phases in an oil-water mixture pipe flow will be discussed. Various closure equations and interphase force correlations will be presented in Section 2.7. Section 2.8 discusses on the conclusions from the reviews.

2.2 FLOW DEVELOPMENT AND FLOW PATTERN MAPS

When two immiscible fluids flow simultaneously in a pipeline (e.g. oil-water flow), a number of different flow regimes will appear depending on how the phases are distributed in a pipe cross section.

The identification of flow regimes is usually studied through visual observations and image recording with high speed cameras. However, visual techniques do not always offer a clear indication of regime transitions and of the oil-water interface especially at high velocities. As such, flow regime transitions are also determined by indirect methods based on the associated flow characteristics (e.g. pressure drop, conductivity, etc). Pressure gradient, for example, will show significant changes during flow regime

transitions. Al-Sarkhi and Soleimani (2004) attributed the pressure gradient changes, during transition from smooth stratified to slug flow, to the formation of interfacial waves that cause significant increase in interfacial and wall shear stresses. Conductivity is also widely used as an indicator for phase distribution if one of the phases is non-conductive. The conductivity methods for detecting the distribution of the two phases also set the foundation for the development of commercialized instruments such as electrical capacitance tomography (ECT) and electrical resistance tomography (ERT).

The experimental observations of these flow regimes are typically mapped with respect to either the fluid superficial velocities or mixture velocities, or phase fraction. An example is presented in Figure 2.1 from the work of N äller and Mewes (1997). It can be seen that different flow patterns can emerge depending on the variations of fluid flow rates or their phase fraction. A number of different names have been given by various investigators on the flow patterns (see Table 2.1).

(a)   (b)
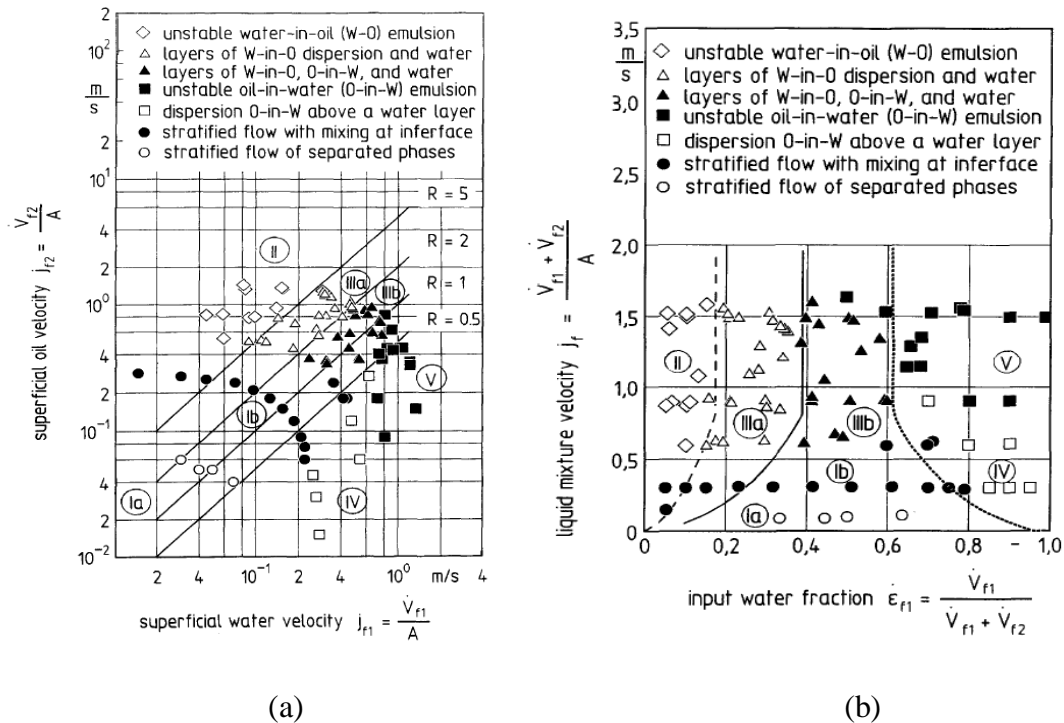
Figure 2.1: (a) Flow regime map that is based on the fluid superficial velocities (b) Flow regime map that is based on input water fraction and mixture velocity.

35

Author	Flow pattern classifications
Russell et al. (1959)	Oil Bubbles in water Stratified flow (SF) Mixed Flow
Guzhov et al. (1973)	Stratified flow SF with mixing at the interface and a water lower layer SF with mixing at the interface and a lower layer of oil/water dispersion Water/oil and oil/water emulsions w/o emulsion oil/water emulsion and a water lower layer oil/water emulsion and a lower layer of oil/water dispersion o/w emulsion
Oglesby (1979)	Segregated Semi-segregated Semi-mixed (oil dominant, water dominant) Mixed (oil dominant, water dominant) Annular or concentric core of one phase within the phase (oil dominant, water dominant) Slug: Phases alternatively occupying the pipe as a free phase or as a dispersion phase (oil dominant, water dominant) Semi-dispersed (oil dominant, water dominant) Fully-dispersed: homogeneous mixture (oil dominant, water dominant)
Nädler & Mewes (1995)	Stratified flow SF with mixing at the interface and a water lower layer SF oil/water dispersion and a water lower layer o/w emulsion SF water/oil dispersion, oil/water dispersion and a water lower layer SF water/oil dispersion and a water lower layer w/o emulsion
Trallero (1995)	Stratified flow SF with mixing at the interface o/w dispersion and free water layer w/o dispersion and o/w dispersion Full o/w emulsion Full w/o emulsion
Brauner (2002)	Stratified flow SF with mixing at the interface SF with a free liquid and a dispersion of another liquid ($D_{o/w}$&w) SF with a free liquid and a dispersion of another liquid ($D_{w/o}$&w) w/o dispersion above o/w dispersion w/o dispersion above o/w dispersion with pure oil at the top and pure water at the bottom Full o/w dispersion Full w/o dispersion Core-annular flow (viscous oil in core and water in annulus) Core-annular flow (water in core and oil in annulus) Core-annular flow (dispersion of w/o in core and water in annulus) Core-annular flow (dispersion of o/w in core and oil in annulus) Core-annular flow (dispersion of one phase in core and dispersion of another in annulus) Intermittent flow Elongated or spherical bubbles of one phase in a continuum of another phase

Table 2.1: Flow pattern classification suggested in various literature.

The main ones are stratified flow, annular flow, dual continuous flow and dispersed flow and are described in more detail below:

a) Stratified flow (ST) – (Figure 2.2a): Stratified flows are generally occurring at low flow rates. Each of the oil and water layers flows as a continuum with a distinct liquid-liquid interface. At the low flow rates, the flow is dominated by the gravitational effect rather than inertia. As such, the separation of the two layers is based on the density difference between the two phases. The oil phase (i.e. the lighter phase) occupies the upper layer while the water phase occupies the lower layer. As the flow rate is increased, waves of various lengths and amplitudes will form at the interface and droplets of one phase may be entrained into the other leading to a transition into the dual continuous flow pattern. A description of this transition is presented by Al-Wahaibi et al. (2007).
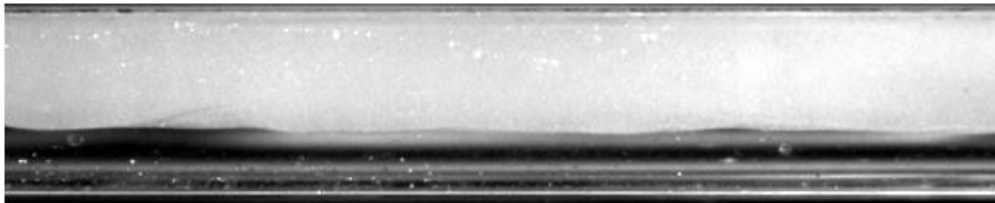
(a)
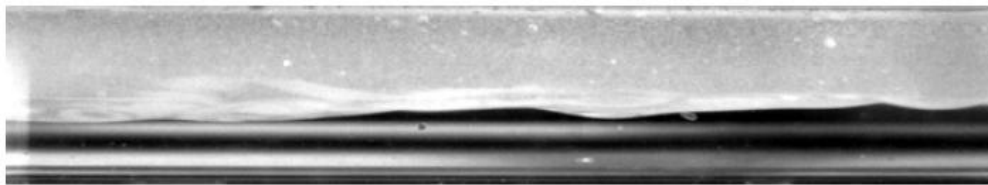
(b)

Figure 2.2: (a) Stratified smooth flow (b) stratified wavy flow with the oil phase on the top layer while the water phase on the bottom layer. (Ngan et al., 2007)

b) Dual continuous flow (DC) – (Figure 2.3): Dual continuous flow generally occurs at intermediate mixture velocities between stratified and fully dispersed flows. The oil and water phases retain their continuity and there is a distinct interface between them. However, one or both phases are entrained into the other as drops. The degree of entrainment varies according to the fluid velocities.

37

The transition into a dual continuous flow generally begins with wave formation from a stratified flow. The interfacial waves are initially long compared to the pipe diameter. As the fluid velocities increase, these waves become shorter. Guzhov et al. (1973) reported that the relative movement of the two liquid phases causes vortex motions due to the shear forces that penetrate the interface boundary. This causes the formation of small droplets of one phase into the other (and is regarded as the onset of entrainment). Once the drops are entrained, the distribution of these drops will depend on the balance between inertial and gravitational forces. At low flow rates, the entrained drops are few and gravity tends to keep them near to the fluid interface. This flow pattern is sometimes referred to as stratified flow with mixing dispersion at the interface. As the flow rate increases, the degree of entrainment increases as drops are more evenly distributed in the opposite layer due to the increased importance of the inertial forces.

Figure 2.3: Dual continuous flow with several oil drops entrained in the water continuous layer. (Ngan et al., 2007)

c) Annular flow (AN) – (Figure 2.4): A core of one phase is surrounded by an annulus of the other. This flow pattern is common when the two phases have equal densities or when one of the phases has a very high viscosity (Russell and Charles, 1959).
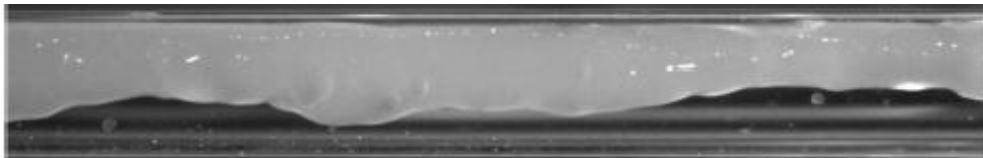
Figure 2.4: Annular flow with an oil core and a water annulus. Small amount of drops are also observed within the oil core in the figure. (Ngan et al., 2007)

d) Dispersed flow (D) – (Figure 2.5): One of the phases loses its continuity and forms drops in the continuum of the other. This pattern occurs at high velocities. There is usually a distribution of drop sizes which depends on the balance of drop break-up and coalescence events. Drops can also be deformed and the deviation from their sphericity can have significant impact on the mixture flow. In addition, gravitational forces affect the vertical concentration of these drops leading to a spatial distribution.

(a)
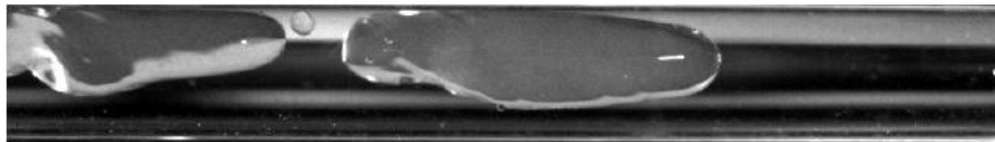
(b)

Figure 2.5: (a) Dispersed flow of oil drops in water. Drops observed are polydispersed and highly deformable. (b) Oil slug flow in water (Ngan et al., 2007).

2.3 PHASE INVERSION

Phase inversion is a commonly observed phenomenon in dispersed liquid-liquid mixtures (e.g. in pipe flow or in stirred vessels) but its mechanism is still not well understood. Two types of dispersions are generally found (i.e. oil-in-water and water-in-oil) according to the phase fraction and initial conditions. Phase inversion is generally found when the mixture undergoes changes in the phase distribution as the phase fraction reaches certain critical values (Yeh et al., 1964; Arirachakaran et al., 1989; Pal, 1993; Pacek et al., 1994; Elseth, 2001; Ioannou et al., 2005; Hu, 2005; Piela et al., 2008). The critical phase fraction where inversion occurs is known as *phase inversion point*. Coalescence and break-up of the dispersed phase occur continuously in a dispersion. At low dispersed

phase fractions, this dynamic process can reach equilibrium. As the dispersed phase fraction increases, the process may be unbalanced and coalescence becomes more prominent due to the proximity of the dispersed drops. Eventually, phase inversion will occur when the two phases switch their continuity. The occurrence of phase inversion and the changes in phase continuity can lead to substantial changes in the mixture rheology causing large fluctuations in pressure gradient during pipe flow (Angeli, 1996; Nädler and Mewes, 1995).

Arirachakaran et al. (1989) has presented the development of the phase inversion process as the initial water dispersed phase fraction is increased (see Figure 2.6). Some authors have suggested that the inversion process is rapid and catastrophic (Smith and Lim, 1990; Tyrode et al., 2005; Vaessen et al., 1996). However, other investigations suggest a gradual inversion process particularly during pipe flow (e.g. Liu, 2005; Piela et al., 2008) when partial inversion occurs at a certain location before the entire mixture is inverted. The details of these observations will be discussed in the subsequent sections on phase inversion in stirred vessels and pipe flow.
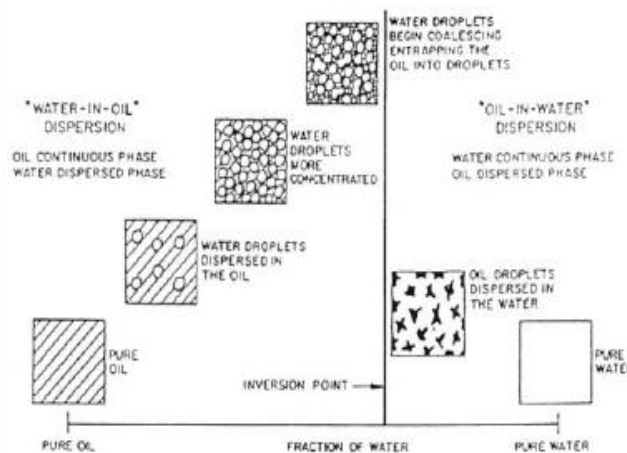
Figure 2.6: A schematic on the proposed phase inversion mechanism by Arirachakaran et al. (1989).

2.3.1 PHASE INVERSION IN STIRRED VESSELS

Investigations on phase inversion have mainly been carried out in stirred vessels and the outcomes from these works can provide valuable information on the phenomenon in pipe flow. Reviews of literature available on phase inversion in stirred vessels can be found in Yeo et al. (2000), Liu (2005) and Hu (2005).

One of the interesting findings in stirred vessel is the hysteresis effect observed when inversion is approached from a water continuous or from an oil continuous dispersion. The term *ambivalent region* has been introduced to define the region of phase fractions where either dispersion can exist. Thus, either type of dispersion can only be clearly defined beyond the ambivalent region. Figure 2.7 presents experimentally found ambivalent region (Noui-Mehidi et al., 2004).
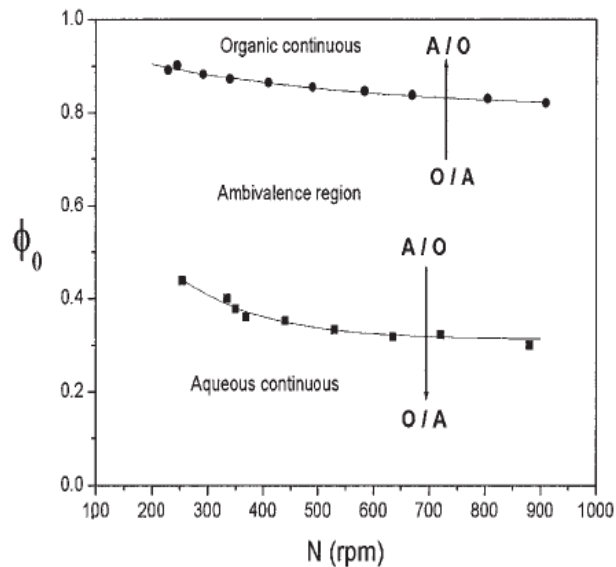
Figure 2.7: The existence of ambivalent region between the aqueous and organic continuous dispersion across the organic phase fraction (Φ_o) (Noui-Mehidi et al., 2004).

Pacek et al. (1994) used video recording to capture the phase inversion process in a stirred vessel and found that the drop size increased significantly near inversion while secondary droplets (i.e. continuous phase drops within the dispersed phase) are formed

41

(Figure 2.8). Pacek et al. (1994) also found that secondary droplets only occur for chlorobenzene in the dispersed glycerol/water phase but not in the opposite dispersion. This difference in the formation of secondary droplets between the organic and the aqueous continuous dispersions could be responsible for the appearance of the ambivalent region. The formation of secondary droplet can have a significant widening in the ambivalent region and hysteresis effect during phase inversion. According to them, the coalescence of the dispersed phase is the most important mechanism controlling phase inversion.
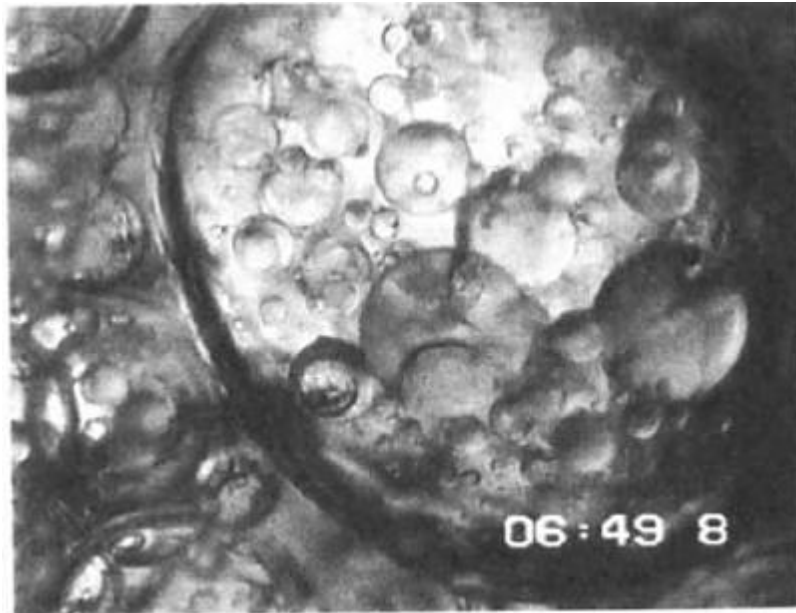
Figure 2.8: Droplet in drop for a glycerol/water and chlorobenzene system captured by Sony video printer (Pacek et al., 1994).

Phase inversion and the ambivalent region are affected by many parameters. For example, Selker and Sleicher (1965) found that the properties of the apparatus used (i.e. size and materials of the vessel and impellers) and the operational conditions (i.e. agitation speed, phase fraction) did not affect significantly the phase inversion. Deshpande & Kumar (2003) also found that the limits of the ambivalent region reach asymptotic values at high agitation speed and thus depend only on properties of the fluid system. According to

Selker and Sleicher (1965), fluid density would affect the ambivalent boundaries if the agitation is slow and settling of the denser phase is prominent. The phase with higher viscosity is also more likely to be the dispersed one. Viscosity also affects the ambivalent region probably because of the lower coalescence rates caused by longer film drainage time (Coulaloglou and Tavlarides, 1977). Interfacial tension has also been reported as an important factor affecting phase inversion. Luhning & Sawistowski (1971) and Norato et al. (1998), for example, showed that a decrease in interfacial tension can lead to a widening of the ambivalent region.

Various empirical correlations have been developed from experiments to predict the boundaries of the ambivalent region. The critical phase fraction of the organic phase, Φ_o, was given by:

Luhning and Sawistowski (1971) for impeller speed between 600 to 1360 rpm:

(1) $\Phi_{o,i} = 0.160 + 6.0 \times 10^{-5}(\text{We}_I)$ for the upper inversion curve (w/o $\rightarrow$ o/w) (2.1)

(2) $\Phi_{o,i} = 0.470 + 2.0 \times 10^{-5}(\text{We}_I)$ for the lower inversion curve (o/w $\rightarrow$ w/o) (2.2)

Fakhr-Din (1973) for impeller speed below 680.85rpm:

(1) $\Phi_{o,i} = 1.32 \times 10^6 \left(\frac{\mu_d}{\mu_c}\right)^{0.32} \left(\frac{\Delta\rho}{\rho_c}\right)^{-0.11} \text{Fr}_I^{0.71} \text{Re}_I^{1.06} \text{We}_I^{-0.25}$ for the upper curve (2.3)

(2) $\Phi_{o,i} = 12.2 \left(\frac{\mu_d}{\mu_c}\right)^{0.31} \left(\frac{\Delta\rho}{\rho_c}\right)^{-0.04} \text{Fr}_I^{0.13} \text{Re}_I^{0.22} \text{We}_I^{-0.03}$ for the lower curve (2.4)

where μ_c and μ_d are the continuous and dispersed phase viscosities (in Pa.s), $\Delta\rho$ is the density difference between phases (in kg/m^3), Fr_I, Re_I and We_I are the Froude number, Reynolds number and Weber number at the impeller region.

The above equations demonstrate the importance of fluid properties on the width of the ambivalent region. Fakhr-Din's correlation also indicates the importance of the agitation speed and impeller dimensions (in the Froude and Reynolds number terms). This may be due to the low agitation speeds used where there may have been a separation of the mixture.

43

Several mechanisms have been suggested by various investigators on the phase inversion mechanism. According to Pacek et al. (1994), it is the imbalance between the break-up and coalescence processes of the dispersed drop. This is also similarly suggested by Arashmid & Jeffreys (1980) and Groeneweg et al. (1998). Phase inversion has also been suggested to occur when the system free energy of the two possible dispersions (oil continuous or water continuous) become equal (e.g. Luhning & Sawistowski, 1971; Tidhar et al., 1986; Yeo, 2002). Yeh et al. (1964) have suggested that inversion occurs when there is no shear between the two phases. However, it is difficult to measure accurately the interfacial area close to and during inversion as well as the drop break-up and coalescence rates. Further details about prediction of phase inversion based on these mechanisms are presented in Section 2.4.

2.3.2 PHASE INVERSION IN PIPE FLOW

The investigation of phase inversion in pipelines can lead to better understanding on the operating conditions and help to improve the pipe design to facilitate the transportation of multiphase mixtures. This is particularly important as the presence of water is inevitable and the mixture can only be separated after it has been transported over miles of pipeline before processing. Inversion has been found to cause significant increase in pressure gradient (Martinez et al., 1988; Angeli, 1996; Valle and Utvik, 1997; Nädler and Mewes, 1997 and Soleimani et al., 1997). A good understanding of the occurrence of phase inversion is necessary to predict and control the pumping power required to transport the mixture across and may lead to poor productivity. The exact relation between phase inversion and pressure gradient is not well understood. For example, Ioannou (2006) has shown that phase inversion occurs at the peak of the pressure gradient for Exxsol D80 but not for Marcol 52 (see Figure 2.9). Exxsol D80 is less viscous (1.7 mPa.s) while Marcol 52 is more viscous (11mPa.s). Due to the high viscosity of Marcol 52, the high pressure gradient caused during the oil continuous flow may have overshadowed the peak in pressure gradient during phase inversion leading to an almost step change as a result.
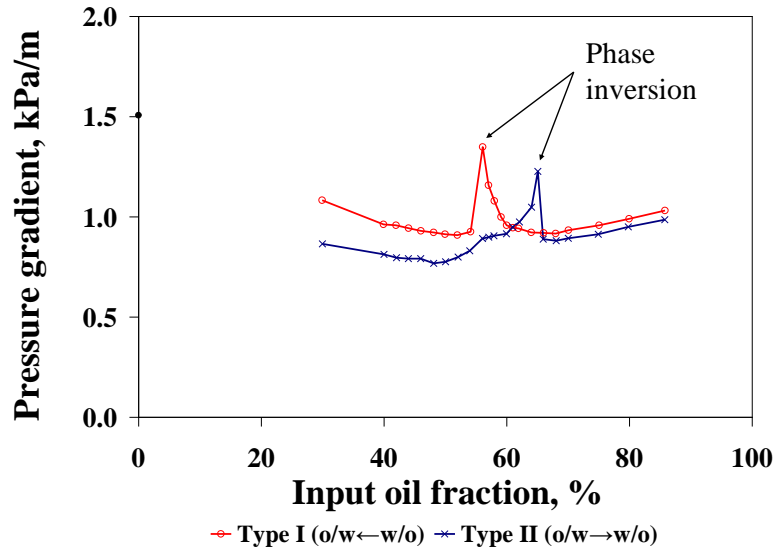
(a)
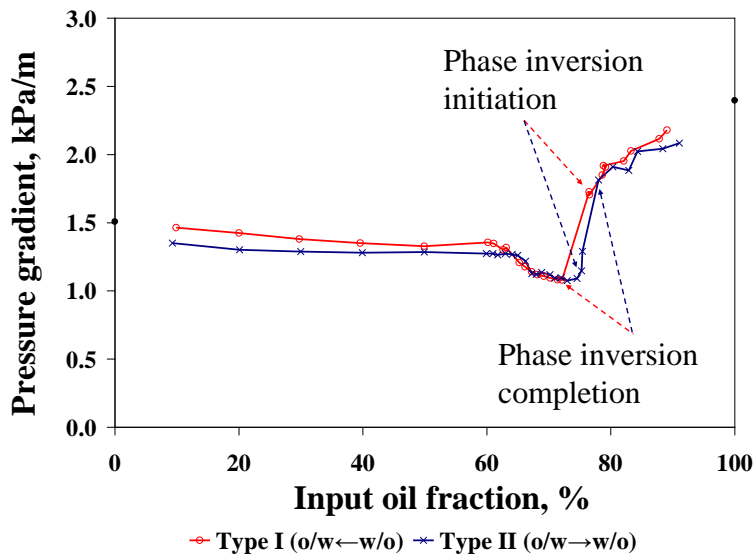
(b)

Figure 2.9: (a) Pressure gradient measurement of a Exxsol D80/water system in a 60mm I.D. pipe (b) Pressure gradient measurement of a Marcol 52/water system in a 60mm I.D. pipe (Ioannou, 2006).

While changes in pressure gradient are direct consequences of the phase inversion process, these changes cannot yet be accurately attributed to the point of phase inversion and thus cannot be used to detect phase inversion. Other system parameters have been used to detect the inversion process, e.g. conductivity. Conductivity measurements are applicable to the flow of oil-water mixtures particularly as one phase is conductive and the other is not. During phase inversion, the change is prominent with sharp changes in conductivity. Conductivity measurements can be used to detect phase continuity at locations where visual observations are not possible (e.g. at the centre of a pipe or in highly concentrated dispersions). Such measurements have indicated that inversion may not occur simultaneously across the whole pipe cross section. Soleimani et al. (2000) reported that the spatial distribution of the two phases can be inhomogeneous due to wetting effects of the pipe wall causing the water phase to concentrate towards the wall and the oil phase concentrate in the pipe core. This inhomogeneity implies that phase inversion may occur locally. Using laser induced fluorescence, Liu et al. (2006) showed that zones of oil and water continuous dispersion appear within the pipe cross section during inversion. This gradual phase inversion process has led to a *transitional region* where phase inversion begins and completes over a range of phase fraction. An example of such gradual inversion can be seen in Figure 2.10 (Hu, 2005) where oil continuous dispersion begins to appear at one phase fraction until water becomes completely dispersed at a higher dispersed phase fraction. Secondary droplets may also appear at certain regions (see Figure 2.11 for example). Piela et al. (2006, 2008) have also reported the formation of multiple dispersions and gradual inversion that spread over the cross section in their pipe flow experiments.
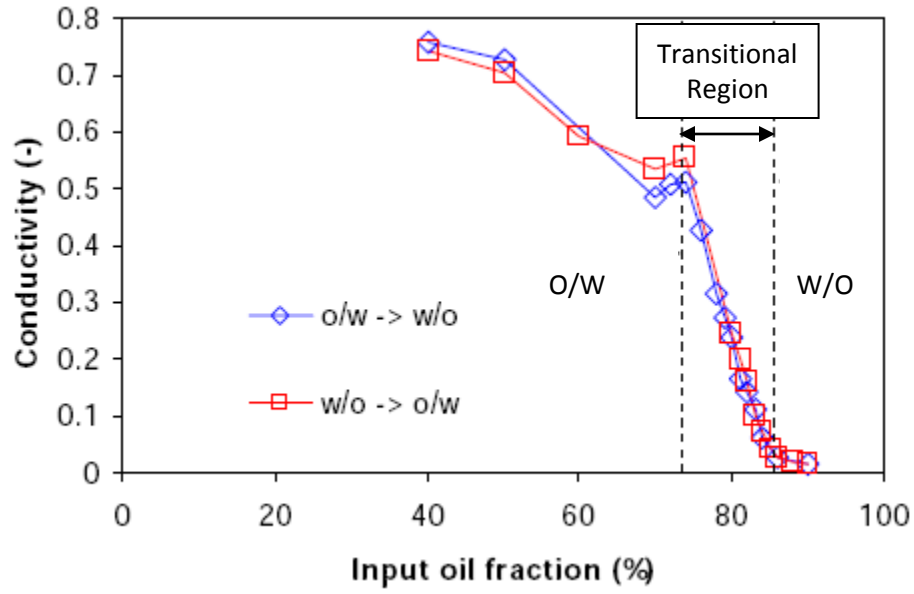
Figure 2.10: Conductivity measurement conducted at the centre of a vertical pipe across the phase inversion process (Hu, 2005).
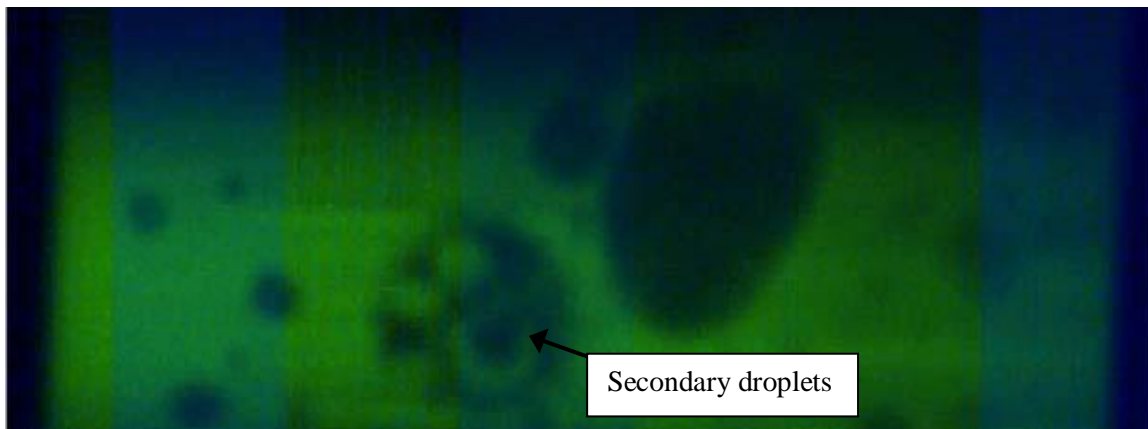
Figure 2.11: Multiple dispersions of an oil/water system at a mixture velocity of 1.5m/s and input oil fraction of 31%. The dark region represents the oil phase and the light region represents the water phase. (Liu et al., 2006)

The effects of various parameters on phase inversion have been studied for pipe flow and a summary of these parameters is presented in Table 2.2. It can be seen that fluid properties, size and material of pipe used as well as operating conditions during the pipe flow are of great importance. These parameters are similar to those observed in stirred vessels.

Parameter investigated	Author (Year)
1. Viscosity	Arirachakaran et al.(1989); Luo et al. (1997); N ädler and Mewes (1997)
2. Pressure drop	Martinez et al.(1988); Angeli et. al (1996, 1998, 2000); Valle and Utvik (1997); Luo et al. (1997); N ädler and Mewes (1997); Soleimani (1999); Ioannou et al. (2004, 2005)
3. Velocity	Luo et al.(1997); Angeli & Hewitt (1998 & 2000)
4. Phase Distribution	Arirachakaran et al.(1989); N ädler and Mewes (1997); Ioannou et al. (2004, 2005)
5. Pipe diameter & Material	Arirachakaran et al.(1989); Ioannou et al.(2004, 2005)
6. Surfactant	Pal (1993); Gillies et al. (2000)
7. Wettability	Ioannou et al.(2004, 2005); Pettersen et al.(2001)
8. Conductivity	Ioannou (2006); Hu (2005)
9. Drop size	Liu et al. (2004) & Liu (2005); Hu (2005)
10. Interfacial tension	Rodriguez and Bannwart (2006)

Table 2.2: Parameters affecting phase inversion in liquid-liquid pipeline flow.

2.3.3 PARAMETRIC STUDY ON PHASE INVERSION

The parameters which affect phase inversion in pipes are discussed in more detail here:

Agitation speed / Mixture velocity in pipe

The speed of agitation and the velocity of the mixture in the pipe flow have been reported to enhance the mixing process and the dynamic processes of drop coalescence and break-up. McClarey and Mansoori (1978) showed phase inversion occurs at a higher volume fraction of the aqueous phase when the impeller speed is increased from 240RPM to 480RPM. However at high impeller speeds (beyond 480RPM), there is no effect of

agitation on the phase inversion hold up. Similar findings were also reported by Quinn and Sigloh (1963), Luhning and Sawistowski (1971), and Deshpande and Kumar (2003). Pacek et al. (1994) found that phase inversion will not occur under certain circumstances if the agitation speed is very high but will occur if the agitation speed is reduced. On the other hand, they also observed that phase inversion will not occur at very low speeds. Efthimiadu and Moore (1994) suggested that the increase in agitation speed will increase the shear rate and will lead to finer and more stable dispersions even at higher dispersed phase fraction.

Similar experiments have been conducted in pipe flows by Arirachakaran et al. (1989) who showed that mixture velocity has little effect on the occurrence of phase inversion. However, Ioannou et al. (2005) found that an increase in mixture velocity increased the fraction of oil continuous phase when inversion occurred.

Fluid Density

The effect of fluid density was previously found to be important in gas-liquid system where the density difference is large. In liquid-liquid dispersed systems, Selker and Sleicher (1965), McClarey and Mansoori (1978) and Norato et al. (1998) have shown that the fluid densities have little effect on the ambivalent region in stirred vessels provided that the difference in density is not large. However, large density difference can lead to difficulty in maintaining the dispersion at low agitation speeds. Thus, more stirring power is required to achieve an homogeneous dispersion. Other investigators have found that a large density difference can increase the tendency for phase inversion (Rodger et al., 1956; Kumar et al., 1991). Chiang and Chen (1994) found that inversion will occur at a higher aqueous phase fraction when water is the dispersed phase for a fluid system with large density difference.

Efthimiadu and Moore (1994) performed their phase inversion experiments in parallel plates and found that the density of the aqueous continuous phase caused a small increase in the volume fraction of the organic phase at inversion. However, these experiments were conducted in conditions where effects of other fluid properties are coupled.

49

Fluid viscosity

Fluid viscosity has been reported in various investigations to be a significant factor affecting phase inversion as well as the ambivalent region. Selker and Sleicher (1965) reported that the viscosity ratio of the two phases in a stirred vessel can influence the ambivalent boundaries. In addition, an increase in the viscosity of one phase will increase its tendency to be the dispersed phase. However, Treybal (1963) suggested that the higher viscosity of one phase will favour it to be the continuous phase. Efthimiadu and Moore (1994) also found that the more viscous phase tends to become continuous in parallel shearing plates (especially if the viscous phase tends to wet the surface). They attribute this finding to be the increased dynamic stability of the dispersion when the viscous phase is continuous. Similar results have also been reported by Norato et al. (1998), who found that the upper and lower limit of the ambivalent region can be widened by increasing the viscosity regardless of whether the phase is continuous or dispersed. The widening behaviour is postulated to be caused by the lower coalescence rate due to longer film drainage time which agrees with the findings from Groeneweg et al. (1998), Coulaloglou and Tavlarides (1977) and Calabrese et al. (1986).

Arirachakaran et al. (1989) from literature data on inversion in pipelines with different viscosity oils found that the more viscous oils tend to be dispersed. Similarly, Ioannou (2006) showed that the more viscous Marcol 52 oil tended to invert at a higher oil fraction. Nädler and Mewes (1997) however using oils with different viscosity (between 22 and 35 mPa.s) found no significant effect on inversion.

Interfacial tension

The effect of interfacial tension is the least well understood among the fluid properties on phase inversion. According to Selker and Sleicher (1965), the magnitude of interfacial tension is unlikely to influence the ambivalence region as the interfacial tension between a pair of fluids is not a function of the interfacial curvature. Yeh et al. (1964) suggested that interfacial tension plays a small role on phase inversion. In the absence of other forces, the interfacial tension will cause inversion to occur at 50% volume fraction.

Luhning and Sawistowski (1971), on the other hand, found that interfacial tension can affect the phase inversion since it affects drop size and interfacial area. Clarke and Sawistowski (1978) later confirmed the change in interfacial area during phase inversion and showed that the width of the ambivalent region is significantly affected by interfacial tension. Lowering the interfacial tension will widen the width.

Norato et al. (1998) also found that decreasing the interfacial tension widens the ambivalent region and makes it more difficult to cause an appearance of phase inversion. According to Coulaloglou and Tavlarides (1977), decreasing the interfacial tension will lead to an increase in drainage time for the film between drops leading to higher drop breakage and lower drop coalescence and as such smaller drop size. A higher dispersed phase fraction will thus be required for inversion to occur. This suggestion has been confirmed by experiments. Efthimiadu and Moore (1994) found that lowering the interfacial tension has a stabilising effect on the type of dispersion which depends also on the other properties of the system. It was also experimentally found that the effect of shear rate (i.e. rotational speed and gap width) is minimised with the decrease in interfacial tension. The influence of the wettability of the contacting surfaces is also reduced.

Surface wettability
The material of construction of the dispersion container (e.g. stirred vessel or pipe) has been suggested to affect the type of dispersion formed and as a result phase inversion and ambivalent region. McClarey and Mansoori (1978) suggested, through their experimental outcome for an equal density and viscosity mixture, that the discrepancies in their inversion curves can be attributed to the difference in wettability of the vessel surface with the two liquids. However, the effect is only found to be significant at low agitation speeds. Giulinger et al. (1988) changed the material used in the stirred vessel from water to oil wetted and showed that the wetting phase was favoured to remain continuous. In stirred vessels, drop break-up generally occurs within the impeller region and coalescence at the other regions. However, Kumar et al. (1991) reported that the drops can coalesce on the impeller and form a thin film if the impeller is preferably wetted by the dispersed

phase. The drops will subsequently be broken at the impeller or at its vicinity. The effects on the coalescence and break-up process can significantly change the phase inversion behaviour.

Efthimiadu and Moore (1994) investigated the effect of material on phase inversion of liquid-liquid dispersions between parallel plates. Their experimental findings indicated that the liquid which preferentially wets the surface of the plates tends to form the continuous phase.

The effect of surface wettability is not well documented for pipeline flow. Angeli and Hewitt (1998) conducted experiments in 24 mm I.D. pipe with Exxsol D80 as the oil phase and water as the aqueous phase. They observed similar range of input water fraction (at 37% - 40%) regardless of the material of the pipe (acrylic and stainless steel). Pettersen et al. (2001) conducted experiments with the same type of oil in PVC and stainless steel pipes of 100 mm I.D. and found that inversion is delayed to a higher oil fraction in PVC compared to the steel one when experiments started from an oil continuous mixture. Ioannou et al. (2005) found that acrylic is wetted more by the oil phase than steel and thus phase inversion occurs at a higher oil fraction for acrylic pipe.

Inlet conditions

Inlet conditions are important as these determine how the two fluids are introduced into the pipe and, coupled with other effects, can affect the phase inversion appearance. Piela et al. (2006, 2008) discussed two approaches in introducing the phases into the test pipe. In the continuous experiment, the continuous phase was introduced in the pipe loop and wetted the pipe wall. The dispersed phase was then injected into the loop and a corresponding volume of mixture was removed to ensure constant mixture velocity of fluid in the system. The dispersed phase fraction was gradually increased with the continuous injection of the dispersed phase until phase inversion occurred. In the direct experiment, the two fluids were introduced as two separate continuous phases and subsequently mixed within the test pipe. The input flow rates of the two phases were adjusted to maintain a constant mixture velocity. From the experimental outcome, the

52

critical fraction of the dispersed phase for inversion can be significantly higher for the continuous experiment than the direct one. The authors also suggested that the phase inversion can be postponed or avoided by altering the inlet conditions.

Dispersion initialisation

The initialisation of the dispersion has been reported to have a strong effect on phase inversion. For example, Selker and Sleicher (1965) found that the inversion point in stirred vessels is strongly influenced by the initial type of dispersion (i.e. water continuous or oil continuous) especially if the phase fraction is within the ambivalent region.

The occurrence of ambivalent region as a direct effect of dispersion initialisation has been seen mainly in stirred vessels but not studied systematically in pipes. Ioannou et al. (2005) observed in their pipe flow experiments that the initial continuous phase will tend to preserve its continuity leading to an hysteresis effect in the occurrence of phase inversion according to the initial dispersion type. Hu and Angeli (2006), however, observed no effect of dispersion initialisation in a vertical pipe flow based on their experimental conditions studied.

2.4 PHASE INVERSION MECHANISMS AND PREDICTION MODELS

Several types of prediction models based on different phase inversion mechanisms have been reported in various literatures. These models will be discussed in detail in the following sections.

2.4.1 MODELS BASED ON RATE OF DROP BREAK-UP AND COALESCENCE

Phase inversion is commonly found in dispersion. Parameters affecting phase inversion are known to also influence the drop coalescence and breakup (e.g. fluid properties, agitation speed, wettability). This has led to various investigations to relate phase

inversion with the dynamic process of drop break-up and coalescence (Arashmid and Jeffreys, 1980; Groeneweg et al., 1998). In a stable dispersion, e.g. O/W, the dynamic process of drop break-up and coalescence is balanced. Increasing the dispersed phase (i.e. oil) will lead to higher collision frequency and coalescence rate. Concurrently, more drops of larger size will also be broken up. Thus, a new equilibrium of this dynamic process will be formed.

According to Arashmid & Jeffreys (1980), collision of drops in a stirred vessel will lead to some drops being coalesced. As the dispersed phase is increased under a constant agitation speed, the chance of successful coalescence for each collision will increase. At phase inversion, it is suggested that coalescence will occur for every collision. Thus, the frequency of drop collision will be equal to the frequency of drop coalescence. Based on Levich (1962)'s collision frequency model and Howarth (1967)'s coalescence frequency model, the dispersed phase holdup (Φ_d^I) at inversion can be expressed as follows:

$$\Phi_d^I = \frac{K}{d_d^2 N_I^{0.48}} \tag{2.5}$$

where K is a constant depending on the type of agitator, d_d is the drop size and N_I is the agitation speed.

Vaessen et al. (1996) applied the idea from Arashmid & Jeffreys (1980) to determine phase inversion. However, they suggested that drop break-up should be part of the inversion process in addition to having coalescence occurring at each collision. At phase inversion, drop break-up is dominated by the drop coalescence process and the equilibrium drop size diverges.

To estimate the drop size at inversion, the following coalescence and break-up rate equations are used.

Coalescence rate (based on Saffman and Turner, 1956):

$$R_c(d) = 6.87\varepsilon^{1/3}d^{1/3}n(d)^2 \tag{2.6}$$

Break-up rate (based on Delichatsios and Probstein, 1976):

$$R_b(d) = 1.37\sqrt{\frac{2}{\pi}}\varepsilon^{1/3}d^{-2/3}\exp(\frac{\sigma}{1.88\varepsilon^{2/3}d^{5/3}})n(d) \tag{2.7}$$

where $R_c(d)$ and $R_b(d)$ are the rates of coalescence and break-up of drops with mean diameter, d, ε is the turbulent energy dissipation rate, σ is the interfacial tension, n(d) is the number density of drops with diameter d.

It can be seen that the break-up process is proportional to the number of drops in a volume while the coalescence process is proportional to the number of drops in a volume squared. The coalescence rate will increase faster as the volume of dispersed phase increases. This leads to phase inversion when the dynamic balance between the two rates collapses.

Groeneweg et al. (1998) suggested that phase inversion is governed by the balance between drop break-up and coalescence which can be altered in favour of coalescence by the increase of the effective volume fraction of the dispersed phase on continuous stirring. This results in the inclusion of the continuous phase into the drops of the dispersed phase forming secondary droplets. The enclosed droplets can also be escaped back to the continuous phase. The effective volume fraction of the dispersed phase will continue to increase as long as the inclusion dominates over the escape. Inversion will start when the effective volume fraction for inversion has been reached. At this point, the droplet size increases significantly and inversion follows.

Desphande and Kumar (2003) proposed that drop break-up and coalescence do not occur independently in high dispersed phase holdups. The ratio of the rates at which the two events occur in turbulent flow field is determined by the average relative separation between the drops and the physical properties of the fluids in the system. It is also

independent of the intensity of the turbulent flow field for sufficiently intense turbulent flow.

Hu et al. (2004) applied the population balance model to predict the birth and death rates of drops of specific size and account for the corresponding drop size distribution. The birth and death of drops are associated with the drop break-up and coalescence. In order to predict the phase inversion, the total volumetric break-up rate will be equal to the total volumetric coalescence rate. With this approach, the ambivalent region can be found. It agrees reasonably well with literature data except in high dispersed phase fraction. The disagreement can be attributed to the coalescence efficiency correlations that are not meant for dense dispersion.

2.4.1.1 SECONDARY DISPERSIONS

With the dynamic process of drop coalescence and break-up, secondary dispersions can also arise in a dispersed flow as the continuous phase entrains in the dispersed phase (e.g. O/W/O dispersion). The formation of secondary dispersions is found to be more likely near the phase inversion point (Luhning and Sawistowski, 1971) and secondary dispersions depend on the continuous phase. For example, Pacek and Nienow (1995) have found that only O/W/O dispersion can exist in a water-kerosene mixture but not W/O/W. Kumar (1996) suggested that secondary droplets are formed when successive coalescence of drops leads to droplets entrained in them. However, two criteria must be met (1) the coalescence efficiency should be high so that the drops can coalesce simultaneously (2) the entrained droplets should be at a stable condition upon entrainment. The absence of W/O/W dispersions could be due to the low coalescence efficiency of the oil drops in water and the secondary water droplets, if any, will have high coalescence efficiency leading to the water droplets escape to the water continuous phase.

Liu et al. (2005) observed secondary droplets using laser induced florescence (LIF) technique in pipe flow (Figure 2.12). The formation of secondary droplets will lead to a higher effective dispersed phase fraction (i.e. the total volume fraction of the primary

drops and the secondary droplets) and would lead to an earlier occurrence of phase inversion than that expected from the actual phase fractions of the two phases.
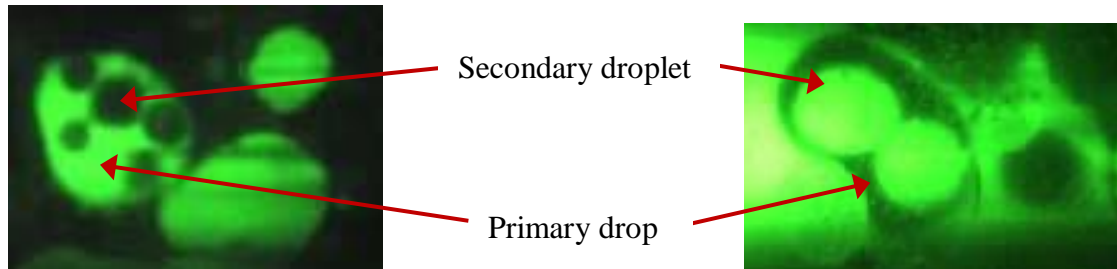
Figure 2.12: Visual observations of (a) O/W/O and (b) W/O/W dispersions using LIF technique. The oil phase is shown in black while the water phase is shown in luminous green (Liu et al., 2005).

2.4.2 MODELS BASED ON MINIMIZATION/EQUAL SYSTEM AND INTERFACIAL ENERGY

Luhning and Sawistowski (1971) suggested that the total energy (including kinetic and interfacial energy) of the system would reach a minimum value at phase inversion and the change in total energy is caused by the fluid system itself. The measured impeller power input in the stirred vessel was observed to remain constant throughout the inversion process.

Other investigators (Tidhar et al., 1986; Decarre and Fabre, 1997; Yeo et al., 2002; Brauner and Ullmann, 2002) have suggested that the surface energies (i.e. interfacial energy and the surface energy of the fluids with the contacting wall) of the two possible types of dispersion, O/W and W/O, should be balanced at phase inversion. To account for the surface energy, the interfacial area can be calculated using Monte Carlo simulation (Yeo et al., 2002) or Population Balance model (Hu, 2005). Brauner and Ullmann (2002) expressed the interfacial area in terms of Sauter mean diameter and derived the following equation for the oil volume fraction at phase inversion.

$$\phi_O^I = \frac{[\sigma/D_{32}]_{w/o} + \frac{s}{6}\sigma\cos\theta}{[\sigma/D_{32}]_{w/o} + [\sigma/D_{32}]_{o/w}} \qquad (2.8)$$

where θ is the solid-liquid surface contact angle with $0 \leq \theta < 90°$ denoting a surface preferentially wetted by water (hydrophilic surface) and $90° < \theta \leq 180°$ denoting a surface wetted by oil (hydrophobic surface), s is the solid surface area per unit volume where s=4/D and D is the pipe diameter, σ is the interfacial tension and D_{32} is the Sauter mean drop diameter.

Equation 2.8 can be simplified as follows when the solid-liquid surface energy is neglected (Yeo et al., 2002):

$$\frac{\phi_O^I}{1-\phi_O^I} = \frac{D_{32_{o/w}}}{D_{32_{w/o}}} \qquad (2.9)$$

While the correlations based on this approach does not account for the existence of ambivalent region, Brauner and Ullmann (2002) suggested that ambivalent region can be regarded as the change in interfacial tension when contaminant is present. Yeo et al. (2002) use different correlations to calculate the Sauter mean drop diameter depending on the dispersed phase fraction. The use of these correlations results in the presence of ambivalent region according to the history of the system.

2.4.3 MODELS BASED ON ZERO SHEAR STRESS AT INTERFACE

Phase inversion has been previously mentioned to be influenced by the viscosities of the liquid phases in the system. Yeh et al. (1964) developed a correlation for predicting the critical phase fraction at inversion as a function of the viscosity ratio of the two phases based on the assumption that the interfacial shear is zero at the point of the inversion (i.e. no tendency to mix or create new surfaces). From the momentum balance of the two phases, they suggested the following correlation for the phase inversion point which was

modified by replacing the viscosity of the continuous phase with the interfacial viscosity (μ_i) and was found to improve on the prediction:

$$\frac{\varphi_d^I}{1-\varphi_d^I} = \left(\frac{\mu_d}{\mu_i}\right)^{1/2} \tag{2.10}$$

where φ_d^I is the dispersed phase fraction at phase inversion, μ_d and μ_i are the dispersed phase and the interfacial viscosity respectively.

Nädler and Mewes (1995, 1997) also used the momentum balance of the phases and the assumptions of zero interfacial shear and no slip between the two phases to develop the following correlation for the initial water fraction at inversion.

$$\varphi_w^I = \frac{1}{1 + k_1\left[\dfrac{C_o}{C_w}\dfrac{\rho_o^{(1-n_o)}}{\rho_w^{(1-n_w)}}\dfrac{\mu_o^{n_o}}{\mu_w^{n_w}}(DU_m)^{n_w - n_o}\right]^{1/k_2}} \tag{2.11}$$

where ρ is the fluid density, subscripts o and w referring to the oil and water phases respectively, D is the pipe diameter, and U_m is the mixture velocity, and C and n are the parameters used in the Blasius friction factor equation, CRe^{-n}, k_1 and k_2 are the empirical parameters depending on the type of dispersion (O/W or W/O) and flow conditions. If both phases are in laminar flow, k_1 and k_2 can be taken as 1 and 2 respectively and equation 2.11 is equivalent to equation 2.10.

2.5 DROP SIZE DISTRIBUTION AND CHARACTERISTIC DIAMETER

As discussed in the previous section, the drop size of the dispersed phase and its distribution are important elements in the models of phase inversion prediction (e.g. based on the dynamic process of drop break-up and coalescence, equal and minimization

of system/interfacial energy). Drop size distributions in liquid-liquid dispersions and the various ways of expressing them are discussed in this section.

2.5.1 TYPES OF DROP SIZE DISTRIBUTION

Coulaloglou and Tavlarides (1977) developed a model for drop size distribution in a stirred vessel based on the effects of drop break-up and coalescence in an isotropic turbulent field. A break-up model was derived by considering drop deformation, break-up under influence of local pressure fluctuation and the time needed for a critically deformed drop to break-up in a locally isotropic field. A coalescence model was also derived based on the assumption that the coalescence rate is proportional to the collision rate and the coalescence frequency in the kinetic regime of locally isotropic turbulent fields. They used a Gaussian probability density function of drop sizes in the feed and found good agreement between the model and experimental distribution in the stirred vessel (see Figure 2.13 for comparison).
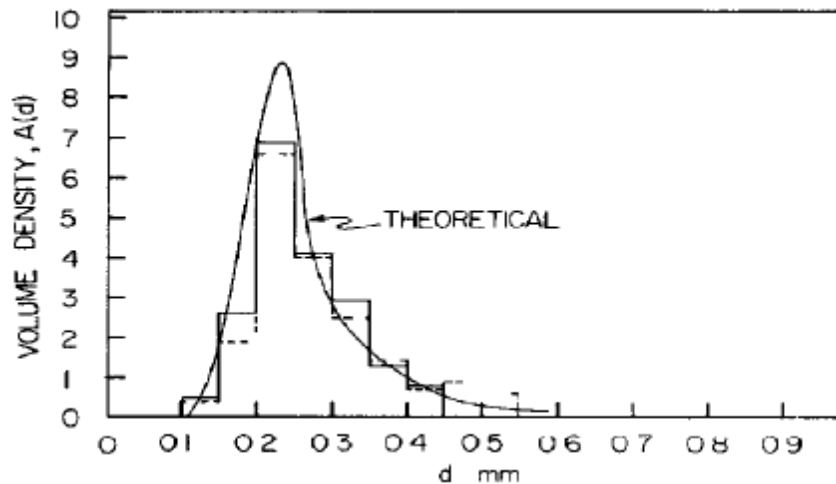
Figure 2.13: Comparison between calculated drop size distribution and experimental drop size data. Dotted line represents the histogram at the circulation region and the solid line represents the histogram at the impeller region. (Coulaloglou and Tavlarides, 1977).

Collins and Knudsen (1970) investigated experimentally dilute O/W dispersions (up to 10% by volume) in pipe flow using 3 different organic phases and did not observe coalescence.

60

They suggested that the drop size distribution in the pipe is a result of two superimposed distributions – (1) produced by the injection nozzle and (2) produced by the turbulence of the flow. The drop size distribution is nearly log-normal at the injection nozzle but deviates from the log-normal type along the flow downstream due to the action of turbulence.

Karabelas (1978) re-examined some of the experimental data from Collins and Knudsen (1970) and compared that with his own experimental results in pipe flow using two different organic phases. He found that the drop size distribution can be fitted with a Rosin-Rammler or an upper limit log-probability distribution. While both distribution types yield similar result, Rosin-Rammler distribution in Equation 2.12 is simpler for use.

$$1 - V_{cum} = \exp\left[-2.996\left(\frac{d}{d_{95}}\right)^n\right] \quad\quad (2.12)$$

where V_{cum} is the cumulative volume fraction of drops with diameter less than d, d is the drop diameter and d_{95} is the drop size corresponding to 95% of drops smaller than d_{95}. n is a fitting parameter of the distribution.

Angeli and Hewitt (1998) investigated the drop size distribution experimentally in an oil/water pipe flow. They observed that the drop size distribution is strongly influenced by the pipe material with drops smaller in steel pipe than acrylic pipe and can be reasonably fitted with a Rosin-Rammler distribution with parameter, n, in Equation 2.12 ranging from 2.1 to 2.8.

Simmons and Azzopardi (2001) also examined the drop size distribution experimentally in a pipe flow. The backscatter technique applied in their experiments allows drop size distribution to be obtained even at highly dense dispersion. From their results, the drop size distribution of the mixture flow fits well with an upper-limit log-normal distribution.

Vielma et al. (2008) compared their experimental results in an horizontal pipe flow of water and mineral oil with various dispersion types – Normal, Log-normal and Rosin-Rammler. They conclude that log-normal distribution is the best probability distribution for all their experimental results regardless of the type of dispersion (O/W or W/O). Figure 2.14 presents one of comparisons of the oil drop size distribution at an oil and water flow velocity of 0.75m/s.
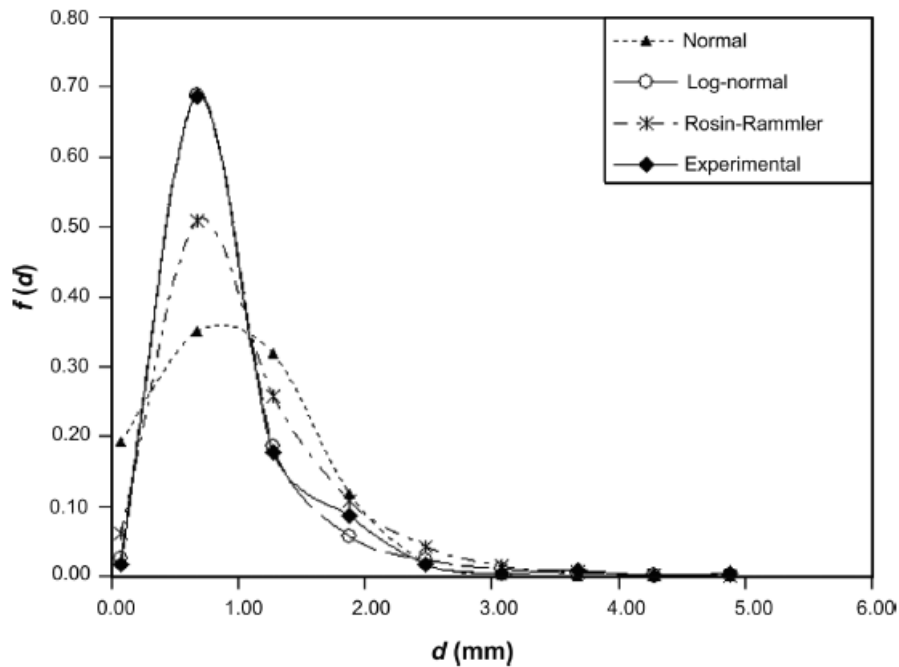
Figure 2.14: Comparison between experimental drop size data and selected drop size distribution types in an horizontal pipe flow (Vso = 0.75m/s, Vsw=0.75m/s, oil drops). (Vielma et al., 2008).

2.5.2 CHARACTERISTIC DIAMETERS OF DROP SIZE DISTRIBUTION

Knowing the changes in drop size distribution is useful to understand the underlying dynamics in the drop break-up and coalescence process. However, the distributions are difficult to compare across different studies. An easier way to characterize a drop size distribution is by using the characteristic mean diameters despite that some information may be neglected. Two common characteristic diameters are the linear mean diameter, d_{10}, and the Sauter mean diameter, d_{32}. They are defined in Equation 2.13 and 2.14

respectively. In this thesis, Sauter mean diameter will be used in general as this diameter is commonly reported in prediction of mean drop size for liquid-liquid dispersions.

(1) Linear mean diameter, d_{10}, which defines the number-averaged drop size.

$$d_{10} = \frac{\sum_{i=1}^{n} d_i}{n} \tag{2.13}$$

(2) Sauter mean diameter, d_{32}, which defines the characteristic diameter that has the same volume/area ratio as the distribution.

$$d_{32} = \frac{\sum_{i=1}^{n} d_i^3}{\sum_{i=1}^{n} d_i^2} \tag{2.14}$$

where d_i is the diameter of the sample drop and n is the number of drops in the sample distribution.

2.6 NUMERICAL SIMULATION ON DISPERSED FLOW

The occurrence of phase inversion is a direct consequence of the dynamic flow behaviour. It involves the interaction of the fluid phases in the system and causes a spatial re-distribution of the phases across the confined system (e.g. pipes). Phase inversion can be influenced by many parameters and these parameters can themselves be inter-related. In addition, empirical correlations on two-fluid flow usually provide global information on the system. The important local information which can have great significance in understanding dynamic phenomena such as phase inversion is neglected by such correlations.

Information on the flow field would be important for understanding phase inversion. This can be achieved by computational fluid dynamics (CFD) modelling. CFD is a computational code for solving the continuity and Navier-Stokes equations using a

number of closure correlations. Various authors have attempted to improve the prediction of multiphase flow and apply the development in simulating complex flows (Hill, 1998; Rusche, 2002; Chesters and Issa, 2004; Liu, 2005; Krepper et al., 2005). While current CFD simulation has been reported to achieve reasonable success in comparison with experimental data, there are still a lot of developments required due to the uncertainty in the actual mechanisms for the occurrence of fluid flow phenomenon (e.g. phase inversion). The development of the CFD code should also be complemented with improved experimental techniques for more detailed investigation on fluid flow.

While many process flows operate at high dispersed fraction, currently CFD handle dilute dispersion with <10% dispersed fraction. This is due to the lack of information on terms such as inter-phase momentum, turbulence effects as well as phenomenon such as phase inversion at high dispersed phase fractions.

The common approaches used in CFD to simulate multiphase flows are (1) Eulerian-Lagrangian, (2) Eulerian-Eulerian and (3) Volume of fluid (VOF). These approaches are discussed below (more detailed discussion can be found in Hill (1998), Rusche (2002), Ranade (2002)). In the Eulerian-Lagrangian (E-L) framework, the dispersed phase is represented by individual dispersed elements (i.e. drops). The trajectories of these drops are tracked by solving the appropriate momentum equations in a Lagrangian framework (i.e. the dependent variables are functions of the properties of the tracked drop). At the same time, the conservation equations for the continuous phase are expressed in the Eulerian framework (i.e. the fluid properties are functions of space and time with respect to the reference volume domain). This approach is good in capturing the flow dynamics of the dispersed phase. The drop size distribution and inter-particle interactions can also be accounted for. However, it is computational intensive especially at large numbers of dispersed drops.

In the Eulerian-Eulerian (E-E) approach, the conservation equations of all the fluid phases are expressed in the Eulerian framework. The fluid phases are assumed to share a volume domain and interpenetrate during their motions. The presence of each phase is

64

accounted for by their velocity fields across the volume domain and their volume fractions. Interphase transport models, such as drag force and lift force, are applied to define the coupling effect between the phases. The Eulerian-Eulerian approach is more efficient in computational resources as the dispersed phase is regarded as a single continuum (and greatly reduces the number of conservation equations needed). This approach is thus well suited for more dense dispersions (Sommerfelds et al., 2008). However, the inter-particle interactions and drop size distribution are difficult to account for. A schematic comparison between the E-E and E-L approach was presented by Rusche (2002) and can be seen in Figure 2.15.

(a)   (b)
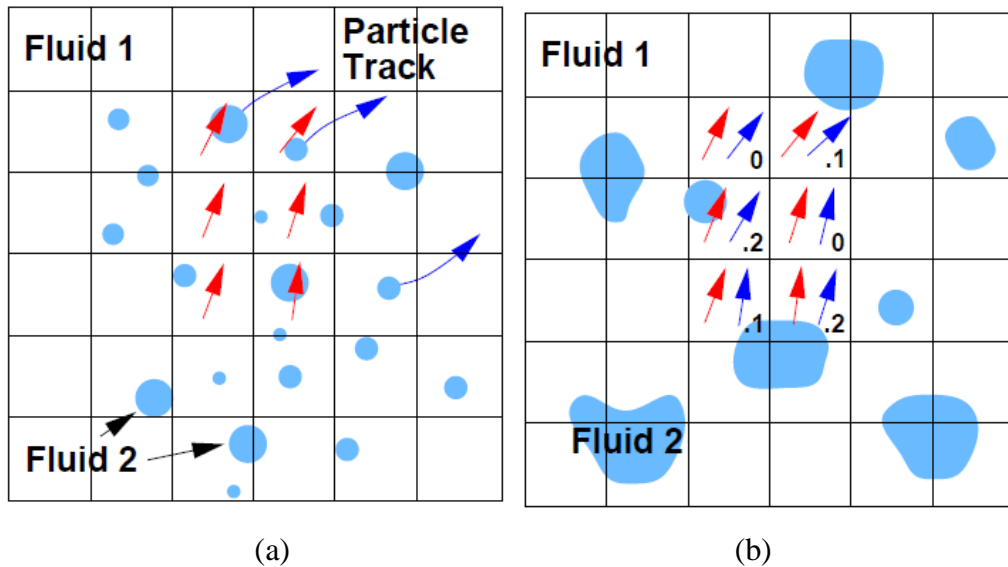
Figure 2.15: Schematic representation on the modelling approaches for two-phase flow: (a) Eulerian-Lagrangian approach and (b) Eulerian-Eulerian approach. The number next to the blue arrow in (b) represents the volume fraction of the dispersed phase within the control volume. (Rusche, 2002)

The Volume of Fluid (VOF) approach aims to simulate the motion of the fluid interface by tracking the motion of the phases in a single set of conservation equations for the mixture (Ranade, 2002). The VOF approach distinguishes the respective fluid phases using a marker function (usually the volume fractions) within the control volume domain in the system. If one phase occupies the entire control volume, its properties will be used to avoid any discontinuity caused by the absence of the other phases. This approach is

suited for investigations where the shape and fluid motion at near the interface are of interest. While it offers better resolution close to the interface, computational resources increase significantly if there is a dense dispersed phase. This approach is thus commonly used to investigate, for example, deformation of single drop in a flow field and the breakup and binary drop coalescence processes (Stover et al., 1997; Delnoij, 1997; Krishna and van Baten, 1999).

2.6.1 CONSERVATION EQUATIONS USED IN CFD

As phase inversion tends to occur in dense dispersions, the simulation of such dispersion will be a valuable source of information in addition to the experimental data. It will also ease the investigation on the effects of various parameters especially with conditions that are difficult to match with experiments. As suggested by Sommerfelds et al. (2008), the numerical simulations used for intermediate and dense dispersion should be based on the Eulerian-Eulerian framework. The Eulerian framework is based on volume-averaged mass and momentum transport equations for the respective fluid phases. For an incompressible multiphase system (e.g. oil/water), the phases are assumed to share the space proportionally to their volume fractions such that:

$$\alpha_d + \alpha_c = 1.0 \tag{2.15}$$

where α is the volume fraction of the respective phases and d, c represent the dispersed and continuous phases respectively.

The continuity equation is:

$$\frac{\partial}{\partial t}(\alpha_k) + \nabla \cdot (\alpha_k \vec{u}_k) = 0 \tag{2.16}$$

The momentum transfer equation is:

$$\rho_k \frac{\partial}{\partial t}(\alpha_k \vec{u}_k) + \rho_k \nabla \cdot (\alpha_k \vec{u}_k \vec{u}_k) = -\alpha_k \nabla p + \rho_k \alpha_k g - \nabla \cdot (\alpha_k \vec{\vec{\tau}}_k) + F_M \tag{2.17}$$

From equations 2.16 and 2.17, the subscript k represents a specific phase (i.e. oil or water in this study), ρ is the mean fluid density, u is the velocity vector given by , u = [u, v, w], g is the gravity, τ is the phase shear stress tensor ($\tau_k = -\mu_k(\nabla u_k + (\nabla u_k)^T)$) and F_M is the interphase force term.

For turbulent flow, the flow variables can be decomposed into two components: (1) a steady mean, e.g. U, and (2) a fluctuating component that oscillates around the mean value, u'(t). This is called the Reynolds decomposition (Hill, 1998; Elseth, 2001). The flow variables of the turbulent flow can be expressed as follows:

$$u(t) = U + u'(t); \; v(t) = V + v'(t); \; w(t) = W + w'(t); \; p(t) = P + p'(t) \tag{2.18}$$

By substituting equation 2.18 into equations 2.16 and 2.17, the effect of turbulence can be accounted for in the conservation equations.

The continuity equation becomes:

$$\frac{\partial}{\partial t}(\alpha_k) + \nabla \cdot (\alpha_k U_k) = 0 \tag{2.19}$$

The momentum equation becomes:

$$\rho_k \frac{\partial}{\partial t}(\alpha_k U_k) + \nabla \cdot (\alpha_k \rho_k U_k U_k) = -\alpha_k \nabla p + \rho_k \alpha_k g + \nabla \cdot T_k + F_M \tag{2.20}$$

where U is the volume averaged velocity in a turbulent flow, and T is the Reynolds stress tensor given by:

$$T_k = \begin{pmatrix} \tau_{xx} & \tau_{xy} & \tau_{xz} \\ \tau_{yx} & \tau_{yy} & \tau_{yz} \\ \tau_{zx} & \tau_{zy} & \tau_{zz} \end{pmatrix} \tag{2.21}$$

The tensor creates six extra stress terms including three normal stresses

$$\tau_{xx} = -\alpha_k \rho_k \overline{u'^2} \qquad \tau_{yy} = -\alpha_k \rho_k \overline{v'^2} \qquad \tau_{zz} = -\alpha_k \rho_k \overline{w'^2} \qquad (2.22)$$

and three shear stresses

$$\tau_{xy} = \tau_{yx} = -\alpha_k \rho_k \overline{u'v'} \quad \tau_{xz} = \tau_{zx} = -\alpha_k \rho_k \overline{u'w'} \quad \tau_{yz} = \tau_{zy} = -\alpha_k \rho_k \overline{v'w'} \qquad (2.23)$$

These six extra stresses are called Reynolds stresses. The inclusion of these terms in equation 2.21 requires a turbulence model to predict the Reynolds stresses. The k-ε model, which will be used in this thesis, is by far one of the most widely used and validated turbulence models. It is based on the assumption that there is an analogy between the action of the viscous stresses and the Reynolds stresses on the mean flow.

According to Boussinesq (1877), the Reynolds stresses can be expressed in the following way:

$$\tau_{xy} = -\rho \overline{u'_x u'_y} = \alpha_k \mu_t \left(\frac{\partial U_x}{\partial x_y} + \frac{\partial U_y}{\partial x_x} \right) - \frac{2}{3} \alpha_k \rho_k k \delta_{xy} \qquad (2.24)$$

where $k = \dfrac{1}{2}(\overline{u'^2} + \overline{v'^2} + \overline{w'^2})$ is the turbulence kinetic energy per unit mass, μ_t is known as the turbulent or eddy viscosity. The Kronecker delta, δ_{xy}, becomes 1 if x=y and 0 if x≠y. The other Reynolds stress terms can be expressed in the same form as Equation 2.24.

F_M is a source term that accounts for the overall effect of various body forces – buoyancy force, lift force, drag & turbulent dispersion force, virtual/added mass effects. Virtual mass effects can be ignored unless the high frequency fluctuations of the relative velocity occur. These high frequency fluctuations are generally not resolved in the CFD code and also tend to be lost in the averaging process (Drew, 1983; Chen et al., 2005).

The conservation equations can be further simplified for the steady-state and incompressible flow with no mass transfer encountered. In addition, the modeling of drop

dynamics and drop size distribution are not included in this thesis to reduce complexity of the simulations and the required run time. With these assumptions, the continuity equation becomes:

$$\nabla \cdot \left(\alpha_k \, U_k \right) = 0 \tag{2.25}$$

and the momentum transfer equation becomes:

$$\underbrace{\nabla \cdot \left(\alpha_k \rho_k U_k U_k \right)}_{\substack{\text{Change of momentum} \\ \text{due to convection}}} = \underbrace{-\alpha_k \nabla p}_{\text{Pressure force}} + \underbrace{\rho_k \alpha_k g}_{\text{Gravitational force}} + \underbrace{\nabla \cdot \left(\alpha_k \tau_k \right)}_{\text{Viscous force}} + \underbrace{F_{\text{lift},k}}_{\text{Lift force}} + \underbrace{F_{\text{int} k}}_{\substack{\text{Drag \& Turbulent} \\ \text{dispersion force}}} \tag{2.26}$$

In order to close the set of equations 2.26, appropriate models for the interphase drag, lift and turbulent dispersion forces are needed.

2.6.2 MODELS FOR SIMULATION OF LIQUID-LIQUID DISPERSED PIPE FLOW

Turbulence models

In order to achieve a balance between the level of accuracy expected from the CFD simulations and the resources required to achieve it, turbulence models have been proposed to simplify the numerical calculations needed to take into account the turbulence. These models will be discussed with special focus on Ansys CFX which is the CFD code used in this study.

Standard k-ε model

The k-ε model is a semi-empirical model based on the solution of two separate transport equations for the mean turbulence kinetic energy, k, and the dissipation of this kinetic energy, ε. The effect of turbulence is accounted for via the turbulence viscosity term (μ_t) without modifying the effect of molecular viscosity (μ_k) in the conservation equations (eddy viscosity hypothesis). Molecular viscosity refers to the viscosity effect caused by the fluids while the turbulence viscosity is an imaginary viscosity effect caused by the turbulence eddies proposed by Boussinesq (1877). The model assumes that the Reynolds

number of the flow is high and the turbulence across the domain is homogeneous. This is valid for a fully developed turbulent flow in a pipe except at locations very near to the wall.

The transport equations for k and ε are:

$$\underbrace{\frac{\partial}{\partial t}(\alpha_c \rho_c k_c)}_{\text{Rate of change of k}} + \underbrace{\nabla \cdot (\alpha_c \rho_c U_c k_c)}_{\text{Transport of k by convection}} = \underbrace{\nabla \cdot \left(\alpha_c \frac{\mu_{t,c}}{\sigma_{k(\varepsilon),c}} \nabla k_c \right)}_{\text{Transport of k by diffusion}} + \underbrace{S_{k(\varepsilon)}}_{\text{Net rate of production/destruction of k}} \qquad (2.27)$$

$$\underbrace{\frac{\partial}{\partial t}(\alpha_c \rho_c \varepsilon_c)}_{\text{Rate of change of }\varepsilon} + \underbrace{\nabla \cdot (\alpha_c \rho_c U_c \varepsilon_c)}_{\text{Transport of }\varepsilon\text{ by convection}} = \underbrace{\nabla \cdot \left(\alpha_c \frac{\mu_{t,c}}{\sigma_{\varepsilon,c}} \nabla \varepsilon_c \right)}_{\text{Transport of }\varepsilon\text{ by diffusion}} + \underbrace{S_\varepsilon}_{\text{Net rate of production/destruction of }\varepsilon} \qquad (2.28)$$

where $\mu_{t,c}$ is the turbulence viscosity of the continuous phase. Among the terms, there are several empirical parameters that have been evaluated through data fitting over a wide range of turbulent flows. The set of constants given by Launder and Spalding (1972) is the most widely used and is the default set of constants for CFX (see Table 2.3).

Model parameter	Suggested value
C_μ	0.09
$C_{1\varepsilon}$	1.44
$C_{2\varepsilon}$	1.92
$\sigma_{k(\varepsilon),c}$	1.00
$\sigma_{\varepsilon,c}$	1.30

Table 2.3: Coefficients for k-ε turbulence model (Launder and Spalding, 1972)

The continuous phase turbulence viscosity can be expressed as follows:

$$\mu_{t,c} = \rho_c C_\mu \frac{k_c^2}{\varepsilon_c} \tag{2.29}$$

The S_k & S_ε terms in equations 2.27 and 2.28 are the sources for the net rate of production/destruction of k and ε. These two terms can be expressed as follows:

$$S_{k(\varepsilon)} = \alpha_c (P_c - \rho_c \varepsilon_c) + T_{cd}^{k(\varepsilon)} \tag{2.30}$$

$$S_\varepsilon = \alpha_c \frac{\varepsilon_c}{k_c} (C_{1\varepsilon} P_c - C_{2\varepsilon} \rho_c \varepsilon_c) + T_{cd}^\varepsilon \tag{2.31}$$

In equations 2.30 and 2.31, the additional T_{cd} term accounts for the extra production and destruction of turbulence due to the presence of the dispersed phase (i.e. turbulence modulation).

The k-ε model reduces the number of equations for turbulence from 7 to 2, and significantly reduces the computational resources required. At the same time, it has reasonable accuracy and takes into account the interaction between the continuous and dispersed phase (Liu, 2005; Krepper et al., 2007).

RNG k-ε model

The RNG k-ε model is based on the renormalization group analysis by Yakhot et al. (1992). The renormalization group is applied to account for the effects of smaller scales of motion. It has the advantage over the standard k-ε by accounting for the effect of different turbulence length scale on the turbulent diffusion. The modified form of the RNG k-ε model leads to different coefficients in the 'ε' equation (2.28 and 2.31).

Model parameter	Suggested value
β_{RNG} for eqn. 2.32	0.012
$C_{\mu,RNG}$	0.085
$C_{1\varepsilon,RNG}$	$1.42 - f_\eta$
$C_{2\varepsilon,RNG}$	1.68
$\sigma_{k(\varepsilon),c,RNG}$	0.7179
$\sigma_{\varepsilon,c,RNG}$	0.7179

Table 2.4: Coefficients for k-ε turbulence model (Adapted from Ansys CFX Manual).

For fη term in Table 2.4,

$$f_\eta = \frac{\eta\left(1 - \dfrac{\eta}{4.38}\right)}{\left(1 + \beta_{RNG}\eta^3\right)} \quad \text{and} \quad \eta = \sqrt{\frac{P_k}{\rho C_{\mu,RNG}\varepsilon}} \tag{2.32}$$

2.7 INTERPHASE FORCES MODELS

In order to account for the interphase momentum interactions between the continuous and dispersed phases in a turbulence model, various closure equations for the interphase forces that contribute to the momentum balance are required. This section will discuss the various interphase forces.

2.7.1 INTERPHASE DRAG

The interphase drag accounts for the resistance force encountered by one phase due to the presence of the other phase. This force has always a direction opposite to the relative velocity and the total drag force exerted on a single spherical drop can be given by:

$$F_D = \frac{1}{2}C_D\rho_c(U_c - U_d)^2 A \tag{2.33}$$

where F_D, the total drag force, is related to the relative velocity of the dispersed (subscript: d) and the continuous (subscript: c) phase; A is the projected area of a single drop in the flow direction; C_D is the drag coefficient which depends on the dispersed phase Reynolds number. In laminar flow, the Stokes' law is valid and C_D is expressed as:

$$C_D = \frac{24}{Re_d} \text{ if the dispersion Reynolds number, } Re_d \langle\langle 1 \tag{2.34}$$

When the dispersed phase Reynolds number is sufficiently large and the inertial effects dominate over the viscous effects, the drag coefficient becomes constant.

$$C_D = 0.44 \text{ if } 1000 \le Re_d \le 2\times10^{-5} \tag{2.35}$$

In the transitional range of Re_d (0.1<Re_d<1000), both inertial and viscous effects are important and the drag coefficient is a complex function of Re_d which needs to be empirically determined.

Schiller and Naumann (1933) provide an empirical correlation for this transitional range.

$$C_D = \frac{24}{Re_d}\left(1 + 0.15Re_d^{0.687}\right) \tag{2.36}$$

In order to account for the total drag force exerted on the dispersed phase by the continuous phase per unit volume, the sum of the drag forces exerted on all the drops is taken.

2.7.1.1 DRAG FORCE IN DENSE DISPERSION

With the presence of adjacent drops in a dense dispersion, the drag force on a drop is significantly different from that on a single drop in a continuous flow. With the change in dispersed phase fraction, the mixture density also changes accordingly. As a result, a small difference in the buoyancy between a specific drop and the surrounding mixture

Authors	Proposed correlation for drag coefficient
Ishii and Zuber (1979)	Mixture viscosity: $$\frac{\mu_m}{\mu_c} = \left(1 - \frac{\Phi_d}{\Phi_{max}}\right)^{-2.5\Phi_{max}(\mu_d + 0.4\mu_c)/(\mu_d + \mu_c)}$$ where Φ_d and Φ_{max} are the dispersed phase fraction and maximum packing factor respectively. In viscous regime where drops are approximately spherical (similar to Schiller Naumann correlation): $$C_D = \frac{24}{Re_m}\left(1 + 0.15 Re_m^{0.687}\right)$$ where $Re_m = \frac{\rho_c |U_d - U_c| d_d}{\mu_m}$ In distorted fluid drop regime: $$C_D(ellipse) = \frac{2}{3}\sqrt{Eo}E(\Phi_d)$$ where $E(\Phi_d) = \frac{(1 + 17.67 f(\Phi_d))^{6/7}}{18.67 f(\Phi_d)}$ and $$f(\Phi_d) = \frac{\mu_c}{\mu_m}\left(1 - \Phi_d\right)^{1/2}$$ In the regime where churn flow is dominant: $$C_D(cap) = \frac{8}{3}\left(1 - \Phi_d\right)^2$$ Ansys CFX provides an automatic selection criterion for the appropriate C_D $C_D = C_D(sphere)$ if $C_D(sphere) \geq C_D(ellipse)$ $C_D = min(CD(ellipse)$ if $C_D(sphere) < C_D(ellipse)$
Kumar and Hartland (1985)	$C_D = \left(0.53 + \frac{24}{Re}\right)\left(1 + 4.56\Phi_d^{0.73}\right)$
Rusche and Issa (2000)	$C_D = C_{D0}\exp\left(k_1\Phi d\right) + \Phi_d^{k_2}$ where k_1 and k_2 are empirical coefficient.

Table 2.5: Drag coefficient correlations for dense homogeneously distributed dispersions.

occurs. An increase in dispersed phase fraction will increase the mixture viscosity. This will in turn increase the drag force exerted on the specific drop. In addition, the effect of drop shape at the presence of adjacent drops will affect the drag force. Some of the common models used for dense dispersions include the Ishii and Zuber (1979) model which applies a mixture viscosity approach to calculate the drag force in a dense dispersion, the Kumar and Hartland (1985) model which is an empirical correlation based on 998 measurements across a range of Reynolds numbers, the Rusche and Issa (2000) model which is also an empirical correlation between drag coefficient and dispersed phase fraction. The correlations of the above models are listed in Table 2.5. In particular, the Ishii and Zuber (1979) model will be applied in this work as it is the only default model available for dense homogeneously distributed fluid dispersed flow within Ansys CFX.

2.7.2 LIFT FORCE

Lift force is exerted on the dispersed drops when the flow field is non-uniform. This generates a velocity gradient within the continuous phase leading to a force acting onto the drops perpendicular to the direction of the relative motion of the two phases. In Ansys CFX, a model for the shear-induced lift force acting on the dispersed phase is used based on the vorticity of the continuous phase (Equation 2.37)

$$F_{lift,c} = -F_{lift,d} = \Phi_d \rho_c C_L (U_d - U_c) \times \mathrm{curl}\, U_c \tag{2.37}$$

where Φ_d is the dispersed phase fraction. Depending on the sign of the lift coefficient, C_L, as well as the direction of the relative velocity, the lift force can significantly affect the radial phase distribution.

2.7.3 TURBULENT DISPERSION FORCE

The turbulent dispersion force accounts for the effect of the turbulent eddies in the continuous phase acting on the drops and leads to the homogenization of the dispersion.

Two models are included in Ansys CFX – the Favre averaged drag model and the Lopez de Bertodano model (1991).

2.7.3.1 FAVRE AVERAGED DRAG MODEL

Favre averaging is an averaging operation for the turbulent terms using a density weighted average of the turbulence terms. This is significant mainly for compressible flow. In the Favre averaged drag model, an additional drag term is added into the momentum equation by expressing the time averaged drag in terms of Favre averaged velocities. The model is implemented in Ansys CFX as follows:

$$F_{TD,c} = -F_{TD,d} = C_{TD}C_{D,c}\frac{\nu_{tc}}{\sigma_{tc}}\left(\frac{\nabla\Phi_d}{\Phi_d} - \frac{\nabla\Phi_c}{\Phi_c}\right) \tag{2.38}$$

where $C_{D,c}$ is the coefficient of the interphase drag force, ν_{tc} is the kinetic eddy viscosity, σ_{tc} is the turbulent Schmidt number for continuous phase volume fraction (default value: 0.9). C_{TD} is the turbulent dispersion coefficient that is defined by the user where the default value for CFX as 1.0.

2.7.3.2 LOPEZ DE BERTODANO MODEL

The Lopez de Bertodano model (1991) is one of the first models developed for the turbulent dispersion force. It aims to physically account for the turbulent diffusion based on the fluctuating components of the turbulent forces acting on the dispersed drops. The model can be presented as follows:

$$F_{TD,c} = -F_{TD,d} = -C_{TD}\rho_c k_c \nabla\Phi_c \tag{2.39}$$

Where k_c is the turbulent kinetic energy and $\nabla\Phi_c$ is the concentration gradient of the continuous phase. C_{TD} values between 0.1 and 0.5 have been used successfully for bubbly flow with bubble diameters in the order of a few millimeters. However, much higher values have been required in some situations (Lopez de Bertodano (1998) and Moraga et al. (2003)).

2.8 SUMMARY OF LITERATURE REVIEW

Previous works on two-phase oil-water flows and particularly the phase inversion phenomenon have been reviewed. Flow regime development and phase inversion were found to depend on the properties of the fluids, pipe configuration, and operational conditions in a pipeline. Phase inversion has been previously studied mainly in stirred vessels but also increasingly on pipe flow. Among the pipe flow investigations, changes in pressure drop have been used as an indication of phase inversion occurrence. However, it is also known that these changes differ across different fluid systems. In addition, the changes in pressure drop have not been clearly associated with the corresponding changes in phase continuity. Inversion has been reported to occur across a range of phase fraction before completion due to the presence of local phase inversion at certain locations within the system. Thus, experimental investigations to understand the changes in phase continuity and distribution (i.e. changes in flow regime) corresponding to that in pressure drop during inversion will be conducted with results presented in Chapter 4. Successful outcome from this investigation will also allow better prediction of the changes in pressure drops as flow regime changes during inversion. A prediction method for these changes in pressure drop is presented in Chapter 7.

From the literatures reviewed, various models have been developed based on mechanisms including the dynamic process of drop coalescence and break-up, minimization/equal system/interfacial energy of the mixture and zero shear stresses at the liquid-liquid interface. While there is no definite mechanism for the occurrence of phase inversion, these models provide important information about phase inversion. For example, interfacial tension is found to be an important factor on the Weber number and phase inversion in many of the correlations. However, the effects of interfacial tension on phase inversion have not been previously established and thus will be studied in this work (Chapter 5).

Momentum balance is regarded as the underlying principle behind the mechanism of zero shear stresses at the interface. Pressure drop across a pipe is the direct effect of the shear stresses at the interfaces in the system and these shear stresses in turn depend on the fluid

viscosities. A prediction model on phase inversion occurrence will be developed based on this relation between viscosity and pressure drop and is presented in Chapter 6.

Computational Fluid Dynamics (CFD) simulation can offer some insight on the behavior of dispersed systems and will be used in this work. A review on numerical simulations using CFD has been presented. In particular, the k-ε model has been proposed for use in subsequent chapter due to its good estimation of the system without a high demand on computational resources. This is especially important at high concentration of the dispersed phase. Closure equations for the interphase interactions are also presented. Some of the more important interactive forces include the drag force, the turbulent dispersion force and the lift force. The effect of these forces on the spatial distribution of the phases in dispersed systems will be investigated in Chapter 8.

Chapter 3: Facility and Instrumentation

3.1 OVERVIEW

This chapter will introduce the flow facility and instrumentation used for the experimental investigations of phase inversion during oil-water pipe flow. The experimental facility has been constructed in the Department of Chemical Engineering, UCL. There are two test sections made of steel and acrylic respectively and two types of inlets, one that ensures minimum mixing of the fluid and the other creates a dispersion at the beginning of the test section. Various measuring probes are used to measure phase continuity and distribution, pressure drop and drop size distribution. This allows detailed investigations of the flow parameters as the system approaches phase inversion.

3.2 TEST FLUIDS

The fluids used for the experimental investigations of the phase inversion phenomenon are Exxsol D140 and tap water. Table 3.1 presents the physical properties of the two fluids.

	Exxsol D140	Tap Water
Density (kg/m^3)	828	1000
Viscosity (mPa.s) @25°C	5.5	1.0
Interfacial Tension (mN/m) @ 25°C	37.04	

Table 3.1: Physical properties of working fluids

The density of the oil phase is based on the data provided by the supplier (Exxon Chemicals). The oil viscosity was measured using a Contraves 155 Rheometer over a range of temperature. The oil-water interfacial tension was measured using the drop volume method in a Krüss Drop Shape Analysis System (DSA100).

3.3 EXPERIMENTAL FLOW FACILITY

The schematic diagram of the flow facility used in the experiments is shown in Figure 3.1. It consists of three main sections – fluid storage, test pipeline and fluid separation units. The test pipeline has been designed to accommodate various instrumentations and inlet to investigate the development of dispersed flow and the occurrence of phase inversion. These will be discussed in detail below.

Fluid Storage Section

This section consists of two fibre-glass storage tanks with a capacity of 880 liters each for oil and water respectively. There are two acrylic baffles in each tank to prevent vortices that may allow air to entrain in the fluids and be transported into the test section. The baffles are also positioned in such a way to allow extra time for separation of the fluids in case one phase enters the storage tank of the other phase. The tanks are similarly connected to the centrifugal pumps on one end and to the separator on the other end. Fresh fluids are manually put into the tanks while the fluid level in each tank is kept at least ¾ of the tank height. Fluids can be recycled from the separator. In addition, fluid from the recycle line of the pump is returned into the tank to regulate the outflow through the pumps into the test pipeline. At high flowrates, water may enter into the oil storage tank. In this case, the oil tank is drained into a spare separation tank from which the oil is recycled bank to its storage tank and water is discarded. Fresh water is consistently used if possible to ensure clean water stream is pumped into the pipeline during experiments. Fresh water is also used to maintain the temperature of the fluid mixture in the test section at approximately 20°C (+/- 5°C).
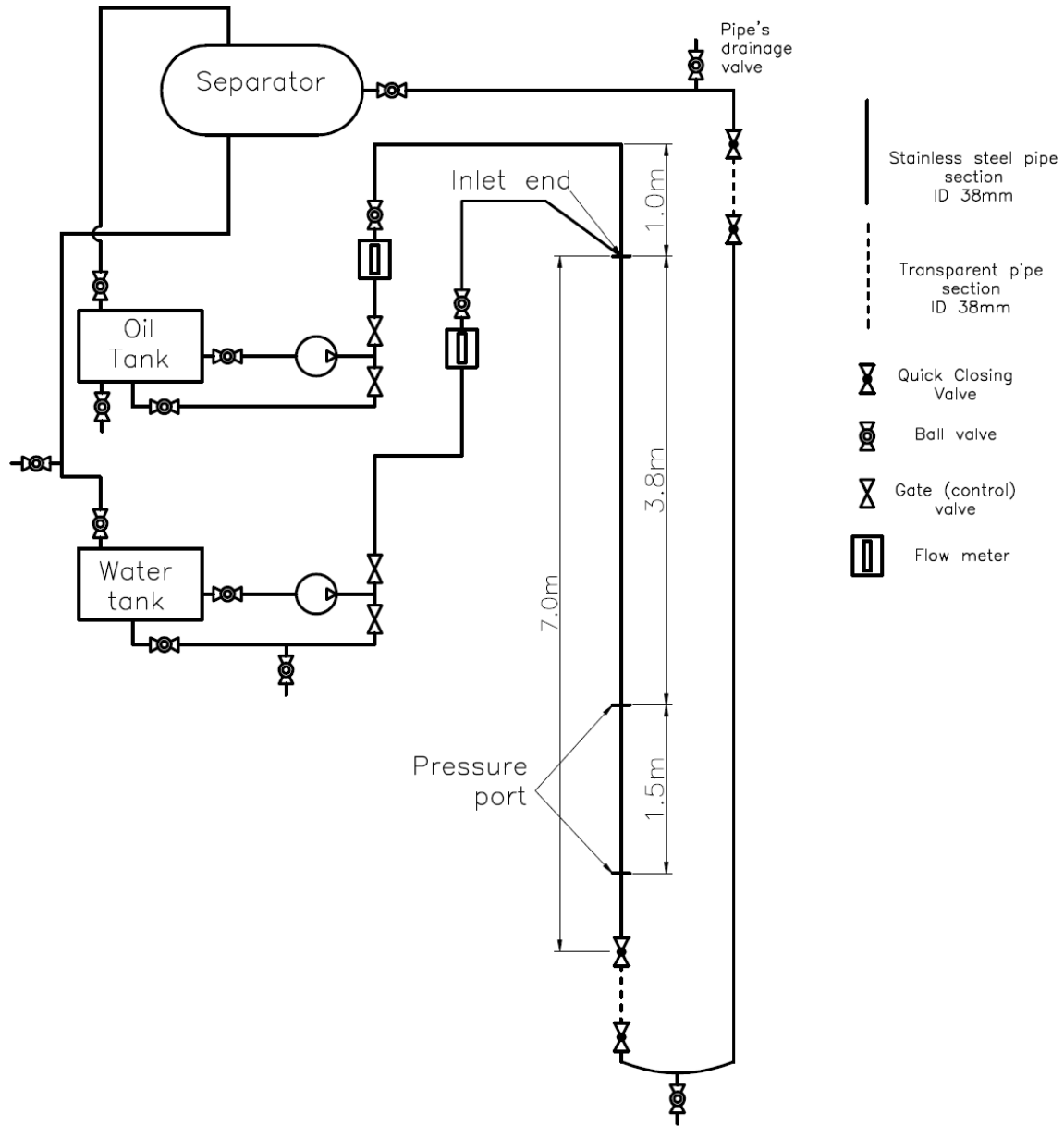
Figure 3.1: Schematic of the pilot scale facility with adjustable sections in the test pipeline.

The centrifugal pumps (Ingresoll-Dresser CPX200) are capable of generating a flow rate of 240l/min. A recycle line back to the storage tank is used to regulate the flow rate of each fluid in the flow meter. Good control over the regulation of the flow rate through the pumps and the recycle streams is crucial in minimizing fluctuation of flow to the test pipe section. This also avoids exceeding the designed capacity of the pumps and cause overheating.

The flow rates of the respective fluids are monitored by two variable area flow meters (ABB Instrumentation 10A5400) with maximum error of 1% of the full scale. The flow meters measure a range between 20 – 240 l/min and are connected to a PC for data logging.

Test Pipe Section

The test pipe has a total length of 16m with an internal diameter of 38mm and is split into the front and back legs connected by an U-bend with a 150mm diameter curvature. Two test pipes have been constructed from stainless steel and acrylic respectively. The entire pipeline consists of sections of 1m and 2m long. This allows the various instruments that are fitted in between two pipe sections to be installed at different axial locations along the test pipe. The sections are either joined by tri-clamps (in the stainless steel pipeline) or flanges (in the acrylic pipeline). These instruments are however fitted away from the U-bend at the end of the first leg of the pipeline to avoid any influence on the flow distribution. The probes can also be located at 7m (~184D) from the inlet when the quick closing valves are not required.
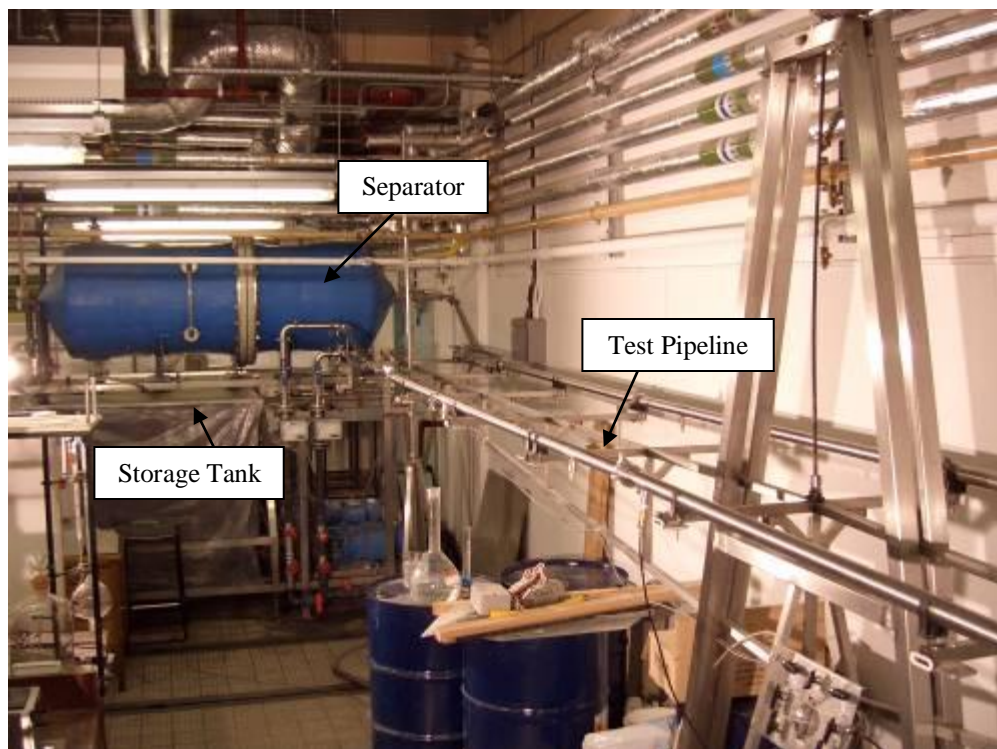
Figure 3.2: Photograph of the pilot scale facility in stainless steel.
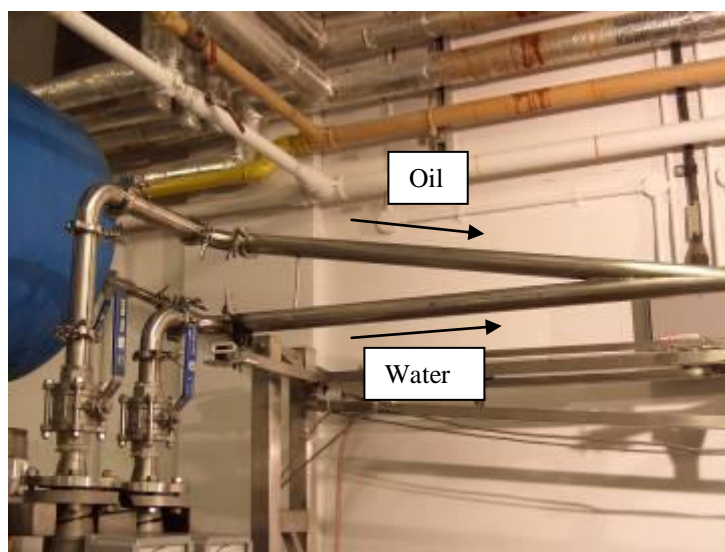
Figure 3.3: Stainless steel Y-inlet where the oil and water phases are joined at the end.

As observed in both Figures 3.2 and 3.3, oil and water are pumped through the inlet to the test section. Two types of inlets were used. A Y-inlet (Figure 3.3 and 3.4) was used to ensure that the fluids join with little mixing. The oil stream flows from the upper inlet pipe and the water stream flows from the lower inlet pipe. The two pipes join with an angle of approximately 15°. In addition in the acrylic inlet section, a splitting plate is added where the two pipes join to further ensure minimum mixing of the two liquids (see Figure 3.4).
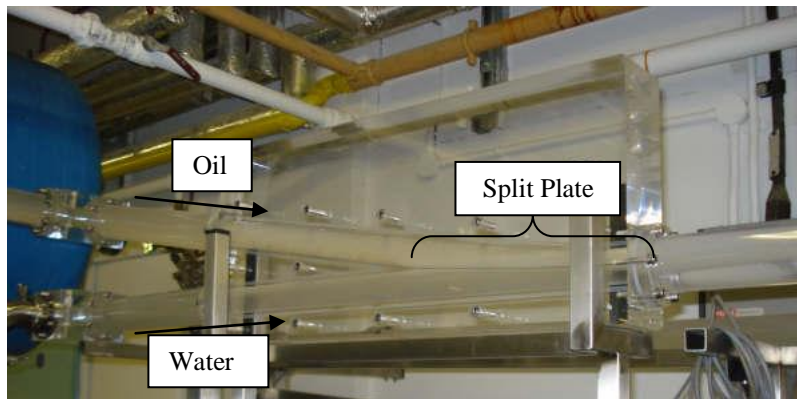
Figure 3.4: Acrylic Y-inlet with a split plate to enhance stratification of the oil and water.

A dispersed inlet (Figure 3.5) was also constructed to create a dispersion from the beginning of the test section and influence the type of dispersion formed. The inlet is made from a steel pipe with a total of 1056 nozzles with heights 2mm and 4mm around its periphery. Nozzles of the two heights are staggered so that the fluid jets from the nozzles have more space to develop and do not coalesce with each other.

(a)   (b)
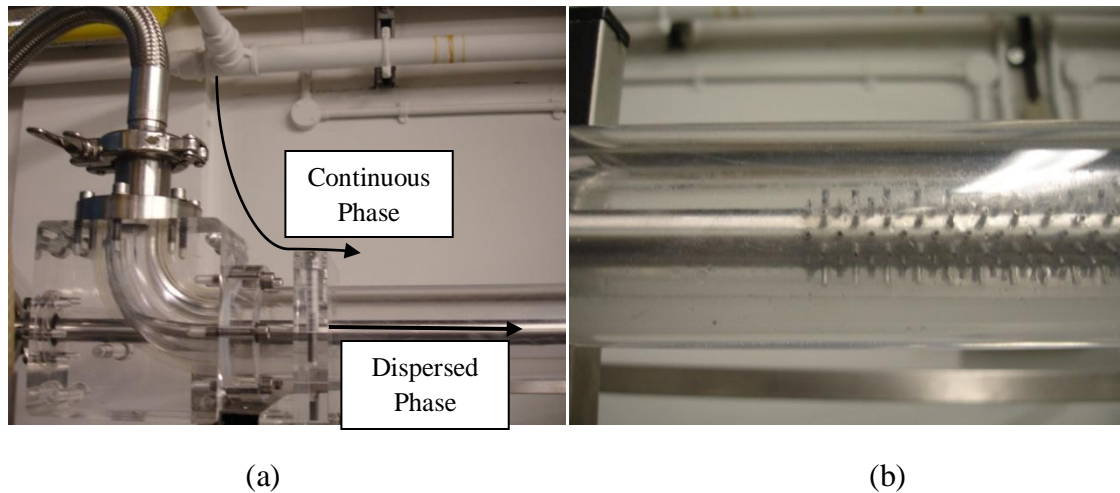
Figure 3.5: Dispersion inlets with staggered nozzles. (a) The dispersed phase flows within the stainless steel pipe while the continuous phase flows in the acrylic pipe. (b) Dispersed phase is ejected from the nozzles.

Separation Section

A horizontal two phase separator is installed at the end of the test section (Figure 3.2) with 800 litre in capacity. The separator contains a KnitMesh (DC 9201/SS/PPL) coalescer to aid the separation process. The coalescer uses a composite of two materials with different surface free energies (metallic and plastic). The junction effect from the combination of the two materials increases the rate of coalescence when the droplets are trapped and move towards the junction points of the coalescer as shown in Figure 3.6. The separator is also used, at the end of each experimental session, for a more thorough separation by gravity. This will generally take about 48 hours before the next experimental run before the fluids are recycled into the storage tanks. In occasions when there is water entrained in the oil storage tank, further separation will take place within the tank and excess water will be removed.
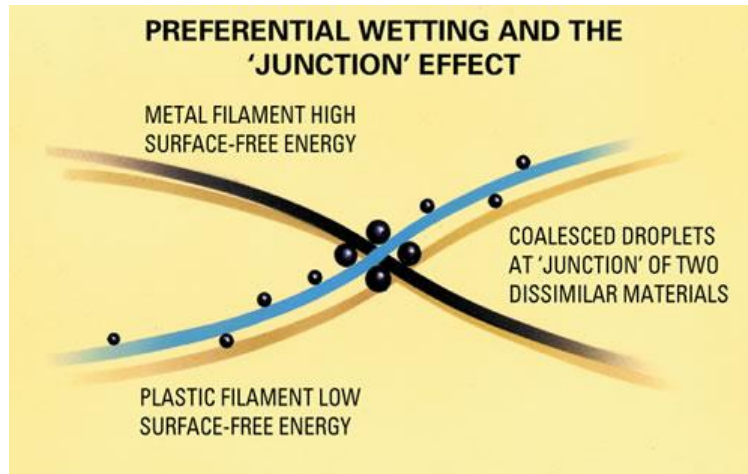
Figure 3.6: Junction effect of the coalescer that enhances separation. (Information from manufacturer - KnitMesh Technologies).

Instrumentation

(a) Visual Observation

Visual observation of the flow development can be captured throughout the acrylic pipeline or through a viewbox in the steel pipeline. Visual imaging is facilitated with a high speed video camera (Kodak HS 4540 MX) which has a capturing rate of 4500 fps and a total recording time of 1.8 second. A monitor is connected for real time visual observation. Figure 3.7 shows the setup of the video camera. The camera is connected to the PC for data capture and storage. Video images can be saved and individual frames extracted for further analysis. Background lighting (Spot light unit) is used to enhance the contrast between the oil and water phases and improve the quality of the images.

Figure 3.7: Setup of the high speed video imaging unit, Kodak HS 4540 MX.

 (b)Fluid hold-up

Average volume fraction is measured using two quick closing valves (QCVs). Two ball valves are fitted on both ends of a transparent pipe section of 1m in length to trap fluid mixture with a volume of 1.13 litre (Figure 3.8). The pipe section is located at 7m (~184D) from the inlet (and also the last section before the U-bend in the setup). Once the pipe section is closed, the mixture can be drained into a measuring cylinder for separation. The respective volume fraction of the two phases can then be identified. A manual hand pump is used to minimize any retention of the oil phase in the pipe. The measurements are repeated several times with 2% deviation across measurements. In the experiments, the two valves are closed simultaneously with the pumps. The trapped mixture is drained in a measuring cylinder where the volume of each phase is identified and recorded.
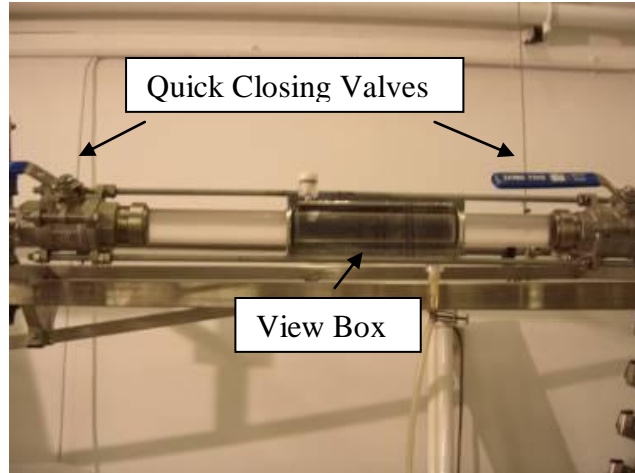
Figure 3.8: Section of pipe with quick closing valves in the 38mm stainless steel pipeline. A viewbox is included to aid visual observation and video capturing.

(c) Instrumentation for phase continuity measurement

1) Conductivity Ring Probe

The ring probe consists of two metallic rings embedded on the pipe perimeter, flush with the wall, and in contact with the fluid mixture. Each ring is 4mm wide and the rings are 38mm apart (Figure 3.9). The conductivity ring probe is generally located at about 7.0m (~184D) from the inlet where the flow is considered as fully developed. The ring probe is normally paired with the conductivity wire probe to measure the conductivity at the test section and provide information on phase continuity and distribution. High conductivity values indicate that a conductive water continuous mixture is in contact with the probes, while low values denote an oil continuous mixture.

Figure 3.9: Conductivity ring probe for phase continuity measurement at the pipe periphery.

2) Conductivity Wire Probe

Each wire probe consists of a pair of bended copper wires with a diameter of 0.5mm (Figure 3.10). The wires are 10mm apart and this gap is assumed to be greater than the largest droplet of the dispersed phase. This will ensure that any change in conductivity signal is due to a change of the continuous phase. It can detect phase continuity at different locations in a pipe cross section using a traversing mechanism. The wires are bent (Figure 3.10b) in L-shape at opposite directions and only the horizontal portions of the wires are exposed to the flow. This provides a large contact surface at particular height in the pipe cross section.

During experiments, the ring probe and the conductivity wire probe are used primarily to detect the phase continuity at the pipe periphery and the centre of the pipe cross section respectively unless otherwise stated. These locations are found to be critical during phase inversion from previous experiments (i.e Hu, 2005, Ioannou, 2006). The electrical resistance tomography will also be used to supplement on the phase continuity investigation on other locations (e.g. top of pipe cross section). The application of the tomographic system will be discussed in the next section.

(a)
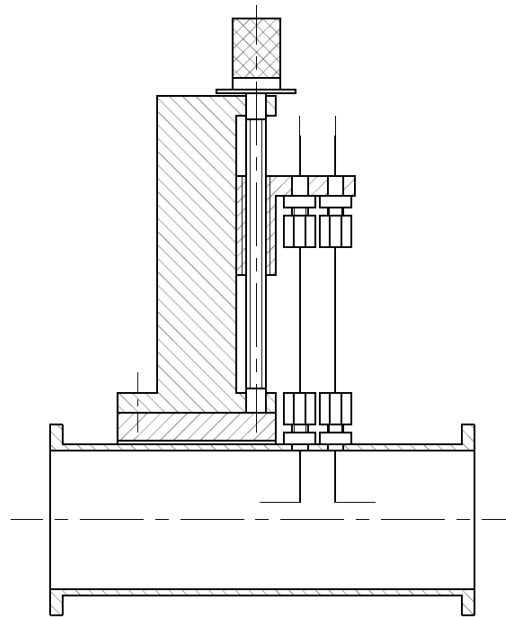
(b)

Figure 3.10: Local conductive wire probe for phase continuity measurement at the localized position. (a) Photo of wire probe (b) Schematic of the interior (side view) of the wire probe.

3) Electrical resistance tomography (ERT)

Electrical resistance tomography provides information on the distribution of the phases in a mixture through a series of electrodes arranged at regular intervals within the boundary of the vessel investigated. A commercial ERT system (Model: M3000 by Industrial Tomography Systems, ITS, plc) is used in the current work. The tomographic sensor consists of 16 electrodes equally distributed around the periphery of an acrylic pipe (Figure 3.11a). Each electrode is made of a 4mm diameter circular stainless steel piece embedded on the acrylic pipe wall and in contact with the mixture inside the pipe. Care is taken to ensure that each electrode is flush with the interior pipe wall. Thus, ERT is considered to be non-intrusive. The ERT can provide a signal as long as there are at least 2 electrodes in contact with the conductive phase (i.e. water) where one electrode acts as a transmitter and the other as a receiver. The tomographic sensor provides a resolution of 316 pixels over the 38mm pipe cross section with each pixel representing approximately 2mm x 2mm.

Electrical signal is transmitted from a transmitting electrode and received by the remaining 15 electrodes. The sample data transmission is repeated in sequence until all 16 electrodes have acted as the transmitting electrode. All the received data will be processed through a reconstruction algorithm to generate the phase distribution through a cross-sectional image. The sampling frequency in this study is set to be 10 images per second. The algorithm used in this study is the Linear Back Projection (LBP) which allows quicker and less computational resource intensive for the reconstruction. This is important in capturing the rapid changes during phase inversion despite the compromise on the resolution of each image. A software (ITS toolsuite) is used to present the reconstructed images (Figure 3.12) for visualization and data analysis. Localised conductivity value at each pixel across the pipe cross section can also be exported to Excel for further data processing.
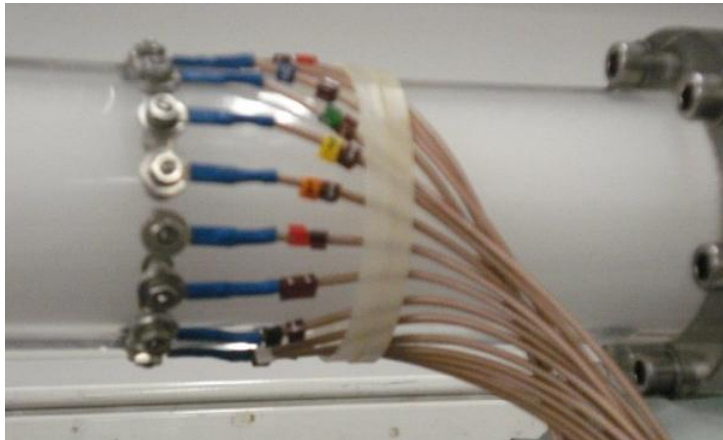
(a)
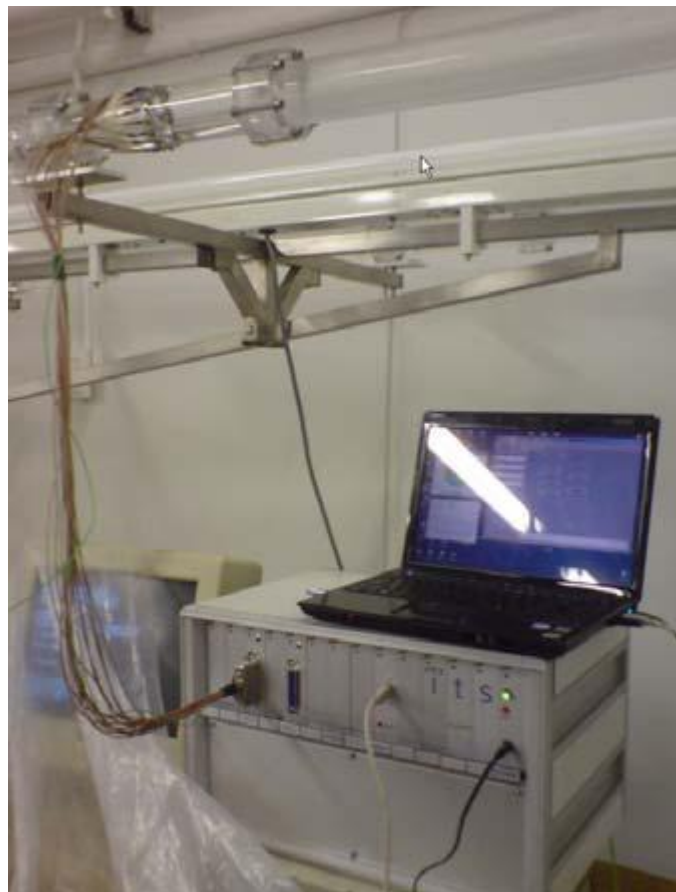
(b)

Figure 3.11: (a) Stainless steel electrodes embedded across the pipe periphery. (b) Experimental setup of the ERT system with a PC for data processing.
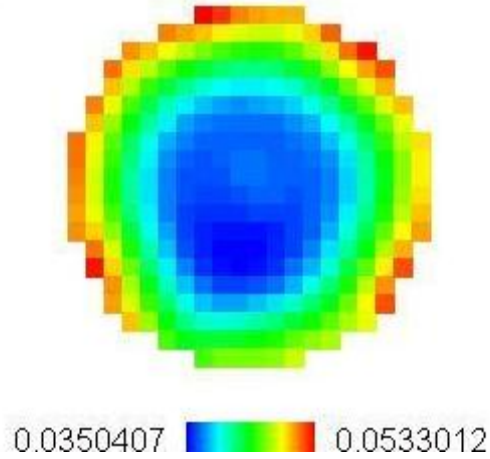
Figure 3.12: Sample ERT reconstructed image generated from ITS toolsuite. The colour bar denotes the range of raw conductivity data with respective to the reference frame.

From the phase distribution data, the fraction of each phase in a pipe cross section can be found. This can be compared with the results from QCVs and an average difference of 5.6% is observed between the two methods. Figure 3.13 presents the results of the comparison. An average deviation of 5.6% from the diagonal line can be found from the ERT measurement while an average deviation of 3.6% from the QCV measurement. It can thus be assumed that the mixture flow across the wide range of phase fraction to have no slip (i.e. the input volume fractions of the oil and water equals to the in-situ phase volume fractions). The ratio between the volume fractions is defined as the slip ratio (S) presented in Equation 3.1 and the slip ratio is 1 when there is no slip.

$$S = \frac{\beta_o / \beta_w}{\varepsilon_o / \varepsilon_w} \tag{3.1}$$

where β_o and β_w are the input volume fractions of the oil and the water phase respectively, and ε_o and ε_w are the in-situ volume fractions of the oil and water phase respectively.
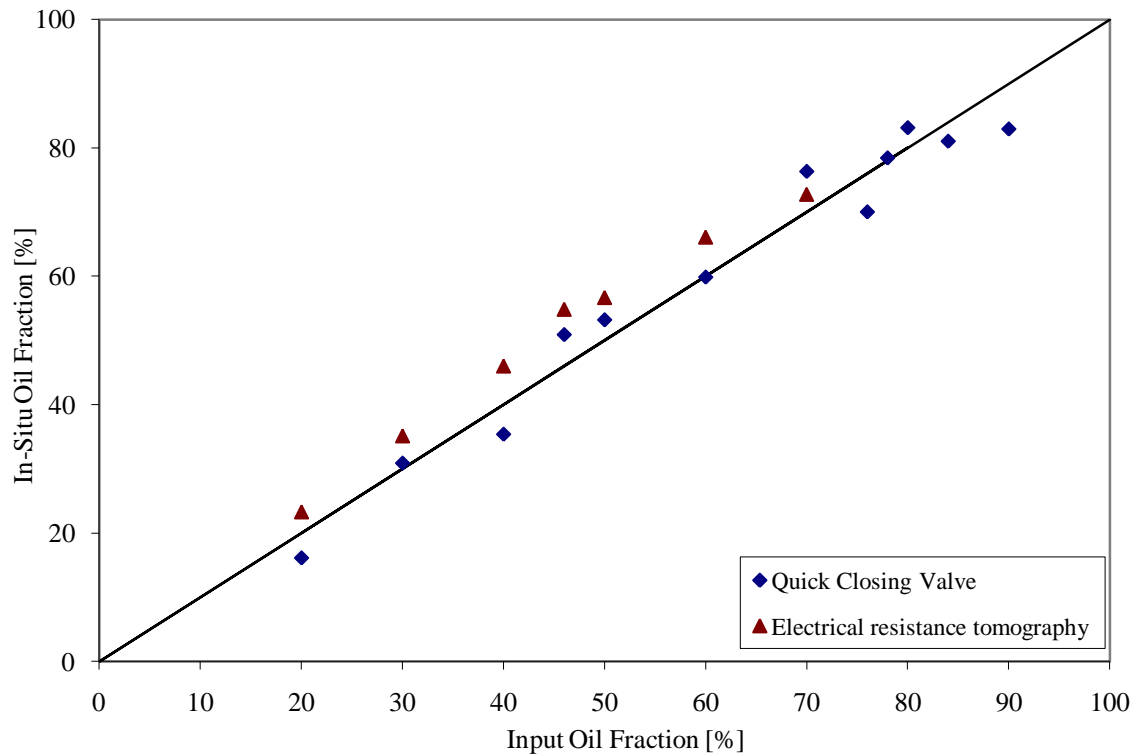
Figure 3.13: In-situ liquid hold-up comparison between electrical resistance tomography (ERT) and quick closing valves across a range of input phase fractions at a mixture flow velocity of 3m/s.

(d) Drop velocity and drop size distribution

The measurement of drop velocity and drop size distribution is made using the dual impedance probe developed by Lovick (2004) at University College London (see Figure 3.14). The details on the development and operation principles can be viewed in his thesis (Lovick, 2004).

As shown in Figure 3.14, the dual impedance probe consists of two coaxial wires which can work independently as sensors detecting the contacting phase at each of the wire tips. Each tip is tapered with insulation in between the coaxial wires as shown in Figure 3.14(b). The coaxial wires are placed at the same housing as the conductivity wire probe presented in Section 3.3 Figure 3.10. The probe tips can thus be moved to measure at different locations in the pipe cross section. The distance

between the two wires is again 10mm and this is assumed that no drop is larger than this distance within the experimental flow conditions used in this work.
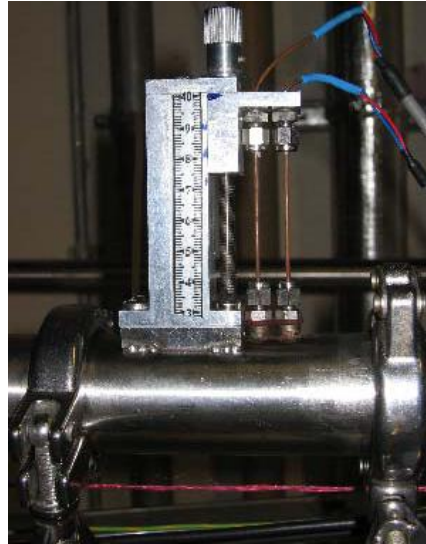
(a)
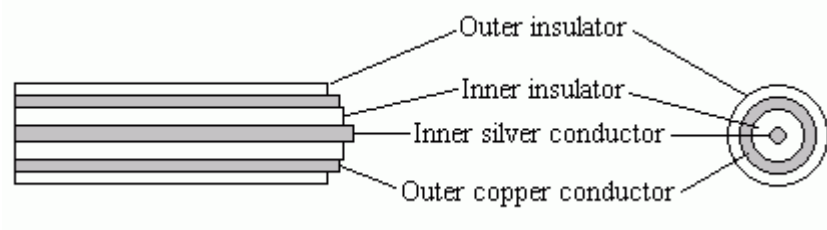
(b)

Figure 3.14: (a) Photograph of the dual impedance probe setup. (b) Probe tip configuration (Lovick, 2004).

Measurements using the dual impedance probe are conducted at 7m from the test section inlet. The impedance wires are set at the same height inside the pipe perpendicular to the flow direction. It is assumed that drops that pass through the first probe will also pass through the second probe. A single frequency regulator controls the frequencies of the two probes to ensure that they are measuring at the same cycle. The sampling frequency is set to 45kHz. At this high frequency, each sampling cycle has a time span of 22μs, and this is capable of measuring a minimum

drop size of 66μm at 3m/s mixture velocity or 88μm at 4m/s mixture velocity. At this high frequency, it is expected that each dispersed drop will cross each probe tip over a succession of sampling cycles (see Lovick, 2004; Hu, 2005; Ioannou, 2006). 120,000 data points are captured at each location. An example of the normalized signal data from the dual impedance probe is presented in Figure 3.15.
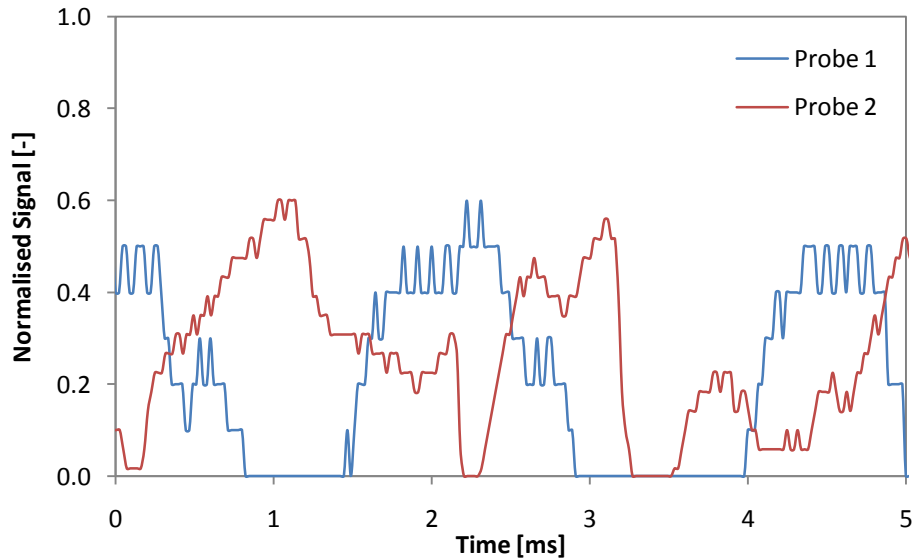
Figure 3.15: A sample set of normalized signal from the two impedance wires at a mixture velocity of 3m/s. Dispersed phase will be in contact with probe 1 before it contacts with probe 2.

The time delay (see highest peak of Figure 3.16) for the drops to pass through the two probes is found by cross correlating the signals of the two probes with a fixed distance of 10mm. By combining with the known distance between the probes, the drop velocity can be found (Lovick, 2004). The chord lengths of the measured drops can be estimated from the signal of either probe by multiplying the drop velocity with the time duration of each drop passage. The duration of each drop passage is obtained by converting the raw signals of the probe into square waves based on the level and slope threshold values (Lovick, 2004 and Hu, 2005). It should also be noted that measurements of chord length through this method tend to be biased

towards the larger drops as they are more likely to pass through the probe tips than the smaller drops.
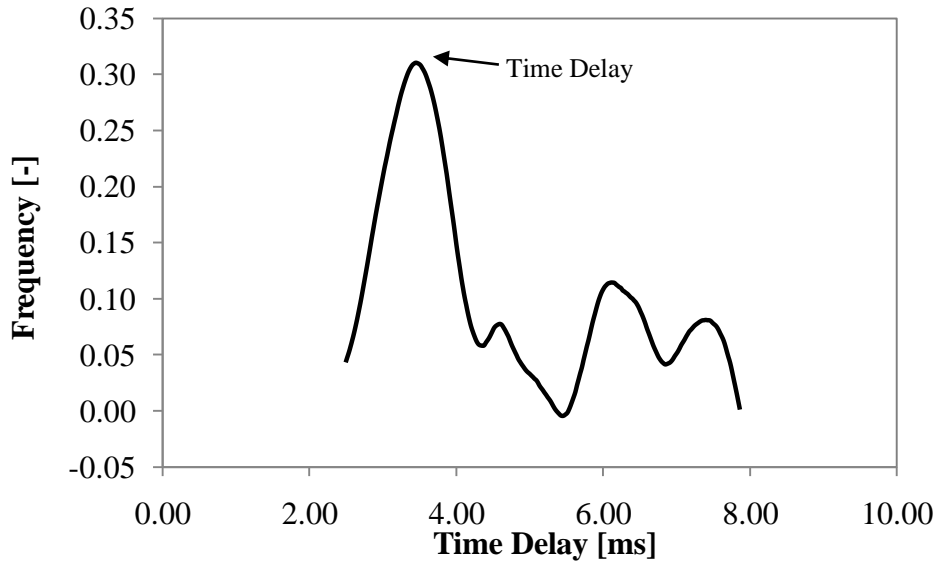
Figure 3.16: A sample frequency plot of the time delay between the two impedance wires. The highest peak denotes the time delay where most dispersed drop take to cross the two wires.

Drop size distribution is then estimated from the chord length measurements. An algorithm by Hu et al. (2006) provides the relationship between the chord length distribution (CLD) and drop size distribution (DSD). In order to apply this algorithm, the measured drops are assumed to be spherical. Sauter mean diameter (d_{32}) can then be calculated from the drop size distribution.

(e) Phase distribution measurements

Phase distribution measurements can be made using the same dual impedance probe as described in the previous section. Only one impedance wire is required (generally the first one to avoid any obstruction) for the measurement. Local phase distribution measurements are made across 20 locations at 2mm intervals vertically across the pipe cross section and diagonally at 45° and 10 locations horizontally. Phase distribution is assumed to be mirrored at the vertical plane and thus the phase

distribution data at the 135° plane is the same as the 45° plane. By interpolating the local measurements over the whole pipe cross section, the in-situ time-averaged volume fraction of the two phases can be found. Phase distribution contour plots can also be created using Matlab and compared with the tomograms generated by the ERT system. Table 3.2 presents the comparison between the impedance phase distribution contour plots and the ERT tomograms.

Input Phase Fraction	80% Water	54% Water	40% Water
Impedance phase distribution contour plot			
ERT tomogram			
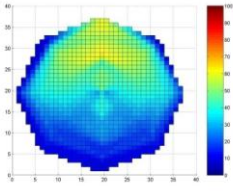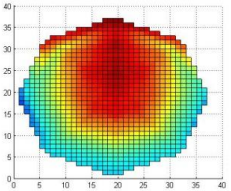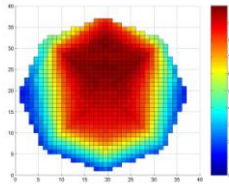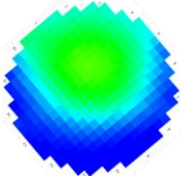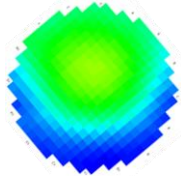
Table 3.2: Comparison of phase distribution contour plot using single impedance probe (red for oil and blue for water) and ERT tomogram (green for oil and blue for water) at different input phase fractions in a 3m/s oil/water mixture flow.

From the table, it can be observed that the phase distribution measured using both methods produce similar phase distribution diagrams. However, the tedious process of generating a single contour plot requires 30 minutes of measurement and processing time while an ERT tomogram requires less than a second for each tomogram. The ERT system will thus be able to provide more instantaneous information about the phase distribution and this will be done so in subsequent studies presented in this thesis.

98

(f) Pressure gradient measurements.

Pressure gradient is measured by a FP2000 wet/wet differential pressure transducer (RDP Electronics Ltd). The pressure transducer is connected to the test section via nylon tubing and quick connect couplings. The first pressure measuring port is located on the test section at 3.8m (~100D) from the inlet and the second port is located 1.5m apart. The male adaptor of the quick connect couplings is connected to the port while the female adaptor is fitted to the nylon tubing as shown in Figure 3.17. These quick connect couplings offer the flexibility to change the location of pressure gradient measurements. During connection and disconnection, the couplings are automatically shut off to avoid any air entrainment or leakage which would affect the pressure gradient measurements. The dimensions of the ports were carefully designed with the bore diameter of the port opening at the test section to be no more than $1/8^{th}$ of the pipe diameter (Perry, 1997). In addition, the pressure transducer is connected to a transducer conditioner (type E308) which is calibrated for pressure gradient data logging. The transducer conditioner has a capability of measuring a maximum pressure of 22kPa and an accuracy of 0.25% of the full scale.

(a)   (b)
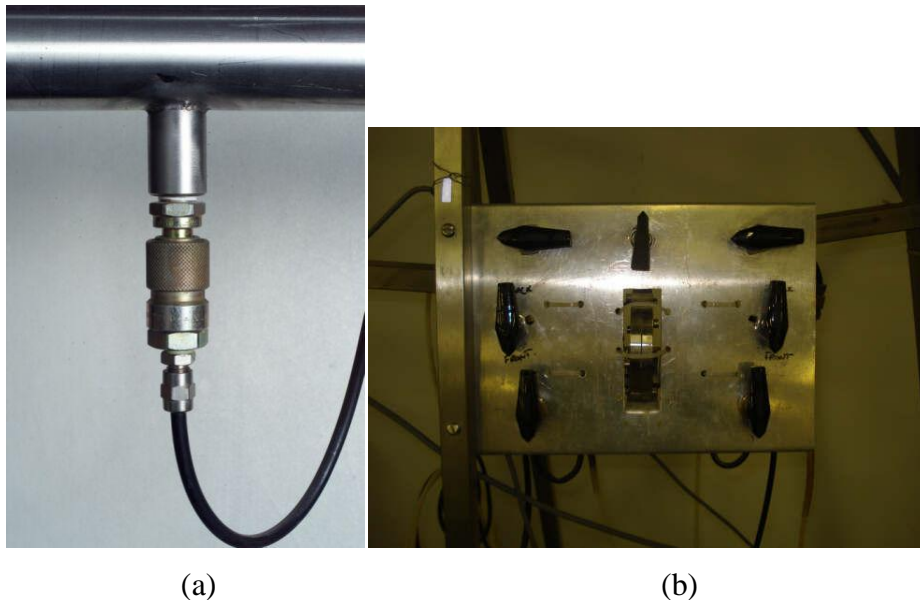
Figure 3.17: (a) Pressure measuring port at stainless steel pipeline. Similar ports are also found in the acrylic pipeline (b) Differential pressure transducer and control valves.

3.4 SUMMARY

In this chapter, the experimental facilities used for the experimental investigation of phase inversion have been discussed. Two test sections were made from stainless steel and acrylic, with 38mm I.D. had been used, and two inlets, a Y-junction and a dispersed inlet, were developed to study their effect on flow patterns and phase inversion.

A number of instruments were used to study the phase continuity, drop size distribution, average holdup and pressure drop. From the various conductivity probes used to detect phase continuity in a pipe cross section, electrical resistance tomography provides faster measurements. However, it cannot detect thin water layers that do not cover at least two sensor electrode and also, in the case of an annular flow with oil in the annulus, it cannot give measurements on phase continuity in the pipe core. A dual impedance probe will also be used to investigate drop size distributions under different conditions. The probe can also provide phase distribution data which is comparable with the ERT results. Nonetheless, ERT has the advantage of quick measurement and will be used for the purpose of accounting the phase distribution in the pipe cross section in experimental studies.

Chapter 4: The occurrence of phase inversion

4.1 OVERVIEW

Phase inversion has been investigated in horizontal pipelines (in stainless steel and acrylic) for mixture velocities between 3.0m/s and 4.0m/s where dispersed flow was observed in previous investigations (Hu, 2005; Ioannou, 2006). Investigations have been conducted for two inversion routes by (1) starting from a water continuous dispersion or pure water phase if possible and increasing the oil input fraction at a constant mixture velocity (o/w → w/o) and (2) starting from an oil continuous dispersion or pure oil phase if possible (w/o → o/w) and increasing the water fraction at a constant mixture velocity.

In Section 4.2, a brief description of the experimental procedure is discussed. The applied procedure is similar to the direct experiments by Piela et al. (2008) where specific phase fractions of oil and water are introduced in the pipe at a constant mixture velocity to allow for flow development along the pipeline. Measurements are conducted at the end of the pipeline where the flow is developed.

Phase inversion is first observed through high speed images and the visual observations are summarized in Section 4.3. Based on the visual observations, the various conductivity probes are positioned and the change in phase continuity during inversion is discussed in Section 4.4. Conductivity ring and wire probes detect the phase continuity of the contacting phase at the pipe periphery and the centre of the pipe respectively. Electrical resistance tomography is also used to support the investigation by identifying the phase fraction at other locations as well as to provide visual images on how the phases are distributed during phase inversion. The use of the various probes is then applied to investigate the effect of inversion route and mixture velocities on the development of phase inversion (Section 4.5 and 4.6).

The associated changes in pressure gradient are presented in Section 4.7 whereby a change in phase distribution can have an impact on the corresponding pressure gradient. Similar changes effected by the inversion route or mixture velocity are also discussed in the section.

As phase inversion leads to significant change in drop size, Section 4.8 aims to investigate the drop size distribution of the dispersed phase as well as a mechanism for phase inversion based on the dynamic balance between drop coalescence and drop break-up.

Lastly, similar investigation has been conducted in a dispersed inlet. The effect of the dispersed inlet is presented in Section 4.9. It is observed in the section that the inversion process is significantly different from the split inlet where the two fluid phases are allowed to mix along the pipeline. With the outcome from this chapter, the results will form the basis for further investigations in the investigation on the effect of interfacial tension on phase inversion in Chapter 5 as well as the data set for comparison with mechanistic models and CFD simulations in Chapter 7 and 8 respectively.

4.2 EXPERIMENTAL PROCEDURE

The experiments for the investigation of phase inversion occurrence were conducted in the pilot scale facility discussed in Chapter 3 with a 38 mm ID test section. An acrylic test section was made to allow visual observations of the flow along the pipeline especially at the initial length when the flow pattern is still developing. A modified inlet with a splitting plate is used to minimise any turbulent mixing caused by the Y-junction inlet. Thus, any mixing along the pipe is assumed to be due to the turbulent flow. High speed images are taken at approximately 7m (~184D) downstream the inlet to visually observe the change in phase distribution as the dispersed phase fraction is increased. Conductivity measurements are also taken to determine phase continuity (See Section 4.4). The conductivity ring probe, mounted on the pipe perimeter, indicates which phase is in contact with the pipe wall. A conductivity wire probe, that can transverse along a

pipe diameter, is used to detect the local phase continuity; the probe tip is set at the centre of the pipe during the current experiments. The probes are located at 7m from the inlet. An electrical resistance tomographic (ERT) system is also used to complement the conductivity probe measurements. In the results reported below, the ERT system is primarily used to detect changes in phase continuity near the top of the pipe. The ERT system is located at approximately the same position as the conductivity probes. Pressure drop is recorded via a pressure transducer which is connected with two measuring ports in the pipe, 1.5m apart, with the first port located at 3.8m (~100D) downstream the inlet. The mixture velocity varies between 3.0 and 4.0 m/s. Previous work showed that the flow is fully dispersed at this velocity range (Ioannou, 2006). Exxsol D140 and tap water are used as the oil and water phase respectively with their properties shown in Table 3.1. Two phase inversion routes are followed (1) starting from an oil-in-water dispersion, or single phase water if possible (2) starting from a water-in-oil dispersion, or single phase oil if possible. In both cases, the initial dispersed phase fraction is gradually increased while the continuous phase fraction is reduced until phase inversion is reached and beyond while maintaining a constant mixture velocity. This approach is similar to the 'direct' experiments conducted by Piela et al. (2008). The intervals in the input phase fractions for measurements are smaller close to the inversion point (i.e. 20% - 60% water fraction) than away from it (ie. below 20% and beyond 60% water fraction). At each phase fraction in a particular mixture velocity (i.e. a single data point), the flow is allowed to establish for approximately 5 minutes before any measurement is taken.

4.3 VISUAL OBSERVATIONS OF PHASE INVERSION

The use of the high speed camera provides the first indication on how the two phases are distributed as they flow together along the test section. These images facilitate the positioning of the various probes for detecting changes in phase continuity. Figure 4.1 shows images from the stainless steel pipe for 3m/s mixture velocity starting with high water fractions where the mixture is water continuous and gradually reducing the water fraction until phase inversion occurs and an oil continuous dispersion is obtained (Camera model: Vision Research Phantom V5.1). The oil phase tends to appear white in

the images and the water phase appears transparent. While the oil drops in an oil-in-water dispersion reflects light from the foreground lighting causing a sparkling appearance, a water-in-oil dispersion tends to be dull white.

| (60%) | (53%) | (40%) |

| (33%) | (20%) | (13%) |
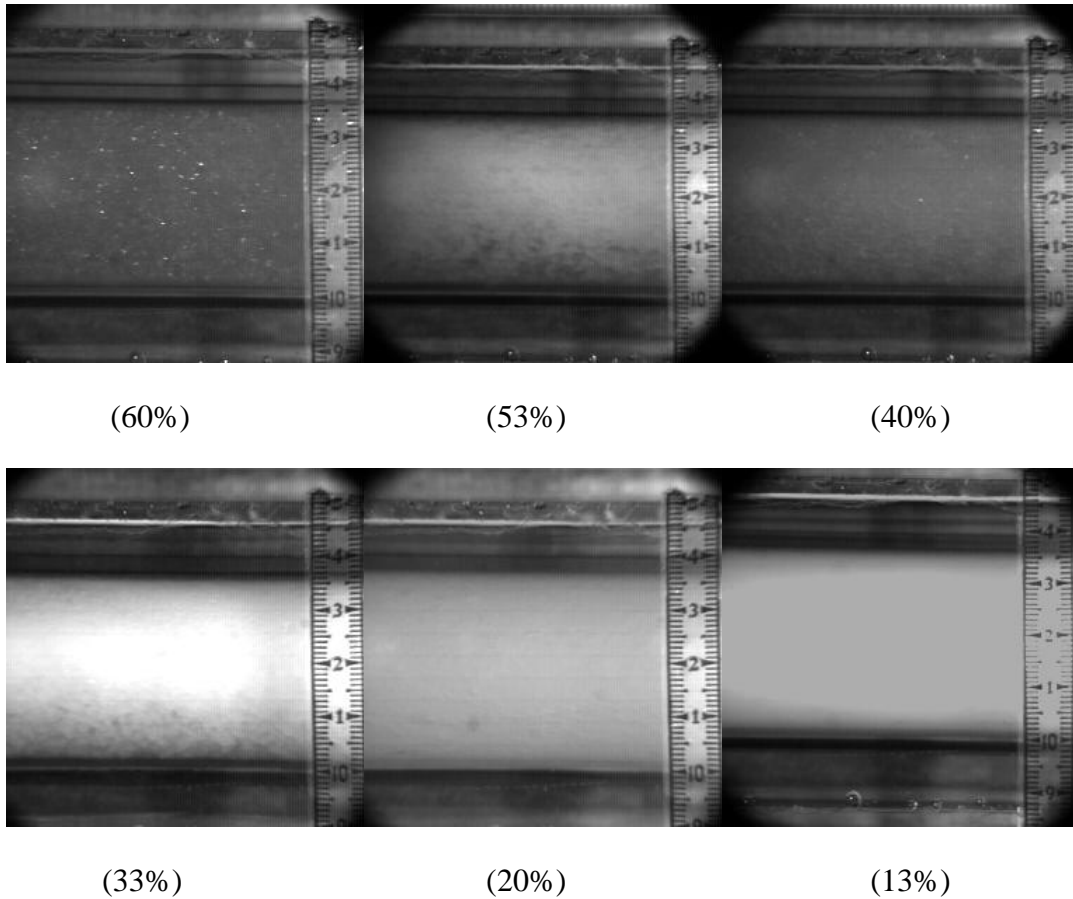
Figure 4.1: Visual images are taken in a stainless steel pipe using an high speed camera (Model: Vision Research Phantom V5.1) at 7m away from the inlet. Mixture velocity is kept constant at 3m/s. The percentage in the bracket represents the input water fraction which the image is taken.

At 60% input water fraction, an oil-in-water dispersion can be seen with the oil drops evenly distributed across the pipe. As the water fraction is reduced to 53%, the oil drops

tend to move towards the centre of the pipe (i.e. milky white region). The region close to the bottom pipe wall appears to remain dominated by the water phase with oil drops flowing within. Further reduction in water fraction to 40% and 33% shows dense dispersions especially at the upper part of the pipe due to buoyancy of the oil drops. Water continuous dispersion can only be identified visually near the bottom pipe wall. At about 20% of water fraction and beyond, the whole pipe is completely dominated by the oil continuous dispersion. With an oil continuous dispersion, water drops cannot be easily seen.

Similar experiments were also carried out in the acrylic test section. The resolution of the images captured in this set of experiments is lower than in the steel pipe because a high speed camera (Model: Kodak HS 4540) with lower resolution and weaker lighting units was used. The difference in appearance between the oil and water phase was still possible to detect.

Figure 4.2 shows the images taken using a cold light unit that illuminates the image from the back. Since water is transparent, light will be able to penetrate through an oil-in-water dispersion (with an appearance of a light grey image). No light can get through a water-in-oil dispersion leading to the appearance of an opaque black image. For example, the oil-in-water dispersion at 60% water fraction has a bright appearance. As more oil is added (34%, 40% and 54% water fraction), the upper part of the pipe becomes opaque as oil drops concentrate here due to buoyancy. The lower region remains bright and complex oil structures can clearly be observed flowing within the continuous water phase. This water continuous region becomes thinner and closer to the bottom pipe wall as more oil is added. From approximately 20% input water fraction and below, the entire pipe is completely opaque indicating that oil is the continuous phase throughout.
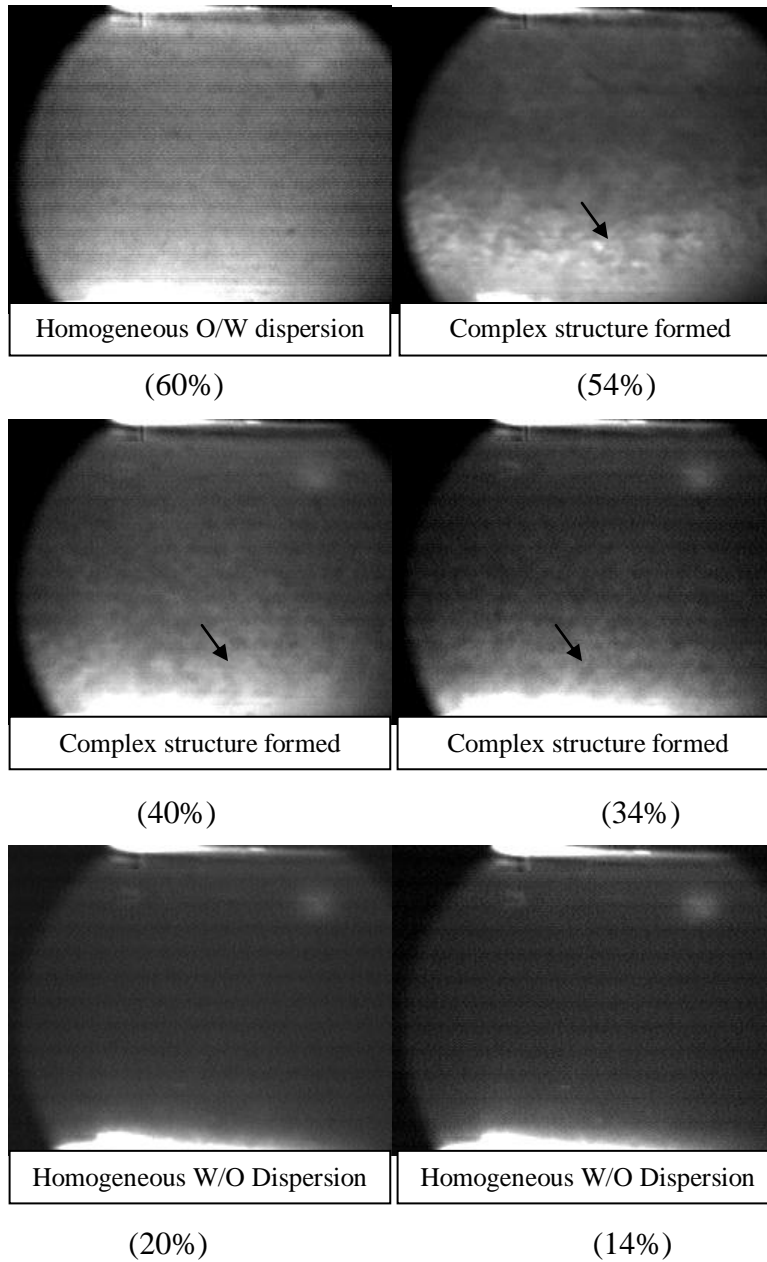
Figure 4.2: Visual images are taken in an acrylic pipe using an high speed camera (Model: Kodak HS 4540) at 7m away from the inlet. Mixture velocity is kept constant at 3m/s. The percentage in the bracket represents the input water fraction at which the image is taken. The arrows present samples of complex structures observed in images.

In both pipes, it can be seen that oil will tend to occupy the upper part of the pipe due to buoyancy as the oil fraction is increased. Phase inversion seems to occur at this part of the pipe first. As more oil is added, phase inversion is completed when the water layer near the bottom is completely consumed. The pipe material does not appear to have a significant effect on how phase inversion occurs. The phase inversion process was also studied in detail with the use of conductivity probes and ERT. The results will be discussed in the following section.

4.4 DETECTION OF PHASE INVERSION OCCURRENCE

The investigation on the occurrence of phase inversion is conducted in both the stainless steel and acrylic pipes. With the acrylic configuration, the Y-junction inlet is modified with a splitting plate to minimise any turbulent mixing at the inlet. The two phases enter the test pipe as stratified flow. The detection of phase inversion is investigated with conductivity probes which provide information on the phase continuity at specific locations. The spatial difference in changes of phase continuity across the pipe cross section determines the phase inversion transition. In addition, the availability of an electrical resistance tomographic system in the acrylic pipe test section provides information about the phase distribution which can substantiate on the visual observations made in the previous section. These conductivity measurements are recorded at 7m downstream from the inlet where previous investigations have found that the flow is fully developed (Ioannou, 2006). The results of measurements for phase inversion occurrence will be presented at a mixture velocity of 3m/s but similar approach of detection is also conducted at a higher velocity (i.e. 4m/s) which will be presented in a later section on the effect of increasing the mixture velocity.

4.4.1 IN-SITU PHASE DISTRIBUTION MEASUREMENTS

As visual images do not provide clear information on the phase distribution especially in the pipe core, an electrical resistance tomographic (ERT) system is used to reconstruct the phase distribution across pipe cross section. For each mixture velocity, the mixture

flow is adjusted to the required input phase fraction and left for approximately 5 min to run before any recordings are made. While the ERT system receives signals from the sensors continuously, selected raw data are used for analysis. After the initial 5 min of stabilisation time, the first 50 – 60 frames are ignored. The subsequent 50 frames are captured which span a duration of approximately 30 sec of run time. This procedure is repeated for all the input phase fractions used in a particular mixture velocity.

Type of dispersion	Tomographic images		
Oil-in-water dispersion	(100%)	(80%)	(60%)
Phase inversion transition	(54%)	(40%)	(26%)
Water-in-oil dispersion	(18%)	(10%)	(0%)
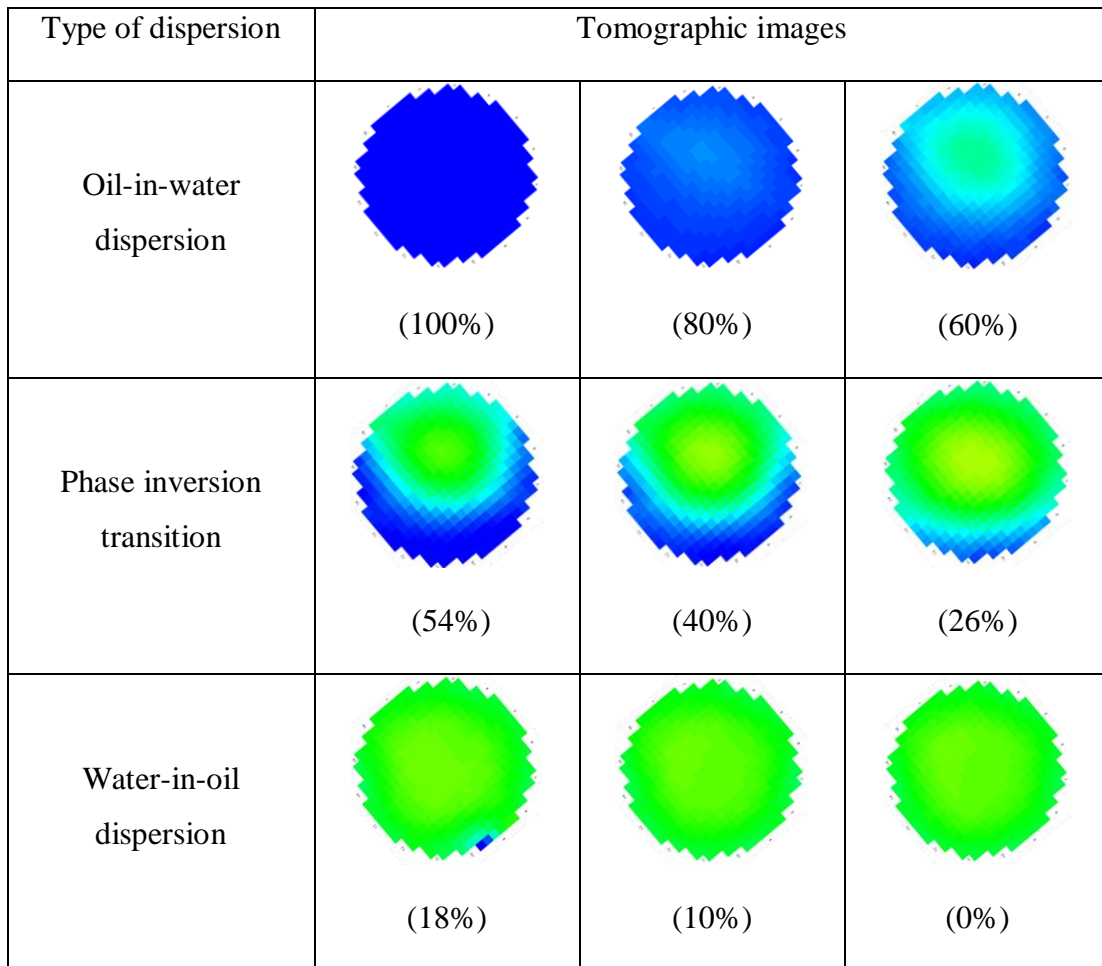
Figure 4.3: Phase distribution in an acrylic pipe cross section during the transition from a water continuous to an oil continuous mixture at a mixture velocity of 3m/s. The percentages in brackets represent the input water fraction.

The tomograms during the phase inversion transition from an oil-in-water dispersion to a water-in-oil dispersion are presented in Figure 4.3. The water phase is represented in blue while the oil phase is represented in green. In the region that is reported as water continuous dispersion (i.e. between 60% - 100% water fraction), it can be observed that the oil drops accumulate near the pipe centre. During the phase inversion transition (i.e. between 20% - 54%), part of the pipe cross section turns to be oil continuous as reflected by the near-zero normalized conductivity in localized positions (e.g. pipe centre or near top wall). With further increase in oil fraction, the wall contacting area by the water phase will be reduced. Phase inversion is completed when the entire tomogram turns green (i.e. water fraction below 20%). Due to the limitation of electrical resistance tomography on non-conductive continuous phase, the distribution of the dispersed water phase cannot be shown.

4.4.2 CHANGES IN PHASE CONTINUITY (PARTIAL PHASE INVERSION)

Based on both the visual images and tomograms, the oil drops tends to move towards the core of the pipe as the oil phase fraction is increased at a constant mixture velocity. As oil starts to accumulate at this location, it seems to be a likely location where a local phase inversion may occur (i.e. if starting from an oil-in-water dispersion). As such, an adjustable wire probe is placed at the centre of the pipe to detect the phase continuity at this location. The measurement of local phase continuity will allow better accountability on whether the pipe core continues to be water continuous with a dense concentration of oil drops or an inverted oil continuous dispersion. Similarly, a conductivity ring probe is used to track on the continuity of the contacting phase with the pipe wall as previous observations have indicated that a water layer remains until the water fraction is greatly reduced (i.e. approximately 20%). The ERT system (where available with the acrylic test section) can also provide local conductivity information at near to the top wall. This allows the differentiation between a dual continuous flow from an annular flow.

The combined conductivity measurements, at different locations, can be used to map out the change in phase continuity during the phase inversion transition. Figure 4.4 presents the combined data in an acrylic pipe at 3 specific locations – near the top wall (4mm from the top), centre of pipe (19mm from the top) and around the pipe periphery. Averaged values over several experimental runs for each probe are presented here.
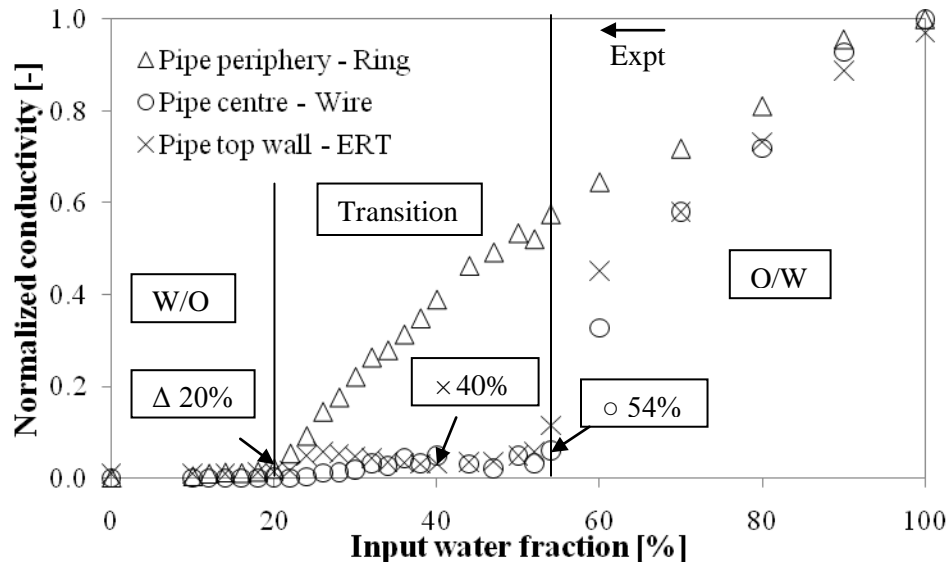
Figure 4.4: Normalized conductivity data of the oil/water system in an acrylic pipe at a mixture velocity of 3m/s from the ring and wire probes as well as the ERT system. The vertical lines limit the phase inversion transition region and are drawn at the first and last near zero conductivity values recorded using the various probes. The percentages represent the water fraction at which the different probes show near-zero conductivity values.

From the figure starting from a pure water flow, the flow tends to be homogenous (at about 90% water fraction) whereby the change in the normalized conductivity is linear to the reduction in water fraction. As more oil is added, the value around the pipe periphery is higher than at other locations. This is due to the formation of water layer at the bottom

as observed in the previous section. With further increase in oil fraction (at 60% water fraction), the value at all three locations are different with the lowest value observed at the centre of the pipe. This indicates that the oil drops are drawn towards the centre of the pipe leaving other regions to have a higher presence of water. At 54% water fraction, the conductivity at the centre of the pipe has reached a near-zero averaged value (i.e. less than 3% deviation from zero). At this fraction, phase inversion has occurred at the centre of the pipe. While the corresponding conductivity at the top is low, it still reflects more than 5% of normalized conductivity. Thus, the flow pattern at 54% appears to resemble an annular flow with an oil continuous core. The conductivity at the top falls to zero at about 40% water fraction. From this phase fraction onwards, the flow pattern switches into a dual continuous flow with an upper oil continuous layer and a lower water continuous layer. This flow pattern persists until 20% water fraction. At 20% and beyond, all three locations show a zero conductivity value. The phase inversion is completed with a full water-in-oil dispersion. Based on the use of the different electrical techniques, similar outcome have been found to observe the transitional stages during a phase inversion process. This outcome agrees well with the observation from both the ERT and visual images.

Similar combined data in stainless steel pipe is presented in Figure 4.5 without the measurements from the ERT system. Nevertheless, previous measurements, by scanning across the vertical pipe cross section using the conductivity wire probe, had found that phase inversion occurs firstly from the centre of the pipe if starting from a water continuous dispersion. As shown in Figure 4.5, the inversion at the centre occurs at 53% water fraction while it completes at about 20% where the conductivity at the pipe periphery falls to a near-zero value. By comparing between the two pipe materials, it is observed that there is no significant difference between the limits on the phase inversion transition and this finding supports what is observed from the visual images in Section 4.3.
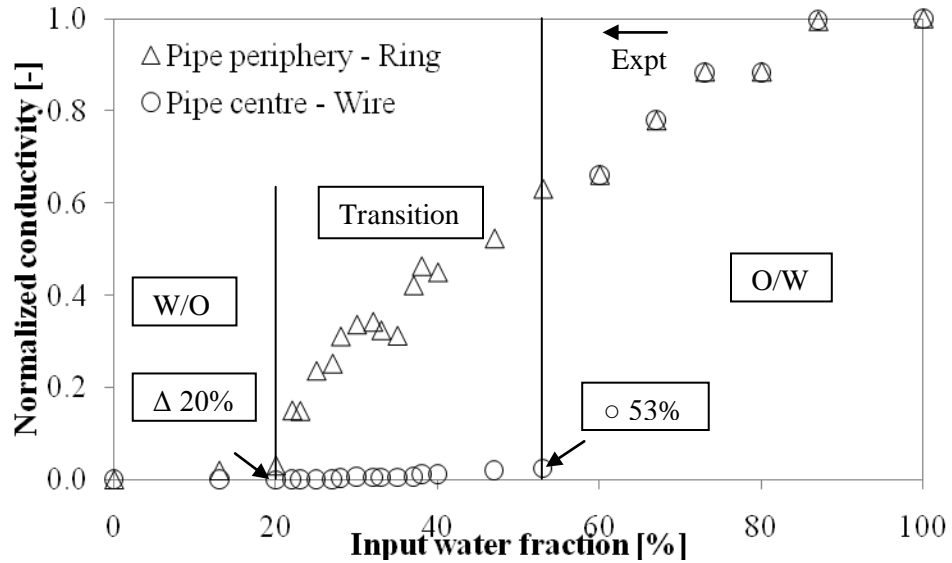
Figure 4.5: Normalized conductivity data of the oil/water system in a stainless steel pipe at a mixture velocity of 3m/s from the ring and wire probes as well as the ERT system. The vertical lines limit the phase inversion transition region and are drawn at the first and last near zero conductivity values recorded using the various probes. The percentages represent the water fraction at which the different probes show near-zero conductivity values.

4.5 EFFECT OF DISPERSION INITIALISATION ON PHASE INVERSION

Previous literatures (e.g. Arashmid et al., 1980, Kumar, 1996, Ioannou, 2006) have reviewed that the initial dispersion condition can affect the occurrence of phase inversion leading to an ambivalent region. In order to find out the effect of dispersion initialization on the phase inversion process, similar set of experiments as those presented in Section 4.4 is carried out starting from an oil continuous dispersion in an acrylic pipe.
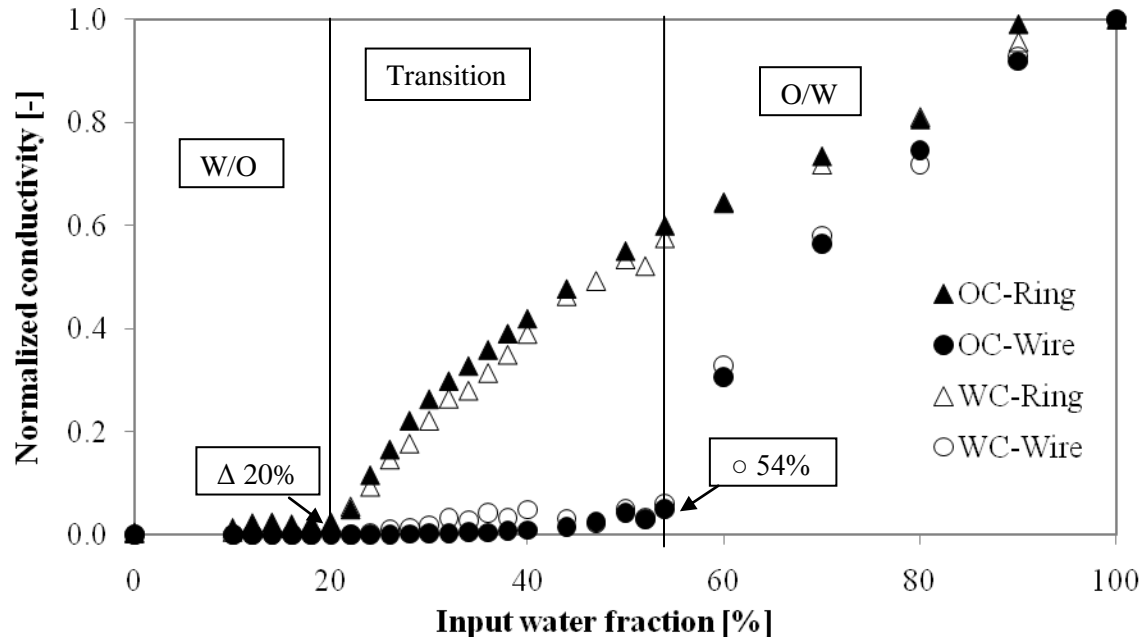
Figure 4.6: Normalized conductivity data for the oil/water system in an acrylic pipe at a mixture velocity of 3m/s from the ring and the wire probes for the two inversion routes (a) starting from oil continuous (OC) and (b) starting from water continuous (WC) mixture. The vertical lines limit the phase inversion transition region and are drawn at the first and last near zero conductivity values recorded from the two probes. The percentages represent the water fraction at which the different probes show near-zero conductivity values.

From Figure 4.6, the results from the wire and ring probes are shown since they represent the pipe centre and periphery respectively where the phase inversion begins and ends. It can be seen that the conductivity values from the ring and wire probes are very close for both inversion routes. Only slight deviation is observed between 20-40% water fractions. This is possibly because of the difference in the mechanism of the phase inversion process. Starting from a water continuous dispersion, the water layer at the bottom of the pipe is likely to have oil drops within it and the conductivity value of that layer will be lower than in the case of pure water. Starting from an oil continuous dispersion, on the other hand, the water layer at the bottom of the pipe is formed by the coalescence and deposition of water drops. As such, there would probably be no oil drops present and the

conductivity will be higher than in the water continuous route. Once the water layer has reached a certain thickness, entrainment of oil drops can occur. In this case, it explains as well the agreement of the data for the two routes beyond 40% water fractions. The wire probe gives a higher conductivity value for the oil continuous route compared to the water continuous route between 20% - 40% due to the opposite effect in the concentration of water phase at the pipe centre.

4.6 EFFECT OF MIXTURE VELOCITY ON PHASE INVERSION

Phase inversion experiments were carried out at a mixture velocity of 4m/s starting from a water continuous dispersion and the phase distribution at decreasing water fractions are shown in Figure 4.7. At high water fraction when the flow is water continuous, the dispersion appears more homogeneous than at 3m/s (comparing with Figure 4.3). At 40% water fraction, the core of the pipe flow becomes oil continuous (green) while it remains water continuous over the pipe annulus. A water layer still remains at the bottom of the pipe but is thinner than the water layer at 3m/s with the same input water fraction (compare 26% water fraction with Figure 4.3). Phase inversion is completed only when this layer of water is also dispersed into the oil (i.e. at about 22% water fraction). Full oil continuous dispersion is achieved at a water fraction below 22%.

The effect of mixture velocity on the changes in phase continuity in the pipe cross section is shown in Figure 4.8. It can be observed that the mixture remains to be water continuous in the pipe centre until a lower water fraction (>40%) at 4m/s compared to 54% at 3m/s. However, phase inversion is completed at approximately the same input water fraction (20%) when the water layer at the bottom of the pipe is dispersed. Thus, increasing the mixture velocity aids the homogenisation of the dispersion leading to a narrower phase inversion transition.

Type of dispersion	Tomographic images		
Oil-in-water dispersion	(80%)	(70%)	(60%)
Phase inversion transition	(54%)	(40%)	(26%)
Water-in-oil dispersion	(22%)	(20%)	(16%)
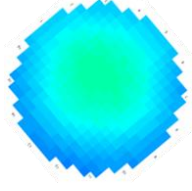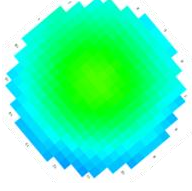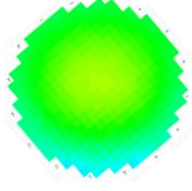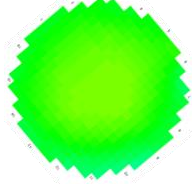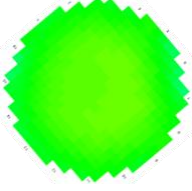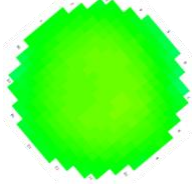
Figure 4.7: Phase distribution in a pipe cross section during the transition from a water continuous to an oil continuous dispersion at a mixture velocity of 4m/s. The percentages in brackets represent the input water fraction.
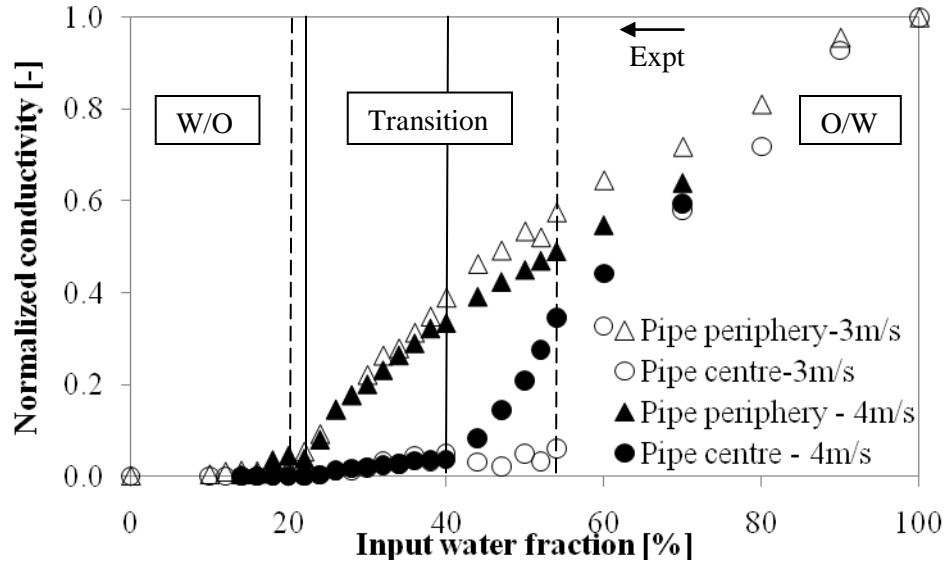
Figure 4.8: Comparison of normalized conductivity data for the oil/water mixture at a mixture velocity of 3m/s and 4m/s using the ring probe and wire probe. The vertical lines determine the phase inversion transition at which the first and last near zero conductivity value are recorded using the various probes – dotted lines for 3m/s and solid lines for 4m/s.

4.7 PRESSURE GRADIENT DURING PHASE INVERSION

The pressure drop, across a 1.5m section of the pipeline, is also measured during the conductivity measurements. Each data point at a specific phase fraction is an average of 3000 measurement points (taken in 30 seconds interval). The data points are then normalized as pressure gradient. Figure 4.9 presents the average pressure gradient at 3m/s mixture velocity starting from a water continuous dispersion across the phase inversion transition.

Starting from 100% water fraction, an increase in the oil phase fraction will lead to a reduction in pressure gradient. This can be attributed to the drag reduction effect due to the presence of the dispersed oil drops in the water continuous phase and the effect has been previously reported in literature (e.g. Arirachakaran et al., 1989, Pal, 1993, Nädler and Mewes, 1997). The pressure gradient continues to reduce while water is still in

contact with the pipe wall. As the water fraction reaches about 40%, the pressure gradient appears to fluctuate significantly especially within the transition region. The large fluctuations are believed to be caused by the presence of both water continuous and oil continuous dispersion co-existing as complex structures. Piela et al. (2008) has reported similar findings where the friction factor is significantly affected by the changes in phase continuity as the probes pass through the complex structures. As the presence of oil continuous dispersion increases and upon the first contact of the oil phase with the pipe wall, the pressure gradient starts to increase towards the single phase oil value as the more viscous oil phase comes into contact with more of the pipe wall.
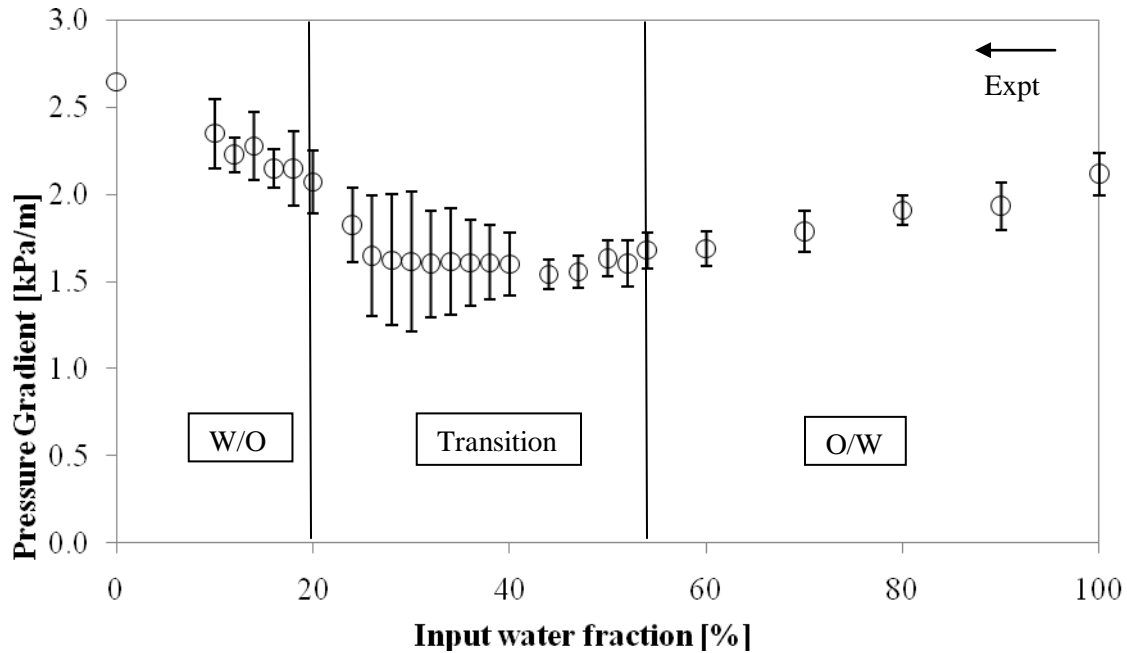
Figure 4.9: Experimental pressure gradients in an acrylic pipe at a mixture velocity of 3m/s. The error bars represent the standard deviation of the fluctuations at each specific phase fraction. The arrow denotes the direction of experiment from water continuous to oil continuous dispersion and the vertical lines represent the boundaries of the phase inversion transition region.

Comparing between the water continuous and oil continuous dispersion, the drag reduction is observed to be stronger in the oil continuous dispersion. Similar observation has also been reported by both Ioannou, 2006 and Hu, 2005 when they conducted their experiments in stainless steel pipes using Exxsol D140 as the oil phase. Pal (1993) has also found that, in stainless steel pipe, unstable water-in-oil emulsions exhibit higher drag reduction than oil-in-water emulsions. Ioannou (2006) has observed that the pipe material has an effect on the drag reduction (when using Marcol 52 with viscosity at 11mPa s) of which acrylic pipe will have a stronger drag reduction with oil-in-water dispersion. However, this effect is not observed in the current experiments.

4.7.1 EFFECT OF INVERSION ROUTE ON PRESSURE GRADIENT

As the presence of oil at the pipe wall can have a significant effect on the changes in pressure gradient, it is of interest to investigate whether the inversion route can influence the pressure gradient by affecting the phase distribution. The pressure gradient results for the two inversion routes are shown in Figure 4.10. In both cases, the minimum pressure gradient falls within the phase inversion transition region. The inversion route does not affect the pressure gradient significantly. This agrees with the phase continuity data that showed changes in the continuity of phases in contact with the wall at similar phase fractions for both inversion routes.

4.7.2 EFFECT OF MIXTURE VELOCITY ON PRESSURE GRADIENT

The results of the pressure gradient data with respect to the different mixture velocity are presented in Figure 4.11 - 4.12. The pressure gradient increases with mixture velocity. Similar to 3m/s, the pressure gradient at 4m/s initially decreases with decreasing water fraction until about 40% and start increasing again towards the single phase oil value. Large fluctuations are again observed between 26% and 54% water fraction. While the absolute values for pressure gradient has increased across the whole range of phase fraction, the difference in pressure gradient appear to be larger both below 20% and beyond 60% water fraction. According to Ioannou (2006), drag reduction increases with

increasing velocity/turbulence as the increased occurrence of drop coalescence and breakup event in the flow can cause a suppression of the velocity/turbulence in the continuous phase. Thus, it is expected to have a wider difference in pressure gradient in a dilute dispersion compared with a dense dispersion.
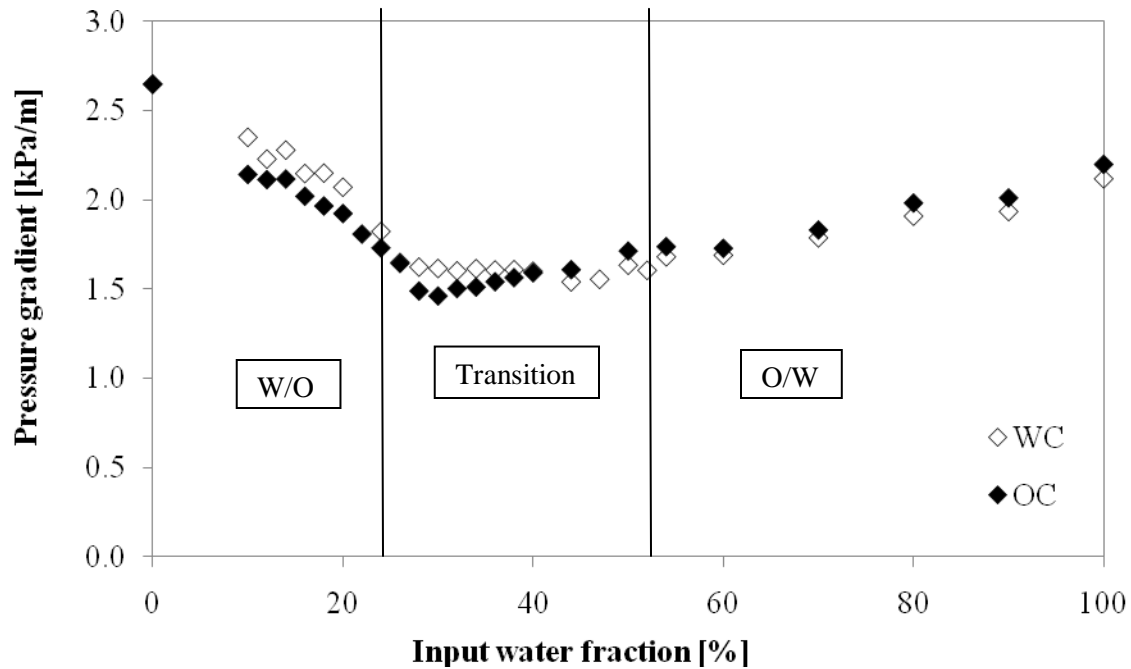
Figure 4.10: Comparison of pressure gradient for the oil/water system in an acrylic pipe at a mixture velocity of 3m/s between the two inversion routes (a) starting from oil continuous dispersion (OC) (b) starting from water continuous dispersion (WC). The vertical lines represent the boundaries of the phase inversion transition region.

Similar trends in pressure gradient are also found for the stainless steel pipe. The minimum in pressure gradient however appears at a lower water fraction indicating that the water layer in the steel pipe persists till a lower water fraction than in the acrylic pipe. Steel is a more hydrophilic pipe material than acrylic pipe (Ioannou, 2006) and this may have aided the water layer to retain longer.
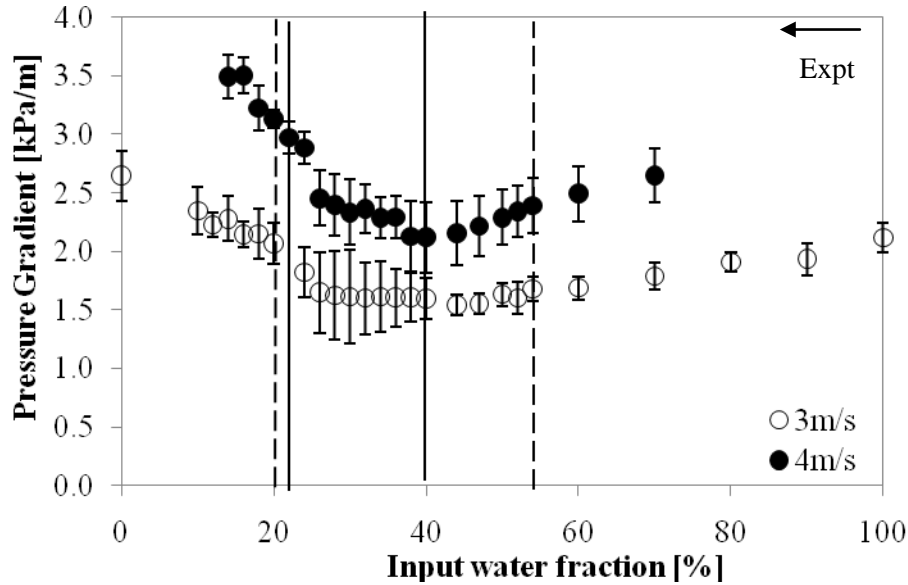
Figure 4.11: Comparison of pressure gradient measurement between mixture velocity of 3m/s and 4m/s in an acrylic pipe. The error bars represent the standard deviation of the fluctuations at each phase fraction. The arrow denotes the direction of experiment from water continuous dispersion to oil continuous dispersion. The vertical lines limit the boundaries for phase inversion transition - dotted lines for 3m/s and solid lines for 4m/s.
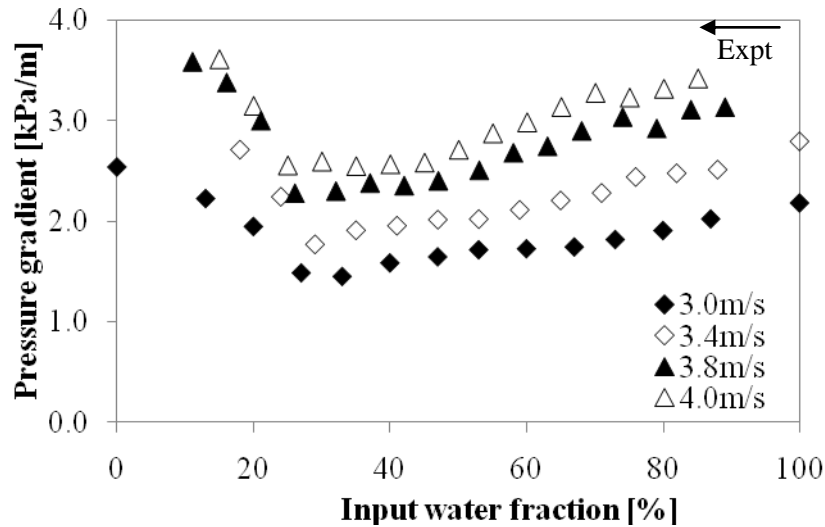
Figure 4.12: Comparison of pressure gradient measurement between mixture velocity of 3m/s and 4m/s in a stainless pipe. The arrow denotes the direction of experiment from water continuous dispersion to oil continuous dispersion.

120

4.8 DROP SIZE DISTRIBUTION IN OIL & WATER DISPERSION

In a liquid-liquid dispersion, the loss of balance between drop breakage and coalescence rates has been considered as a possible mechanism for phase inversion (Coulaloglou & Tavlarides, 1977; Kumar, 1996; Yeo et al., 2000). Breakage and coalescence rates depend on drop size and dispersion phase fraction. Other criteria for phase inversion such as equating the surface energy between water continuous dispersion and oil continuous dispersion is also a relation with the drop size. In addition, the various forces that act on the drops which determine their movements and placement in the flow field and eventually the phase distribution also depend on the drop size. Thus, drop sizes and their distribution are important in understanding phase inversion.

Drop size measurements are conducted with the dual impedance probe (see Chapter 3) for a range of phase fractions. Measurements are taken for both inversion routes (starting both from O/W and from W/O dispersions). Based on the conductivity probe experiments (see Figure 4.4), it can be seen that the phase inversion region is within two boundaries (1) the boundary at high water fraction beyond which the dispersion is water continuous and (2) the boundary at low water fraction below which the dispersion is oil continuous. The second boundary (2) involves an inversion of the water continuous layer at the bottom of the pipe. Detection of drop size using the dual impedance probe can be difficult at that location due to the possible interference of interfacial waves with the thin water layer. Therefore, the investigation of drop size before and after inversion is focused on the first inversion boundary (1) occurring at the pipe centre.

During the experiment, the drop velocity is calculated from the cross-correlation of signals for the two dual impedance probe sensors (see Lovick, 2004 and Hu, 2005). The calculated drop velocity together with the time duration of the drops in the signal of either of the two impedance sensors will provide a drop chord length. The chord length distribution from the measured drops can be further converted into drop size distribution based on an algorithm developed by Hu et al. (2006).

4.8.1 DROP SIZE DISTRIBUTION MEASUREMENT

During the experiment, it was found that no cross correlation could be obtained at dilute dispersions because of the small number of drops passing through the impedance sensors. Therefore, drop size distributions are obtained from 60% water fraction across the first inversion boundary and down to 40% water fraction at different locations along the vertical pipe diameter. Drop size measurements are also conducted for the two inversion routes (i.e. o/w → w/o and w/o → o/w).

Figure 4.13 represents a sample of chord length measurements an oil-in-water dispersion (60% water fraction) at different locations along the vertical pipe diameter for a mixture velocity of 3m/s and both inversion routes. Any chord length larger than 10mm has been ignored since this exceeds the physical distance between the two impedance sensors. It can be seen that the chord length distributions are similar for both inversion routes. Larger drops can be seen at the centre of the pipe (see Figure 4.13 (c)) where, as discussed before, the dispersed oil phase tends to accumulate. The higher fraction would favour drop coalescence and increase the drop size. Data at other phase fractions are given in Appendix A. As the dispersed oil fraction is increased, very few or no drop can be captured at about 6mm from the top wall.

The probability density functions of an oil-in-water dispersion and a water-in-oil dispersion are presented in Figure 4.14. For the same conditions as Figure 4.13 and at, example, 14mm, it can be seen that a log-normal distribution fit the data well as this has also been previously reported by other investigators for dispersed pipe flow (e.g. Karabelas (1978), Simmons & Azzopardi (2001)). There is predominantly a large number of small drops with approximately 1-2 mm in diameter. The long tail of large drops (>5mm) may be caused by irregular drop structures but these large structures account for less than 3% of the drop number. From the figure, the oil-in-water dispersion has a narrower distribution than the water-in-oil dispersion which at the same time is shifted towards smaller drop sizes. This has also been observed by Piela et al. (2008), Hu (2005) and Liu et al. (2005). As suggested by Kumar (1996), the difference in drop size may be
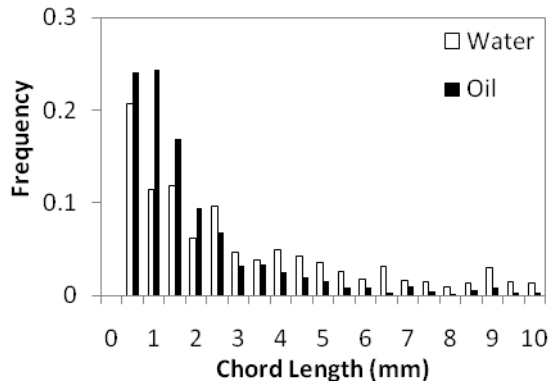
(a) 6mm
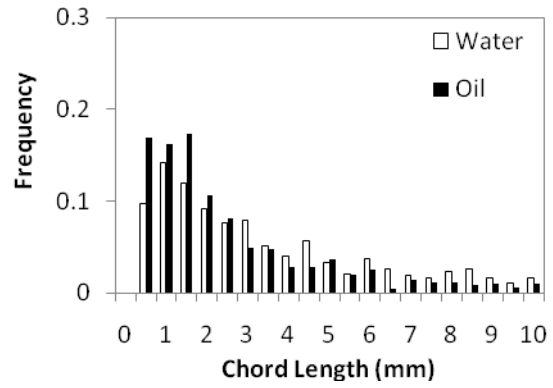
(b) 14mm
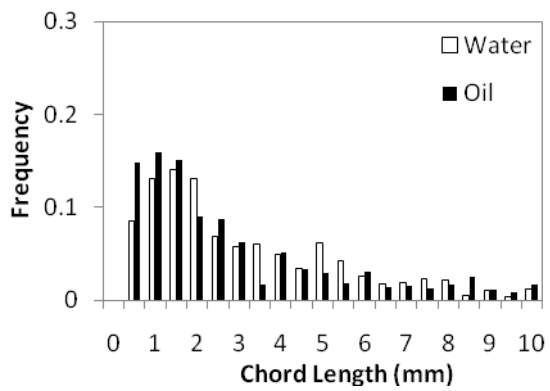
(c) 20mm
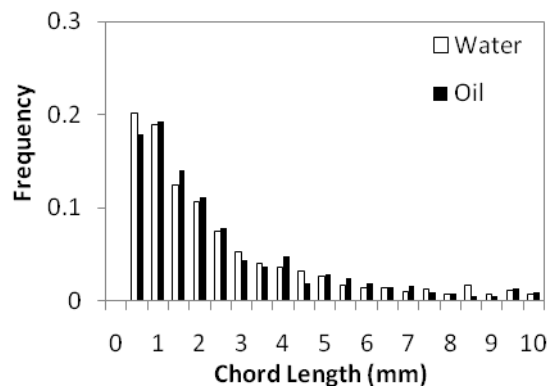
(d) 26mm
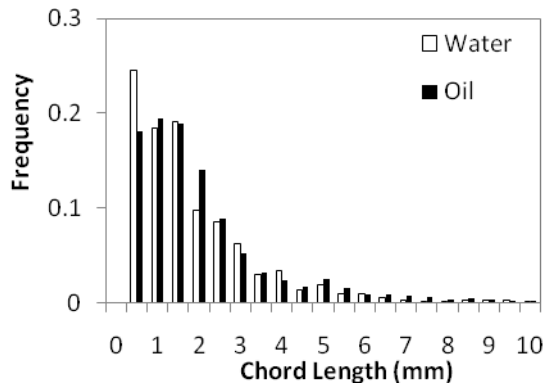
(e) 32mm

Figure 4.13: Chord length distribution of oil drops in water (60% water fraction) at a mixture velocity of 3m/s at (a) 6mm (b) 14mm (c) 20mm (d) 26mm (e) 32mm from the top wall of the pipe. The distributions of the two inversion routes are given – starting from a O/W dispersion (□) and from a W/O dispersion (■).

due to the different dielectric constants of the two phases. Oil drops in water experience repulsive forces due to the overlapping of the electrical double layers forming in water and thus have lower coalescence efficiencies whereas water drops in oil of low dielectric constants (which applies to Exxsol D140) do not experience similar repulsion and therefore have higher coalescence efficiencies. Coalescence efficiency also depends on the continuous phase viscosity (Coulaloglou & Tavlarides, 1977; Tsouris & Tavlarides, 1994; Liu & Li, 1999). Based on the larger water drops in oil, it appears that the viscosity of Exxsol D140 does not significantly affect the film drainage and lower the coalescence efficiency in relation to other influencing factors.

The evolution of drop size during inversion can be seen in Figure 4.15. In terms of average Sauter mean diameter, d_{32}, for a mixture velocity of 3m/s and both inversion routes. The results are from the core of the pipe (14mm from the top wall) where inversion across boundary (1) occurs. It can be seen that the oil drops in water are smaller than water drops in oil, regardless of the inversion route. The drop size, at 54% water fraction, is higher than at either 40% or 60% water fraction. Based on previous investigations, the large Sauter mean diameter is likely caused by the presence of irregular complex structures as well as coalesced large drops especially at a location where phase inversion is prominent. When comparing the effect of inversion route, no significant difference can be seen on the drop size across the inversion boundary (1). This may explain the reason for the same phase fraction when phase inversion occurs for inversion boundary (1) reported in Figure 4.6.
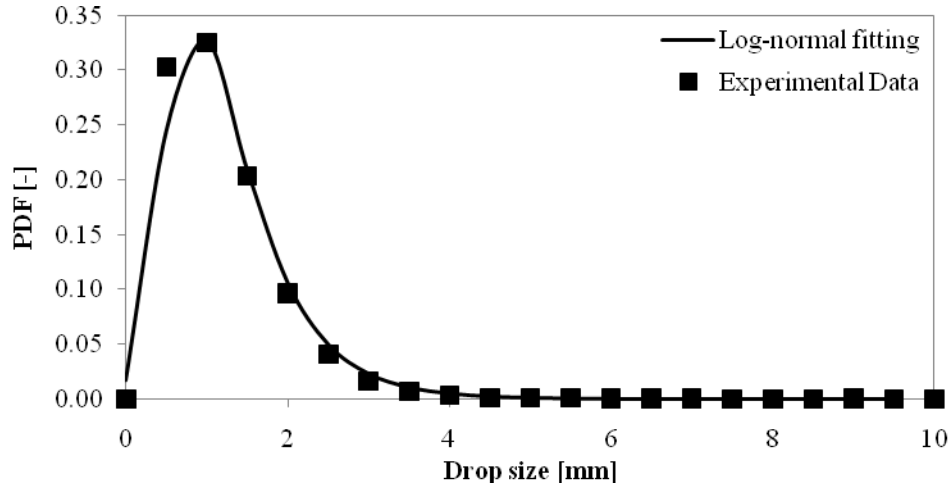
(a) O/W
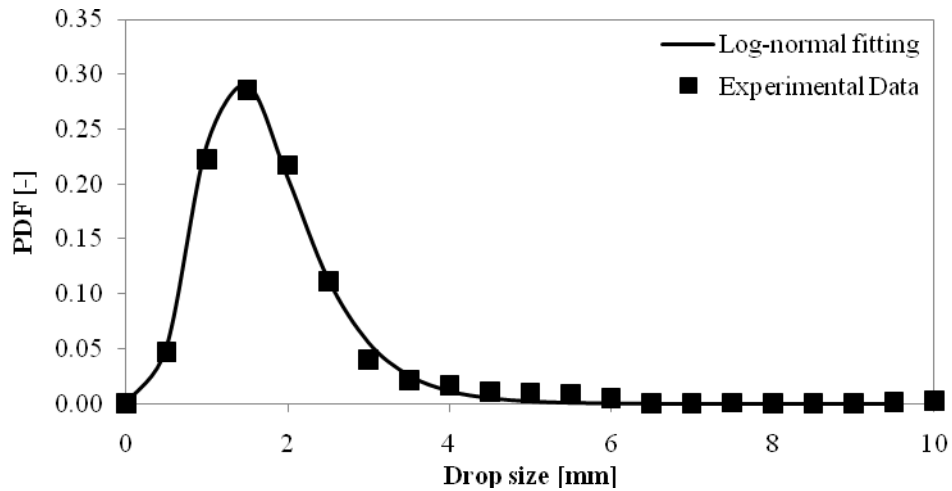
(b) W/O

Figure 4.14: Sample drop size distribution is recorded at 14mm from the top wall with a mixture velocity of 3m/s (a) oil-in-water dispersion (60% water fraction). The experimental data is compared with a log-normal distribution with a mean of 1.51mm and a variance of 0.238. (b) water-in-oil dispersion (40% water fraction). The experimental data is compared with a log-normal distribution with a mean of 2.07mm and a variance of 0.451.
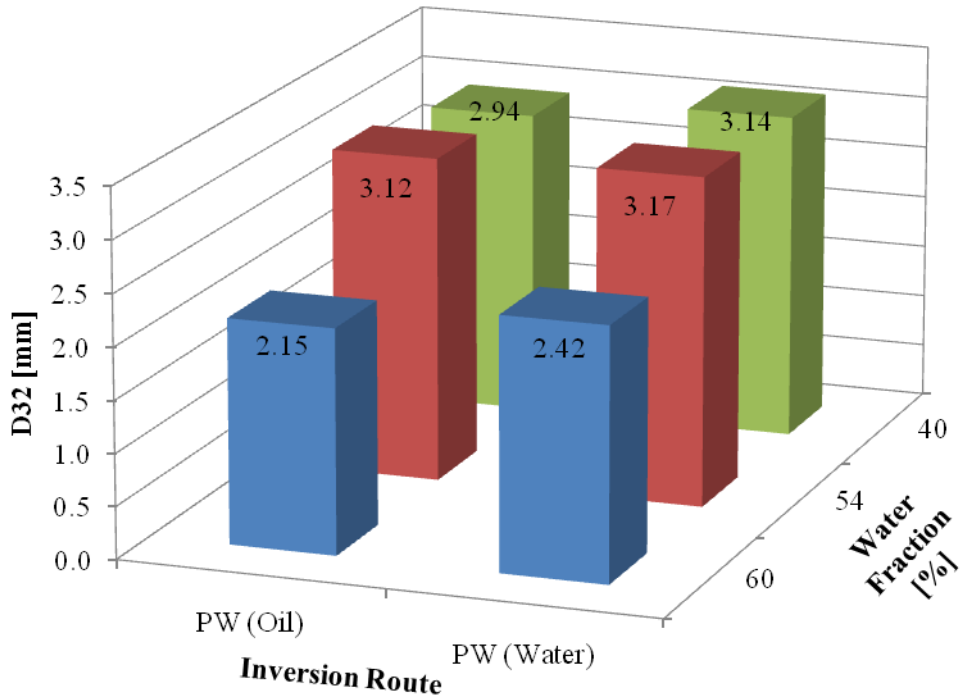
Figure 4.15: Sauter mean diameter at different input water fraction across the phase inversion boundary (1). The phase in brackets represents the initial continuous phase and the number in each column represents the Sauter mean diameter at the specific sample.

4.9 EFFECT OF DISPERSION INLET ON PHASE INVERSION

With previous sections discussed on a split inlet where the flow is gradually developed, phase inversion occurs across a transitional region due to partial inversion occurring at different input water fraction. It is interesting to investigate the effect of phase inversion if the two phases are introduced as a full dispersion straight from the inlet. Thus, a dispersion inlet is developed and the design of the inlet was discussed in Chapter 3. Figure 4.16 presents the conductivity data from the ring and wire probes. Measurements are conducted at the centre of the pipe (with the conductivity wire probe) and at the periphery of the pipe (with the ring probe) similar to the configuration as presented in Section 4.4.2.

126
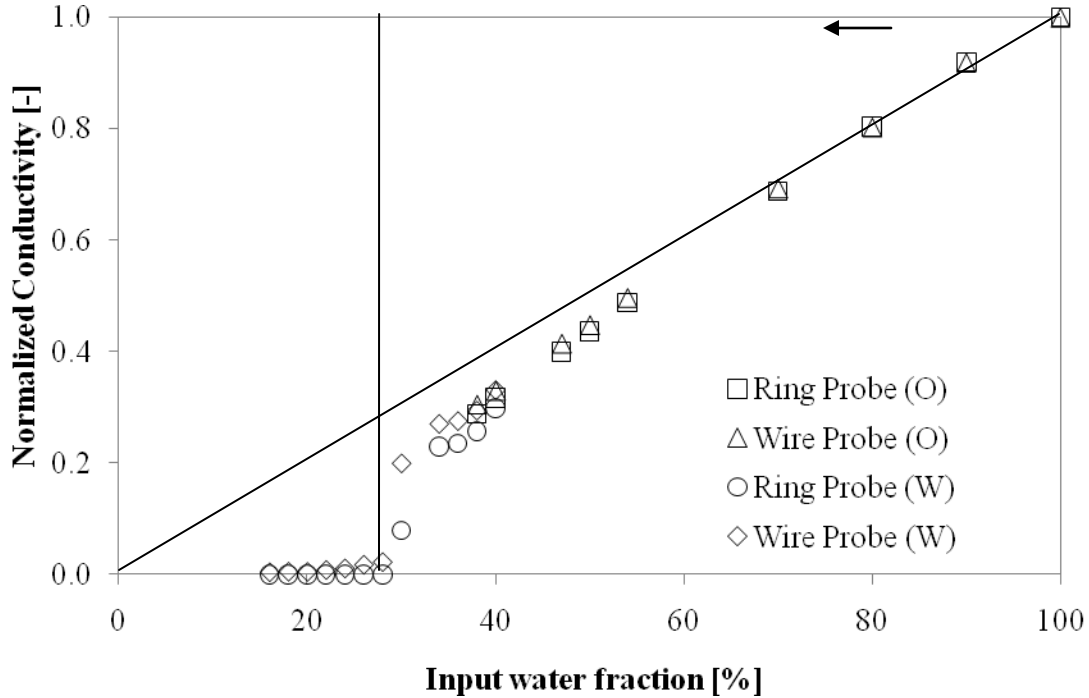
Figure 4.16: Normalized conductivity data for an oil/pure water mixture at a mixture velocity of 3m/s using the ring probe and wire probe. The letter in bracket represents initial dispersed phase – (W) water (O) oil. The arrow denotes the direction of experiment and the vertical line denotes the first input water fraction where phase inversion occurs.

As can be seen in figure, the conductivity data from both probes are very close for all input water fractions indicating that the flow is fully dispersed for all phase fractions at the mixture velocity of 3m/s. As a result, the change from a water continuous dispersion to an oil continuous dispersion (and vice versa) occurs throughout the pipe cross-section and at a particular phase fraction rather than over a transitional region as in the case with a split inlet. The decrease in conductivity is almost linearly proportional to the decrease in the water phase. Phase inversion occurs at a single phase fraction of about 28% input water fraction.

The effect of the dispersion initialization conditions is shown in Figure 4.17. There is only very small difference on the phase inversion point between the two inversion routes, 28% input water fraction for an initial O/W dispersion and 26% water fraction for an

initial W/O dispersion. It should be noted that 2% is the minimum step change in phase fraction that can be achieved in the experimental set up.
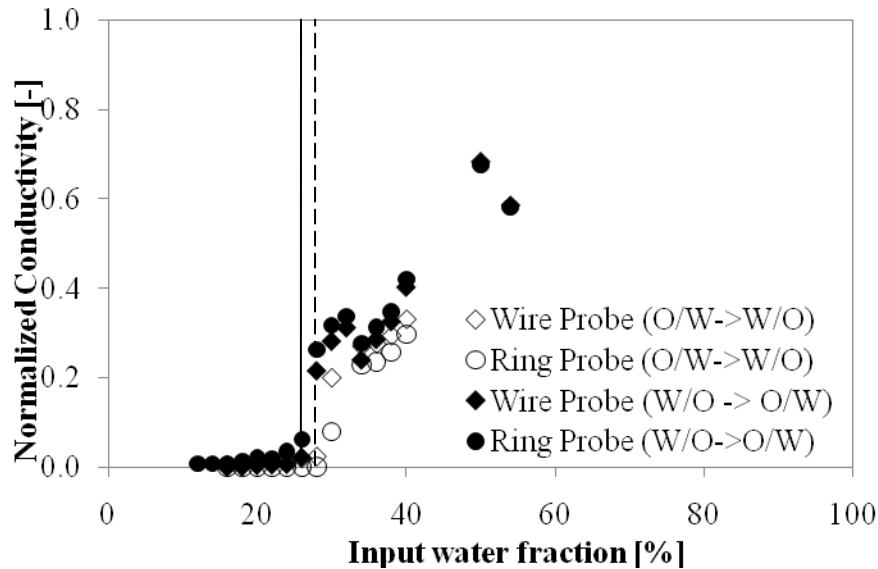
Figure 4.17: Normalized conductivity data for an oil/pure water mixture at a mixture velocity of 3m/s using the ring probe and wire probe through two initialization conditions – starting from water continuous dispersion (empty symbols) and starting from oil continuous dispersion (solid symbols). The dotted vertical line represents the phase inversion point starting from water continuous dispersion and the solid line represents the phase inversion point starting from oil continuous dispersion.

The pressure gradient across the phase inversion is presented in Figure 4.18. It can be observed that the gradual increase in the dispersed phase (oil) by reducing the input water fraction at a constant mixture velocity leads to a gradual increase in pressure gradient (i.e. between 40% and 100% water fraction). This is possibly due to the higher effective viscosity of the mixture in the pipe flow. Starting from 36% water fraction and below, the pressure gradient has a sudden drop which is likely due to the drop coalescence and deformation. The deformable drops can fill up the interstitial spaces leading to higher fluidity of the mixture flow (i.e. lower mixture viscosity & pressure gradient in a pipe flow). The pressure gradient reaches a minimum at the phase inversion point (i.e. 26%) and, beyond this point, the oil continuous phase will lead to a gradual increase possibly

because the deformed or coalesced drops are likely to be separated as the mixture is diluted. This will result in a more narrowly distributed drop size and, thus, reducing the fluidity of the mixture flow once again. The relatively higher pressure gradient by the oil continuous dispersion is also due to the higher oil viscosity as the continuous phase.
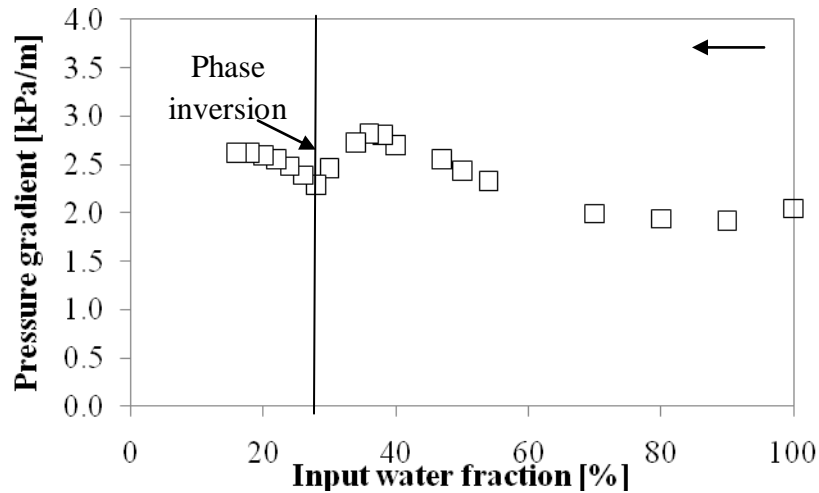
Figure 4.18: Experimental pressure gradients for a dispersed inlet configuration at a mixture velocity of 3m/s. The arrow denotes the direction of experiment from water continuous to oil continuous dispersion and the vertical line represents the phase inversion point.

In order to determine the change in drop size during the phase inversion process for the dispersed inlet configuration, Figure 4.19 presents the chord length distribution at different phase fractions. The chord length distribution can be seen to be narrow when the input water fraction is higher than 36%. The distribution becomes broader with longer chord length between 26% and 36% water fraction of which drop deformation/coalescence was previously suggested to occur. The distribution is the widest at about 26% where phase inversion is observed. At 20% water fraction (W/O dispersion is formed), the distribution becomes narrower beyond the phase inversion point. The corresponding drop size (by converting the chord length based on the method by Hu (2005) of the W/O dispersion is also found to be higher than O/W dispersion.

129
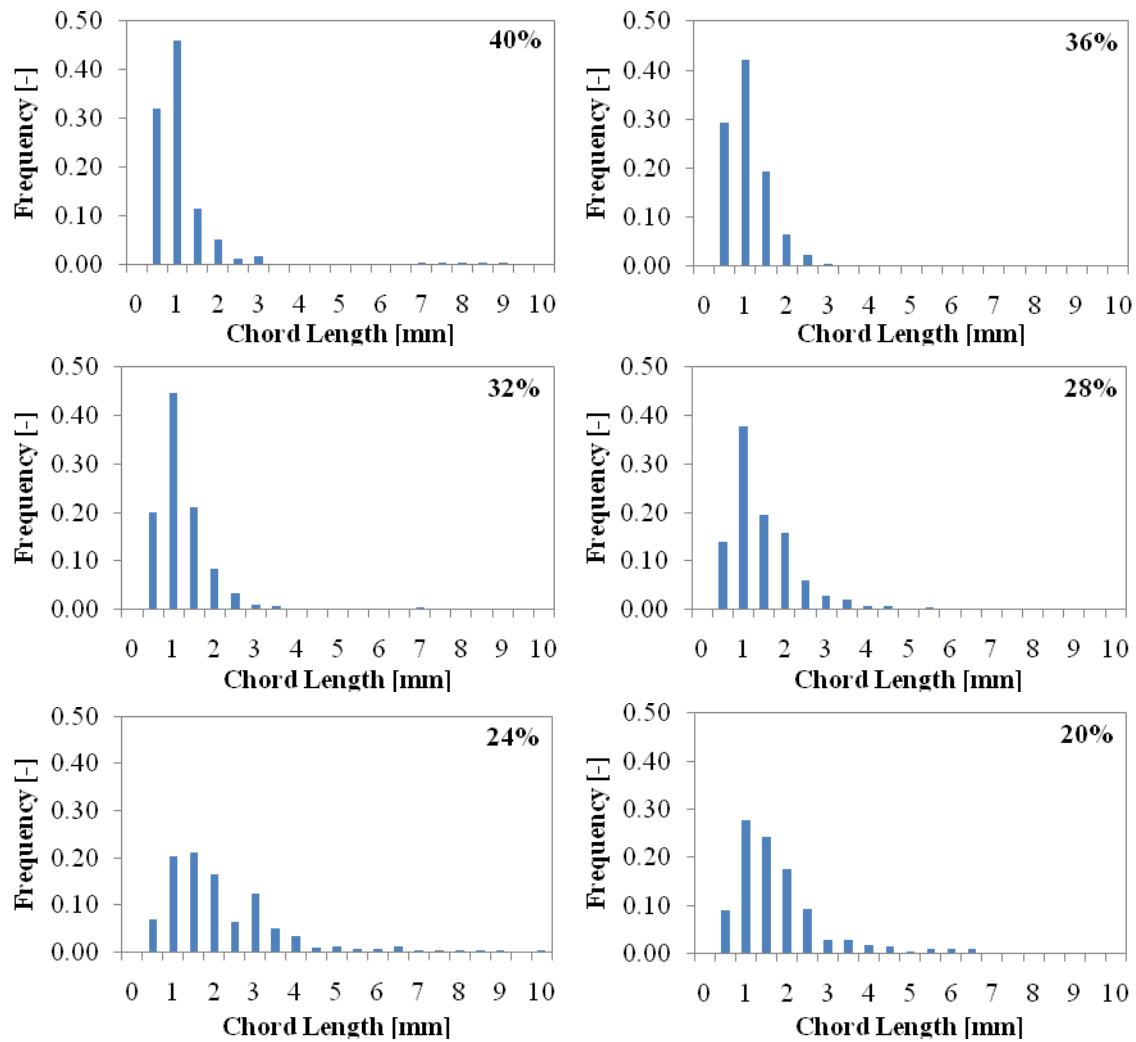
Figure 4.19 Comparison of chord length distribution at different input water fraction (fraction in bracket) across the phase inversion process at 3m/s mixture velocity.

4.10 CONCLUSION

The phase inversion transition of an oil-water dispersion was investigated in this chapter. The ERT system revealed the distribution of the phases and the respective flow patterns while the conductivity data from the ring and wire probes as well as the ERT provide further information on the phase continuity in a pipe cross section. The following mechanism for phase inversion is proposed based on the data from the split inlet configuration.

For inversion starting from an oil-in-water dispersion:

(1) At low oil fraction, the added oil phase is initially dispersed in the continuous water phase.
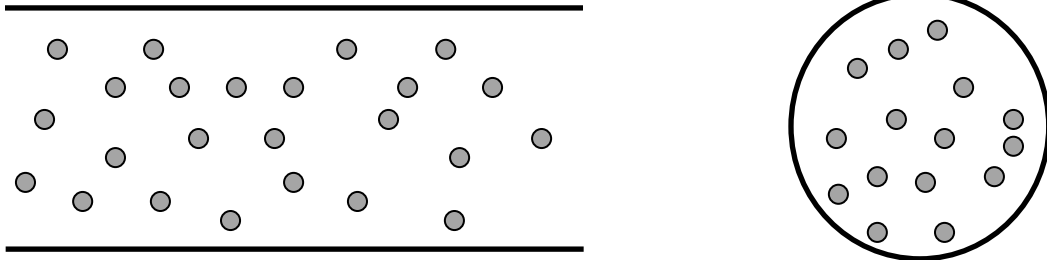
(2) As the oil fraction increases, the oil drops will accumulate at the pipe centre where they coalesce and the mixture inverts.
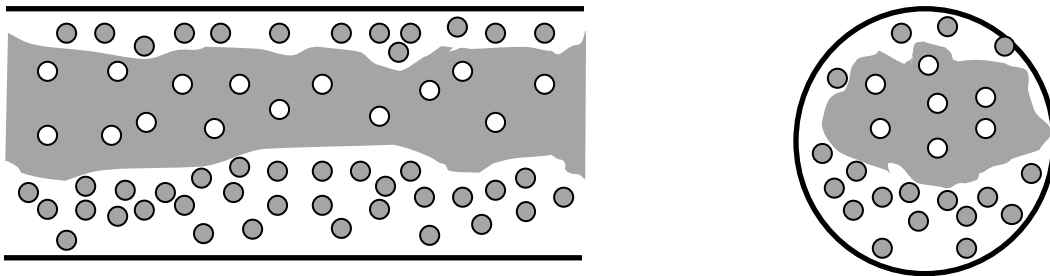
(3) With the mixture also inverts at the top of the pipe, a dual continuous flow pattern is formed with oil as the continuous phase at the top of the pipe and water as the continuous phase at the bottom.
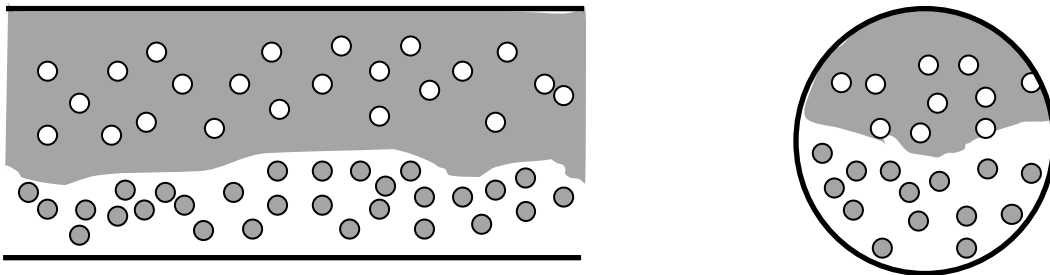
(4) At high oil fractions, the thin layer of water at the bottom of the pipe also disperses and the flow becomes fully dispersed with oil as the continuous phase.
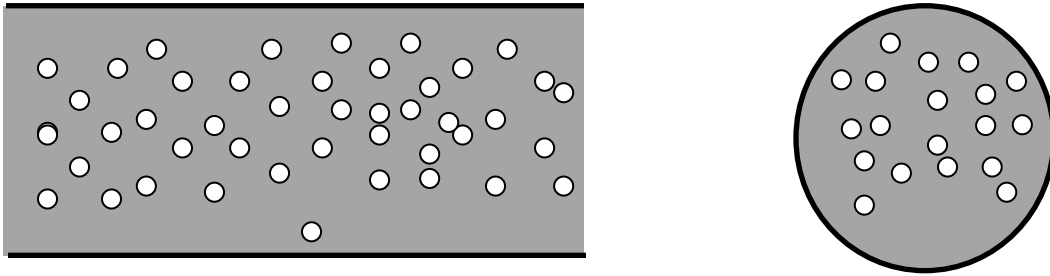
The change from a water continuous to an oil continuous dispersion occurs over a range of volume fractions and is bounded by two lines: the first line is related to the inversion at the pipe centre and the second line is related to the diminution/formation of the water layer at the bottom of the pipe depending on the inversion route. However, no significant difference was found in the phase inversion transition boundaries between the two inversion routes. With increasing mixture velocity, the transitional region over which phase inversion occurs reduces in size.

Change in phase distribution during the phase inversion transition is found to affect the pressure gradient. Starting from a water continuous dispersion, the addition of dispersed phase initially led to drag reduction. Pressure gradient continued to reduce even after inversion has occurred at the centre of the pipe. When the water layer at the bottom of the pipe eventually disperses and the viscous oil phase comes in contact with the whole pipe wall, the pressure gradient starts to increase again. There is no significant difference in pressure gradient between the two inversion routes. The V-shaped trend, which the changes in pressure gradient exhibits, is similar regardless of mixture velocity and pipe materials. The degree of changes is found to be higher at higher mixture velocity possibly because of higher drag reduction. There is also observed, in the stainless pipe, a shift in the minimum pressure gradient leftward with the increase in mixture velocity.

In addition to the change in flow conditions (e.g. mixture velocity, dispersion initialization), the change in the inlet configuration (to a dispersed inlet) has led to a

132

significant change in the phase distribution in the mixture flow. This results in a substantial difference in the phase inversion occurrence from a phase inversion transition across a range of phase fraction into a phase inversion point. The pressure gradient increases with the initial increase in the dispersed phase (i.e. oil) until drop coalescence/deformation become prominent. During the rearrangement of the deformable drops and until phase inversion has occurred, the pressure gradient has a sharp drop. The higher oil viscosity will subsequently led the increase in pressure gradient beyond phase inversion.

For the split inlet, drop size measurements are in accordance with the phase distribution data. Larger drop sizes are found at the pipe core just before inversion from O/W to W/O dispersion where the dispersed phase has concentrated. Differences are also seen between the sizes of oil drops in water and water drops in oil regardless of the inlet configuration. From the drop size measurement, it can also be concluded that drop coalescence and deformation is a critical process during phase inversion.

The understanding on how phase inversion progresses during pipe flow will form the basis of the investigation in the following chapters – effect of interfacial tension on phase inversion (Chapter 5), prediction model of phase inversion based on flow regimes (Chapter 7) and CFD simulation on the interaction of the dispersed and continuous phase in a pipe flow (Chapter 8).

Chapter 5: Effect of interfacial tension on phase inversion

5.1 OVERVIEW

The pipeline flow of two immiscible liquids, usually an aqueous and an organic, is commonly encountered in process industries and during oil production. Depending on the flow rates and phase fractions, dispersed flow can establish either the water (O/W) or the oil (W/O) as being the continuous phase. At some critical operational conditions, phase inversion occurs whereby the initial dispersed phase becomes continuous and the continuous phase becomes dispersed. The change in phase continuity can have a significant effect on the mixture rheology and on frictional pressure drop while the nature of the continuous phase is related to pipeline corrosion and to the rate of the mixture separation at the end of the process. It is important, therefore, to understand and be able to predict the conditions under which inversion appears.

Many factors have been reported to affect phase inversion and the *phase inversion point*, i.e. the volume fraction of the liquids at inversion. Experimental work has mainly been carried out in stirred vessels (for a review see Yeo et. al, 2000) where it was found that phase inversion is affected not only by the fluid properties such as viscosity, density and interfacial tension, but also by the stirred vessel geometric configuration (e.g. type of impeller), the vessel and impeller material wettability and the experimental set up (e.g. the phase that the impeller is in at the beginning of the experiment). In contrast to stirred vessels, there is less information available on the effect of various parameters on phase inversion during pipeline flows. Apart from fluids properties, parameters such as mixture velocity, rate at which the dispersed phase is added in the continuous, size of the pipe and wettability of the pipe material have also been found to influence phase inversion (Angeli and Hewitt, 2000; Ioannou et. al, 2005; Luo et. al, 1997; Piela et. al, 2008).

Among the fluid properties, viscosity is considered to have a significant impact on phase inversion. Selker and Sleicher (1965) found that as the viscosity of one phase increases, its tendency to be dispersed also increases, i.e. the minimum fraction that the phase can be continuous will decrease and the maximum fraction that it can be dispersed will increase. Notably, many models for the prediction of the phase inversion fraction are based on the liquid viscosities (Arirachakaran et. al, 1989; Nädler and Mewes, 1995; Ngan et al., 2009; Yeh et al., 1964). Density does not seem to affect inversion significantly especially when the density difference between the two liquids is small but it will influence the homogeneity of the dispersion (McClarey and Mansoori, 1978; Selker and Sleicher, 1965). However, systems with large density difference between the phases show an increased tendency to invert (Kumar et. al, 1991).

The effect of interfacial tension is the least understood. In agitated vessels, Selker and Sleicher (1965) suggested that interfacial tension cannot affect the type of dispersion since it is not a function of the sign of the interfacial curvature. However, the suggestion was not further investigated. According to Yeh et. al (1964) interfacial tension will cause inversion of a dispersion to occur at equal volumes of the two liquids in the absence of other influencing parameters. Luhning and Sawistowski (1971), in contrast, stated that interfacial tension is important and found that the limits of the ambivalent region were correlated with the impeller Weber number (for Weber numbers between 350 and 4000). A decrease in interfacial tension will make inversion more difficult to occur and will widen the boundaries of the ambivalent region (Clarke and Sawistowski, 1978; Norato et. al, 1998). Interfacial tension is also related to drop break up and coalescence (Coulaloglou and Tavlarides, 1977; Luo and Svendsen, 1996; Prince and Blanch, 1990; Sovová, 1981; Tsouris and Tavlarides, 1994) that define the size of the dispersed phase. The evolution of the dispersed phase size and the departure from equilibrium between break up and coalescence rates have been used to predict phase inversion in stirred vessels (Arashmid and Jeffreys, 1980; Groeneweg et. al, 1998; Hu et. al, 2005), thus indicating a strong dependence on interfacial tension. There is no reported work on the effect of interfacial tension on phase inversion in pipeline flow of liquid-liquid dispersions. This is not because interfacial tension was kept constant during

135

investigations of the fluid properties, rather that it was not monitored. It is actually quite difficult to vary a liquid property without affecting at the same time to some extent the interfacial tension. In this chapter, the interfacial tension of an oil-water mixture is varied in a controlled way in order to investigate its effect on phase inversion during pipeline flow while keeping all other fluid properties constant as shown in Table 5.1.

5.2. EXPERIMENTAL SETUP

The experimental investigations in this study were conducted in a pilot scale liquid-liquid flow facility (See Chapter 3 for the detailed description of the experimental setup). A 38mm I.D acrylic test section will be used in all experiments during this study to minimize any effect on phase inversion caused by the experimental configuration. In this study, Exxsol D140 (density of 828 kgm^{-3}, viscosity of 5.5 mPa.s) is used as the oil phase while tap water or a glycerol solution is used as the aqueous phase. The two fluids are joined at the end of a Y-junction inlet to ensure that the two fluids join with minimum mixing at the inlet.

For each experiment, simultaneous measurements of pressure gradient and phase continuity were carried out. Pressure gradient was measured with a differential pressure transducer between two ports 1.5m apart, with the first port located at 3.8m (~100D) from the inlet. Two types of conductivity probes were used to detect phase continuity and the appearance of phase inversion, namely a ring and a wire probe. These probes were located at 7m (~184D) from the inlet. High conductivity values indicate that a water/glycerol solution continuous mixture is in contact with the probes, while low values denote an oil continuous mixture. The ring probe consists of a pair of metallic rings, 4mm thick and 38mm apart, embedded on the pipe perimeter, flush with the wall, and in contact with the fluid mixture. This probe provides information on the continuity of the mixture adjacent to the pipe wall. The wire probe is made of two conducting wires with 0.5 mm diameter set 10 mm apart. It detects the phase continuity at different locations in a pipe cross section using a traversing mechanism. In this work, it was placed in the middle of the pipe.

An Electrical Resistance Tomographic (ERT) imaging system was also used. ERT tomograms were taken at the same axial location (i.e. 7m from the inlet) as the measurements of the two conductivity probes. In addition, the conductivity data from the ERT system were measured at 4mm from the top pipe wall in conjunction with the data from the conductivity probes to study changes in the mixture continuity in a pipe cross section at different phase volume fractions. Conductivity data for all three sensors were time averaged when the conductivity measurements were stabilized and over a period of 30 seconds. The data were normalized with respect to the values of single phase water. It was previously found that, at the same pipe cross section location, the normalized conductivities from the different sensors differ by 1% and can be regarded to have sufficient precision to relate the conductivity data from the various systems across a pipe cross section for a given phase fraction.

A dual impedance probe using alternating current was also implemented to determine the drop size distribution in the dispersion. During the experiment, the probe is positioned at 7 m downstream of the inlet. Sampling rate is set at 45kHz and a total number of 120,000 data points is collected. This high rate ensures that each dispersed drop is represented by more than one data points in the probe output signal. The probe measures chord lengths from which drop diameters can be calculated (Hu et. al, 2006).

The experiments were carried out at 3m/s mixture velocity and phase inversion was investigated starting from the aqueous phase as being continuous as well as from the organic phase. Each experiment started with a single phase flow of an initial continuous phase where the flow rate of the dispersed phase was gradually increased while that of the continuous phase was reduced to maintain a constant mixture velocity until phase inversion has occurred and beyond. The same experimental run was repeated at least three times and the averaged results are reported in Section 5.3.

The effect of glycerol addition on the physical properties of water and on the oil-water interfacial tension is shown in Table 5.1. These measurements were conducted at ambient temperature ($\sim 20^{\circ}C \pm 0.4^{\circ}C$). Dilute glycerol solutions (0.5% and 1% v/v) were chosen to

137

ensure that the glycerol addition only affects interfacial tension and not the other properties of the aqueous phase. The density of water and glycerol solutions was measured using a weighing flask and the viscosity was measured using the Bohlin Gemini rheometer by Malvern Instruments over a range of shear rates. For the interfacial tension with Exxsol^{TM} D140, a Krüss Contact Angle Measuring System (DSA100) was used. The viscosity measurements also revealed that the glycerol solutions are Newtonian. As shown in Table 5.1, while the density and viscosity of the aqueous phase do not change significantly with the addition of glycerol at both concentrations, the oil-water interfacial tension is reduced when glycerol is added. With the suggested concentrations of glycerol, it can be regarded that interfacial tension will be the influencing factor on the correlations for drop size (e.g. Brauner and Ullmann, 2002) as well as the critical phase fraction for inversion (e.g Fakhr-Din, 1973) through the Froude number, Reynolds number and Weber number terms.

	Pure water	Water with 0.5% glycerol	Water with 1% glycerol
Density (kg/m^3)	996	1004 (0.80%)	1007 (1.10%)
Viscosity (cp)	1.031	1.036 (0.48%)	1.024 (-0.68%)
Interfacial Tension with Exxsol^{TM} D140 (mN/m)	48.14	44.84 (-6.86%)	41.75 (-13.27%)

Table 5.1: Properties of the glycerol solutions. The number in bracket represents the percentage change in the value of the respective physical property compared to that of pure water.

5.3. PHASE INVERSION RESULTS

The changes in phase continuity and distribution were first studied in a water-oil system starting from single phase water and gradually adding the oil phase while keeping the mixture velocity constant at 3m/s. The mixture conductivity values, from the various probes, which denote phase continuity at different locations in a pipe cross section, are shown in Figure 5.1(a). Phase distribution tomograms by ERT at representative phase fractions can be seen in Figure 5.1(b).
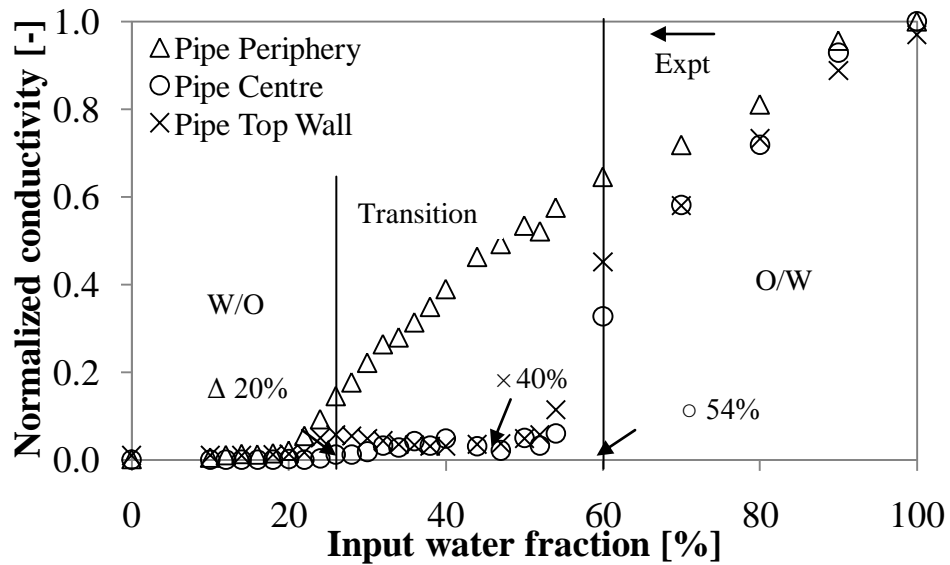
Figure 5.1: (a) Normalized conductivity data of the oil/water system at a mixture velocity of 3m/s from the ring and wire probes and the ERT system. The direction of the experiment from water to oil continuous is shown by the arrow. The vertical lines denote the boundaries of the phase inversion transition region and are drawn at the first and last near zero conductivity values recorded using the various probes. The percentages represent the water fraction where conductivity approaches zero at the various locations in the pipe cross section.
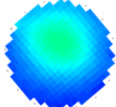
Type of dispersion	Tomographic images		
Oil-in-water dispersion	(100%)	(80%)	(60%)
Phase inversion transition	(54%)	(40%)	(26%)
Water-in-oil dispersion	(20%)		

Figure 5.1: (b) Phase distribution in a pipe cross section during the transition from a water continuous to an oil continuous dispersion at a mixture velocity of 3m/s. The percentages in brackets represent the input water fraction. Blue denotes the region of the water phase and green denotes the region of the oil phase. Last tomogram (i.e. water-in-oil dispersion) represents the completion of phase inversion upon which ERT measurement fails.

Initially (at pure water and high water fractions) the conductivity values are high throughout the pipe cross section which means that the mixture is water continuous (shown in Figure 5.1(b) as oil-in-water, O/W, dispersion). At low oil (high water) fractions, the mixture is almost a uniform dispersion. As the fraction of the non-conductive dispersed oil phase increases, the conductivity values begin to decrease. The phase distribution also indicates that the dispersion is not as uniform any more but there is higher concentration of oil in the middle of the pipe (see 60% water fraction in Figure 5.1(b)). The mixture however remains water continuous. At an input water fraction of 54%, the conductivity value in the middle of the pipe reduces to near zero (Figure 5.1(a)) indicating that the continuous phase at this location has changed from water to oil. However, the conductivity values at the top and the periphery of the pipe are still high

which means that a flow pattern has formed with an oil continuous region in the middle of the pipe and a water continuous region as an annulus around it. The water continuous layer is thinner at the top of the pipe and finally it inverts as well at approximately 40% water fraction. The flow regime then becomes dual continuous with an oil continuous region at the upper part of the pipe and water continuous region at the lower part. The respective tomogram in Figure 5.1(b) also shows the segregation of the phases at this fraction. This transitional regime persists with a further decrease in the water fraction until about 20% where the conductivity from the pipe periphery also reduces to zero (Figure 5.1(a)) indicating that an oil continuous mixture is now established throughout the pipe cross section.
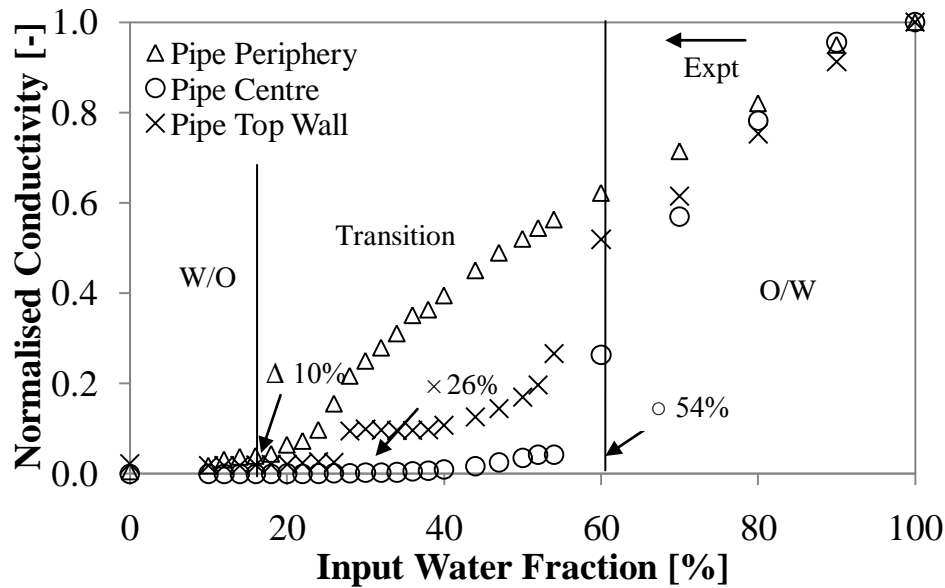
Figure 5.2: (a) Normalized conductivity data of the oil/1% glycerol solution system at a mixture velocity of 3m/s from the ring and wire probes and the ERT system. The direction of the experiment from water to oil continuous is shown by the arrow. The vertical lines denote the boundaries of the phase inversion transition region and are drawn at the first and last near zero conductivity values recorded using the various probes. The percentages represent the water fraction where conductivity approaches zero at the various locations in the pipe cross section.

141

Type of dispersion	Tomographic images		
Oil-in-water dispersion	(100%)	(80%)	(60%)
Phase inversion transition	(54%)	(40%)	(26%)
Water-in-oil dispersion	(18%)	(10%)	

Figure 5.2: (b) Phase distribution in a pipe cross section during the transition from a 1% aqueous continuous to an oil continuous dispersion at a mixture velocity of 3m/s. The percentages in brackets represent the input water fraction. Blue denotes the region of the water phase and green denotes the region of the oil phase. Last tomogram (i.e. water-in-oil dispersion) represents the completion of phase inversion upon which ERT measurement fails.

Similar conductivity curves are obtained when 1% glycerol solution is used as the aqueous phase. As can be seen in Figure 5.2(a), the inversion in the middle of the pipe appears at the same phase fraction, 54% water, as that in the oil/pure water mixture. Interestingly, the inversion at the top of the pipe appears at an input water fraction of 26% when glycerol is present, which is lower to that for pure water (40%). It seems that with the addition of glycerol, oil tends to concentrate in the middle of the pipe more than when only water is used while the aqueous phase is being driven to the outer part of the pipe. This is supported by the conductivity values which in the middle of the pipe are slightly lower and close to the pipe wall are higher for the glycerol solution than for pure water (see Figure 5.3 for water fractions between 26% and 44%). It can also be seen from Figures 5.2(a) and 5.3 that the water layer near the bottom of the pipe persists over lower

water fractions in the presence of glycerol and the inversion to fully dispersed oil continuous flow occurs at 10% water fraction compared to the 20% of the pure water system.
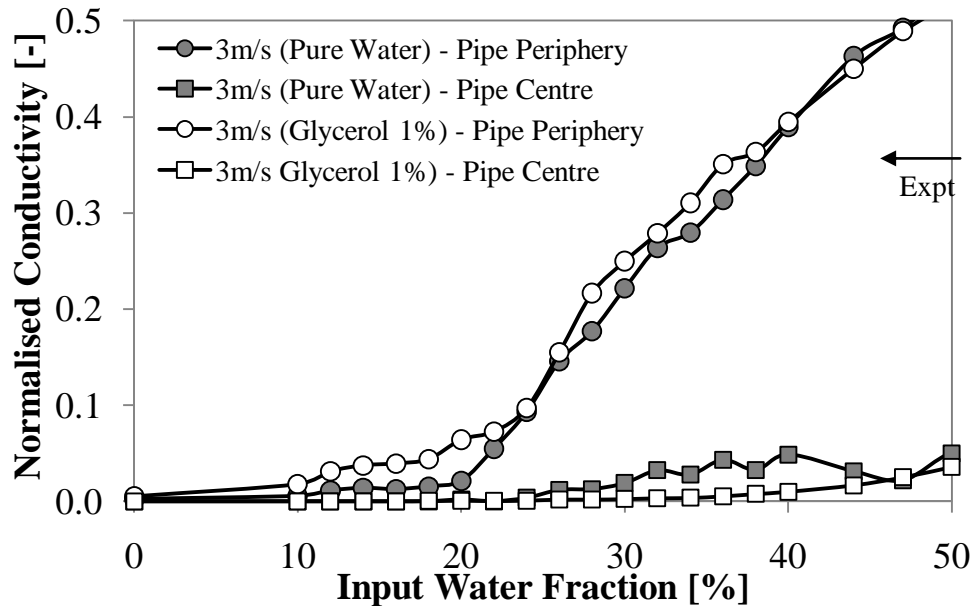
Figure 5.3: A comparison of the normalised conductivities in the middle of the pipe and the pipe periphery between the 1% glycerol solution and the pure water dispersions at a mixture velocity of 3m/s.

Similar results are obtained with the 0.5% glycerol solution (Figure 5.4). As with the 1% glycerol solution, the inversion in the middle of the pipe again occurs at 54%, the inversion at the top occurs at 20% water fraction while fully dispersed oil continuous flow establishes at 10% water fraction. The addition of glycerol seems to affect the inversion behaviour of the oil-water mixture but, at least for the conditions tested, the concentration of glycerol does not appear to play a significant role.
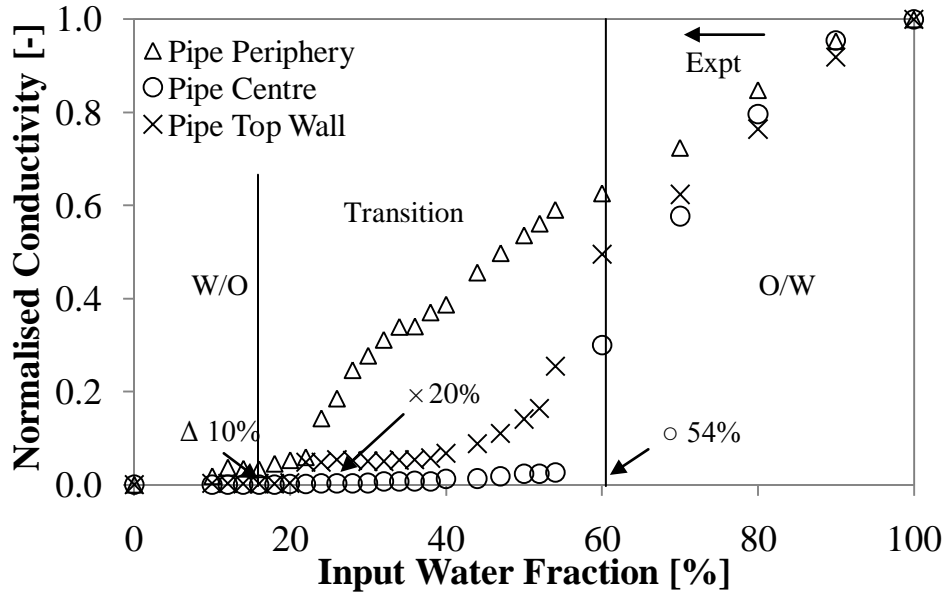
Figure 5.4: Normalized conductivity data of the oil/0.5% glycerol solution system at a mixture velocity of 3m/s from the ring and wire probes and the ERT system. The direction of the experiment from water to oil continuous is shown by the arrow. The vertical lines denote the boundaries of the phase inversion transition region and are drawn at the first and last near zero conductivity values recorded using the various probes. The percentages represent the water fraction where conductivity approaches zero at the various locations in the pipe cross section.

5.4. EFFECT OF GLYCEROL ADDITION ON PRESSURE GRADIENT DURING PHASE INVERSION

The changes in phase distribution and flow pattern during the inversion of the oil/water dispersion, which were discussed in the previous section, are expected to affect the frictional pressure gradient. The variation in pressure gradient as the oil fraction increases (inversion from O/W to W/O) can be seen in Figure 5.5 for a mixture velocity of 3m/s and for the three aqueous phases used, namely pure water, 0.5% and 1% glycerol solutions.

144
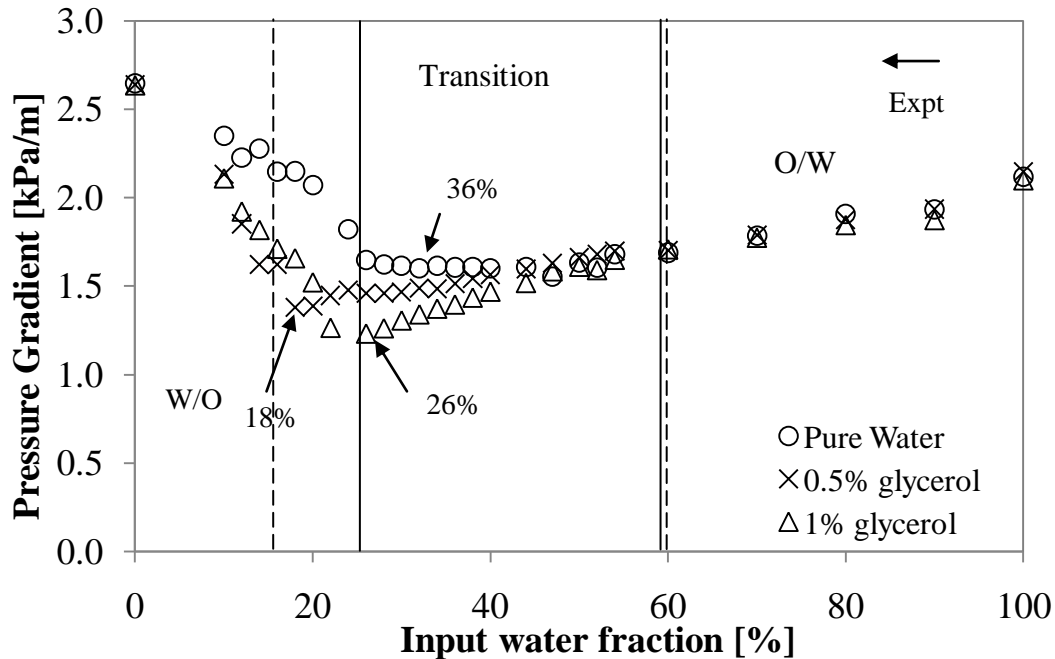
Figure 5.5: Experimental pressure gradient for pure water, 0.5% 1% glycerol solutions at different input water fractions at a mixture velocity of 3m/s. The vertical lines indicate the boundaries of the phase inversion transition region for pure water (solid lines) and both glycerol solutions (dotted lines). The percentages indicate the water fractions where pressure gradient shows a minimum. The arrow denotes the direction of experiment from aqueous to oil continuous dispersion.

Pressure gradient is found to be the same for the single phase flow of either water or glycerol solutions indicating that the addition of glycerol at these concentrations does not affect the frictional pressure gradient because it does not alter significantly the density or the viscosity of the aqueous phase. As the oil fraction increases, pressure gradient remains the same for all fluid pairs used, while a drag reduction phenomenon is observed, where the presence of the dispersed phase causes a decrease from the single phase value of the continuous phase at the same as the mixture velocity (Pal, 1993). The initial inversion in the middle of the pipe at 54% water fraction is the same for all three systems and does not affect the pressure gradient possibly because the continuity of the phase in contact with the pipe wall has not changed. Pressure gradient for pure water starts to

increase at about 36% water fraction after the mixture at the top of the pipe has inverted (see Figure 5.1 (a)). Beyond this fraction, the more viscous oil phase comes in contact with part of the pipe wall. The increase in pressure gradient for the two glycerol solutions occurs at lower water fractions of about 18% and 26% for the 0.5% and 1% glycerol solutions respectively. These changes again happen after the mixture at the top of the pipe inverts from water to oil continuous. With further increase in the oil fraction (decrease in water fraction), more oil contacts the pipe wall and the pressure gradient continues to increase as phase inversion spreads across the pipe until all three systems reach the single oil phase value. Similar results were found for the opposite experiment starting from an oil continuous mixture.

5.5. EFFECT OF GLYCEROL ON DROP SIZE DISTRIBUTION IN OIL AND WATER CONTINUOUS DISPERSIONS

Drop size distributions were measured using the dual impedance probe. The measurements were conducted for both dispersion initialization conditions, i.e. starting from oil continuous and from water continuous flows, and for the three aqueous solutions considered, i.e. pure water, 0.5% and 1% glycerol. It was found that drop size measurements in dilute solutions could not be obtained as the signals of the two sensors of the dual impedance probe did not cross-correlate well probably because of the small number of drops present. The same happened in the inversion transition region just after the first inversion in the middle of the pipe when glycerol was present in the water phase. Based on the tomographic images, the reason for this is probably the better separation between the two phases in the transition region when glycerol is added which leaves a lower concentration of the dispersed water phase in the middle where measurements are taken. Drop size measurements were therefore conducted for input water fractions between 40% and 60%. Measurements were carried out in the middle of the pipe (approximately 14mm from the top pipe wall). This location was chosen because the inversion at 54% allows both oil and water continuous dispersions to be investigated while it is also away from the interface formed during the dual continuous flow that may affect the measurements if any waves are present. Results are shown below for two

indicative fractions, 60% O/W and 40% W/O dispersion. To compare the drop sizes the average Sauter mean diameter, d_{32}, is used.

The Sauter mean diameters calculated for systems with pure water (PW), 0.5% and 1% glycerol solutions can be seen in Figure 5.6(a) for an initial water continuous dispersion and in Figure 5.6(b) for an initial oil continuous dispersion. In general, oil drops (at 60% water fraction) are smaller than water drops (at 40% water fraction), and this difference is more obvious for the pure water system. The addition of glycerol does not seem to affect the oil drop size significantly, which may explain why the initial inversion in the middle of the pipe from water to oil continuous mixture occurs at the same input phase fraction for all the three aqueous solutions. In contrast, the size of water drops is reduced when glycerol is added although the glycerol concentration does not seem to play an important role. It has been found that water drops in oil tend to coalesce faster when glycerol is added (Wang et. al, 2009); this would have resulted in larger drops when glycerol is present which seems to contradict the current result. However, it is possible that these larger drops will also tend to precipitate in the water layer that is still present at the bottom of the pipe at 40% input water fraction. This agrees with the findings of the ERT system which showed reduced concentration of water in the middle of the pipe and an increase in the water layer at 40% water fraction when glycerol is present compared to pure water (see Figures 5.1b, 5.2b and also the comparison of the conductivity values in Figure 5.3). Similar results were found for the opposite experiment starting from an oil continuous mixture (Figure 5.6(b)).
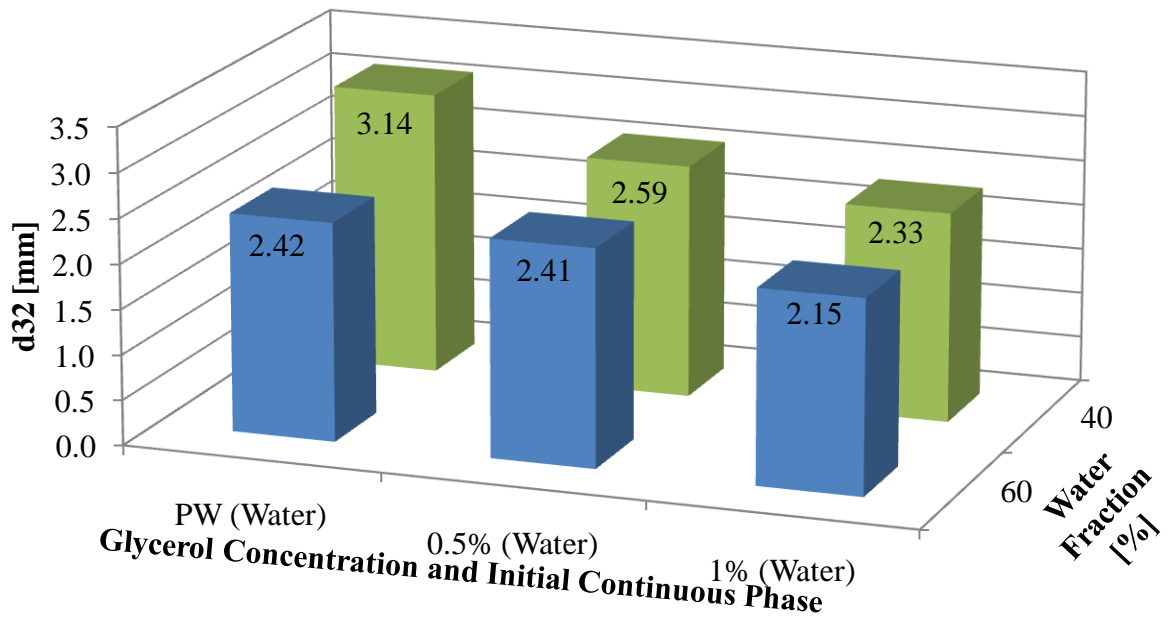
(a)
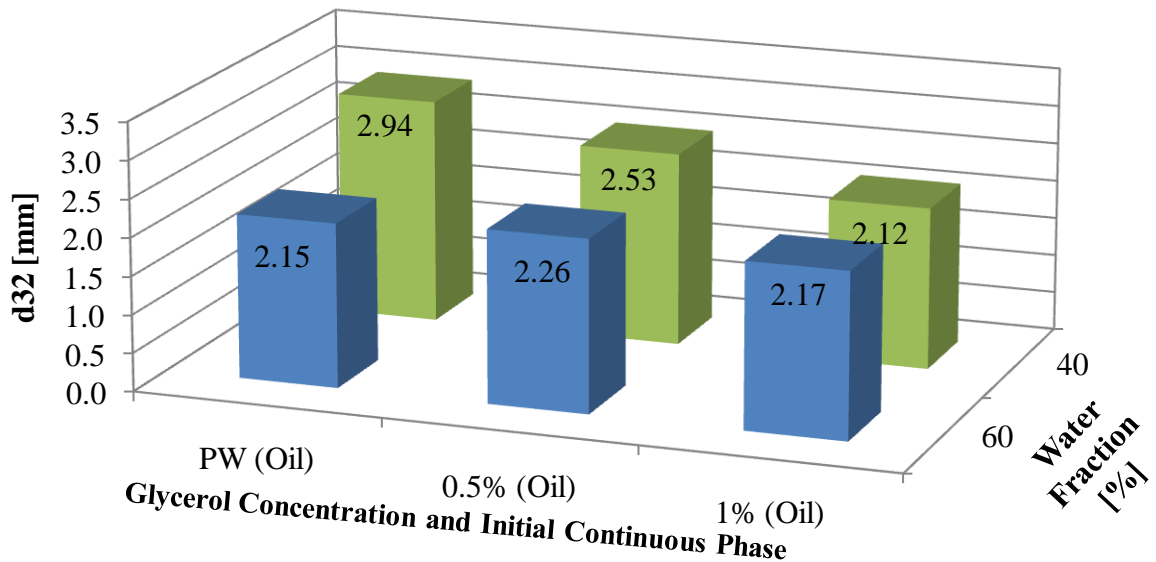
(b)

Figure 5.6 Sauter mean diameter for pure water, 0.5% and 1% glycerol solutions starting from (a) a water continuous dispersion and (b) an oil continuous dispersion. The phase in the bracket represents the initial continuous phase. The numbers on the columns represent the d_{32} diameter of the respective sample in mm.

5.6 CONCLUSION

The effect of interfacial tension on the phase inversion procedure of an oil-water mixture in pipe flow was investigated in this paper. By adding small concentrations of glycerol to water, the interfacial tension was reduced but the density and viscosity of the aqueous phase were not significantly affected.

For all fluid pairs tested initially at low oil fractions, the dispersion was water continuous with a fairly uniform distribution of the dispersed drops, as revealed by tomograms. As the oil fraction increased for the same mixture velocity, the mixture at the centre of the pipe inverted to become oil continuous. With a further increase in the oil fraction, inversion spread to the top and finally the bottom of the pipe and the mixture became oil continuous. It was found that while the addition of glycerol in water did not affect the phase fraction where the first inversion in the middle of the pipe occurred, it delayed the overall inversion at the rest of the pipe to higher oil (lower water) fractions. Drop size measurements in the middle of the pipe revealed that the size of the oil drops before inversion was not significantly affected by the addition of glycerol but the size of water drops after inversion was reduced. Although with the addition of glycerol, larger water drops are expected to form through coalescence; it is possible that these large drops also separate more easily due to gravity leaving only the smaller ones in the pipe centre to be measured. This settling would also explain the higher water concentration at the pipe periphery which delays the inversion in these regions when glycerol is added.

A drag reduction phenomenon was seen and pressure drop decreased as the oil fraction increased. Only when the mixture at the top of the pipe inverted and an oil continuous phase came in contact with the top pipe wall did the trend reverse and the pressure drop started to increase with further increase in the oil fraction.

Chapter 6: Prediction of phase inversion through fluid viscosities

6.1 OVERVIEW

Dispersions of two immiscible liquids, usually an organic and an aqueous, where one phase is in the form of drops within the continuum of the other, are very common in oil production and transportation. One of the characteristic but least understood phenomena in dispersions is *phase inversion*, where the dispersed phase changes to become continuous and vice versa. Knowing the phase fraction where inversion occurs (*phase inversion point*) is important for the processing of dispersions since such change results to a mixture with different properties (e.g. rheology, drop size). The significant consequence to the transportation of dispersions is the observed change in pressure gradient that accompanies phase inversion (Arirachakaran et al., 1989; Angeli and Hewitt, 1998; Ioannou et al., 2005) which can have implications for the flow rate in pipelines.

Previous phase inversion studies have mainly focused on dispersions formed in mechanically agitated batch or semi–batch vessels (see review by Yeo et al., 2000), but are significantly less for dispersions in pipeline flows. Investigations of oil-water pipe flows (Arirachakaran et al., 1989; Pal, 1993; Nädler and Mewes, 1997; Soleimani, 1999; Liu et al., 2005; Ioannou et al., 2004 & 2005; Chakrabarti et al. 2006; Hu and Angeli, 2006) revealed that the phase inversion point is affected by phase viscosity ratio, velocity, flow orientation and pipe diameter and material. It was also suggested that the change in the mixture continuity does not happen at one particular volume fraction but over a range, during which the flow is transitional.

Several physical mechanisms for phase inversion have been suggested in the literature. These include instability of the dispersed phase drop size where drop coalescence dominates over drop break up (Vaessen et al., 1996); minimum system energy or equal surface energy of the two possible dispersions (oil-in-water and water-in-oil) at phase

inversion (Tidhar et al., 1986; Brauner and Ullmann, 2002); zero interfacial shear stress (Yeh et al., 1964; Nädler and Mewes, 1997). It is, however, difficult to test these models mainly due to lack of appropriate data.

From the various parameters that affect phase inversion, the viscosities of the phases in particular, and consequently the dispersion mixture viscosity, appear to play a significant role. As such, the aim of the chapter is to derive a method to identify phase inversion based on the fluid viscosities. Section 6.2 presents the proposed method for determining the phase inversion point. The various mixture viscosity models are listed in Section 6.3 which will be selected as the best model using the proposed methodology to identify the phase inversion point. The prediction method is tested against 3 different oil/water system presented by Ioannou (2006) (Section 6.4) and also tested against Yeh et al. (1964) systems in Section 6.5. Comparison with other literature correlation on phase inversion prediction is also conducted in Section 6.5. In addition, a dispersed experimental setup is constructed to produce a homogeneous dispersion and the experimental outcome is tested against the prediction method (Section 6.6). Lastly, a conclusion on the applicability of the prediction method will be made in Section 6.7.

6.2. SUGGESTED METHOD FOR DETERMINING THE PHASE INVERSION POINT

The methodology for identifying the phase inversion point is demonstrated in Figure 6.1 for a dispersion of oil with viscosity 5.5 mPa s and water. The viscosities of the two types of dispersions, water continuous and oil continuous, are calculated from the viscosity model by, for example, Brinkman/Roscoe (1952) given by Equation (6.7) in Table 6.1 (other viscosity models are discussed in the following section).
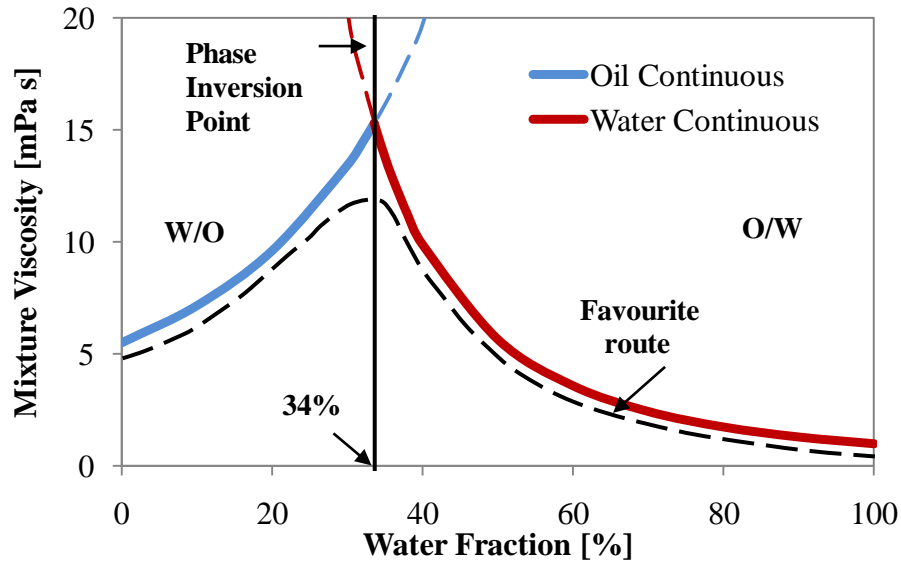
Figure 6.1: Prediction of phase inversion point for the Exxsol D140-water dispersion. Phase inversion occurs at the phase fraction where the difference in viscosity between the oil continuous and the water continuous dispersions becomes 0. The Brinkman/Roscoe (1952) model is used for calculating the viscosity of the dispersions.

The mixture viscosities for oil and water continuous dispersions at dispersed phase volume fractions from 0% to 100% are plotted together in Figure 6.1. The two viscosity plots intercept at a point where the mixture viscosities of the two dispersions are the same. Phase inversion is proposed to occur at this phase fraction where the two mixture viscosities become equal. The mixture viscosity is related to the pressure gradient which drives the dispersion. In the example of Figure 6.1 starting from an oil continuous dispersion the mixture viscosity increases with the water fraction. If the mixture was to remain oil continuous for water fractions above 34% then its viscosity (and in effect the pressure drop) would be higher than if it inverted to water continuous. By inverting to water continuous the mixture viscosity decreases with any further increase in the water fraction. By adopting the continuous phase that results in the lower viscosity for a given phase fraction therefore suggests that with inversion the mixture follows a more favourable route. A similar change of viscosity of the dispersion with phase inversion was found by Pal (1993).

The methodology for identifying the inversion point depends on the mixture viscosity model used. There are a number of dispersion viscosity models in the literature and these are briefly reviewed below and summarised in Table 6.1.

Author	Model	Remarks	Eq.
Einstein (1906, 1911)	$\dfrac{\mu_\varphi}{\mu_c} = 1 + 2.5\Phi$	Monodispersed system	(6.2)
Taylor (1932)	$\dfrac{\mu_\varphi}{\mu_c} = 1 + 2.5\Phi\left(\dfrac{0.4 + \mu_d/\mu_c}{1 + \mu_d/\mu_c}\right)$	Monodispersed system	(6.3)
Furuse (1972)	$\dfrac{\mu_\varphi}{\mu_c} = \dfrac{(1 + 0.5\Phi)}{(1 - \Phi)^2}$	Monodispersed system	(6.4)
Yaron and Gal-Or (1972)	$\dfrac{\mu_\varphi}{\mu_c} = 1 + \Phi\left\{\dfrac{5.5[4\Phi^{7/3} + 10 - (84/11)\Phi^{2/3} + (4/K)(1 - \Phi^{7/3})]}{10(1 - \Phi^{10/3}) - 25\Phi(1 - \Phi^{4/3}) + (10/K)(1 - \Phi)(1 - \Phi^{7/3})}\right\}$	Cell model, spherical drops	(6.5)
Choi and Schowalter (1975)	$\dfrac{\mu_\varphi}{\mu_c} = 1 + \Phi\left\{\dfrac{2(5K+2) - 5(K-1)\Phi^{7/3}}{4(K+1) - 5(5K+2)\phi + 42K\phi^{5/3} - 5(5K-2)\Phi^{7/3} + 4(K-1)\Phi^{10/3}}\right\}$	Cell model, spherical drops	(6.6)
Brinkman (1952)/ Roscoe (1952)	$\dfrac{\mu_\varphi}{\mu_c} = (1 - \Phi)^{-2.5}$	Polydispersed system	(6.7)
Krieger & Dougherty (1959)	$\dfrac{\mu_\varphi}{\mu_c} = \left(1 - \dfrac{\Phi}{\Phi_{max}}\right)^{[C]\cdot\Phi_{max}}$	Intrinsic viscosity, [C]=-2.5 Monodispersed system	(6.8)
Phan-Thien and Pham (1997)	$\left[\dfrac{\mu_\varphi}{\mu_c}\right]^{2/5}\left[\dfrac{2\eta_r + 5K}{2 + 5K}\right]^{3/5} = (1 - \Phi)^{-1}$	Polydispersed system, spherical drops	(6.9)
Mooney (1951)	$\dfrac{\mu_\varphi}{\mu_c} = \exp\left(\dfrac{2.5\Phi}{1 - k\Phi}\right)$	Crowding factor. 1.35<k<1.91 Monodispersed system	(6.10)
Pal and Rhodes (1989)	$\dfrac{\mu_\varphi}{\mu_c} = \left[1 + \dfrac{0.8415\phi/(\phi)_{\mu_r=100}}{1 - 0.8415\phi/(\phi)_{\mu_r=100}}\right]^{2.5}$	Semi-empirical correlation	(6.11)
Pal Eq. 16 (2001)	$\mu_r\left[\dfrac{2\mu_r + 5K}{2 + 5K}\right]^{3/2} = \exp(2.5\Phi)$	$\mu_r = \dfrac{\mu_\varphi}{\mu_c}$	(6.12)
Pal Eq. 27 (2001)	$\mu_r\left[\dfrac{2\eta_r + 5K}{2 + 5K}\right]^{3/2} = \left[1 + \dfrac{\Phi}{\Phi_m}\right]^2$	$\mu_r = \dfrac{\mu_\varphi}{\mu_c}$ Based on Brinkman/Roscoe (1952)	(6.13)
Pal Eq. 29 (2001)	$\mu_r\left[\dfrac{2\eta_r + 5K}{2 + 5K}\right]^{3/2} = \dfrac{9}{8}\left[\dfrac{(\Phi/\Phi_m)^{1/3}}{1 - (\Phi/\Phi_m)^{1/3}}\right]$	$\mu_r = \dfrac{\mu_\varphi}{\mu_c}$ Based on Frankel and Acrivos (1967)	(6.14)

Table 6.1: Literatures for dispersion viscosity models.

6.3. LITERATURE MIXTURE VISCOSITY MODELS

Various models for calculating the viscosity of liquid-liquid dispersions can generally be grouped into three main categories, namely linear, exponential and power function models. A linear dispersion viscosity model was first suggested by Einstein (1906, 1911) for an infinitely dilute suspension of small solid spheres (Equation (6.2), Table 6.1). However, this theory would not account for non-spherical particles at high concentrations or for particle size distributions. Still for near spherical drops and infinite dilution Taylor (1932) extended Einstein's equation to fluid dispersions (Equation (6.3), Table 6.1) by considering the internal circulation in the drops caused by the tangential stresses on the drop surface. Equation (6.3) can be reduced to Einstein's model for solid particles when $\mu_d \gg \mu_c$ while a corresponding lower limit is for gas bubbles where $\mu_d \ll \mu_c$. Attempts to extend Einstein's theory to high dispersion concentration, Φ, faced many challenges. Theoretical approaches based on a reflection technique led to power series models, as generally described by Equation (6.1).

$$\frac{\mu_\phi}{\mu_c} = 1 + K_1 \Phi + K_2 \Phi^2 + K_3 \Phi^3 + \ldots \tag{6.1}$$

The contributions of the high order terms, though, in these models are extremely complex to estimate and only the first order terms can be evaluated which result in equations similar to that by Einstein (e.g. Guth and Gold, 1938). Furuse (1972) considered the importance of the hydrodynamic effects of neighbouring particles in a concentrated solution. By extending Einstein's model, a power law model was derived (Equation (6.4), Table 6.1) to account for the higher order terms that were ignored by Einstein. An alternative approach was the cell model (Yaron and Gal-Or, 1972, Equation (6.5), Table 6.1; Choi and Schowalter, 1975, Equation (6.6) Table 6.1) in which a certain number of drops are confined within a representative cell to achieve a phase fraction that resembles the concentration in the bulk surrounding the cell. However, Yaron & Gal-Or's expression failed to reduce to Taylor's equation in the limit of $\Phi \rightarrow 0$ (Pal, 2001).

Brinkman (1952) and Roscoe (1952) followed a slightly different approach by accounting for the incremental change in viscosity caused by the addition of one extra solute particle to a dispersion of known concentration (Equation (7), Table 1). As there is no assumption on the shape and size of droplets, this model allows polydispersity but the interactions between adjacent particles when they are closely packed are ignored. Krieger and Dougherty (1959) applied Mooney's (1951) concept of crowding factor (which is inversely proportional to the maximum drop packing fraction defined as the maximum dispersed phase fraction in a confined space assuming monodispersed spherical drops) to Brinkman's equation, in order to include the effect of close packing on the mixture viscosity (Equation (6.8), Table 6.1). Pham-Thien and Pham (1997) extended Brinkman's approach to evaluate the effect of a dispersed drop size distribution (Equation (6.9), Table 6.1).

In terms of exponential models, Vand (1948) developed a kinematic model by Couette streaming of dispersion mixture. As the rate of shear is directly proportional to the dispersion concentration, the mixture viscosity was found to be an exponential function of the concentration. Mooney (1951) modified Vand's approach by including a crowding factor (Equation (6.10), Table 6.1). Mooney's model was reported to correlate well with various experimental data. This approach is similar to that by Arrhenius (1887). Barnea and Mizrahi (1973) presented a generalised exponential equation, identical to that by Mooney based on the empirical solution by Thomas (1965). The authors have subsequently added a term to include the effect of internal drop circulation. From Vand to Barnea and Mizrahi, these models have marked the development of exponential functions for mixture viscosity.

Pal and Rhodes (1989) and Pal (2001) suggested a number of viscosity models (some are given in Equations 6.11-6.14, Table 6.1). Pal (2001) evaluated various single parameter viscosity models against experimental data and found that Yaron and Gal-Or (1972) performed best for dispersed phase volume fractions up to about 55%. He also suggested a number of new two parameter power and exponential function viscosity models but found that, in overall, the model given by Equation 6.14 in Table 6.1 performed best.

155

Models used in the current study are presented in Table 6.1. Although all models were tested using the proposed methodology for predicting phase inversion, only selected ones are included in the graphs that follow. These were selected because (a) they are simple to use (e.g. Brinkman/ Roscoe (1952)), (b) have been shown to give the best predictions of dispersion viscosity (e.g. Yaron and Gal-Or (1972); Equation 6.14 by Pal (2001)) and (c) represent a category of viscosity models (e.g. linear, exponential and power law).

6.4. COMPARISON BETWEEN PREDICTED PHASE INVERSION POINTS AND EXPERIMENTAL RESULTS FROM LITERATURE

The phase inversion points predicted by the methodology described above are compared against available experimental data from oil-water pipeline flows by Ioannou (2006). Details of the properties of the three oils and of the test sections used can be found in Table 6.2. Phase inversion was experimentally determined through conductivity measurements obtained either at the flow perimeter with ring probes or at various locations (e.g. pipe centre) within the pipe cross section with local conductivity wire probes. At the operated range of mixture velocity, the liquid-liquid dispersion can be inhomogeneous at high dispersed phase fraction close to phase inversion and phase inversion may thus appear at certain parts of the pipe first before it spreads to the whole pipe cross section. For example in an oil continuous dispersion in a horizontal pipe, inversion would first occur at the bottom of the pipe where the dispersed water drops tend to accumulate due to gravity (Ioannou et al., 2004). A hysteresis effect has also been reported where the phase inversion point depends on the initial continuous phase (oil or water) which results in an ambivalent range similar to that seen in stirred vessels (Ioannou et. al., 2005). Some investigators have also found that inversion may not happen at one particular volume fraction but is a transition occurring over a range of fractions during which complex multiple dispersion structures form (Liu et al., 2005; Piela et. al., 2008). Pipe material has also been found to affect the inversion point due to the wettability of the fluid with the pipe wall. Thus for a given oil-water fluid pair in dispersed pipe flow there is a range of phase volume fractions (*phase inversion range*)

within which inversion will occur that accounts for the effects of pipe material, size, initial continuous phase and mixture velocity. Only outside the phase inversion range will the dispersion be either oil or water continuous with certainty.

	Density (kgm^{-3})	Viscosity (mPa s)	Pipe Property
Water	1000	1.0	
Exxsol D80	796	1.7	60mm ID acrylic and steel pipe
Exxsol D140	828	5.5	38mm ID steel pipe
Marcol 52	835	11	60mm ID acrylic and steel pipe

Table 6.2: Physical properties of fluids and pipes used in the phase inversion experiments.

The phase fractions where the mixture viscosities between the oil and the water continuous dispersions become equal (as described schematically in Figure 6.1) for selected viscosity models from Table 6.1 are shown in Figure 6.2 for the three oils considered. In these figures (Figure 6.2(a)-(c)), the vertical lines denote the phase inversion ranges found experimentally for each of these three oil-water pairs and include data from different pipe materials, mixture velocities and initial continuous phase. In the implementation of the viscosity models it was assumed that the dispersed drops are spherical for the whole range of volume fractions, while the maximum packing factor, Φ_{max}, was taken equal to 0.74 (and 0.637 for the model by Pal (2001)) for a monodispersed mixture (Yeh et al., 1964) with a corresponding crowding factor, k, of 1.35 (i.e. $k=1/\Phi_{max}$). From the figures, it is apparent that most viscosity models can predict the equal mixture viscosities point and hence the phase inversion point within the experimental phase inversion range. From the models shown, Taylor's linear model (Equation 6.3) falls, as expected, outside the range. Additionally, the exponential model by Mooney (Equation 6.10) always predicts the phase fraction to be 0.5 regardless of the oil used. All the other viscosity correlations shown in Table 6.1 have also been tested and it is found that power function models give better predictions. It can also be seen that the experimental range of water volume fractions where inversion occurs shifts to lower values as the oil viscosity increases which agrees with previous findings (Arirachakaran,

157

1989; Selker & Sleicher, 1965; Yeh et al., 1964); the predicted inversion points follow the same trend.

The predicted phase inversion points for Marcol 52 are compared in Figures 6.3 - 6.5 against the phase inversion ranges obtained under different experimental conditions. The effect of dispersion initialisation conditions is demonstrated in Figure 6.3, where it can be seen that the inversion range depends on which phase is initially continuous. Mixture velocity is also found to affect the boundaries of the phase inversion range and this is demonstrated in Figure 6.4. With increasing flow velocity, the inversion region width decreases as the dispersion becomes more homogeneous. While a transitional region in the experimental outcome is maintained in the current operation conditions, a clear trend of narrowing of this region to a specific phase fraction is observed if the mixture velocity increases leading to higher turbulence and homogeneous dispersion (similar to Brauner and Ullmann, 2002, and Chakrabarti et. al., 2006). Thus, the prediction of a phase inversion point through the dispersion viscosity still valid as long as it falls within the transitional region. The pipe material effect on the inversion range is shown in Figure. 6.5. The phase inversion range is shifted to lower water fractions in the acrylic pipe compared to the steel one. In all the above cases the predicted phase inversion points (equal mixture viscosities), when the viscosity models by Brinkman/Roscoe (1952), Furuse (1972) and Equation 6.14 by Pal (2001) are used, consistently fall within the phase inversion ranges. Similar results were found for the other two oils investigated.
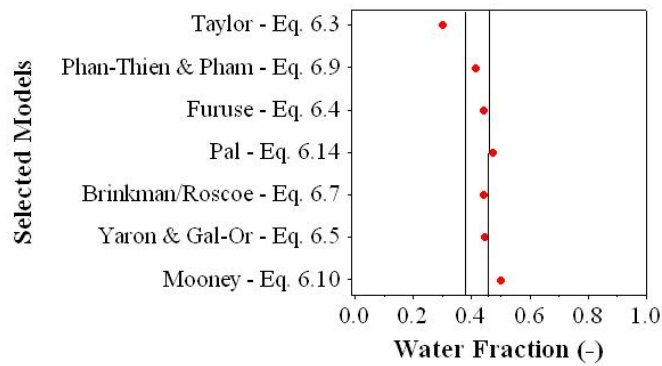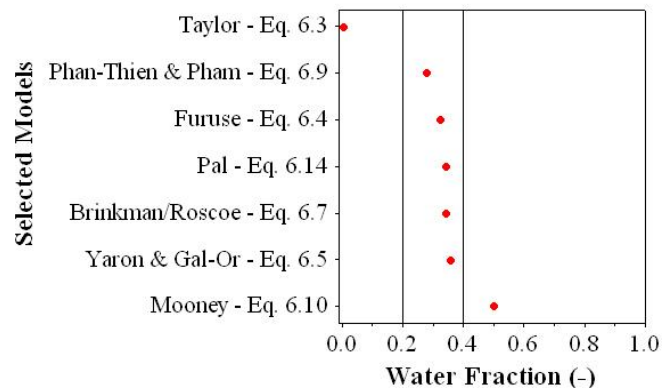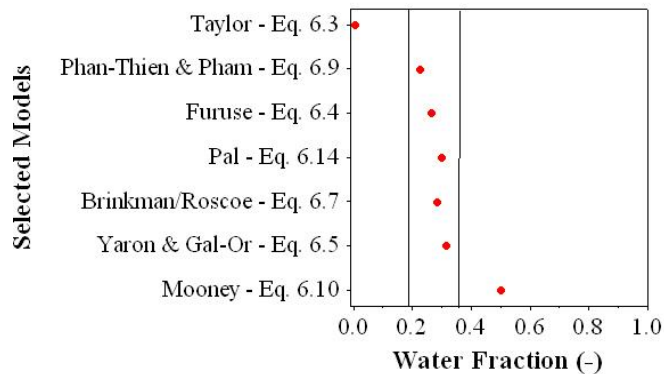
Figure 6.2: Predicted inversion points using different dispersion viscosity models against the experimental phase inversion range for a dispersion of water and (a) Exxsol D80 (1.7mPas), (b) Exxsol D140 (5.5mPas), (c) Marcol 52 (11mPas) (data in stainless steel pipe by Ioannou, 2006). Points in graph refer to the model predictions while the lines represent the experimental phase inversion region.

159
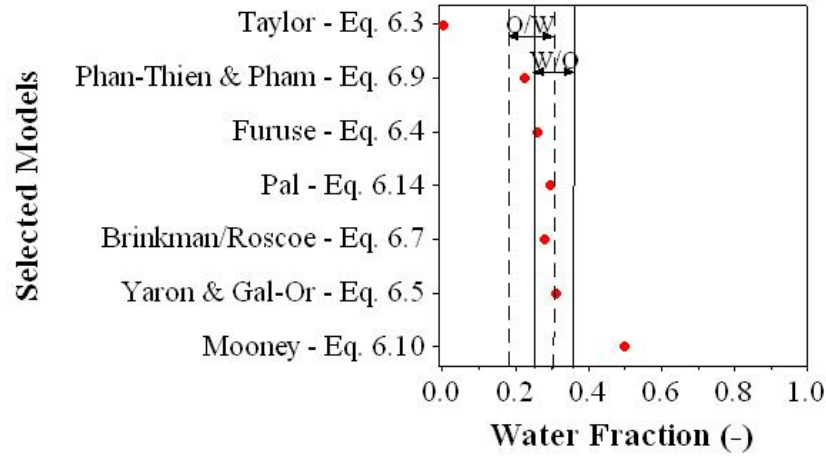
Figure 6.3: Predicted inversion points using different dispersion viscosity models against the experimental phase inversion ranges in stainless steel pipe obtained starting from oil continuous and from water continuous dispersions for a water-Marcol 52 mixture. Points in graph refer to the model predictions while the lines represent the experimental phase inversion region.
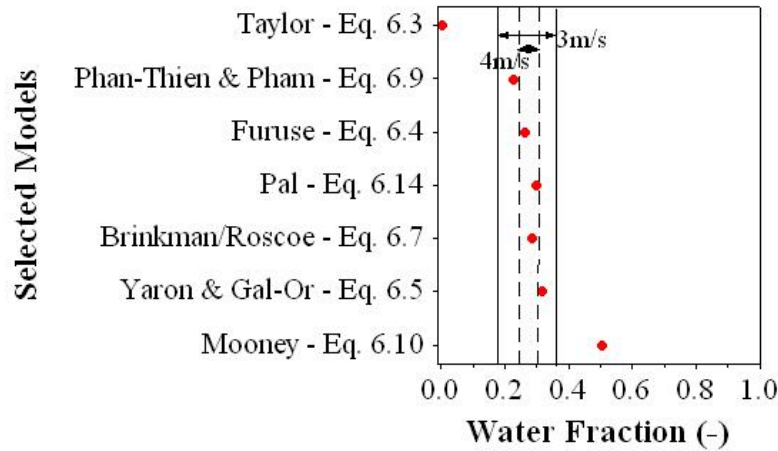
Figure 6.4: Predicted inversion points using different dispersion viscosity models against the experimental phase inversion ranges in stainless steel pipe obtained at different mixture velocities for a water-Marcol 52 mixture. Points in graph refer to the model predictions while the lines represent the experimental phase inversion range.

160
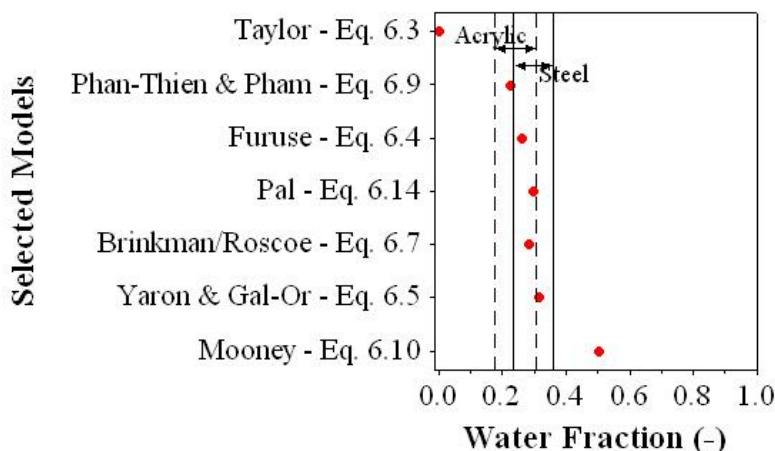
Figure 6.5: Predicted inversion points using different dispersion viscosity models against the experimental phase inversion ranges obtained with different test sections for a water-Marcol 52 mixture. Points in graph refer to the model predictions while the lines represent the experimental phase inversion range.

6.5. COMPARISON OF THE PROPOSED METHODOLOGY WITH LITERATURE CORRELATIONS

The phase inversion points predicted with the equal mixture viscosities methodology for the three oils used are compared against those found from the models by Yeh et al. (1964), Arirachakaran et al. (1989) and Nädler and Mewes (1997) (see Table 6.3). From Figure 6.6, it can be seen that only Yeh et al.'s model (Equation (6) in Yeh et al. (1964)) predicted phase inversion points fall within the phase inversion ranges for all oils studied. In addition, the proposed methodology, using the Brinkman/Roscoe (1952) viscosity model, is found to predict well Yeh et al.'s own experimental data that included a large range of oil viscosities (see Table 1 in Yeh et al. (1964)), with error ranging from 0.08% (water-Chlorobenzene) to 8% (water-Nitrobenzene) and an average error of approximately 3% across the different organic-aqueous fluid pairs. The deviations were similar to those of Yeh et al.'s own correlation (Equation (6) in Yeh et al. (1964)), while, interestingly, the inversion points found by the current methodology were closer to the

predictions of a modified equation suggested by Yeh et al. (Equation (6a) in Yeh et al. (1964)) where the interfacial viscosity is used instead of the water phase viscosity. To develop his model, Yeh et al. assumed that there are no interfacial shear stresses at the point of phase inversion indicating a momentum balance at the fluid interface. The proposed methodology can also predict well with a wide range of oil/water system reported in Arirachakaran et al. (1989).

In Figure 6.7, the proposed method is compared with the experimental data from both Yeh et al. (1964) and Arirachakaran et al. (1989). It is also compared with the suggested models proposed by the respective authors. From the figure, it can be shown that the models from Yeh et al. (1964) and Arirachakaran et al. (1989) can only predict limited range of viscosity ratio with Yeh et al. predicting well with the lower viscosity range and Arirachakaran et al. (1989)'s at the higher viscosity range. In comparison, the proposed method can predict very well across the wide range of viscosity ratio from an organic viscosity of 0.235mPa.s and about 1500mPa.s. It demonstrates that the phase inversion point is not a linear function of the logarithmic relation with the viscosity ratio. In fact, it appears to reach an asymptote of about 0.23 for water fraction as the viscosity ratio increases. This may be because the organic phase in the lower viscosity pairs can be deformed more easily than that of the higher viscosity. This leads to the prediction of Yeh et al. (1964)'s model to a lower water fraction for phase inversion as it extrapolates across the range of viscosity ratio tested. However, the increase in viscosity ratio is likely to affect the deformation of the dispersed phase leading to a maximum packing that the dispersed phase can sustain and beyond which a phase inversion will occur.
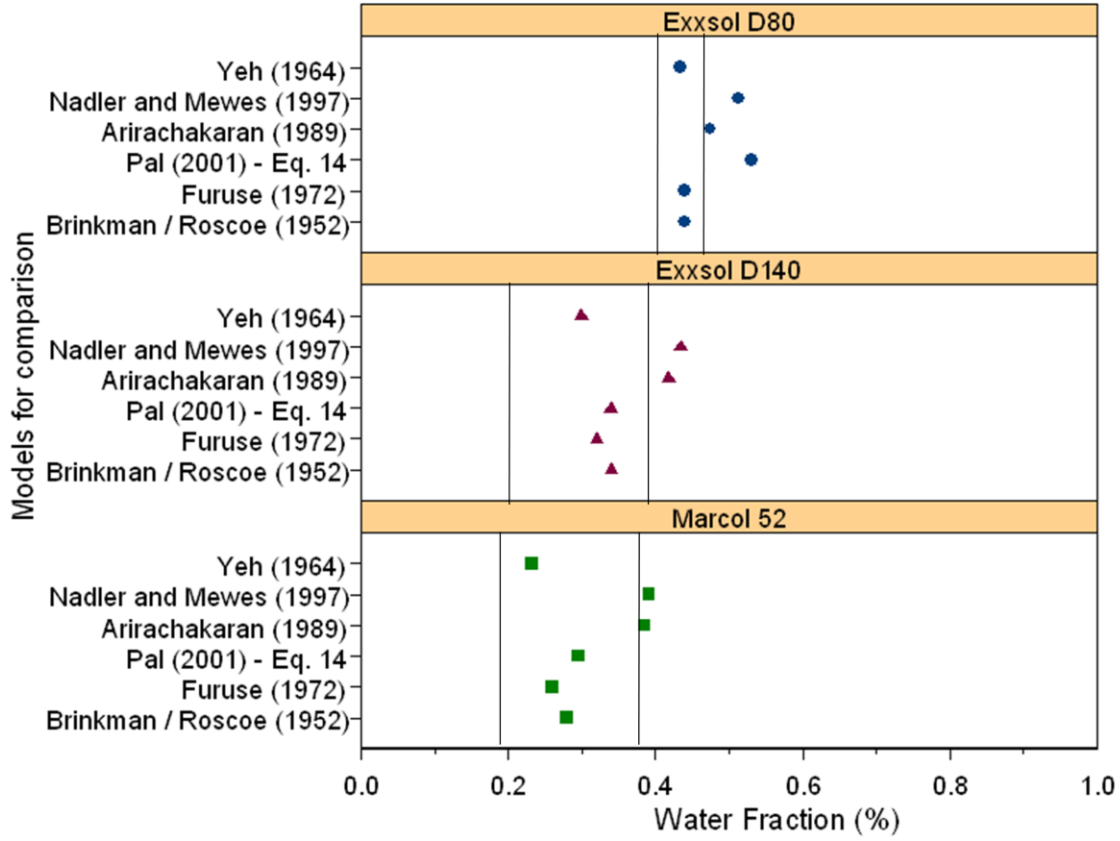
Figure 6.6: Comparison between proposed methodology (suggested best models) and models for critical phase fraction from literature.

Author	Model	Eq.
Arirachakaran et al. (1989)	$$\varphi_w^I = 0.5 - 0.1108 log \frac{\mu_o}{\mu_w}$$	(6.15)
N ädler and Mewes (1997)	$$\varphi_w^I = \frac{1}{1 + k_1 \left(\frac{C_o}{C_w} \frac{\rho_o^{(1-n_o)}}{\rho_w^{(1-n_w)}} \frac{\mu_o^{n_o}}{\mu_w^{n_w} (DU_m)^{(n_w - n_o)}} \right)^{1/k_2}}$$	(6.16)
Yeh et al. (1964)	$$\varphi_w^I = \frac{1}{1 + \left(\frac{\mu_o}{\mu_w} \right)^{0.5}}$$	(6.17)
Yeh et al. (1964)	$$\varphi_w^I = \frac{1}{1 + \left(\frac{\mu_o}{\mu_I} \right)^{0.5}}$$	(6.18)

Table 6.3: Critical phase fraction models for phase inversion from literature.
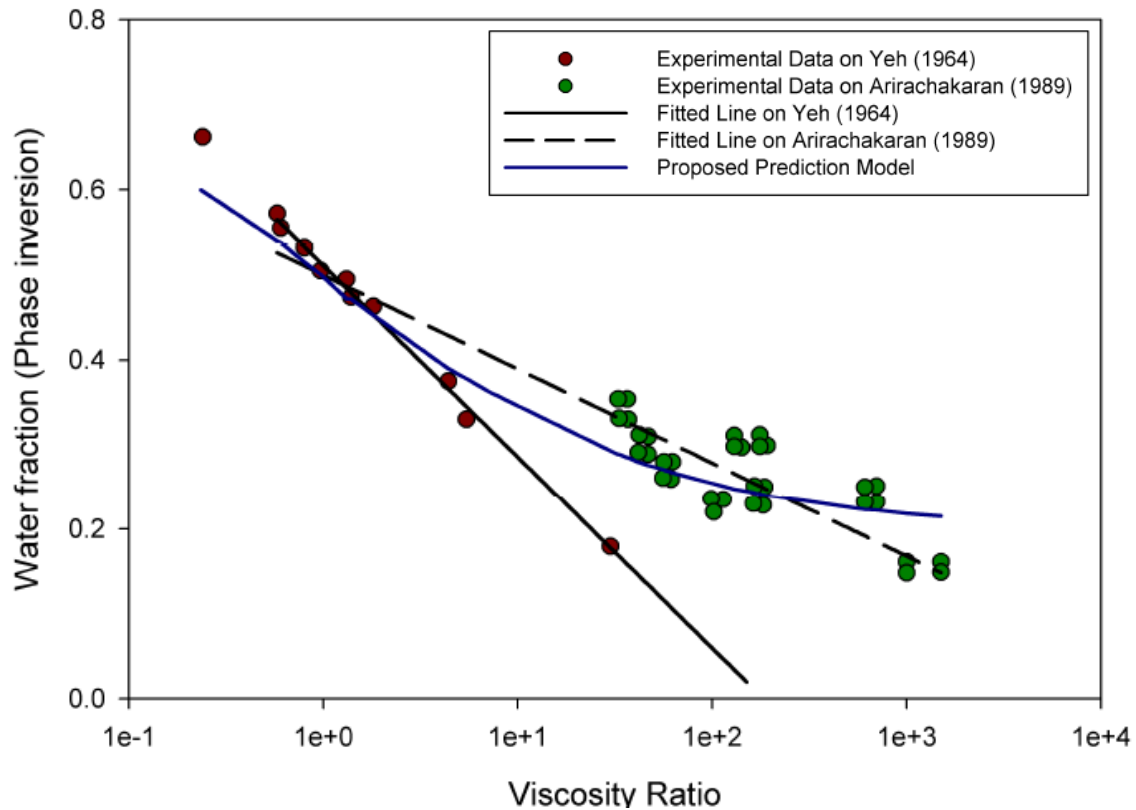
Figure 6.7: Application of proposed model on various systems from Yeh et al. (1964) and Arirachakaran et al. (1989). The solid line represents the prediction model by Yeh et al. (1964) (see Equation 6.17) and the dotted line represents the prediction model by Arirachakaran et al. (1989) (see Equation 6.15).

6.6.   REVIEW   ON   PREDICTION   MODEL   WITH   AN EXPERIMENTAL HOMOGENEOUS DISPERSED FLOW

The proposed method for phase inversion prediction is now tested against the phase inversion data obtained in the experimental facility using the dispersed inlet. As shown in Chapter 4 with this inlet setup, the flow is fully dispersed for all phase fractions at the mixture velocity of 3m/s. As a result, the change from a water continuous dispersion to an oil continuous dispersion (and vice versa) occurs throughout the pipe cross section at a particular phase fraction rather than over a transitional region as in the case of a split inlet. The experimental phase inversion points from the dispersed inlet are therefore well suited

for comparison with the phase inversion prediction model since the mixture viscosity models used are derived from homogeneously dispersed mixtures.

In order to compare with the prediction model, the pressure gradient from the prediction model is firstly calculated using Brinkman (1952)'s mixture viscosity equation and apply that to a single phase mixture equation for pressure gradient (Equation 6.19).

$$\frac{\Delta P}{l} = \frac{2f\rho_m U_m^2}{D}$$
(6.19)

where $\Delta P/l$ is the pressure gradient across a pipe, f is the friction factor ($f=0.046Re_m^{-0.2}$), ρ_m is the mixture density, U_m is the mixture velocity and D is the pipe diameter. The calculated pressure gradient is then compared with the experimentally measured pressure gradient together with the conductivity data on phase continuity switch.

From Figure 6.8, it can be observed that the experimental pressure gradient closely resemble the trend deduced by the correlation (Equation 6.19) between 38% and 100% water fraction. The difference between the experimental result and model outcome may be due to the presence of drag reduction that is not accounted for in the correlation. There is a sharper drop in pressure gradient for the experimental result between 26% and 38% water fraction and subsequently an increase in pressure gradient below 26%.

Based on the prediction from the interception point in Figure 6.8, the predicted phase inversion point (at 34%) falls in the phase fraction range where the pressure gradient is decreasing. From the investigation outcome in Chapter 4, this lies at the range of phase fraction where drop coalescence becomes prominent with likely formation of complex structures. While the conductivity measurements detects a change in phase continuity at a lower phase fraction (26%), the predicted phase inversion point can be considered to be within close proximity because the process of drop coalescence can lead to the formation of oil pockets (if starting from an O/W dispersion) as presented in Piela et al. 2008. These oil pockets may not be easily detected by the conductivity wire and ring probe but nonetheless an important stage in the onset of phase inversion. As such, the prediction can be considered to have good prediction with the experiments conducted.

165
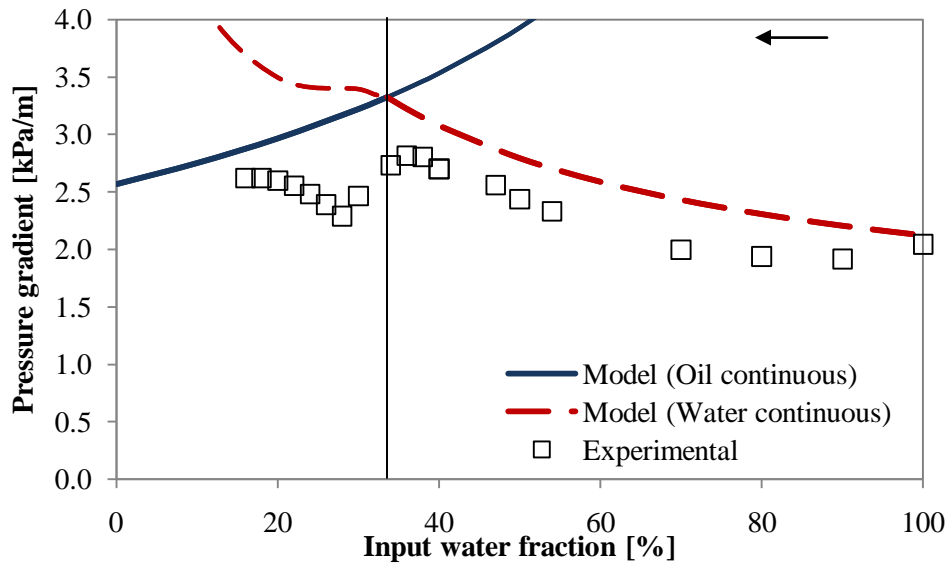
Figure 6.8: Comparison of pressure gradient at different phase fraction between experimental data (□) and modeling outcome via Brinkman/Roscoe (1952)'s mixture viscosity correlation. The solid arrow (←) represents the direction for the experiment and the vertical line denotes the predicted phase inversion point.

6.7. CONCLUSION

A methodology has been introduced to identify the inversion point during oil-water dispersed flow. It is suggested that inversion will occur at the phase fraction where the mixture viscosities of the oil and the water continuous dispersions become equal. The approach was tested against extensive available experimental data on phase inversion where oil viscosity, pipe material, mixture velocity and dispersion initialisation conditions were varied. From the available literature dispersion viscosity models tested, the power function correlations by Brinkman (1952)/Roscoe (1952), Furuse (1972) and Equation (14) by Pal (2001) always predicted inversion within the experimental phase inversion range. The proposed methodology was also tested against the predictions of literature correlations on phase inversion point. Very good agreement was found across a wide range of two phase systems with organic viscosity of 0.235mPa.s and about 1500mPa.s from Yeh et al. (1964) and Arirachakaran et al. (1989).

The suggested prediction method with Brinkman (1952)/Roscoe (1952) mixture viscosity model was subsequently tested with experimental data of an homogeneous dispersed flow. Similar increasing mixture viscosity can be observed as the dispersed phase fraction is increased. The method shows closely at the phase fraction (i.e. 36% water fraction) where the mixture viscosity is highest (and resulting in a corresponding maximum pressure gradient). Below 34% water fraction, the dispersion appears to encounter drop deformation/coalescence which leads to the complete change in phase continuity at 26% water fraction. Pressure gradient of an inverted W/O system subsequently shows a significant increase due to the higher viscosity by the continuous oil phase.

From this chapter, a conclusion can be drawn that the viscosity of the liquid-liquid mixture is important for understanding phase inversion. The prediction method falls within close proximity with the experimentally detected change in phase continuity. Despite that there is a discrepancy within the two values, the predicted phase inversion point highlights a point where drop coalescence/deformation becomes dominant in the system and the coalescence process is a key factor for the inversion process. Further work is needed to understand the changes in the mixture morphology as it approaches phase inversion. Such studies will help to better describe the phase inversion phenomenon and will also improve the model by including, for example, the drop packing and size distribution.

Chapter 7: Prediction of pressure gradient during phase inversion

7.1 OVERVIEW

Multiphase flow of two or more fluids is commonly encountered in the petroleum industry during oil production and transportation. Water often appears in oil wells particularly in the later years of production. At high velocities, the mixture of oil and water is transported as a dispersion with either oil (water-in-oil, W/O) or water (oil-in-water, O/W) as the continuous phase. The type of dispersion depends on the phase ratio, rheological properties of the two fluids, wetting properties of the pipe material and the operation initialisation conditions (Yeo et. al, 2000; Ioannou, 2006). Interestingly, the continuous phase of the dispersion changes under certain conditions to become the dispersed one and vice versa (*phase inversion* phenomenon). The phase fraction where this change occurs is called the *phase inversion point*. During pipeline flow, however, it has been found that inversion occurs over a range of input phase fractions. This transitional range can be attributed to phenomena such as formation of multiple dispersions (Liu et al., 2005) and partial or local inversion as the dispersed phase fraction increases (Ioannou, 2006; Piela et al., 2008). Partial inversion results in stratification of the flow with two layers that have different continuous phase.

The changes in the spatial distribution of the phases as their volume fractions change can have significant impact on pressure drop and pose great challenges in its modelling. To predict pressure drop in dispersed oil-water flows, the homogeneous model is often used where the fluids are considered as one "pseudofluid" and single phase flow equations are used with a weight averaged mixture density and an empirically determined mixture viscosity (viscosity models by e.g. Brinkman, 1952; Yaron & Gal-Or, 1972; Choi & Schowalter, 1975; Pal, 2001). However, the homogeneous model does not accurately represent the phase distribution in horizontal pipelines where stratification due to gravity can appear even at high mixture velocities. To account for the separation of the two fluids,

the two-fluid model (TFM), developed for stratified flows (e.g. Brauner & Moalem Maron, 1989), can be applied.

In this chapter, experimental results on phase inversion and pressure drop during horizontal oil-water dispersed flows are presented (Section 7.2). A methodology (see Section 7.3) is developed based on a two layer flow configuration, in order to predict the phase volume fractions where the mixture is completely dispersed or there is stratification of the two fluids. The entrainment fractions in each layer are calculated from previously developed correlations, while a phase inversion criterion is used to determine the continuity of each continuous layer in the model. The outcome of the developed model will be compared with experimental results in Section 7.4 and conclusions on the quality of the model are made in Section 7.5.

7.2 EXPERIMENTAL INVESTIGATION

Experimental studies on phase inversion were conducted in the pilot scale liquid-liquid flow facility (See Chapter 3). The test section is an acrylic pipe with 38mm ID. Exxsol D140 oil (density of 828 kgm^{-3}, viscosity of 5.5mPa.s) and tap water were used as test fluids. The two fluids were pumped from storage tanks via variable area flow meters into the test section inlet where they were joined in a modified Y-junction to ensure minimum mixing. Experiments were conducted at mixture velocities 3m/s and 4m/s where previous work indicated that the flow was in the dispersed regime. At each velocity the experiments were started with single phase water. Oil was then introduced into the pipe. The oil flowrate was gradually increased while at the same time that of the water decreased in order to increase the oil fraction while keeping the mixture velocity constant. The experiments continued until phase inversion was observed and beyond until about 80% input oil fraction. Pressure drop was measured via a differential pressure transducer (Validyne DP103) between two measuring ports 1.5m apart, with the first port located at 3.8m (~100D) from the inlet. A conductivity wire probe was used to identify phase continuity at different locations (i.e. every 2mm intervals) along the vertical diameter in a pipe cross section and thus to understand the development of phase inversion. The probe was located at 7m (~184D) from the inlet.
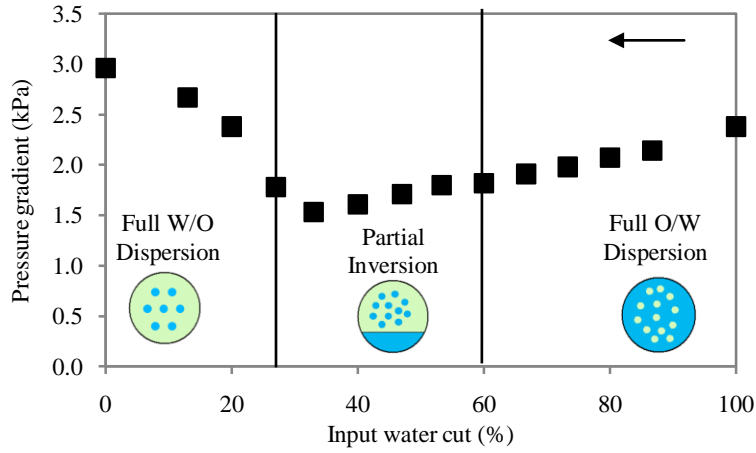
(a) 3m/s mixture velocity
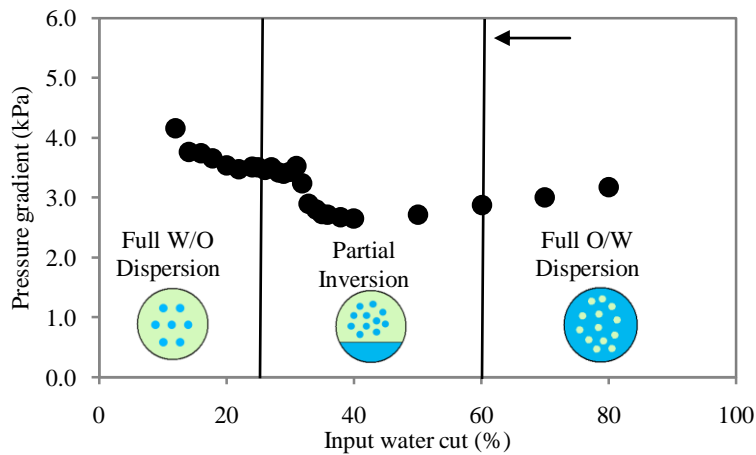
(b) 4m/s mixture velocity

Figure 7.1: Pressure gradient at mixture velocity (a) 3m/s and (b) 4m/s measured experimentally. The solid lines represent the boundaries of the transitional region between water continuous and oil continuous fully dispersed flow. The arrow indicates the direction of the experiment.

The pressure gradients measured at mixture velocities of 3m/s and 4m/s are depicted in Figure 7.1 (a) & (b) respectively. At high water cuts the conductivity probe showed that the mixture was water continuous in the whole pipe cross section. By gradually increasing the oil fraction (as indicated by the direction of the arrow) the flow remains fully dispersed with water as the continuous phase until about 60% water cut in both mixture velocities, while the pressure gradient decreases. This indicates a drag reduction phenomenon that has also been reported before (see Pal, 1993). Beyond this volume fraction, partial inversion takes place at the top part of the pipe and the pattern is now dual continuous with a water continuous layer at the bottom of the pipe and an oil continuous layer at the top of the pipe, as indicated by the measurements of the conductivity probe. At about 34% water cut, the pressure gradient reaches a minimum and with further decrease in the water fraction it increases again. This increase coincides with the change of the flow pattern from dual continuous to fully dispersed with oil as the continuous phase. In these experiments inversion from the O/W to the W/O dispersion occurs through a transitional region which is enclosed in Figure 7.1 between the solid vertical lines.

7.3 DEVELOPMENT OF MODEL FOR THE PREDICITON OF PRESSURE DROP

A methodology was developed to predict the flow configuration, dual continuous or fully dispersed, as well as the pressure gradient during the flow of liquid-liquid mixtures.

7.3.1 PREDICTION OF FLOW CONFIGURATION

For each phase fraction it is assumed initially that the mixture has a dual continuous configuration with a water continuous layer with oil drops dispersed in it at the bottom and an oil continuous layer with water drops dispersed in it at the top of the pipe. A range of interfacial heights is then considered with an interval of 0.1mm. At each interfacial height, the dispersion in each layer is assumed to be homogeneously distributed. The amount of dispersion of one phase into the other is calculated using the entrainment model described in Section 7.3.2. By comparing the phase fractions in each layer with a

171

criterion for the phase inversion point, the continuous phase in that layer can be determined. The phase inversion point ($WF_{Critical}$) is calculated using the methodology developed by Ngan et al. (2009) according to which phase inversion will occur at the phase fraction where the viscosities of the two possible dispersions, oil continuous and water continuous, are equal. For the Exxsol D140-water mixture used in this work, the critical water fraction for phase inversion is found to be 34%. According to this, the possible scenarios for the two layer mixture are:

Water entrainment in upper (W/O) layer (Entu)	Oil entrainment in lower (O/W) layer (Entl)	Flow Pattern		Valid
		upper layer	lower layer	
$Entu < WF_{Critical}$	$Entl < (1- WF_{Critical})$	W/O	O/W	Yes
	$(1- WF_{Critical}) < Entl < 1$	W/O	W/O	Yes
$WF_{Critical} < Entu < 1$	$Entl < (1- WF_{Critical})$	O/W	O/W	Yes
	$(1- WF_{Critical}) < Entl < 1$	O/W	W/O	No

Notes:
1) The entrainment fraction cannot be above 1.
2) The less dense oil cannot be continuous underneath the more dense water.

Table 7.1: Flow patterns resulting from the application of a critical water fraction for phase inversion ($WF_{critical}$) in each of the upper and lower layers of a dual continuous flow configuration.

A two-fluid model, as detailed in Section 7.3.3, is then applied for each interfacial height only to the valid cases in Table 7.1. The model has a solution when the pressure gradients of the upper and lower layers are the same within a 2% difference. If there is no solution of the two fluid model for the entire range of interfacial heights for the particular phase fraction, then the dual continuous flow configuration cannot exist and the mixture is fully dispersed. This happens when the comparisons with the critical phase fraction have indicated that both layers have the same continuity. In that case the homogeneous model (see Section 7.3.4) is used to predict the pressure gradient.

7.3.2 ENTRAINMENT MODEL

To calculate the entrainment fraction in each layer of the dual continuous configuration, the model developed by Al-Wahaibi and Angeli (2009) was used. According to the model, drops will form from the crests of unstable waves at the oil-water interface when the drag force on the waves exceeds the stabilising interfacial tension force. At steady state, the rate of drop entrainment will be equal to the rate of drop deposition. According to Al-Wahaibi and Angeli (2009), the rate of entrainment (R_{ent}) can be calculated as follows:

$$R_{ent} = \frac{V_{ent} \rho_d |U_w - U_o|}{S_i - \lambda^2} \tag{7.1}$$

where ρ_d is the density of the entrained phase, V_{ent} is the volume of the entrained phase from each wave crest, λ, is the wave length, which, based on experimental observations and for simplicity is taken equal to the pipe diameter and S_i is the length of the interface.

The rate of deposition (R_{dep}) is equal to:

$$R_{dep} = k_D \left(\frac{W_d}{Q \cdot S_v} \right) \tag{7.2}$$

where W_d is the mass flow rate of the dispersed phase in the layer, Q is the volumetric flow rate of the mixture in a layer and S_v is the slip ratio between the dispersed drops and the continuous phase. In this work, no slip is assumed between the dispersed and continuous phases (i.e. $S_v=1$). k_D is an empirically determined deposition rate constant which was found by Al-Wahaibi (2006) to be equal to

$$k_{D(O/W)} = 0.051 \cdot \left(\frac{U_{so}}{U_m} \right) \cdot U^* \tag{7.3}$$

$$k_{D(W/O)} = 0.077 \cdot \left(\frac{U_{sw}}{U_m}\right) \cdot U^* \tag{7.4}$$

where U_s is the superficial velocity and U^* is the frictional velocity. Subscripts, o and w, represents the oil and water phases.

By equating the rates of entrainment and deposition, the entrainment fraction (W/W) in a layer can be found as follows:

$$\frac{V_{ent}\rho_d|U_w - U_o|}{S_i \cdot \lambda^2} = k_D \cdot E\big[(1-E) \cdot \rho_c + E \cdot \rho_d\big] \tag{7.5}$$

where E is the steady state entrainment fraction, ρ_c and ρ_d are the densities of the continuous and the dispersed phases respectively. The calculated entrainment fraction is in w/w and for the application in the two-fluid model it is converted to v/v.

7.3.3 TWO FLUID MODEL

For a steady state, fully developed dual continuous flow configuration with an oil continuous dispersed layer at the top and a water continuous dispersed layer at the bottom the one-dimensional momentum equations for each layer are given by:

$$\left(\frac{dP}{dx}\right)_u = -\tau_u \cdot \left(\frac{S_u}{A_u}\right) \mp \tau_i \cdot \left(\frac{S_i}{A_u}\right) \tag{7.6}$$

$$\left(\frac{dP}{dx}\right)_l = -\tau_l \cdot \left(\frac{S_l}{A_l}\right) \pm \tau_i \cdot \left(\frac{S_i}{A_l}\right) \tag{7.7}$$

where τ is the shear stress, S is the perimeter covered by the respective layer and A is the pipe cross sectional area. In the above equations, subscripts "u" and "l" denotes the upper and lower layers and subscript "i" denote the interface between the two layers.

The shear stresses in Equations (7.6) and (7.7) can be found as follows:

$$\tau_u = f_u \frac{\rho_u U_u^2}{2} \qquad \tau_l = f_l \frac{\rho_l U_l^2}{2} \qquad \tau_i = f_i \frac{\rho_f (U_u - U_l)|U_u - U_l|}{2}$$

U is the in-situ velocity of the respective layer, ρ denotes the weight-averaged mixture density, f is the frictional factor and ρ_f denotes the density of the faster layer. In all cases investigated both upper and lower layers were in turbulent flow and the friction factors were calculated from $0.046Re^{-0.2}$, where Re is the Reynolds number of the respective layer. The Reynolds number in each layer is calculated based on the mixture fluid properties and velocity of that layer. The interfacial Reynolds number is calculated based on the faster phase properties while the interfacial frictional factor is the maximum between 0.014 and $0.046Re_i^{-0.2}$. To account for the drag reduction observed during fully dispersed flow (dispersion pressure gradient less than that of the single phases at the same mixture velocity) the following equation is used for calculating a modified friction factor (Rozentsvaig, 1982).

$$f_{DR} = \frac{f_{original}}{1 + n\varepsilon} \tag{7.8}$$

where $f_{original}$ is the original friction factor ($f_{original} = 0.046Re^{-0.2}$) and f_{DR} is the modified friction factor due to drag reduction, n is an empirical coefficient with a suggested value of 1.125 and ε is the fraction of the dispersed phase in the layer.

The mixture density in each layer is equal to the weight averaged densities of the two phases while for the calculation of the mixture viscosity Brinkman's (1952) correlation is used.

$$\rho_m = \varepsilon \cdot \rho_d + (1-\varepsilon) \cdot \rho_c \qquad (7.9)$$

$$\mu_m = \mu_c \cdot (1-\varepsilon)^{-2.5} \qquad (7.10)$$

7.3.4 HOMOGENEOUS MODEL

According to the homogeneous model the pressure gradient is found from:

$$\frac{dP}{dx} = \frac{2f\rho_m U_m^2}{D} \qquad (7.11)$$

where f is the friction factor ($0.046Re^{-0.2}$), ρ_m is a weight-averaged density (Equation (7.9)), U_m is the mixture velocity and D is the pipe diameter. Drag reduction is similarly accounted for by Rozentsvaig's equation (Equation (7.8)).

7.4. COMPARISON OF MODEL PREDICTIONS WITH EXPERIMENTAL DATA

The model predictions on the flow pattern that establishes in the pipe and on pressure drop for the different volume fractions at mixture velocities 3m/s and 4m/s are shown in Figure 7.2 against the experimental results. Experimentally it was found that the flow at 3m/s is fully dispersed with water as the continuous phase for input water fraction above 62% and with oil as the continuous phase for input water fraction below 28%. In between 28-62% input water fraction there is stratification of the flow with an oil continuous dispersed layer at the top of the pipe and a water continuous dispersed layer at the bottom, as found by the conductivity probe. According to the model, flow stratification occurs between 34-66% while below and above these fractions the mixture is oil and water

continuous respectively. Similarly, at 4m/s mixture velocity the experimental transitional region between the two types of dispersion was between 32-60% input water fraction while that predicted one was between 33-70% water fraction. The transitional regions for phase inversion in both experimental and predicted results are within close range.

It can also be seen from Figure 7.2 that the predicted pressure gradients, calculated from the two-fluid model in the transitional region and from the homogeneous model in the fully dispersed regions, are in good agreement with the experimental data. The experimental drag reduction is captured well by the model. The model is also able to predict the increase in pressure gradient after the mixture becomes fully oil continuous. Discrepancies between the experimental and predicted data appear at the oil continuous region and particularly for the lower mixture velocity. It is believed that the discrepancies are due to lack of uniform drop distribution as assumed in the homogeneous model, because under the effect of gravity water drops would tend to accumulate closer to the pipe bottom compared to the top. Dispersion inhomogeneity is expected to be more pronounced in the oil continuous dispersion compared to the water one because the oil viscosity is higher and the turbulent mixing will be less intense. In addition, it is more apparent at the low mixture velocity tested compared to the high one where again mixing is less intense.
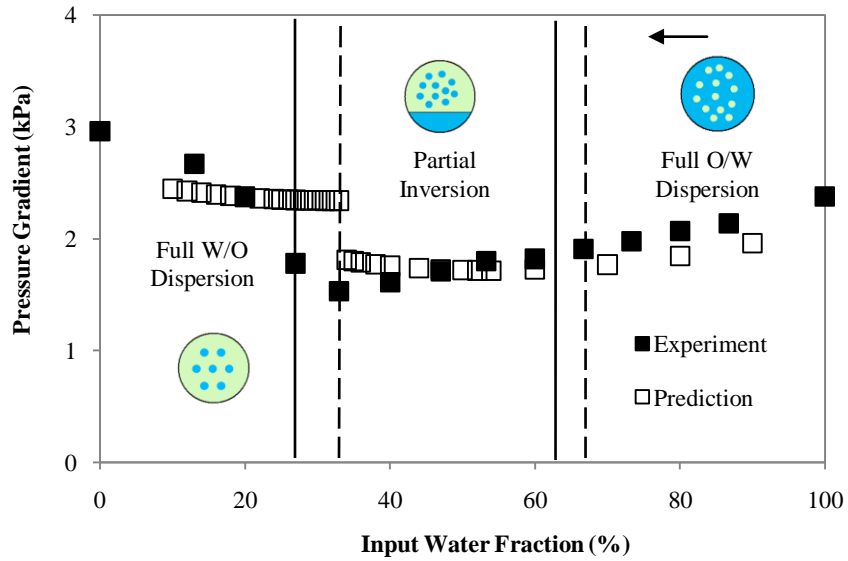
(a) 3m/s mixture velocity
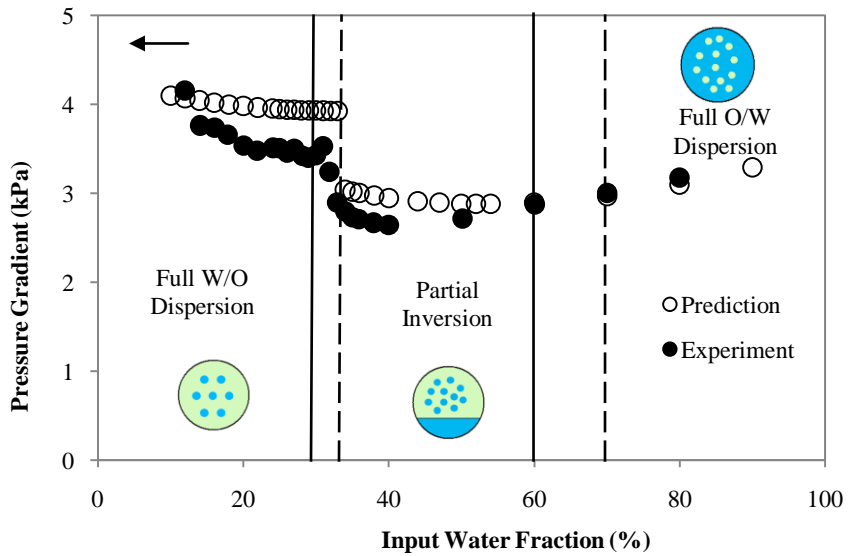
(b) 4m/s mixture velocity

Figure 7.2: Experimental and predicted pressure gradient at (a) 3m/s and (b) 4m/s predicted from two-fluid model. The lines represent the boundaries of the transitional region between water continuous and oil continuous fully dispersed flow, solid for experimental and dotted for predicted fractions. The arrow indicates the direction of the experiment.

7.5. CONCLUSION

Phase inversion during horizontal oil-water flow was investigated experimentally with the use of a local conductivity probe that identifies phase continuity. It was found that for the mixture velocities studied there was a region of flow stratification between the fully dispersed oil and water continuous flows. A methodology was suggested that predicted the range of volume fractions where flow was separated and the pressure gradient. This was based on the assumption of a two layer flow configuration, where the entrainment in each layer was calculated and the continuity of the layer was decided based on a phase inversion criterion. There was good agreement between the model predictions and the experimental data apart from the oil continuous dispersed flow at the low mixture velocity. This discrepancy was attributed to the inhomogeneous distribution of the dispersed water drops in the pipe cross section.

Chapter 8: CFD simulation of horizontal two-phase pipe flow

8.1 OVERVIEW

It was shown in the previous chapters that the spatial distribution of oil and water can be significantly changed according to the input phase fractions. This consequently leads to a change in flow regime (e.g. from a fully oil-in-water dispersion to a dual continuous mixture). In this chapter, computational fluid dynamics (CFD) simulations will be developed to predict phase distribution and flow characteristics for some of the conditions used in experiments in Chapter 4. The results will be compared against the experimental data. Use of CFD can provide information on flow characteristics that are not easy in many cases to measure experimentally and thus offer insight on flow behavior in combination with experiments. Validated CFD models can also be used for prediction without the need to resort to experiments. Various commercial CFD codes have been developed with multiphase flow capability (e.g. CFX, Fluent, Star-CD). In the current study, CFX will be used. The outcome of the chapter will aim to have a better insight on the effect of the different interphase force terms on the distribution of the mixture. The chapter is organised in the following sections: description of CFX software package (Section 8.2); description of the geometry and conditions simulated (Section 8.3); comparison between the simulation and the experimental results (Section 8.4). In the conclusions section, criteria in running a simulation of dense two-phase pipe flow will be presented (Section 8.5).

8.2 DESCRIPTION OF ANSYS CFX SOFTWARE PACKAGE

The chosen CFD software, Ansys CFX, by Ansys Inc., is a commercial computational fluid dynamics software package that has been widely used in solving a wide range of fluid flow problems. The code has been applied to a number of multiphase flow systems such as Krepper et al., 2005, Lucas et al., 2007 and Vallée et al., 2007. Many models

have been implemented to predict the various momentum transport terms allowing users to predict the respective influence by the phases especially during dispersed flow.

Ansys CFX consists of four main modules:

- Geometry construction and Meshing Module (via Ansys ICEM CFD)
- Pre-processing Module (CFX-Pre)
- Solver Module (CFX-Solver)
- Post processing Module (CFX-Post)

The construction of the geometry (i.e. the pipe) and the creation of a computational grid to define the points for computation (commonly known as meshing) are done via the Ansys ICEM CFD module. The geometry is constructed in scale with the actual construction process similar to the way a CAD package is used. Once the geometry is constructed, the structure is subsequently divided into a grid with specified grid points where the computation of the fluid motion is conducted. As the whole process is operated interactively via the Graphical User Interface (GUI), the mesh can easily be refined at specific locations (e.g. close to pipe wall) to improve predictions.

Through the CFX-Pre interface, the boundary and operation conditions of the simulation are defined on the meshed structure (e.g. fluid properties, input phase fraction, phase continuity, fluid velocities, wall roughness, and turbulence). A definition file with the specified conditions and the system geometry will then be saved for the subsequent calculations.

The solver module involves integrating the governing equations over the defined mesh grid points using the finite volume method. This permits the mass, momentum and energy terms to be conserved within each control volume. In Ansys CFX, a co-located (non-staggered) grid layout is used whereby the control volumes for the pressure and velocity transport equations are identical. Figure 8.1 presents the iterative method for solving the governing equations for both transient and steady-state simulations.
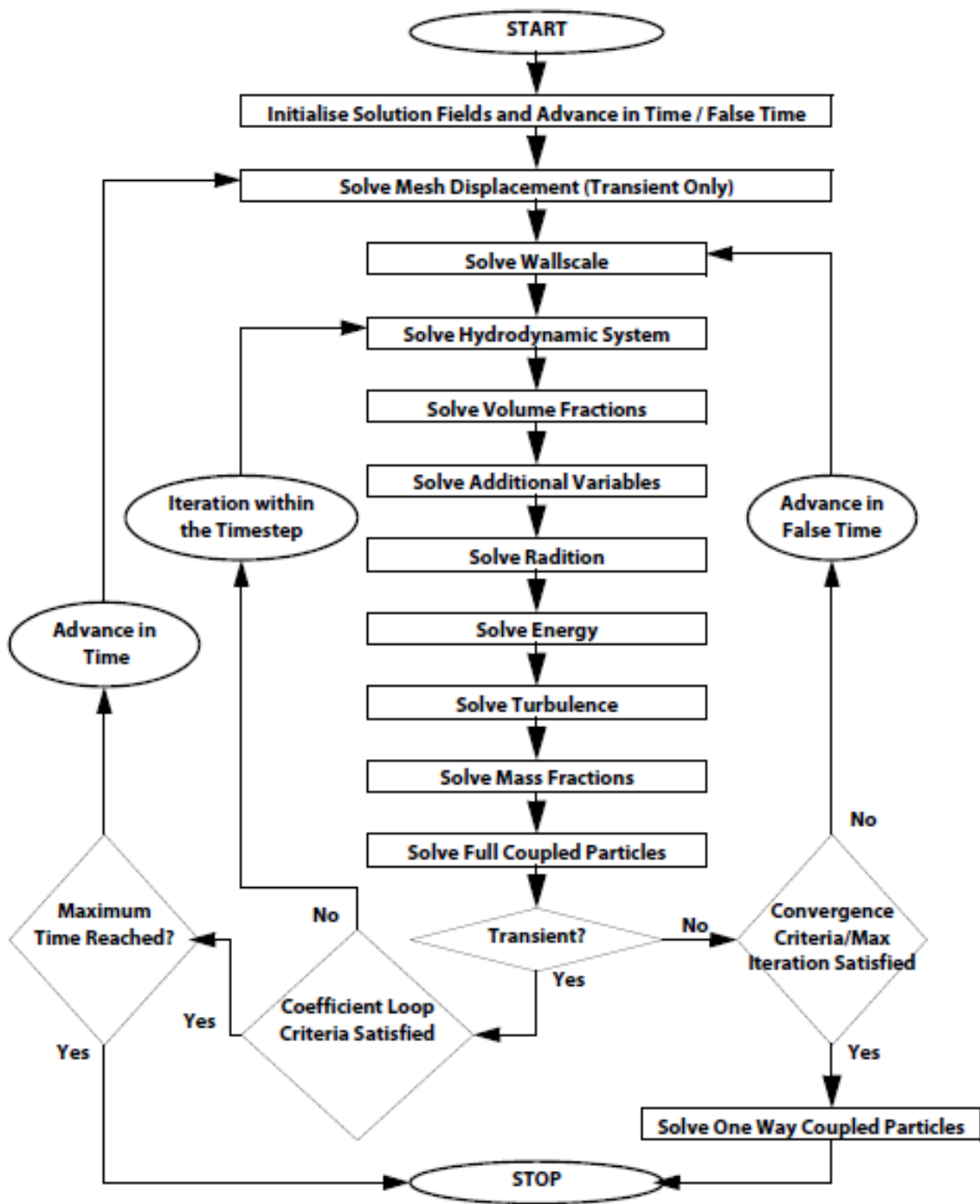
Figure 8.1: Schematic diagram on the iterative method for solving the conservation equations (Ansys CFX Manual).

The post processing module provides the environment to evaluate visually the results of the simulation through vector, contour or streamline plots. Raw numerical data can also be plotted into graphs (e.g. velocity profile, phase distribution profile). Numerical data can be exported (as a whole domain or within specific region) to Excel for further processing.

8.3 MODEL GEOMETRY AND SIMULATION CONDITIONS

Model Geometry

Due to the high computational effort for multiphase flow simulations, the geometry adopted in this chapter is 2-dimensional. Due to the limitation of Ansys CFX in true 2D simulation, the geometry used in this work is a rectangular slab with a width equal to 1% of the pipe diameter. The final geometry of the 2D pipe is 3.0m in length and 19mm in height (i.e. equivalent hydraulic diameter for a 38mm 3D pipe as according to Russell and Charles (1959) and Agtersloot et al. (1996)). A length of 3.0m was chosen as previous simulations for the same flow velocity showed that the flow is fully developed beyond 2.5m. At the inlet, a splitting plate is used and located at the centre of the pipe cross section with 100mm in length. This resembles the inlet configuration used in the experimental setup. The grid points along the radial direction are non-uniform with more grid points along the pipe wall. The shortest space between two grid points is 0.5mm and the longest space is approximately 0.75mm (at the centre of the pipe). Figure 8.2 presents the schematic of the pipe section with the boundaries used in the simulations. A total grid size of 183000 is used after a grid sensitivity study (see Appendix C) was conducted by adjusting the number of cells on the vertical height of the slab.
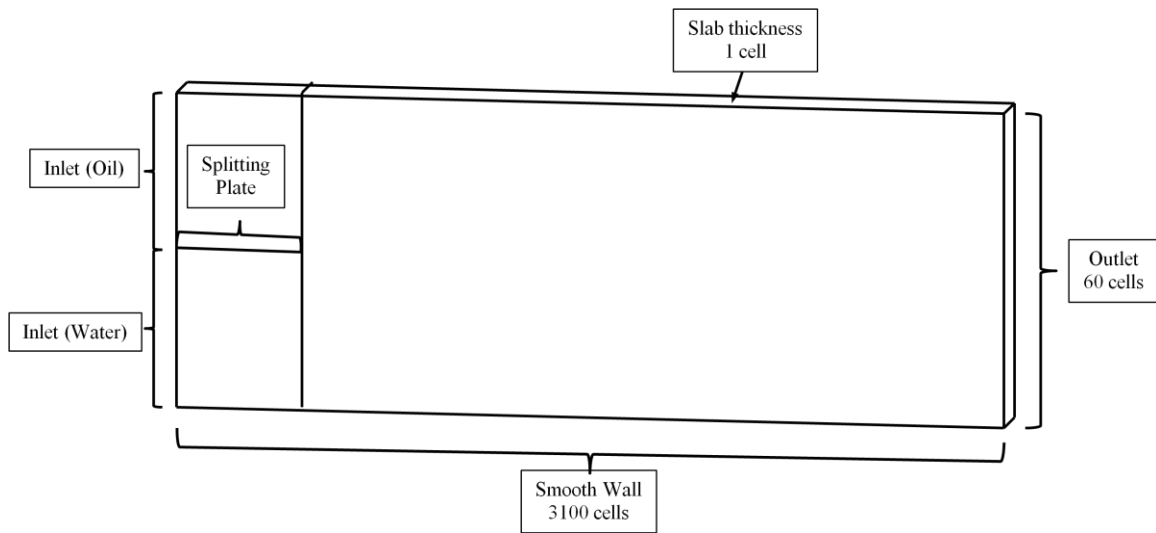
(a)
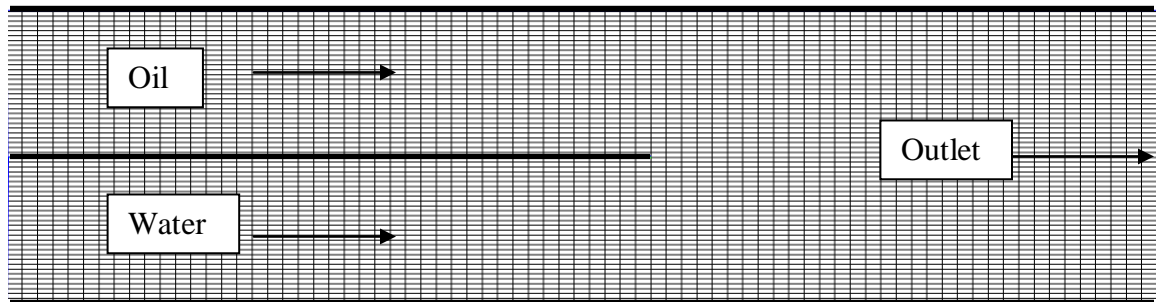
(b)

Figure 8.2: (a) Schematic diagram of the grid structure for the 2-D pipe section for the CFD simulations. (b) Part of the mesh of the 2-D pipe section with the thick lines representing the smooth walls in the simulation.

Boundary conditions

The following boundary conditions are used to define the solution domain:

1. Inlet: Two inlet sections are set up in the geometry separated by the plate – oil enters the pipe from the top section and water from the bottom. The fluid velocity is set at the boundary according to the relevant input phase fraction required. The inlet velocity is uniform over the inlet cross section and normal to the inlet boundary. Equation 8.1 presents the inlet velocity of phase k (i.e. either oil or water).

$$U_k = \alpha_k \times Q_m \times A_k \qquad\qquad\qquad (8.1)$$

where U is the input velocity, α is the phase fraction and A is the occupied area of the pipe by phase k. Q_m is the total volumetric flow rate of the mixture.

2. Outlet: A pressure specific boundary condition is used in the simulation. A reference pressure is set equal to the atmospheric pressure.

3. Wall: The wall boundary conditions include the wall surface of the pipe and the splitting plate at the inlet. No slip conditions are set at the walls. The wall is also assumed to be smooth.

4. Symmetry planes: The two side planes are assumed to be symmetric. This imposes constraints on the conditions of flow on either side of the plane.

Inlet and initial conditions

The properties of the two fluids introduced used in the simulation are the same as those used in the experiments (i.e. Exxsol D140 and water). The two fluids are regarded as incompressible with constant density. The inlet phase fraction is set by adjusting the flow velocities of the phases while maintaining the mixture velocity to be constant at 3m/s. As an initial condition, the decision for the phase continuity is based on the phase inversion point calculated in Chapter 6 (i.e. 34% water fraction). Below 34% water fraction, water is regarded as the dispersed phase and vice versa. The dispersed phase will be introduced

into the simulation inlet despite that it is flown as a single phase through the inlet section of the slab. The drop size for the dispersed phase is taken to be 1.0 mm (unless otherwise stated) as it has the highest frequency in a drop size distribution based on previous experiments (see Chapter 4). It is also assumed that the dispersed phase drops are spherical with uniform size for simplicity in this study. In addition, all simulations are run at a constant temperature and no thermal effect on the fluid will be considered.

The initial turbulence level is set by estimating the turbulence intensity. In all simulations, the intensity is taken to be 5% (i.e. the default value in CFX) which is also close to the calculated value for experimental results according to the following equation.

$$I = 0.16 \text{Re}_m^{-1/8} \tag{8.2}$$

From the initial turbulence intensity, the initial turbulent kinetic energy (k) and the energy dissipation (ε) can be found.

$$k = \frac{3}{2}\left(\frac{u_c}{\Phi_c}I\right)^2 \qquad \text{and} \qquad \varepsilon = C_\mu^{3/4}\frac{k^{3/2}}{L} \tag{8.3}$$

where L is the turbulent length scale that can be estimated by L=0.07D.

Convergence of solution

Convergence of the simulation is ensured by monitoring the residuals (i.e. the difference in solution between the current step and the previous step) of the solutions of the hydrodynamic equations. Convergence has been reached when the residuals are 10^{-6} or less. The time step for each iteration is set to at least below 0.002s. With the current setup, this ensures that the Courant number to be within 1 or less. This is suggested to be the optimal configuration for numerical calculation with the current grid size.

8.4 RESULTS AND DISCUSSION

CFD simulations were carried out for a mixture velocity of 3m/s and three input water fractions – 40% (dual continuous dispersion), 60% (dense O/W dispersion) and 80% (dilute O/W dispersion). Results on phase distribution will be compared against the experimental data (see Chapter 4). The phase distribution data along a vertical pipe diameter for these water fractions obtained by the electrical resistance tomographic (ERT) system are shown in Figure 8.3.

At 80% input water fraction, the dispersion is almost homogeneously distributed along the whole vertical diameter. With the decrease in water fraction to 60%, inhomogenity arises as the dispersed oil drops start accumulating at the core of the pipe. Further decrease in water fraction (40%) leads to dual continuous.
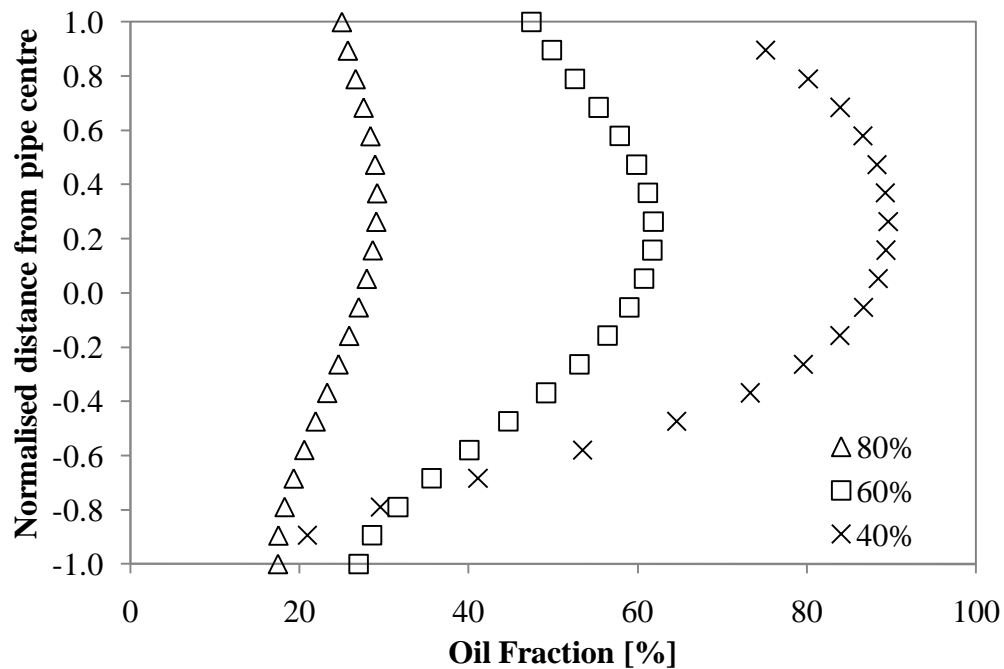
Figure 8.3: Experimental oil phase distribution along a vertical pipe diameter at a mixture velocity of 3m/s. Data is extracted from ERT measurements at 7m from the inlet where flow is fully developed.

Base case simulation

The following simulation is set as the base case before the effects of various parameters are explored in subsequent sections. A mixture velocity of 3m/s is used and an input water fraction of 80% is set while oil is the dispersed phase. The drop size is set at 1.0mm. No lift force is applied. The Lopez de Bertodano model is chosen for the turbulence dispersion and the Ishii Zuber model is chosen for the drag coefficient. Figure 8.4 presents the result of the base case against the experimental data.
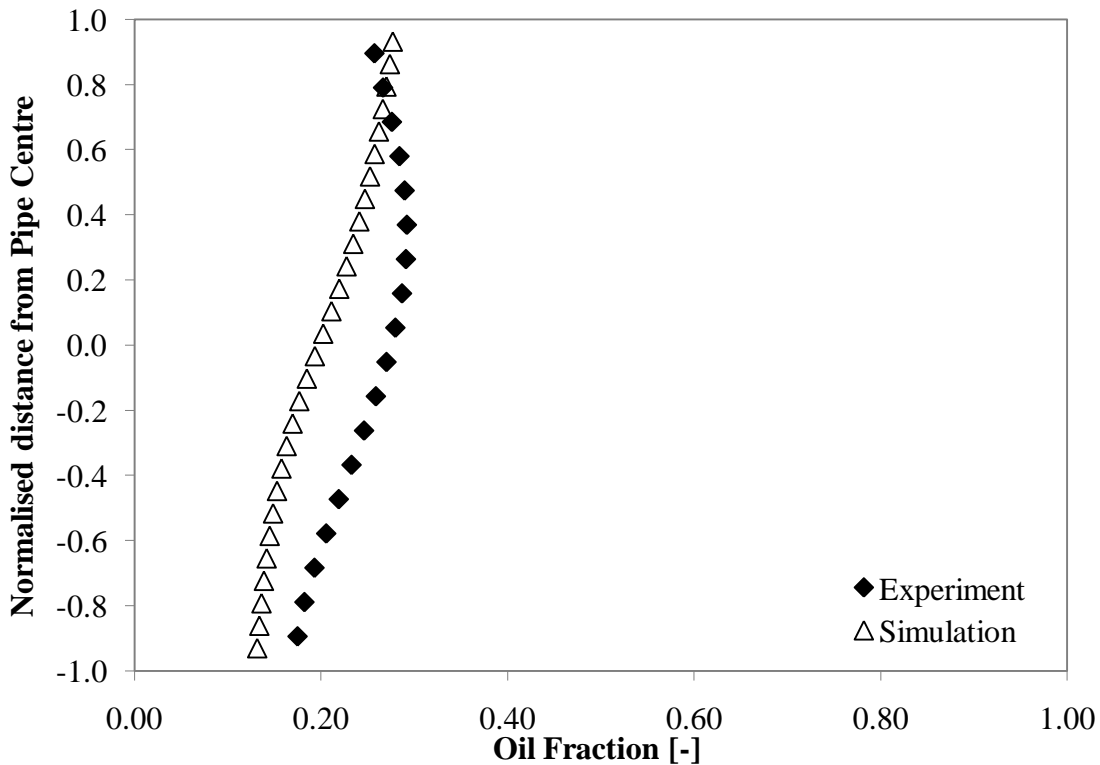
Figure 8.4: Comparison between simulated (base) and experimental (ERT) dispersed phase fractions at an input water fraction of 80% and mixture velocity of 3m/s. The simulated data is extracted at 3m from the inlet and the experimental data at 7m where the flow is fully developed.

As can be seen, the simulated phase distribution shows more stratification of the flow than the experimental one. There is a higher concentration of oil drops at the top of the pipe. In the following sections, the effect that the various interphase forces have on the phase distribution will be explored. As mentioned in Chapter 2 that the Ishii and Zuber

(1979) model is the only model for dense dispersion within CFX, no investigation on the effect of drag force will be conducted.

Effect of lift force coefficient on phase distribution

The effect of lift force on phase distribution will be investigated here. The lift force is proportional to the cross product between the relative velocity and the curl of the continuous phase velocity (Equation 2.37). A positive cross product will lead to an upward lift force by the continuous phase on the dispersed drops and a negative cross product will lead to a lift force in the opposite direction. Figure 8.5 presents the effect of the lift force coefficient on phase distribution. With a negative lift force coefficient (LF_-0.5), a stratification of the phases can be observed. However, the difference between the case with no lift force (LF_0) and a positive lift force coefficient (LF_0.5) is not significant except at the lower part of the pipe where some homogenization of the dispersion can be observed.
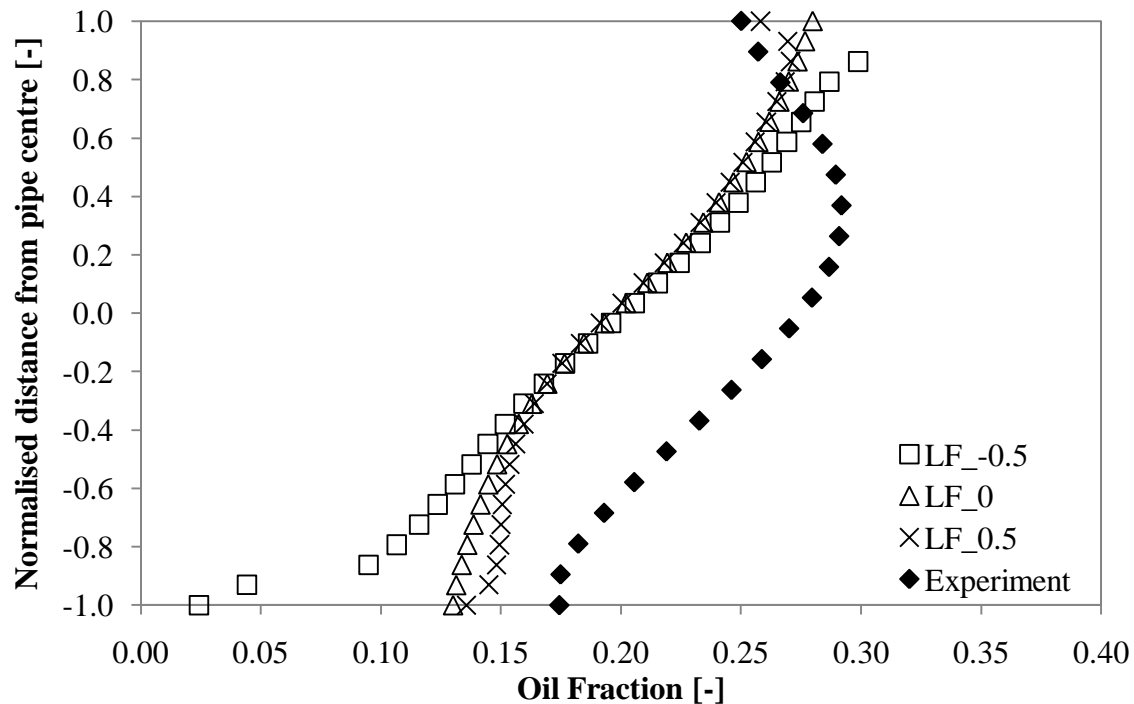
Figure 8.5: Effect of lift force on phase distribution at mixture velocity of 3m/s and input water fraction of 80%. LF in the legend represents the lift coefficient applied to Equation 2.37.

To further understand the impact of lift force on phase distribution, Figure 8.6 presents the lift force at different locations along the vertical diameter. The lift force is calculated from Equation 2.37 assuming that the continuous phase is flowing only in the axial direction. Other velocity components of the continuous phase are negligible and will not affect the curl U_c term. A negative lift force coefficient (LF_-0.5) leads to a positive lift force throughout the pipe. As a result, there is an upward force acting on the drops, which is stronger near the walls that explains the stratification of the phases seen in Figure 8.5. With a positive lift force coefficient (LF_0.5), the lift force is negative apart from the region close to the lower pipe wall. This implies an inward drive of the dispersed drops away from the bottom wall. The fact that the lift force acts on the opposite direction at the lower part of the pipe can explain the greater homogenization of the flow at this region (Figure 8.5).
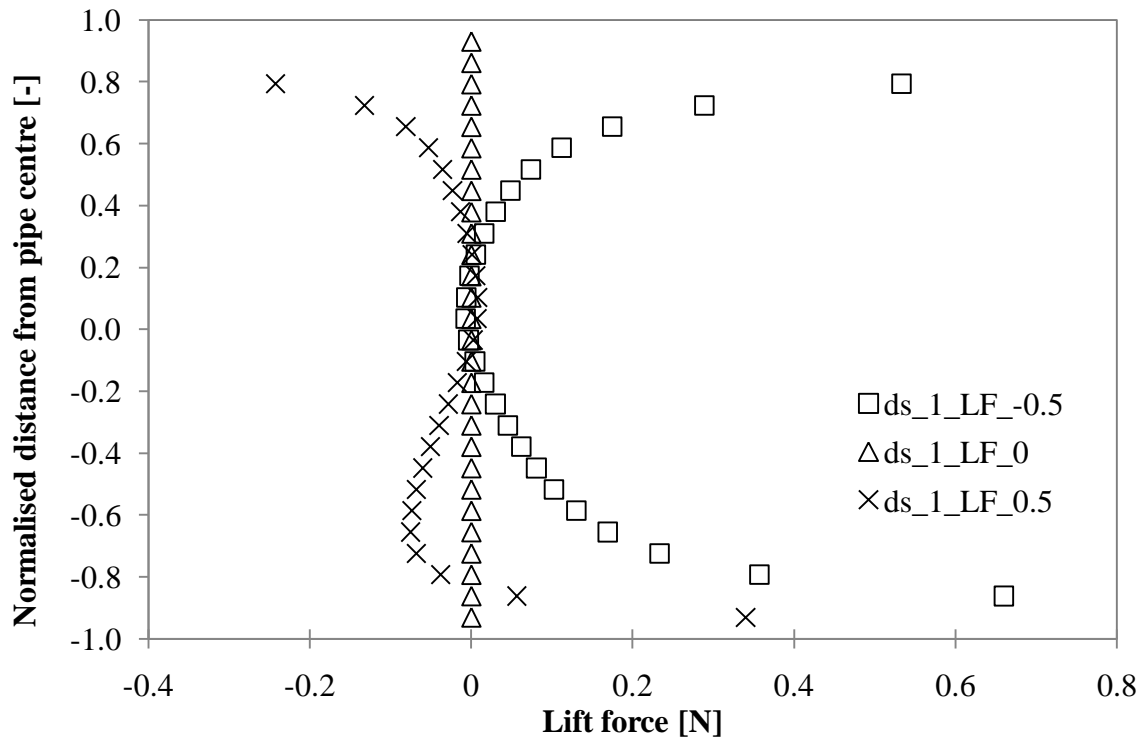
Figure 8.6: Effect of lift force coefficient on the lift force term at a mixture velocity of 3m/s and an input water fraction of 80%. ds represents the drop size in mm and LF represents the lift force coefficient applied to Equation 2.37.
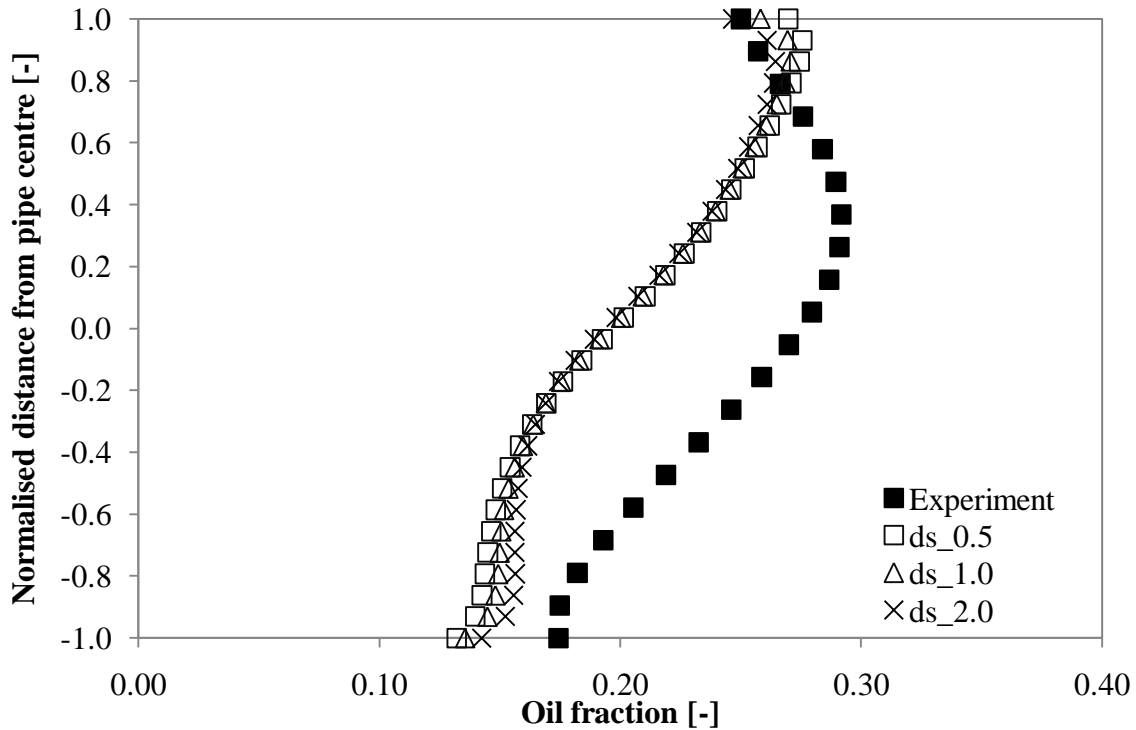
Figure 8.7: Effect of drop size on phase distribution at a constant lift coefficient (LF=0.5) at a mixture velocity of 3m/s and input water fraction of 80%. ds represents the drop size in mm.

According to Tomiyama et al., 1995, drop size is used to determine the Eötvös number and influence the lift force coefficient. The effect of drop size is presented in Figure 8.7. Interestingly, it is observed that in general the effect of drop size is small and that a dispersion with larger drop size (i.e. ds_2.0) is only slightly more homogenous than the small size dispersions. The effect is more distinctive at the regions between 0.4R<R<0.8R and -0.8R<R<-0.4R. No noticeable difference is seen at the centre of the pipe (i.e. -0.4R<R<0.4R). The lift force term is plotted for different drop sizes in Figure 8.8. It can be seen that the magnitude of lift force increases with drop size while its direction of motion remains the same for all three cases i.e. negative along the whole vertical pipe diameter apart from the region close to the bottom wall where it is positive. This implies that the lift force will be more effective in pushing the large oil drops away from the top wall where they would tend to concentrate due to gravity and help the homogenization of the mixture. However, the opposite direction of the force close to the

lower wall also prevents the drops from accumulating in that area. In addition, the volume of a large 2mm drop is 64 times the volume of a small 0.5mm drop. This implies that any movement of a large drop will lead to a much larger change in phase fraction compared to a small drop. The large change in dispersed phase fraction will likely lead to counteracting forces that are related to concentration gradient (such as the turbulent dispersion forces) tend to keep the dispersion mixed.
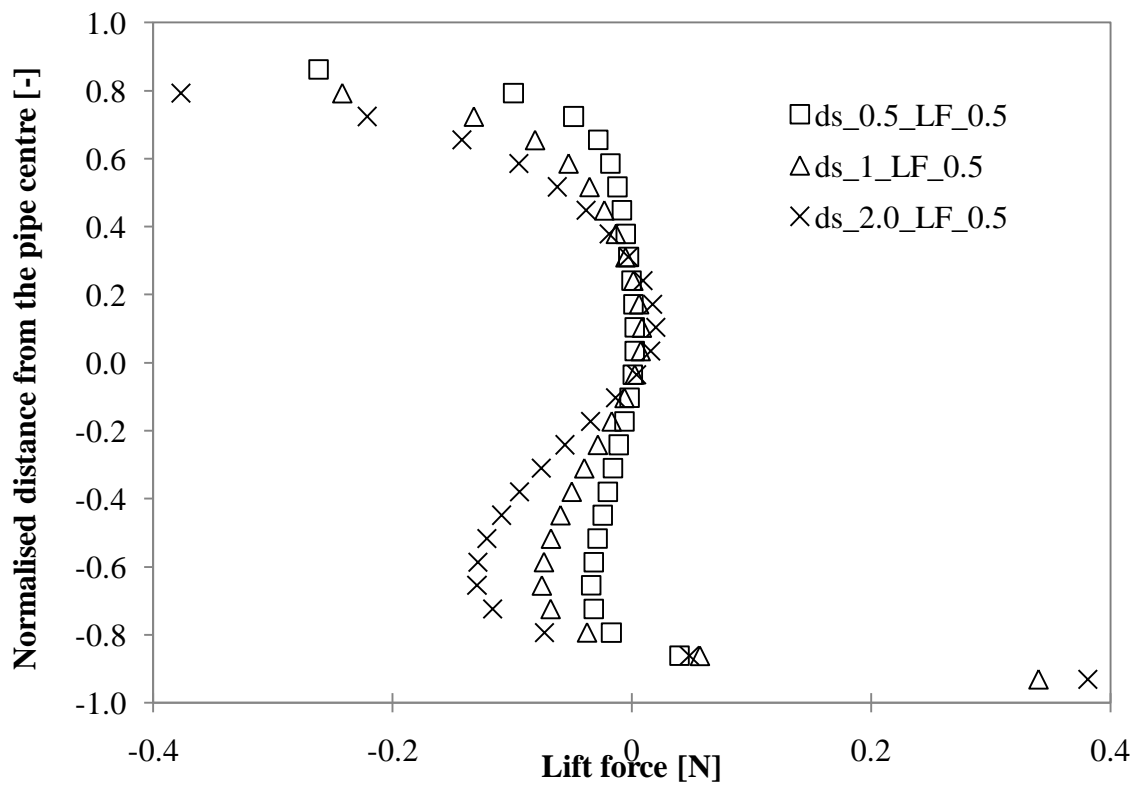
Figure 8.8: Effect of drop size on the lift force of a constant lift coefficient (LF=0.5) at a mixture velocity of 3m/s and input water fraction of 80%. ds represents the drop size in mm.

Effect of turbulent dispersion force on phase distribution

The changes in the lift force coefficient did not seem to homogenize the mixture to the extent that it matches the experimental data. The effect of the turbulent dispersion force is investigated as it can also act to homogenize the mixture.

Figure 8.9 presents the effect of increasing the turbulent dispersion force coefficient on the phase distribution for a lift coefficient of 0.5 which gave the best results compared to experimental data. As the coefficient is doubled, the distribution becomes more homogeneous which agrees better with the experimental result. It is possible that the deviations from the experimental data are due to the polydispersity of the real system compared to the single drop size used in the simulations.
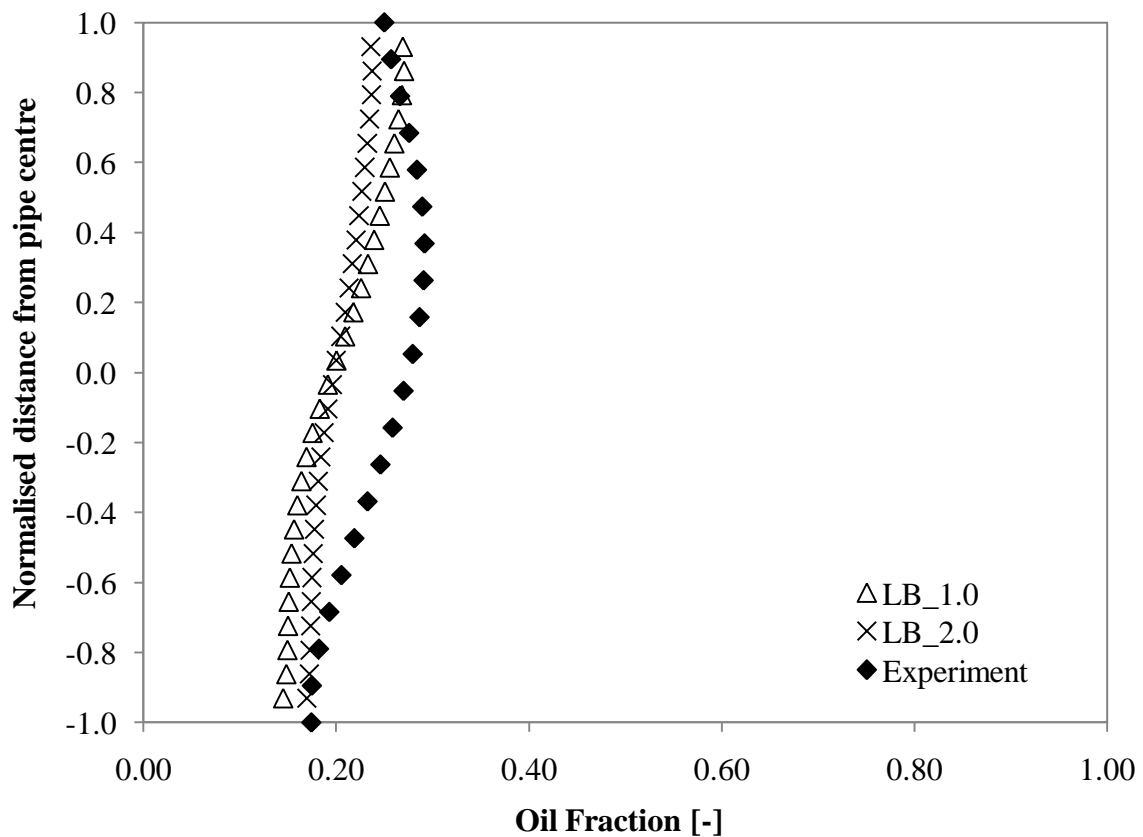
Figure 8.9: Effect of turbulent dispersion force coefficient on phase distribution at a mixture velocity of 3m/s and input water fraction of 80%. LB represents the coefficient for the Lopez de Bertodano model in Equation 2.39.

Effect of lift and turbulent dispersion force on dispersion of different phase fraction

The force coefficients that were found in previous sections to give the best agreement against the experimental data (i.e. lift force coefficient of 0.5 and turbulent dispersion force coefficient of 2) are used here to simulate the flow for different input water fractions at 40% and 60%. The results can be seen in Figure 8.10 against the experimental data. The polydispersity of the experimental mixture may have accounted for the deviation of the simulated results from experimental. Krepper et al. (2004) demonstrated that a bimodal distribution can have a different phase fraction profile compared to either mono-sized distribution.

The discrepancy is larger for 40% water fraction where the simulations show that the flow is highly stratified while the experiments reveal a large concentration of oil drops at the middle of the pipe. The high concentration of oil drops in the middle of the pipe resulted in experiments is due to phase inversion (see Section 4.4). However, no accounting of phase inversion is available in CFX. The available models in CFX are also limited in simulating a very dense dispersion coupled with the occurrence of phase inversion. As a result, the phase fraction distribution cannot be correctly modeled at this fraction.
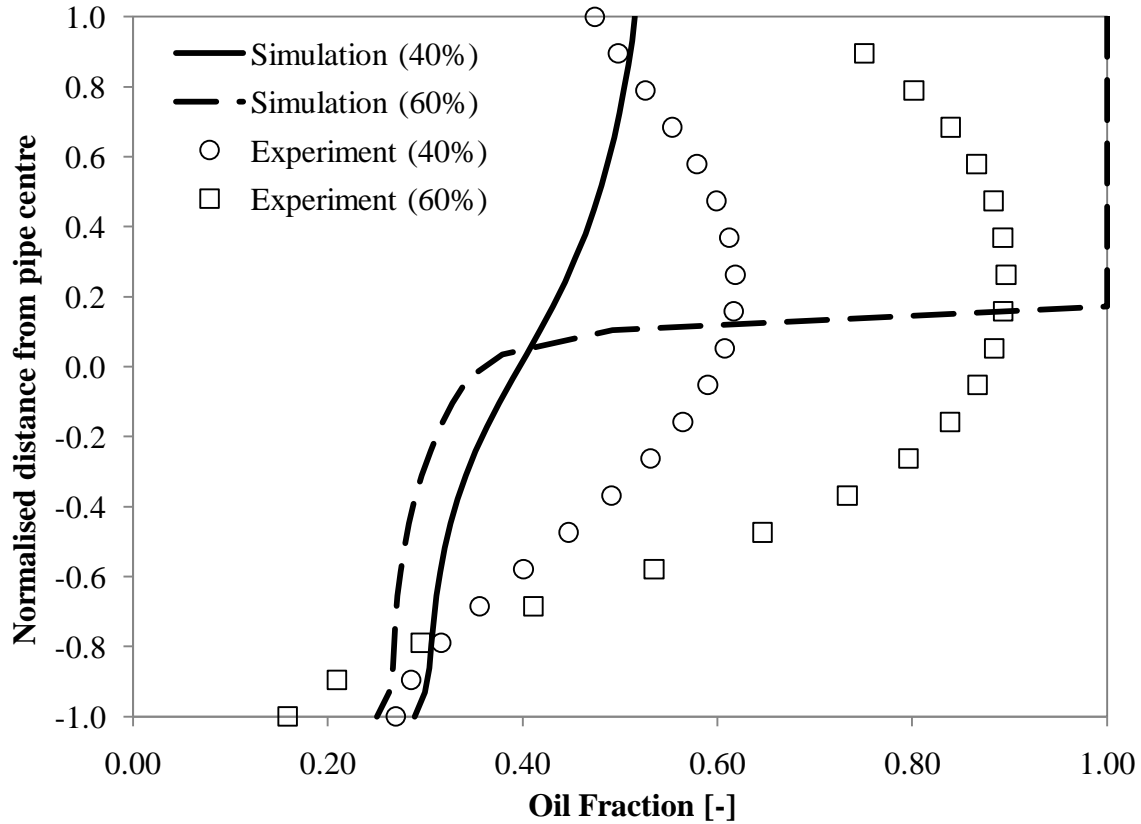
Figure 8.10: Comparison between experimental and simulated phase fraction distributions for 40% and 60% input water fractions at a mixture velocity of 3m/s and drop size of 1mm. Oil is set to be the dispersed phase in the simulation. The lift force coefficient is 0.5 and the turbulent dispersion force coefficient is 2.

8.5 CONCLUSION

It was shown in previous chapters that the dispersed drops migrate towards the centre of the pipe. The CFD simulations in this chapter offer some insight on the forces acting on the dispersed drops and on how they influence drop movements. Lift and turbulent dispersion forces can counteract the upward buoyancy acting on the dispersed oil drops. Lift force depends on the velocity profile of the continuous phase and the relative velocity of the dispersed phase. The turbulent dispersion force is driven by the concentration gradient and tends to homogenize the dispersion.

For dilute dispersions (80% water fraction), the results showed that a positive lift force coefficient (negative lift force) drives the drops away from the pipe wall, while the magnitude of the force is larger for larger dispersed drops. This suggests that the larger drops are more likely to be driven towards the centre of the pipe. An increase in the turbulent dispersion force was also shown to improve the homogenization of the mixture.

Higher dispersed phase fractions (i.e. 40% and 60% water fraction) were also simulated. There is a reasonable agreement between experimental and simulations for 20% and 40% dispersed fraction. This may be further improved if a drop size distribution is taken into account in the simulations (e.g. by using the MUSIG code) since it was found that the magnitudes of the forces depend on drop size. However, the simulations fail to predict the experimental results at 60%. This is probably because phase inversion has occurred experimentally at this fraction which cannot be accounted for in CFX.

Chapter 9: Conclusions and Recommendations

9.1 OVERVIEW

Phase inversion in a dispersed pipe flow has been investigated experimentally using various types of instrumentation. The effect of interfacial tension has also been studied as it has been the least understood fluid property influencing the inversion process. Based on the experimental outcome, prediction models have been developed to estimate the phase fraction at which inversion will occur as well as the pressure gradient during the change in phase fraction across an inversion process. Lastly, computational fluid dynamic simulations were studied to understand the interactions between the fluid phases using established models in Ansys CFX.

A summary of the main conclusions from the experimental and theoretical studies will be given in Section 9.2, followed by recommendations for future studies in Section 9.3.

9.2 CONCLUSIONS

9.2.1 CONCLUSIONS FROM EXPERIMENTAL STUDIES

The occurrence of phase inversion

- ERT tomography and other conductivity measurements reveal that the dispersion in the pipe undergoes a change in flow regime from a fully dispersed flow to a dual continuous flow during phase inversion. This transition is due to the gravitational stratification of the fluid phases.
- Phase inversion is also observed to be a gradual process across a range of phase fraction. The range of phase fraction during inversion is regarded as the *transitional region*. This transitional region narrows as the mixture velocity of the fluids increases.
- Phase inversion is observed to occur firstly at the centre of the pipe (if starting from an O/W dispersion). The accumulation of oil continuous dispersion will move towards the top of the pipe forming a dual continuous flow. Finally, phase

197

inversion is completed as the lower water layer is being dispersed into the oil phase. The reverse process will occur starting from a W/O dispersion.

- Pressure gradient along the pipe is found to be closely related to the distribution of the phases contacting with the pipe wall. Drag reduction is first observed as the dispersed phase is increased in an initial dispersion (e.g. O/W). As phase inversion occurs at the centre of the pipe, no significant increase in pressure gradient is observed. However, inversion will begin to increase once the oil continuous dispersion is in contact with the pipe wall and before phase inversion is completed across the pipe cross section.

- The introduction of a dispersed inlet produces an homogeneous dispersion and phase inversion occurs at a specific phase fraction (spontaneous inversion).

- Pressure gradient is found to differ with an homogeneous dispersion. Pressure gradient increases with the introduction of the dispersed phase. This is possibly because of the increase in effective mixture viscosity. There is a suddenly drop at 36% water fraction likely due to drop coalescence and deformation of the closely packed drops. Pressure gradient will fall to a minimum at the phase inversion point before it gradually increases beyond inversion.

- The drop size of the dispersion is found to fit well with a log-normal distribution. It is also found that the O/W dispersion has a smaller drop size than the W/O dispersion. The dispersed inlet also produces a narrower dispersion than the split inlet.

- The drop size distribution during phase inversion becomes wider due to the dominance of coalescence of the dispersed phase.

Effect of interfacial tension on phase inversion

- The addition of glycerol to the water phase has shown significant decrease in interfacial tension while it does not significantly affect the density and viscosity of the solution.

- The presence of glycerol does not appear to affect the inversion of the dispersed oil phase to become continuous. However, it retains the continuity of the water phase before the water phase is inverted at a lower water fraction.

198

- Changes on pressure gradient are similar to pure water system with an initial decrease due to drag reduction and increases again once the more viscous oil phase is in contact with the pipe wall.

- Drop size measurements in the middle of the pipe reveals that the size of oil drops before inversion is not significantly affected by the addition of glycerol while the size of the water drops after inversion is reduced. While larger water drops are expected with the addition of glycerol, the smaller size is possibly due to better coalescence of the water drop and the formation of the water layer at the bottom of the pipe.

9.2.2 CONCLUSIONS FROM THEORETICAL STUDIES

Prediction of phase inversion through fluid viscosities
- Pressure gradient was previously reported to reach a peak at phase inversion. The change of pressure gradient is primarily caused by the shear stress of the mixture with the pipe wall which is related to the fluid viscosities. A prediction model for phase inversion is thus proposed by assuming equal mixture viscosities of the oil and water continuous dispersions during inversion.

- Various correlations for mixture viscosities from literatures have been applied. Brinkman (1952)/Roscoe (1952) is found to have the best agreement with experimental data of oil/water systems of different oil viscosities regardless of its mixture velocity, dispersion initialisation and pipe material.

- The proposed model with Brinkman (1952)/Roscoe (1952) also agrees with experimental data from Yeh et al. (1964) and Arirachakaran et al. (1989).

- While the predicted phase fraction using the proposed model deviate from the inversion point from the homogeneous dispersed flow, the predicted phase fraction falls closely with the fraction at which maximum pressure gradient is observed. The deviation with the inversion point maybe due to drop deformation and coalescence which cannot be accounted by the applied mixture viscosity correlations.

Prediction of pressure gradient during phase inversion

- Based on the experimental observation during inversion, the change in flow regime (from fully dispersed flow to dual continuous flow) forms the basis for the development of a prediction model for pressure gradient during phase inversion.

- The main difference in these two flow regimes is the presence of the interfacial height during dual continuous flow. This is the selection criteria to choose between the two layered flow model and the homogeneous flow model for the prediction of pressure gradient. A phase inversion criteria is also set based on the developed prediction model from fluid viscosities.

- The proposed prediction model for pressure gradient agrees well with the experimental data at two different mixture velocities apart from the oil continuous dispersed flow at low mixture velocity. This discrepancy is attributed to the inhomogenous distribution of the dispersed water drops in the pipe cross section.

CFD simulation of horizontal two-phase pipe flow

- Lift force and turbulent dispersion force are found to be important to homogenize the dispersion. The magnitude of the lift force is larger for larger dispersed drops resulting larger drops move faster towards the centre of the pipe. An increase in the magnitude of the turbulent dispersion force will also improve the homogenization of the mixture.

- Good agreement of the CFD simulation with experimental results can be observed at lower dispersed phase fraction (i.e. 20% and 40%). However, the simulation fails to predict at 60% dispersed phase fraction. This is probably due to the limitation of the CFD code to account for the occurrence of phase inversion.

9.3 RECOMMENDATIONS

The experimental and theoretical investigations in this work help towards a better understanding on aspects affecting the phase inversion process in an horizontal pipe flow.

However, further work would be recommended to allow further depth into the existing investigations.

Recommendations for experimental studies

- At present, only one type of oil (Exxsol D140) is used throughout the whole study. With existing instrumentation for phase inversion detection, it will be beneficial to re-examine the oil/water system conducted by Angeli (1996) and Ioannou (2006) using Exxsol D80 and Marcol 52. This will have a broader understanding of the inversion process by having information about the changes in phase distribution of different fluid mixtures during inversion using the ERT tomography.

- Investigation conducted at a different pipe size will lead to significant difference in changes of flow regimes. Smaller pipes, for example, will lead to relatively higher influence of the surface wettability at the pipe wall on the fluid distribution. Thus, difference in the occurrence of phase inversion will be expected.

- More drop size results should be obtained at different location across the pipe cross section to have a better understanding of the local drop size distributions during inversion.

- Measurement technique should be developed to account for the drop size of the secondary droplets as the presence of secondary droplets can significantly affect the occurrence of phase inversion.

- Use of an oil-based surfactant to influence the interfacial tension and compare the similarity/difference in the occurrence of phase inversion with the current use of glycerol to the water phase.

Recommendations for theoretical studies

- Mixture viscosity correlations should be modified to include dispersion packing and drop size distribution of the dispersed phase. This aims to account for drop deformation and polydispersity in a dense dispersion.

- Pressure gradient prediction model should include the selection criteria from fully dispersed flow to annular flow (when local inversion begins to appear at the centre of the pipe) and from annular flow to dual continuous flow (due to the gravitational stratification of the two continuous dispersions (O/W and W/O)).

- Apply the pressure gradient prediction model to a wider range of experimental conditions. This can help in improving the robustness of the model by using more appropriate correlations.

- Apply Multiple Size Group (MUSIG) model in CFD simulation to account for the drop size distribution of the dispersed phase.

- 3-dimensional (3D) geometry for CFD simulation should be used to account for the lateral forces exerted from the sides of the pipe. This may improve the prediction of phase distribution between the dispersed and continuous phases in a pipe cross section.

Reference

- Agtersloot, R., Vuik, C., Zijlema, M. (1996). A comparison of two CFD packages and engineering formulae for fluid flow problems. Report 96-93, Faculty of Technical Mathematics and Informatics, Delft Univ. of Tech.

- Al-Sarkhi, Soleimani, A. (2004). Effect of drag reducing polymer on two-phase gas-liquid flows in a horizontal pipe. Trans IChemE., 82(Part A): 1583-1588.

- Al-Wahaibi, T. (2006). Investigations on the transition between stratified and non-stratified horizontal oil-water flows. Ph.D. thesis, UCL, UK.

- Al-Wahaibi, T., Smith, M., Angeli, P. (2007). Effect of drag-reducing polymers on horizontal oil-water flows. J. of Petroleum Sci. and Eng., 57(3-4): 334-346.

- Al-Wahaibi, T., Angeli, P. (2009). Predictive model of the entrained fraction in horizontal oil-water flows. Chem. Eng. Sci., 64(12): 2817-2825.

- Ansys CFX reference guide Version 11.0. . (2006).

- Angeli, P. (1996). Liquid-liquid dispersed flows in horizontal pipes. Ph.D. thesis, Imperial College London, UK.

- Angeli, P., Hewitt, G. F. (1998). Pressure gradient in horizontal liquid-liquid flows. Int. J. Multiphase Flow, 24(7): 1183-1203.

- Angeli, P., Hewitt, G. F. (2000). Flow structure in horizontal oil-water flow, Int. J. Multiphase Flow, 26: 1117-1140.

- Arashmid, M., Jeffreys, G. V. (1980). Analysis of phase inversion characteristics of liquid-liquid dispersions. AIChE J., 26(1): 51-55.

- Arirachakaran, S., Oglesby, K. D., Shoulam, O., Brill, J. P. (1989). An investigation of oil water flow phenomena in horizontal pipes, Paper SPE 18836, Society of Petroleum Engineers.

- Arrhenius (1887). Zeits. f. physic. Chemie 1: 285.

- Barnea, E., and Mizrahi, J. (1973). A generalized approach to the fluid dynamics of particulate systems: Part 1. General correlation for fluidization and sedimentation in solid multiparticle systems. Chem Eng. J., 5: 171-189.

- Batchelor, G. K. (1956). The theory of homogeneous turbulence. Cambridge University Press, Cambridge.

- Boussinesq, J. (1877). Théorie de l'Écoulement Tourbillant. Mem. Présentés par Divers Savants Acad. Sci. Inst. Fr., 23: 46-50.

- Brauner, N., Moalem Maron, D. (1989). Two-phase liquid–liquid stratified flow. Physico-Chem. Hydrodynam. 11, 487–506.

- Brauner, N. (2002). Liquid-liquid two-phase flow systems. Modelling and control of two-phase phenomena. V Bertola (Ed.), CISM Center, Udine, Italy.

- Brauner, N., Ullmann, A. (2002). Modelling of phase inversion phenomenon in two-phase pipe flow. Int. J. Multiphase Flow. 28(1): 55-68.

- Brinkman, H. C. (1952). The viscosity of concentrated suspensions and solutions. J. of Chem. Phy., 20(4): 571.

- Calabrese, R. V., Chang, T. P. K., Dang, P. T. (1986). Drop breakup in turbulent stirred-tank contactors. Part I: Effect of dispersed-phase viscosity. AIChE J., 32(4): 667-676.

- Chakrabarti, D. P., Das, G., Das, P. K. (2006). Transition from water continuous to oil continuous flow pattern. AIChE J., 52(11): 3668-3678.

- Chen, P., Dudukovic, M.P., Sanyal, J. (2005). Three-dimensional simulation of bubble column flows with bubble coalescence and breakup. AIChE J., 51: 696-712.

- Chesters, A. K. (1991). The modeling of coalescence processes in fluid-liquid dispersions: A review of current understanding. Chemical Engineering Research & Design, Transaction IChemE (Part A), 69: 259-270.

- Chesters, A. K., Issa, R. (2004). A framework for the modeling of phase inversion in liquid-liquid systems. Proc. 5th Int. Conf. on Multiphase Flow.

- Chiang, C. L., Chen, C. M. (1994). Characteristics of phase inversion in a turbine-type agitator. J. Chinese Inst. Chem. Eng., 25(6): 367-374.

- Choi, S. J., Schowalter, W. R. (1975). Rheological properties of nondilute suspensions of deformable particles. Physics of Fluids, 18(4): 420-427.

- Clarke, S. I., Sawistowski, H. (1978). Phase inversion of stirred liquid/liquid dispersions under mass transfer conditions, Trans. IChemE, 56: 50-55.

- Collins, S. B., Knudsen, J. G. (1970). Drop-size distributions produced by turbulent pipe flow of immiscible liquids. AIChE J., 16(6): 1072–1080.

- Coulaloglou, C. A., Tavlarides, L. L. (1977). Description of interactions processes in agitated liquid-liquid dispersions, Chem. Eng. Sci., 32: 1289-1297.

- Delnoij, E., Kuipers, J. A. M., van Swaaij, W. P. M. (1997). Computational fluid dynamics applied to gas-liquid contactors. Chem. Eng. Sci. 52: 3623-3638.

- Delichatsios, M.A., Probstein, R.F. (1976). The effect of coalescence on the average drop size in liquid–liquid dispersions. Ind. Eng. Chem. Fund., 14: 134-138.

- Deshphande, K. B., Kumar, S. (2003). A new characteristic of liquid-liquid systems-inversion holdup of intensely agitated dispersions. Chem. Eng. Sci., 58: 3829-3925.

- Drew, D.A (1983). Mathematical modeling of two phase flow. Annual review of fluid mechanics. 15: 261 – 291.

- Efthimiadu, I., Moore, I. P. T. (1994). Phase inversion of liquid-liquid dispersions produced between parallel shearing plates. Chem. Eng. Sci., 49: 1439-1449.

- Einstein, A. (1906). Eine neue bestimmung der moleküledimensionen, Annalen Phys., 19: 289-306.

- Einstein, A. (1911). Berichtigung zu meiner Arbeit: Eine neue bstimmung der moleküledimensionen. Annalen Phys., 34: 591-592.

- Elseth, G. (2001). An experimental study of oil/water flow in horizontal pipes. Ph.D. thesis, NTNU Trondheim, Norway.

- Fakhr-Din, S. M. (1973). Phase inversion and drop size measurements in agitated liquid-liquid systems. Ph. D. thesis, University of Manchester, UK.

- Furuse, H. (1972). Viscosity of concentrated solution. Jap. J. of Applied Physics, 11(10): 1537.

- Gillies, R. G., Sun, R., Shook, C. A. (2000). Laboratory investigation of inversion of heavy oil emulsion. Can. J. Chem. Eng., 78: 757-763.

- Groeneweg, F., Agterof, W. G. M., Jaeger, P., Janssen, J. J. M., Wieringa, J. A., Klahn, J. K. (1998). On the mechanism of the inversion of emulsions. Trans IChemE, 76 (Part A).

- Guilinger, T. R., Grislingas, A. K., Erga, O. (1988). Phase inversion behavior of water-kerosene dispersions. Ind. & Eng. Chem. Res., 27(6): 978-982.

- Guth, E. and Gold, O. (1938). On the hydrodynamical theory of the viscosity of suspensions. Phys. Rev. 53: 322.

- Guzhov, A. I., Grishin, A. D., Medredev, V. F., Medredeva, O. P. (1973). Emulsion formation during the flow of two liquids in a pipe. Neft Hhoz (in Russian). 8: 58-61.

- Hill, D. (1998). The computer simulation of dispersed two-phase flows. Ph.D. thesis, Imperial College London, UK.

- Hu, B. (2005). Experimental and theoretical investigation of phase inversion in liquid-liquid dispersions. Ph.D. thesis, UCL, UK.

- Hu, B., Matar, O.K., Hewitt, G.F., Angeli, P. (2005). Prediction of phase inversion in agitated vessels using a two-region model. Chem. Eng. Sci., 60: 3487-3495.

- Hu, B., Angeli, P. (2006). Phase inversion and associated phenomena in oil-water vertical pipeline flow. Can. J. Chem. Eng., 84(1): 94-107.

- Hu, B., Angeli, P., Matar, O. K., Lawrence, C. J., Hewitt, G. F. (2006). Evaluation of drop size distribution from chord length measurements. AIChE J., 52(3): 931-939.

- Ioannou, K., Bin, H., Matar, O. K., Hewitt, G. F., Angeli, P. (2004). Phase inversion in dispersed liquid-liquid pipe flows, Proc. 5th Int. Conf. on Multiphase Flow.

- Ioannou, K., Nydal, O. J., Angeli, P. (2005). Phase inversion in dispersed liquid-liquid flows. Experimental thermal and fluid science. 29(3): 331-339.

- Ioannou, K. (2006). Phase inversion phenomenon in horizontal dispersed oil/water pipeline flows. Ph.D. thesis, UCL, UK.

- Ishii, M., Zuber, N. (1979). Drag coefficient and relative velocity in bubbly, droplet or particulate flows. AIChE J., 25: 843-855.

- Karabelas, A. J. (1978). Droplet size spectra generated in turbulent pipe flow of dilute liquid/liquid dispersions. AIChE J., 24: 170–180.

- Kennard, E. H. (1938). Kinetic theory of gases. McGraw-Hill, New York.

- Krepper, E., Lucas, D., Prasser, H. M. (2005). On the modelling of bubbly flow in vertical pipes. Nuclear Engineering and Design, 235: 597–611.

- Krepper, E., Vanga, B. N. R., Zaruba, A., Prasser, H. M., Lopez de Bertodano, M. A. (2007). Experimental and numerical studies of void fraction distribution in rectangular bubble columns. Nuclear Engineering and Design. 237: 399-408.

- Krieger, I. M., and Dougherty, T. J., 1959. A mechanism for non-Newtonian flow in suspensions of rigid spheres. J. of Rheology, 3(1): 137-152.

- Krishna, R., van Baten, J. M. (1999). Rise characteristics of gas bubbles in a 2D rectangular column - VOF simulations vs Experiments. Int. Comm. in Heat and Mass Transfer. 26: 965-974.

- Kumar, A., Hartland, S. (1985). Gravity settling in Liquid/Liquid Dispersions. Can. J. Chem. Eng., 63: 368-376.

- Kumar, S., Kumar, R., Gandhi, K. S. (1991). Influence of the wetting characteristics of the impeller on phase inversion. Chem. Eng. Sci., 46(9): 2365-2367.

- Kumar, S. (1996). On phase inversion characteristics of stirred dispersions. Chem. Eng. Sci., 51(5): 831-834.

- Launder, B. E., Spalding, D. B. (1972). Lectures in mathematical models of turbulence. Academic Press, London, England.

- Leporcher, E., Delaytermoz, A., Renault, J. F., Gerbier, A., Burger, O. (2001). Deployment of multiphase pumps on a North Sea Field. Paper SPE 71536, Society of Petroleum Engineers.

- Levich, V. G. (1962). Physicochemical Hydrodynamics. Prentice-Hall, Englewood Cliffs, New Jersey.

- Liu, L. (2005). Optical and computational studies of liquid-liquid flows. Ph.D. thesis, University of London, UK.

- Liu, L., Matar, O.K., Perez de Ortiz, E.S., Hewitt, G.F. (2005). Experimental investigation of phase inversion in a stirred vessel using LIF. Chem. Eng. Sci., 60(1): 85-94.

- Liu, L., Matar, O., Lawrence, C., Hewitt, G. (2006). Laser-induced fluorescence (LIF) studies of liquid-liquid flows. Part I: Flow structures and phase inversion. Chem. Eng. Sci., 61: 4007-4021.

- Liu, S., Li, D. (1999). Drop coalescence in turbulent dispersions. Chem. Eng. Sci., 54(23): 5667–5675.

- Lopez de Bertodano, M., (1991). Turbulent Bubbly Two Phase Flow in a Triangular Duct. Ph. D. Thesis, Rensselaer Polytechnic Institute, New York.

- Lopez de Bertodano, M., (1998). Two fluid model for two-phase turbulent jet. Nucl. Eng. Des., 179: 65 - 74.

- Lovick, J. (2004). Horizontal oil-water flows in the dual continuous flow regime. Ph.D. thesis, UCL, UK.

- Lucas, D., Krepper, E., Prasser, H. M. (2007). Use of models for lift, wall and turbulent dispersion forces acting on bubbles for poly-disperse flows. Chem. Eng. Sci., 62(15): 4146 – 4157.

- Luhning, R. W., Sawistowski, H. (1971). Phase inversion in stirred liquid-liquid systems. Proceeding of the International Solvent Extraction Conference, The Hague, 873-887, Society of Chemical Industry, London.

- Luo, H., Svendsen, H. F. (1996). Theoretical model for drop and bubble breakup in turbulent dispersions. AIChE J., 42(5): 1225-1233.

- Luo, Y. S., Chen, T. K., Cai, J. Y. (1997). Frictional pressure loss and phase inversion point for oil-water emulsion in vertical tube. Int. Symp on multiphase fluid, non Newtonian fluid & physicochemical fluid flows. 3: 53-58.

- Martinez, A. E., Intevep, S. A., Arirachakaran, S., Shoham, O., Brill, J. P. (1988). Prediction of dispersion viscosity of oil/water mixture flow in horizontal pipes. Paper SPE 18221: 427-438, Society of Petroleum Engineers.

- McClarey, M., Mansoori, G. (1978). Factors affecting the phase inversion of dispersed immiscible liquid-liquid mixtures. AIChE J., 74: 134-139.

- Mooney, M. (1951). The viscosity of a concentrated suspension of spherical particles. J. Colloid Sci, 6: 162.

- Moraga, J. F., Larreteguy, A. E., Drew, D. A., Lahey, R. T. (2003). Assessment of turbulent dispersion models for bubbly flows in the low Stokes number limit. Int. J. multiphase flow, 29: 655.

- Nädler, M., Mewes, D. (1995). Intermittent three-phase flow of oil, water and gas in horizontal pipes. Proc. 5th Int. Offshore and Polar Eng. Conf.

- Nädler, M., Mewes, D. (1997). Flow induced emulsification in the flow of two immiscible liquids in horizontal pipes. Int. J. Multiphase Flow, 23(1): 55-68.

- Ngan, K. H., Linnenberg, S., Al-Wahaibi, T., Angeli, P. (2007). Effect of Drag Reducing Polymers on Oil-Water Flows. Int. Conf. on Multiphase Flow, Germany.

- Ngan, K.H., Ioannou, K., Rhyne, L.D., Wang, W., Angeli, P. (2009). A methodology for predicting phase inversion during liquid-liquid dispersed pipeline flow. Chem. Eng. Res. Des., 87:318-324.

- Norato, M. A., Tsouris, C., Tavlarides, L. L. (1998). Phase inversion studies in liquid-liquid dispersions, Can. J. Chem. Eng., 76: 486-494.

- Noui-Mehidi, M., Wu, J., Zhu, Y. (2004). A few new findings on phase inversion in a liquid/liquid system. AIChE J., 50: 3281-3283.

- Oglesby, K. D. (1979) An experimental study on the effects of oil viscosity, mixture velocity, and water fraction on horizontal oil-water flow. M.S. thesis, University of Tulsa, Oklahoma.

- Pacek, A. W., Moore, I. P. T., Nienow, A. W. (1994). Video technique for measuring dynamics of liquid-liquid dispersion during phase inversion. AIChE J., 40(12): 1940-1949.

- Pacek, A. W., Nienow, A. W. (1995). A problem for the description of turbulent dispersed liquid-liquid systems. Int. J. Multiphase Flow, 21(2): 323–328.

- Pal, R., Rhodes, E. (1989). Viscosity/Concentration relationships for emulsions. J. Rheol., 33(7): 1021-1045.

- Pal, R. (1993). Pipeline flow of unstable and surfactant-stabilized emulsions. AIChE J., 39 (11): 1754-1764.

- Pal, R. (2001). Single-parameter and two-parameter rheological equations of state for nondilute emulsions, Ind. Eng. Chem. Res., 40: 5666-5674.

- Perry, R. H., Green, D. W. (1997). Perry's Chemical Engineers' Handbook. 7th Ed. McGraw-Hill, New York.

- Pettersen, B.H., Langsholt, M., and Ødegård, J. (2001). Pressure drop and wall wetting: the effect of pipe wall material in multiphase flow. Proc. 10th International Conference of Multiphase Flow, Cannes, France.

- Phan-Thein, N., Pham, D. C. (1997). Differential multiphase models for polydispersed suspensions and particulate solids. J. Non-Newtonian Fluid Mech., 72: 305.

- Piela, K., Delfos, R., Ooms, G., Westerweel, J., Oliemans, R.V.A., Mudde, R.F. (2006). Experimental investigation of phase inversion in an oil-water flow through a horizontal pipe loop. Int. J. Multiphase Flow, 32(9): 1087-1099.

- Piela, K., Delfos, R., Ooms, G., Westerweel, J., Oliemans, R.V.A. (2008). On the phase inversion process in an oil-water pipe flow. Int. J. Multiphase Flow, 34(7): 665-677.

- Prince, M., Blanch, H. W. (1990). Bubble coalescence and break-up in air-sparged bubble columns. AIChE J., 36(10): 1485–1499.

- Quinn, J. A., Sigloh, D. B. (1963). Phase inversion in the mixing of immiscible liquids. Can. J. Chem. Eng., 41: 15-18.

- Ranade, V. (2002). Computational flow modeling for chemical reactor engineering. Process Systems Engineering Vol. 5. Academic Press, California.

- Rodger, W. A., Trice, Jr., V. G., Rushton, J. H. (1956). The effect of fluid motion on interfacial area dispersions. Chem. Eng. Prog., 52(12): 515-520.

- Rodriguez, O. M. H., Bannwart, A. C. (2006). Analytical model for interfacial waves in vertical core flow. J. of Petroleum Sci. and Eng., 54 (3-4).

- Roscoe, R. (1952). The viscosity of suspensions of rigid spheres. British journal of applied physics, 267-269.

- Rotta, J. C. (1972). Turbulente Strömungen. B. G. Teubner, Stuttgart.

- Rozentsvaig, A. K. (1982). Turublent pipe flow of concentrated emulsions with a nonequilibrium disperse phase. Inzh.-Fiz. Zh., 42(3), 366-372.

- Rusche, H., Issa, R. I. (2000). The Effect on voidage on the drag force on particles in dispersed two-phase flow. Japanese-European two phase flow meeting, Tsukuba, Japan.

- Rusche, H. (2002). Computational fluid dynamics of dispersed two-phase flows at high phase fractions. Ph.D. thesis, Imperial College London, UK.

- Russell, T., Hodgsen, G., Govier, G. (1959). Horizontal pipeline flow of mixtures of oil and water. Can. J. Chem. Eng., 37: 9-17.

- Russell, T.W.F., Charles, M.E., (1959). The effect of the less viscous liquid in the laminar flow of two immiscible liquids. Can. J. Chem. Eng. 37: 18–24.

- Saffman, P. G., Turner, J. S. (1956). On the collision of drops in turbulent clouds. J. Fluid Mech., 1: 16-30.

- Schiller, L., Naumann, Z. (1933). Über die grundlegenden Berechungen bei der Schwerkraftbereitung. Z. Ver. Deutsch. Ing., 77: 318 -320.

- Schwartzberg, H.G., Treybal, R. E. (1968). Fluid and particle motion in turbulent stirred tanks. Ind. & Eng. Chem. Res. Fund., 7: 1-6.

- Seklker, A. H., Sleicher, Jr., C. A. (1965). Factors affecting which phase will disperse when immiscible liquids are stirred together. Can. J. Chem. Eng., 43:298-301.

- Simmons, M. J. H., Azzopardi, B. J. (2001). Drop size distributions in dispersed liquid-liquid pipe flow. Int. J. Multiphase Flow, 27: 843-859.

- Smith, D. H., Lim, K. (1990). An experimental test of catastrophe and critical-scaling theories of emulsion inversion. Langmuir, 6: 1071-1077.

- Soleimani, A., Lawrence, C. J., Hewitt, G. F. (1997). Effect of mixers on flow pattern and pressure drop on horizontal oil-water pipe flow. Int. Symp. on liquid-liquid two phase flow and transportation phenomena, Turkey.

- Soleimani, A. (1999). Phase distribution and associated phenomena in oil-water flows in horizontal tubes. Ph.D. thesis, Imperial College London, UK.

- Soleimani, A., Lawrence, C. J., Hewitt, G. F. (2000). Spatial distribution of oil and water in horizontal pipe flow. SPE Journal, 5(4): 394-401.

- Sommerfelds, M., Wachem, B.V., Oliemans, R.V.A (2008). Best practice guidelines for computational turbulence dispersed multiphase flows. Seminar presentation, SIAMUF, Chalmers University.

- Sovová, H. (1981). Breakage and coalescence of drops in a batched stirred vessel – II. Comparison of model and experiments. Chem. Eng. Sci., 36(9): 1567-1573.

- Stover, R. L., Tobás, C. W., Denn, M. M. (1997). Bubble coalescence dynamics. AIChE J., 43: 2385-2392.

- Taylor, G. I. (1932). The viscosity of a fluid containing small drops of another fluid. Proc. R. Soc., 138: 41.

- Thomas, D. G. (1965). Transport characteristics of suspensions: VII. A note on the viscosity of Newtonian suspensions of uniform spherical particles. J. Colloid Sci., 20: 267-277.

- Tidhar, M., Merchuk, J. C., Sembira, A. N., Wolf, D. (1986). Characteristics of a motionless mixer for dispersion of immiscible fluids- Phase inversion of liquid-liquid systems. Chem. Eng. Sci., 41(3): 457-462.

- Tomiyama, A., Zun, I., Kanami, N., Sakaguchi, T. (1995). Effects of Eötvös number and dimensionless liquid volumetric flux on lateral motion of a bubble in a laminar duct flow. Adv. Multiphase Flow, 3-15.

- Trallero, J. L. (1995). Oil water flow patterns in horizontal pipes. Ph.D. thesis, University of Tulsa, Oklahoma.

- Treybal, R. E. (1963). Liquid Extraction. 2nd Edition, McGraw-Hill, New York.

- Tsouris, C., Tavlarides, L. L. (1994). Breakup and coalescence models for drops in turbulent dispersion. AIChE J., 40(3): 395-406.

- Tyrode, E., Allouche, J., Choplin, L., Salager, J. (2005). Emulsion catastrophic inversion from abnormal to normal morphology. 4. Following the emulsion viscosity during three inversion protocols and extending the critical dispersed-phase concept. Ind. & Eng. Chem. Res., 44: 67-74.

- Vaessen, G. E. J., Visschers, M., Stein, H. N. (1996). Predicting catastrophic phase inversion on the basis of droplet coalescence kinetics. Langmuir, 12: 875-882.

- Valentas, K.J., Bilous, O., Amundson, N.R. (1966). Analysis of breakage in dispersed phase systems. Ind. Eng. Chem. Fundamentals, 5: 271–279.

- Valle, A., Utvik, O. H. (1997). Pressure drop, flow pattern and slip for two phase crude oil-water flow. Int. Symp. on liquid-liquid two phase flow and transportation phenomena, Turkey

- Vallée, C., Höhne, T., Prasser, H.M., Sühnel, T. (2007). Experimental investigation and CFD simulation of slug flow in horizontal channels. Forschungszentrum Dresden-Rossendorf, Report FZD-485, Dresden, Germany.

- Vand, V. (1948). Viscosity of solutions and suspensions. I – Theory. J Phys Coll Chem, 52: 277–299.

- Vielma, M., Atmaca, S., Sarica, C., Zhang, H. (2008). Characterization of Oil/Water Flows in Horizontal Pipes. Paper SPE 109591, Society of Petroleum Engineers.

- Wang, W., Gong, J., Ngan, K. H., Angeli, P. (2009). Effect of glycerol on the binary coalescence of water drops in stagnant oil phase, Chem. Eng. Res. Des., 87(12): 1640-1648.

- Wilcox, D.C. (1986) Turbulence Modelling for CFD. DCW Industrie.

- Yakhot, V., Smith, L.M. (1992). The renormalization group, the ε-expansion and the derivation of turbulence models. J. Sci. Comp, 7: 35-61.

- Yaron, I., Gal-Or, B. (1972). On viscous flow and effective viscosity of concentrated suspensions and emulsions – Effect of particle concentration and surfactant impurities. Rheologica Acta, Band 11, Heft 3/4: 245 – 252.

- Yeh, G. C., Haynie Jr., F. H., Moses, R. A. (1964). Phase-volume relationship at the point of phase inversion in liquid dispersions. AIChE J., 10(2): 260-265.

- Yeo, L. Y., Matar, O. K., Perez de Ortiz, E. S., Hewitt, G. F. (2000). Phase inversion and associated phenomena. Multiphase Science and Technology, 12(1): 51-116.

- Yeo, L. Y. (2002). Modelling of phase inversion and associated phenomena in liquid-liquid systems. Ph.D. thesis, University of London, UK.

Appendix A – Chord Length Measurement during Phase Inversion

Chord length distribution during the phase inversion is measured at various vertical locations across the pipe cross section using a dual impedance probe discussed in Section 4.8. To supplement the data in Figure 4.13, the chord length distribution between 40% and 54% water fraction are presented below.

(a) 14mm

(b) 20mm

(c) 26mm

(d) 32mm
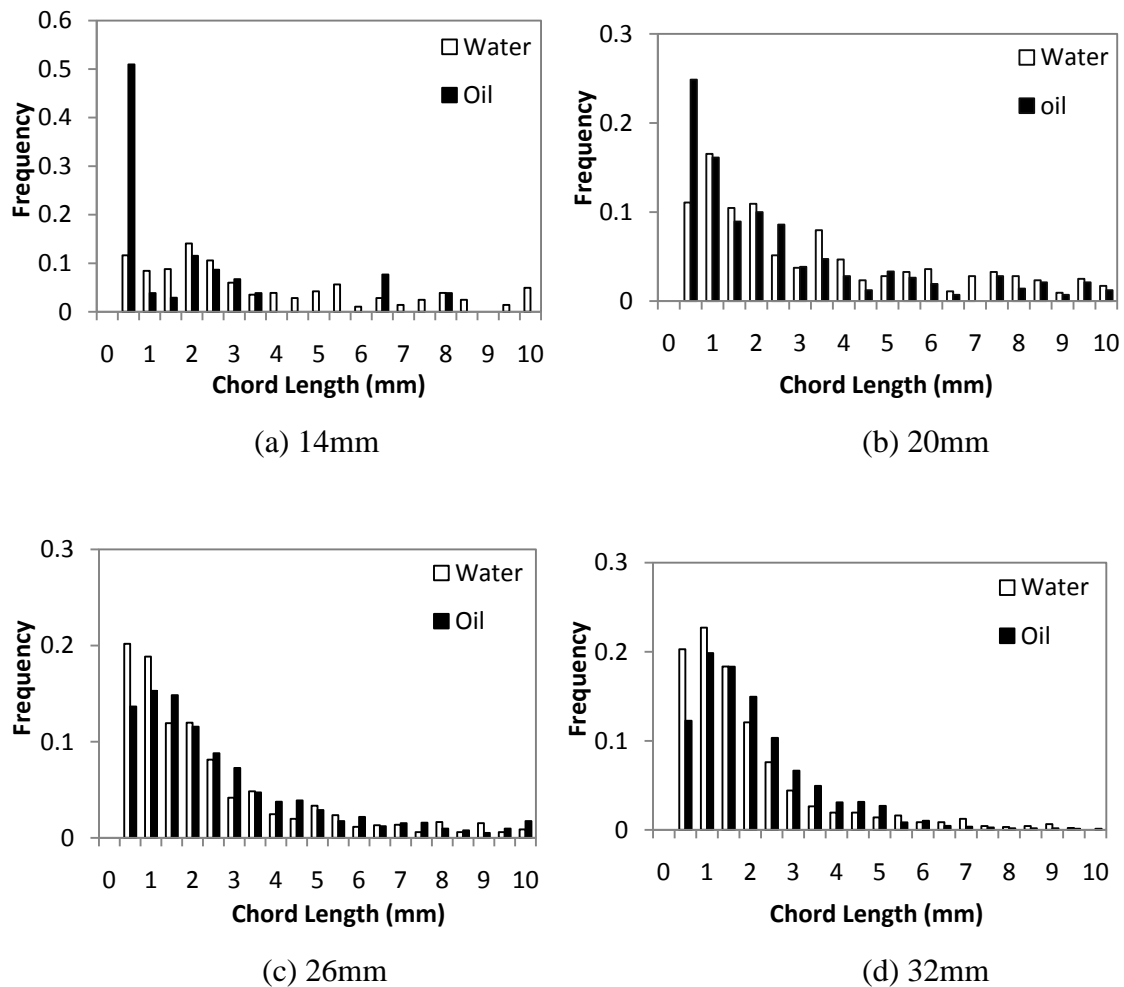
Figure A-1: Chord length distribution of oil drops in water (54% water fraction) at various locations from the top wall of the pipe with a mixture velocity of 3m/s. The distributions of the two inversion routes are given – starting from a O/W dispersion (□) and from a W/O dispersion (■).
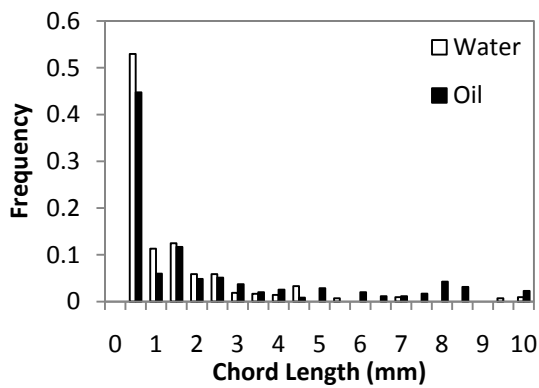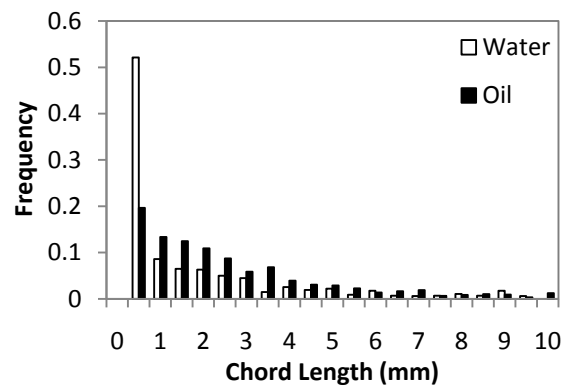
(a) 20mm   (b) 26mm
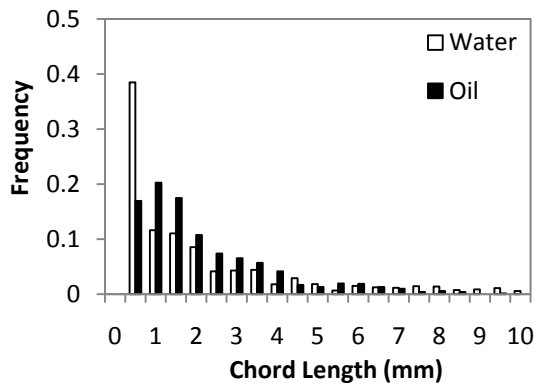
(c) 32mm

Figure A-2: Chord length distribution of oil drops in water (50% water fraction) at various locations from the top wall of the pipe with a mixture velocity of 3m/s. The distributions of the two inversion routes are given – starting from a O/W dispersion (□) and from a W/O dispersion (■).

(a) 26mm   (b) 32mm
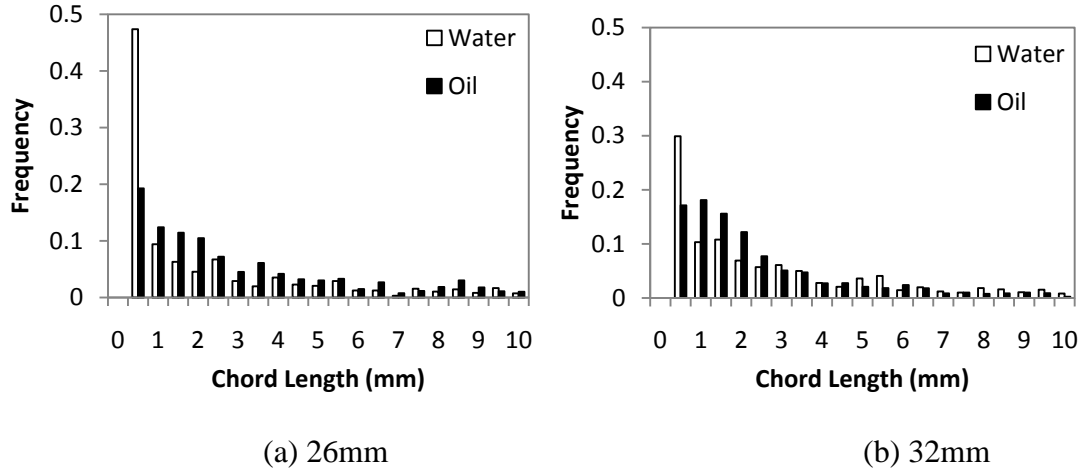
Figure A-3: Chord length distribution of oil drops in water (40% water fraction) at various locations from the top wall of the pipe with a mixture velocity of 3m/s. The distributions of the two inversion routes are given – starting from a O/W dispersion (□) and from a W/O dispersion (■).

From the above figures, only detectable chord length distributions are presented. At 54% water fraction, it can be observed that the distribution becomes wider at 20mm (i.e. centre of pipe) where it is previously found to be the beginning of phase inversion. As the water fraction decreases, it can also be observed that the distribution becomes wide across all the measured locations and the phenomenon spreads towards the bottom of the pipe cross section. This supports the observation found using the ERT system in Figure 4.3 where the phase inversion process has the same downward shift.

Appendix B – Matlab Code for Pressure Gradient Prediction

A. MAIN EXECUTION CODE

```
%%%%%%%%%%%%%%%%%
%Fluid properties%
%%%%%%%%%%%%%%%%%

%density of oil (denso), density of water (densw)
denso=828; densw=1000;
%viscosity of oil (visco), viscosity of water (viscw)
visco=5.5*0.001; viscw=1.0*0.001;
%Interfacial tension (ST)
ST=39.6*0.001;

%%%%%%%%%%%%%%%%
%Operation Input%
%%%%%%%%%%%%%%%%

%gravity (g), pipe diameter (D)
g=9.81;  D=0.038;
%Pipe area (A)
A=pi*D^2/4;
%Curvature (0-Flat Interface, 1-Curved Interface)
curve=0;

%%%%%%%%%%%%%%%%%%%%%%%%%%%%%%%
%Critical amplitude at the onset of entrainment (Talal 2006)%
%%%%%%%%%%%%%%%%%%%%%%%%%%%%%%%

a_oil=D/10;
a_water=D/10;
hwstart=min(a_oil,a_water);

%%%%%%%%%%%%%%%%%
%Flow rate (l/min)          %
%%%%%%%%%%%%%%%%%

Flow_rates=[ ];
```

```
%%%%%%%%%%%%%
%flow rate conversion (m3/s)%
%%%%%%%%%%%%%%%

conversion=0.0000166667;
Q=conversion*Flow_rates;

%Friction factor mode (refer to fric.m for detail)
fric_no=2;

%Critical water fraction for phase inversion
wfc=0.34;

%Initialisation (Do Not Change)
N_hw=(D-2*hwstart)/0.0001;
N_fr=size(Q,1);
output=[];
output1=[];
output2=[];

%Execution Script (Do Not Change)
for m=1:N_fr
    Qo=Q(m,2);
    Qw=Q(m,1);
    hwnew=hwstart;
    fr=Qw/(Qw+Qo)*100
    olddiff=6000;
    count=0;
    for i = 1:N_hw
        if hwnew<D-hwstart
            [Ento_w,Entw_o]=entrain1(Qo,Qw,hwnew,D,denso, densw, visco, viscw, ST,
a_oil, a_water, curve, fric_no);
            if (Entw_o >=1)||(Ento_w>=1)||(imag(Ento_w) || imag(Entw_o))
            elseif (Entw_o>=wfc)&&(Ento_w>=(1-wfc))
            else
                count=count+1;
                [dPu,dPl, dPa,UL,LL,Entw,Ento, Reu, Rel, Au,Al]=dP1(hwnew, Qo, Qw,
denso, densw,Entw_o,Ento_w, visco, viscw, D, curve, fric_no, wfc);
                if abs((dPu-dPl)/dPa*100)>=2 || ((UL==1)&&(LL==1))||((UL==2)&&(LL==2))
                else
                    output=[output;fr hwnew UL LL dPa/1000 abs((dPu-dPl)/dPa*100)];
                end
            end
            hwnew=hwnew+0.0001;
        else
            break
```

```
        end
    end
    OP=isempty(output);
    if (OP==1)
        [dPa]=homo(Qo, Qw, denso, densw, visco, viscw, D, curve, fric_no);
        output1=[output1;fr 0 0 0 dPa/1000 0];
    else
        output2=sortrows(output,[1,6]);
        idx=find(min((output2(:,6))));
        output1=[output1;output2(idx,:)];
        output=[];
    end
end

csvwrite('output.csv', output1)
```

B. ENTRAINMENT MODULE

```
function [Ento_w1,Entw_o1]=entrain(Qo,Qw,hwnew,D,denso, densw, visco, viscw, ST,
a_oil, a_water, curve, fric_no)

%Calculating entrainment fraction
%Entw_o is the entrainment fraction of water in oil
%Ento_w is the entrainment fraction of oil in water
%Um=mixture velocity
Entw_o=0;
Ento_w=0;
[Si,So,Sw,A,Ao,Aw,Hw,Ho]=geo(hwnew,D,curve);
Um=(Qo+Qw)/A;
Usw=Qw/A;
Uso=Qo/A;

hwinput=hwnew;
[Tw,To,Ti]=hwF(hwinput, Usw, Uso,  D, denso, densw, visco, viscw, curve, fric_no);
Uw=Usw/Hw;
Uo=Uso/Ho;

if Uo/Uw>=0.98 && Uo/Uw<1.05
    Dw=4*Aw/(Sw); Do=4*Ao/(So);
elseif Uo>Uw
    Dw=4*Aw/(Sw); Do=4*Ao/(So+Si);
else
    Dw=4*Aw/(Sw+Si); Do=4*Ao/(So);
end
```

```
%Reynolds number
Rew=Dw*Uw*densw/viscw;
Reo=Do*Uo*denso/visco;

%Drag coefficient
Cd=2.7e-7*Reo^(0.77)*Rew^(0.86);

%Wavelength (lamda)
lamda=1*D;

%Prediction of entrainment fraction of oil in water (Ento_w)
%Calculating the critical amplitude of oil waves at the new conditions
%amplitude (al)
al=0.00;
k=real((D-hwnew)/0.000001);
   for m=1:k
      al=al+0.000001;
      hap=hwnew+al;
      [Siap,Soap,Swap,A,Aoap,Awap,Hwap,Hoap]=geo(hap,D,curve);
      Soapeak=Soap;
      Siapeak=Siap;
      Aoapeak=Aoap;
      Awapeak=Awap;

      hat=hwnew-al;
      [Siat,Soat,Swat,A,Aoat,Awat,Hwat,Hoat]=geo(hat,D,curve);
      Siatrough=Siat;
      Soatrough=Soat;
      Aoatrough=Aoat;
      Awatrough=Awat;

      Aw1=Awapeak;
      Aw2=Awatrough;
      Ao1=Aoapeak;
      Ao2=Aoatrough;

      Uo2=Uo*(Ao/Ao2);
      Uw2=Uw*(Aw/Aw2);

      %Drag force (Fd)
      Fd=0.5*densw*(Aw-Aw2)*Cd*(Uw2-Uo2)^2;

      %Surface tension force (Fst)
      L=(al^2+(lamda/2)^2)^0.5;
      Fst=2*Si*ST*(lamda/2)/L;
      Total=Fd-Fst;
```

```
    if Total>=0
        break
    end
    end
  end

%Amount of oil transfer to the water phase
Vent_o=0.5*((a_oil-al)*lamda*Si/(pi));
vdfo=0.051*(Uso/Um)^-2.08*(Tw/densw)^0.5;

%Calculation of the entrainment fraction of oil in water (Ento_w)
C_oil=Vent_o*denso*abs(Uw2-Uo2)/(Si*lamda^2*vdfo);
Ento_w=((densw)-((densw)^2-4*(densw-denso)*C_oil)^0.5)/(2*(densw-denso));

%Calculating the critical amplitude of water waves at the new condition
%amplitude (au)
au=0.00;
k=real((D-hwnew)/0.000001);
  for m=1:k
    au=au+0.000001;
    hap2=hwnew+au;
    [Siap2,Soap2,Swap2,A,Aoap2,Awap2,Hwap2,Hoap2]=geo(hap2,D,curve);
    Soapeak=Soap2;
    Siapeak=Siap2;
    Aoapeak=Aoap2;
    Awapeak=Awap2;

    hat2=hwnew-au;
    [Siat2,Soat2,Swat2,A,Aoat2,Awat2,Hwat2,Hoat2]=geo(hat2,D,curve);
    Siatrough=Siat2;
    Soatrough=Soat2;
    Aoatrough=Aoat2;
    Awatrough=Awat2;

    Aw1=Awapeak;
    Aw2=Awatrough;
    Ao1=Aoapeak;
    Ao2=Aoatrough;

    Uo1=Uo*(Ao/Ao1);
    Uw1=Uw*(Aw/Aw1);

    %Drag force (Fd)
    Fd=0.5*densw*(Aw1-Aw)*Cd*(Uw1-Uo1)^2;

    %Surface tension force (Fst)
    L=(au^2+(lamda/2)^2)^0.5;
```

```
        Fst=2*Si*ST*(lamda/2)/L;
        Total=Fd-Fst;
        if Total>=0
            break
        end
    end
end
%Amount of water transfer to the oil phase
Vent_w=0.5*((a_water-au)*lamda*Si/(pi));
vdfw=0.077*(Usw/Um)^-1.8*(To/denso)^0.5;

%Calculation of the entrainment fraction of oil in water (Ento_w)
C_water=Vent_w*densw*abs(Uw1-Uo1)/(Si*lamda^2*vdfw);
Entw_o=((denso)-((denso)^2-4*(denso-densw)*C_water)^0.5)/(2*(denso-densw));

Ento_w1=(Ento_w)/(1-Ento_w+densw/denso);
Entw_o1=(Entw_o)/(1-Entw_o+denso/densw);
```

C. SHEAR STRESS MODULE

```
function [Tw,To,Ti]=hwF(hwinput, Usw, Uso,  D, denso, densw, visco, viscw, curve,
fric_no)

[Si,So,Sw,A,Ao,Aw,Hw,Ho]=geo(hwinput,D,curve);
Uw=Usw/Hw;
Uo=Uso/Ho;

if Uo/Uw>+0.98 && Uo/Uw<1.05
    Dw=4*Aw/(Sw); Do=4*Ao/(So);
elseif Uo>Uw
    Dw=4*Aw/(Sw); Do=4*Ao/(So+Si);
else
    Dw=4*Aw/(Sw+Si); Do=4*Ao/So;
end

%Reynolds number
Rew=Dw*Uw*densw/viscw;
Reo=Do*Uo*denso/visco;

%Reynolds number of interface
if Uo>Uw
    Rei=Si*Uo*denso/(pi*visco);
    densf=denso;
else
    Rei=Si*Uw*densw/(pi*viscw);
    densf=densw;
end
```

```matlab
%friction factors
[fw,fo,fi]=fric(Rew,Reo,Rei,Ho,Hw,Do,Dw,fric_no);

%shear stress
Tw=fw*densw*Uw*abs(Uw)/2;
To=fo*denso*Uo*abs(Uo)/2;
if Uo/Uw >= 0.98 && Uo/Uw<1.05
    Ti=0;
else
    Ti=fi*densf*(Uo-Uw)*abs(Uo-Uw)/2;
end

%Two Fluid Model
%Fhw=To*So/Ao+Ti*Si*(1/Aw+1/Ao)-Tw*Sw/Aw;
```

D. DIFFERENTIAL PRESSURE MODULE (LAYERED FLOW)

```matlab
function [dPu,dPl, dPa,UL,LL,Entw,Ento, Reu, Rel, Au,Al]=dP1(hwinput, Qo, Qw,
denso, densw,Entw_o,Ento_w, visco, viscw, D, curve, fric_no, wfc)

%Geometry
[Si,Su,Sl,A,Au,Al,Hw,Ho]=geo(hwinput,D,curve);

%Error test for Input Entrainment
if (imag(Ento_w) | imag(Entw_o))~=0
  Entw_o=NaN;
  Ento_w=NaN;
end

%Error test for entrainment
if Ento_w==NaN
  Ento1=NaN;
  return
end

if Entw_o==NaN
  Entw1=NaN;
  return
end

%Phase Inversion
%Flow Pattern: 1-W/O, 2-O/W, 3-Pure oil, 4-Pure water
if Entw_o<wfc
        if Ento_w<(1-wfc);
        Entw=Entw_o;
```

223

```
      viscu=visco;
      Uo=Qo/(Au);
      Ento=Ento_w;
      viscl=viscw;
      Uw=Qw/(Al);
      UL=1;
      LL=2;
   elseif Ento_w<1
      Entw=Entw_o;
      viscu=visco;
      Uo=Qo/(Au);
      Ento=(1-Ento_w);
      viscl=visco;
      Uw=Qw/(Al);
      UL=1;
      LL=1;
   else
      %Invalid Scenario
      Entw=Qw/(Qo+Qw);
      viscu=visco;
      Uo=Qo/(Au);
      Ento=0;
      viscl=visco;
      Uw=Qw/(Al);
      UL=1;
      LL=3;
   end
elseif Entw_o<1
      if Ento_w<(1-wfc);
        Entw=(1-Entw_o);
      viscu=viscw;
      Uo=Qo/(Au);
      Ento=Ento_w;
      viscl=viscw;
      Uw=Qw/(Al);
      UL=2;
      LL=2;
   elseif Ento_w<1
      %Invalid Scenario
      Entw=(1-Entw_o);
      viscu=viscw;
      Uo=Qo/(Au);
      Ento=(1-Ento_w);
      viscl=visco;
      Uw=Qw/(Al);
      UL=2;
```

```matlab
          LL=1;
      else
          %Invalid Scenario
          Entw=(1-Entw_o);
          viscu=visco;
          Uo=Qo/(Au);
          Ento=0;
          viscl=visco;
          Uw=Qw/(Al);
          UL=2;
          LL=3;
      end
  else
      if Ento_w<(1-wfc);
          %Invalid Scenario
              Entw=0;
          viscu=viscw;
          Uo=Qo/(Au);
          Ento=Ento_w;
          viscl=viscw;
          Uw=Qw/(Al);
          UL=4;
          LL=2;
      elseif Ento_w<1
          %Invalid Scenario
          Entw=0;
          viscu=viscw;
          Uo=Qo/(Au);
          Ento=(1-Ento_w);
          viscl=viscw;
          Uw=Qw/(Al);
          UL=4;
          LL=1;
      else
          %Invalid Scenario
          Entw=0;
          viscu=viscw;
          Uo=Qo/(Au);
          Ento=0;
          viscl=viscw;
          Uw=Qw/(Al);
          UL=4;
          LL=3;
      end
  end
```

```matlab
%Mixture Density
densu=(Entw)*densw+(1-Entw)*denso;
densl=(Ento)*denso+(1-Ento)*densw;

%Mixture Viscosity
muu=viscu*(1-Entw)^-2.5;
mul=viscl*(1-Ento)^-2.5;

if Uo/Uw>+0.98 && Uo/Uw<1.05
    Dw=4*Al/(Sl); Do=4*Au/(Su);
elseif Uo>Uw
    Dw=4*Al/(Sl); Do=4*Au/(Su+Si);
else
    Dw=4*Al/(Sl+Si); Do=4*Au/Su;
end

%Reynolds number
Rel=Dw*Uw*densl/mul;
Reu=Do*Uo*densu/muu;

%Reynolds number of interface
if Uo>Uw
    Rei=Si*Uo*densu/(pi*muu); densf=densu;
else
    Rei=Si*Uw*densl/(pi*mul);densf=densl;
end

%friction factors
[fw,fo,fi]=fric(Rel,Reu,Rei,Ho,Hw,Do,Dw,fric_no);
if LL==1
    fl=fw/(1+1.125*Ento);
else
    fl=fw/(1+1.125*Ento);
end

if UL==1
    fu=fo/(1+1.125*Entw);
else
    fu=fo/(1+1.125*Entw);
end

fi=fi;

%shear stress
Tl=fl*densl*Uw*abs(Uw)/2;
Tu=fl*densu*Uo*abs(Uo)/2;
```

```
if Uo/Uw >= 0.98 && Uo/Uw<1.05
   Ti=0;
else
   Ti=fi*densf*(Uo-Uw)*abs(Uo-Uw)/2;
end

%Two Fluid Model
if Uo>Uw
   dPu=Tu*Su/Au-Ti*Si*(1/Au);
   dPl=Tl*Sl/Al+Ti*Si*(1/Al);
else
   dPu=Tu*Su/Au+Ti*Si*(1/Au);
   dPl=Tl*Sl/Al-Ti*Si*(1/Al);
end

dPa=(dPu+dPl)/2;
Ento1=100*Ento;
Entw1=100*Entw;
```

E. PRESSURE GRADIENT MODULE (HOMOGENEOUS MODEL)

```
function [dPa]=homo(Qo, Qw, denso, densw, visco, viscw, D, curve, fric_no)

A=pi*D^2/4;
fr=Qo/(Qw+Qo)*100;
WF=Qw/(Qo+Qw);
OF=Qo/(Qo+Qw);
densm=denso*OF+densw*WF;
muw=visco*(1-WF)^-2.5;
muo=viscw*(1-OF)^-2.5;
if muw<=muo
   mum=muw;
else
   mum=muo;
end

Um=(Qo+Qw)/A;
Reh=densm*D*Um/mum;
[fh]=hfric(Reh,fric_no);
if muw<=muo
   fh1=fh/(1+1.25*WF);
else
   fh1=fh/(1+1.25*OF);
end

dPu=0;
```

```
dPl=0;
dPa=(2*fh1*densm*Um^2)/D;
```

F. GEOMETRY MODULE

```
function [Si,So,Sw,A,Ao,Aw,Hw,Ho]=geo(hwinput,D,curve)

if curve==0
   %disp('flat interface');
   hw=hwinput;
   h=2*(hw/D)-1;
   Si=D*((1-h^2)^(1/2));
   So=D*acos(h);
   Sw=D*pi-So;
   A=pi*D^2/4;
   Ao=D*((So)-(Si*h))/4;
   Aw=A-Ao;
   Hw=Aw/A;
   Ho=Ao/A;
elseif curve==1
   %disp('curved interface')
   hw=hwinput;
   X=(hw^2+4*(D/2)*hw)/(2*(D/2)+2*hw);
   teta1=2*acos(((D/2)-X)/(D/2));
   teta2=2*acos((2*(D/2)-(X-hw))/(2*(D/2)));
   A=pi*D^2/4;
   Aw=(0.5*((D/2)^2)*(teta1-sin(teta1)))-(0.5*(2*(D/2)^2)*(teta2-sin(teta2)));
   Ao=A-Aw;
   Sw=(D/2)*teta2;
   So=pi*D-Sw;
   Si=2*(D/2)*teta2;
   Hw=Aw/A;
   Ho=Ao/A;
end
```

G. FRICTION FACTOR MODULE (LAYERED FLOW)

```
function [fw,fo,fi]=fric(Rel,Reu,Rei,Hu,Hl,Do,Dw,fric_no)

%Friction factor for Upper Layer
%if Reu<4000
   %fo=(1/(-
2*log10((0.015/3.70)+((4.518*log10(1/7*Reu))/(Reu*(1+1/29*Reu^0.52*(0.015)^0.7))))
))^2;
   %fo=7e-10*(Reu)^2; %(S.W. Churchill (1973), AIChE J, 19(2):375)
```

```
   %fo=sqrt(1/(-2*log10((0.0015/3.7065)-(5.0272/Reu)*log10((0.0015/3.827)-
(4.567/Reu)*log10((0.0015/7.7918)^0.9924+(5.3326/(208.815+Reu))^0.9345)))));
   %fo=16*Reu^-1;
%else
   if fric_no==1
      fo=0.079*Reu^-0.25;
   elseif fric_no==2
      fo=0.046*Reu^-0.2; % Taitel & Dukler (1976)
   elseif fric_no==3
      fo=0.764*(Hu*Reu)^(-0.562); %Srichai (1994)
   elseif fric_no==4
      fo=(-3.6*log10((6.9/Reu)+(1*10^(-5)/(3.7*Do))^1.1))^(-2); %Haaland (1983);
Hadzlabdic & Oliemans (2007)
   elseif fric_no==5
      fo=(-4*log10((1*10^(-5)/(3.7*Do))-(5.02/Reu)*log10((1*10^(-5)/(3.7*Do))-
(5.02/Reu)*log10((1*10^(-5)/(3.7*Do))+(13/Reu)))))^(-2); %Zigrang & Sylvester (1982)
   else
      return
   end
%end
```

## H. FRICTION FACTOR MODULE (HOMOGENEOUS MODEL)

```
function [fh]=hfric(Reh,fric_no)

if fric_no==1
   fh=0.079*Reh^-0.25;
elseif fric_no==2
   fh=0.046*Reh^-0.2;
else
   disp('No friction factor model chosen')
   return
end
```

Appendix C – Grid Sensitivity Test for CFD Simulation

A grid sensitivity test was conducted to define the optimal grid structure for the CFD simulations conducted in Chapter 8. The optimal grid structure will be used to simulate a pipe section of 3m in length and 38mm in internal diameter. The test was done by changing the number of cells in the vertical height of a rectangular slab (see Figure C-1). Three structures of different grid sizes are chosen – 40 cells (grid 40), 60 cells (grid 60) and 80 cells (grid 80). The length of the slab is kept at 3100 cells including 100 cells to represent the splitting inlet as introduced in Chapter 3. Table C-1 presents the total number of grid points and elements in each structure.
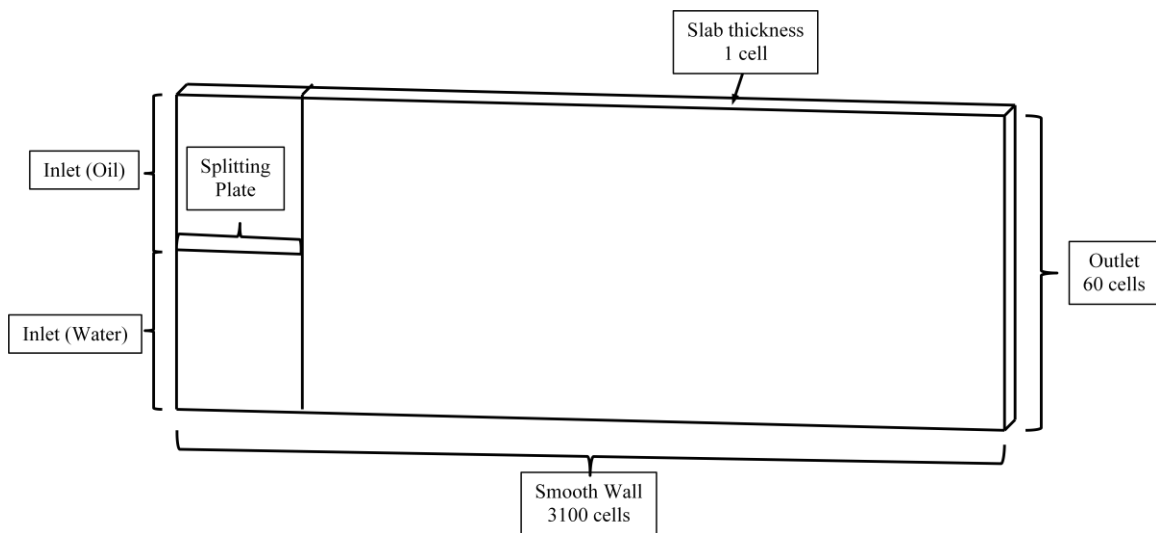
Figure C-1: Sample schematics of simulation domain with a vertical height consisting of 60 cells.

The simulation was tested by running an oil/water flow at a mixture velocity of 3m/s. Oil was inputted as the dispersed phase while the water being the continuous phase. Drop size was set at 0.5mm (smallest drop size group found in experiment). An input dispersed phase fraction of 0.2 was chosen. k-ε turbulence model was used. Ishii and Zuber (1979) model was applied as the drag force for the dispersion. Lift force with coefficient of 0.5

was used together with Lopez de Bertodano model for the turbulent dispersion force (coefficient: 1.0).

The calculations achieved convergence of less than 10^{-6} in approximately 2 hours (grid 40), 48 hours (grid 60) and 120 hours (grid 80) using a workstation having 4GB RAM and 3.0GHz Pentium Core2Duo CPU processor.

Case Name	Grid 40	Grid 60	Grid 80
Vertical Cell Size	40	60	80
Number of Grid Points	250282	372322	494362
Number of Cell Elements	122000	183000	244000

Table C-1: Number of grid points and cell elements in structures used in the grid sensitivity test.
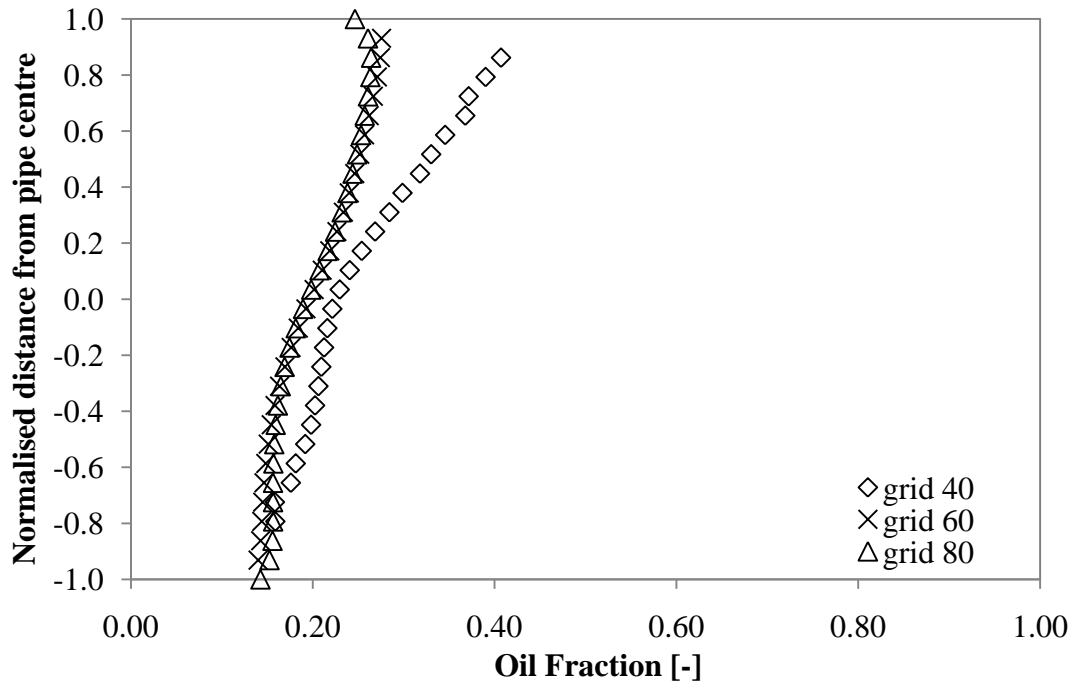
Figure C-2: Comparison of results on the dispersed phase fraction along a vertical diameter at the end of the pipe with 3m in length. An input dispersed phase fraction of 0.2 is chosen for all 3 cases.

231

Figure C-2 presents the comparison of oil fraction at the end of the grid structure (i.e. 3m from end of split plate). While all 3 cases have shown mixing of the two phases, grid 40 deviates from the other cases. The results from grid 60 and grid 80 are comparable with an average difference of 3.5%. A possible reason for the deviation of grid 40 is because the grid size may be too large and fails to simulate the motion of the 0.5 mm drops.

In conclusion, grid 60 will be used for subsequent simulations in Chapter 8 as it offers the optimal grid structure with a relatively short runtime compared with grid 80.